

**AN ANALYSIS OF A PRESSURE COMPENSATED CONTROL SYSTEM
OF AN AUTOMOTIVE VANE PUMP**

by

Ryan P. Jenkins

A Dissertation

Submitted to the Faculty of Purdue University

In Partial Fulfillment of the Requirements for the degree of

Doctor of Philosophy



School of Mechanical Engineering

West Lafayette, Indiana

May 2019

**THE PURDUE UNIVERSITY GRADUATE SCHOOL
STATEMENT OF COMMITTEE APPROVAL**

Dr. Andrea Vacca, Chair

Department of Agricultural and Biological Engineering

Dr. Peter H. Meckl

Department of Mechanical Engineering

Dr. Steven F. Son

Department of Mechanical Engineering

Dr. Dennis Buckmaster

Department of Agricultural and Biological Engineering

Approved by:

Dr. Jay P. Gore

Head of the Graduate Program

Dedicated to my God and Family

ACKNOWLEDGMENTS

First, I must acknowledge my Heavenly Father and Savior Jesus Christ for their role in leading me to attend Purdue University and accept a position at the Maha Fluid Power Research Center. All I have accomplished is because of the strength, intelligence, talents, and opportunities they have blessed me with. I thank them for all of the answered prayers and inspiration through the Holy Ghost that I have received along the way.

Second, I would like to thank my incredible wife Jessica for all her support, love, patience, and encouragement as we've taken this journey together. I could not have done this without her. I would also like to thank my amazing kids, Hannah and Matthew, for providing the much needed and looked forward to diversions every evening to keep me from burning out. I also want to thank my currently unborn second daughter for providing a compelling reason to finish strong at the beginning of the year before she joined the party.

Third, I would like to recognize my advisor, Monika Ivantysynova, for her patience, support, and guidance. This research, and each of my publications, would have turned out much differently without her experience and insights. I'm very grateful for the opportunity to work with her and deeply saddened that she passed away before the completion of this work. In many ways, the last chapters of this thesis are dedicated to her as she helped me get everything I needed (even if I still had work to do) for them before her passing and well before I arrived at the writing stage.

Fourth, I would like to recognize Andrea Vacca for stepping in as my committee chair and supporting me in my work after Monika's passing. I know this was a challenging time for him and will always be impressed with how he handled it and grateful for the opportunity to work more closely with him.

Finally, I would like to thank the many others have helped me along the way in reaching various checkpoints in my research. Specifically, I would like to acknowledge the contributions of Pratik Chawla, Giovanni Napolitano, Raphael Seifried, and Xiaofan Guo at various stages of the development of the experimental setup used for much of this research and in the analysis of the resulting data. I would also like to acknowledge Anthony Franklin for his invaluable assistance in constructing and assembling the experimental setup and Ford Motor Company for providing various key components.

TABLE OF CONTENTS

LIST OF TABLES	8
LIST OF FIGURES	9
LIST OF ABBREVIATIONS.....	15
NOMENCLATURE	16
ABSTRACT.....	20
1. INTRODUCTION	21
1.1 Background.....	21
1.2 Pump Pressure Control	22
1.3 A Case Study.....	25
1.3.1 The Variable Displacement Vane Pump.....	25
1.3.2 The Pressure Compensation Control Circuit.....	27
1.3.3 Typical Operating Conditions.....	28
1.4 Research Objectives.....	30
1.5 Dissertation Organization	31
2. STATE OF THE ART	32
2.1 VDVP Plant Modeling.....	32
2.1.1 Modeling Approaches.....	32
2.1.2 Model Validation	35
2.2 System Identification	38
2.3 Advanced Pump Control Systems	39
2.4 Intended Contributions.....	41
3. LUMPED PARAMETER VDVP DC MODULE	43
3.1 DC Pressure Build Up Equation	44
3.2 Pump Geometry	45
3.3 DC Volume Calculation.....	48
3.4 DC Volume Rate of Change	49
3.5 DC Flow Equations.....	50
3.6 Equivalent Area Files.....	51
3.7 Oil Model.....	56

3.8	Port Modules.....	57
3.9	Internal Forces: Rotor Torque.....	58
3.10	Internal Forces: Moment Applied to Stator.....	61
3.11	Summary.....	67
4.	EXPERIMENTAL VALIDATION SETUP.....	68
4.1	Modified Case Study Pump.....	69
4.1.1	Top Case Modifications.....	69
4.1.2	Pump Wall Modification.....	72
4.1.3	Pump Shaft Extension.....	74
4.2	Pump Mounting Flange.....	75
4.3	Reservoir Design.....	76
4.4	Port Adapter Blocks.....	76
4.5	Additional Test Rig Hardware.....	77
4.6	Data Acquisition and Control System.....	78
5.	DC MODULE VALIDATION STUDY.....	80
5.1	DC Pressure Profile Post-Processing Algorithm.....	81
5.2	Measured DC Pressure Profile.....	86
5.3	Validation Comparison.....	88
5.4	Additional Simulation Results and Comparisons.....	91
5.5	Effect of External Leakages.....	94
5.6	Takeaways.....	97
6.	ADJUSTMENT SYSTEM DYNAMICS MODULE.....	101
6.1	Experimental Setup.....	103
6.2	Damping Coefficient CS	105
6.3	Nonlinear Spring Rate k	106
6.4	Model Validation of the Stator Equation of Motion.....	108
6.5	Control Chamber Pressure Model.....	110
6.6	Summary.....	114
7.	BASELINE PUMP CONTROL SYSTEM.....	115
7.1	V2 Representation.....	117
7.2	V3 Representation.....	119

7.3	V1 Representation.....	124
7.4	Performance Analysis	128
7.5	Summary.....	135
8.	PROPOSED PUMP CONTROL SYSTEM	136
8.1	Required Valve Characteristics.....	137
8.2	Proof of Concept in Simulation	140
8.2.1	Control Valve Model	140
8.2.2	Simplified Plant	142
8.2.3	Initial Controller Design	144
8.2.4	Results.....	145
8.3	Experimental Proof of Concept	146
8.3.1	Test Setup	147
8.3.2	Measurement Results.....	148
8.3.3	Model Validation.....	151
8.4	Summary.....	153
9.	ADVANCED PRESSURE COMPENSATION CONTROL.....	155
9.1	Cascaded Control Scheme	155
9.2	Control Valve Flow Control	157
9.3	VDVP Displacement Control	160
9.4	Supervisory Level Pressure Control	163
9.5	Results and Comparison	164
9.6	Summary.....	167
10.	CONCLUSIONS.....	168
	REFERENCES	170
	APPENDIX A.....	177
	APPENDIX B	182
	APPENDIX C	211
	APPENDIX D.....	214
	VITA.....	215
	PUBLICATIONS.....	216

LIST OF TABLES

Table 1: Comparison of the measured and nominal (from CAD and assumed in the DC Module) angular spans for each DC in the case study pump.	86
Table 2: Comparison of simulated and measured pump efficiencies.	92
Table 3: Summary of the relative sensitivity of various pump performance parameters to changes (one at a time) in air content, fluid temperature, pump pressure levels, and pump speed.	98
Table 4: Calculated bias spring rates for various combinations of spring parameters.	106

LIST OF FIGURES

Figure 1: Schematic representations of a direct pump pressure control and a pilot operated pump pressure control.	23
Figure 2: Schematic representation of a basic electrohydraulic pump pressure control assembly.	24
Figure 3: Component identification illustration of the 7-vane pivoting-cam type variable displacement vane pump analyzed in the case study.	26
Figure 4: Baseline pressure compensation pump control system architecture for an automatic transmission supply VDVP evaluated in the case study.	27
Figure 5: Duty cycle representative of the typical operation of the pressure compensated VDVP for an automatic transmission supply analyzed in the case study.	29
Figure 6: Transducer locations for the measurement setup described in [32].	37
Figure 7: Pressure transducer tubing geometry, adapted from [33].	37
Figure 8: Overview of modeling approach illustrating major system model components.	43
Figure 9: General system model block diagram highlighting the degree of complexity in each module of the overview presented in Figure 8.	44
Figure 10: Coordinate system used in the VDVP model along with some basic geometric parameters.	45
Figure 11: Naming convention of the individual DC with their respective angular spans from the case study 3D CAD model.	46
Figure 12: Triangles used to define λ_i	47
Figure 13: Network of orifice connections between the various control volumes considered in the lumped parameter pump model.	51
Figure 14: Example control volume geometries extracted from the 3D CAD model of the pump representing the suction port (blue), delivery port (red), and a single DC at an arbitrary position close to ϕODC at maximum β	53
Figure 15: Illustrative example of the procedure of analyzing section cuts in the 3D CAD model to evaluate the area file value for a given fluid geometry configuration. Image A: Streamlines from 3D CFD simulation. Image B: 3D CAD model at the same position. Image C: Section cut using the DC geometry. Image D: Resulting fluid geometry of the port. Image E: Comparison of the measured areas of faces 1 and 2, with face 2 being the	

minimum perpendicular area along the streamlines indicated by the CFD simulation results shown in Image A.....	54
Figure 16: Example DC 2 area file results showing the IDC transition region in detail to illustrate the timing effects and relative magnitude of the restricted area regions. The ϕ angles here are measured clockwise from ϕODC at maximum eccentricity.	55
Figure 17: Detail view of the IDC region comparing the DC 1 and DC 2 area files at full displacement to show timing effects with ϕ again measured clockwise from ϕODC	56
Figure 18: Diagrams used to determine expressions to calculate rotor torque.	58
Figure 19: Diagram showing vector definitions used in determining the DC pressure induced stator moment.....	61
Figure 20: Hydraulic circuit diagram for the custom test rig featuring the baseline control system used in the case study application.	68
Figure 21: DC pressure transducer locations and orientation relative to other pump components as shown by the 3D CAD model.....	69
Figure 22: 3D CAD image showing location of the DC pressure transducer pilot holes relative to the rotor and stator bodies.....	70
Figure 23: Target viewing windows for the six pressure transducers installed in the case study pump to measure the DC pressure profile.....	71
Figure 24: Parameter definitions used in converting the linear displacement of the stator measured by the LVDT to angular displacement in terms of β	73
Figure 25: 3D CAD rendering of the modified pump assembly complete with the inlet adapter block, LVDT, and pump inlet instrumentation.	74
Figure 26: 3D CAD rendering of the custom pump mounting flange.	75
Figure 27: 3D CAD rendering of the test rig assembly to illustrate the general spatial orientation of the components relative to one another and their relative sizes.	77
Figure 28: Picture taken of the completed experimental setup in April of 2016 with the polycarbonate cover removed.	78
Figure 29: Overview of the DAQ/Control setup showing the NI cRIO products used and the sampling rates set for each of the modules for the DC pressure measurement study.....	79
Figure 30: Raw DC pressure profile measurements from the DC Module validation study.	82
Figure 31: Angular distances between pilot hole locations for Sensor 3 and Sensors 1 and 2 for use in determining offsets.	83

Figure 32: Illustration of the “baton passing” post-processing algorithm.	85
Figure 33: First example of a measured DC pressure profile.	87
Figure 34: Histogram showing standard deviation between the measured DC pressure profiles over five revolutions for the first example.....	87
Figure 35: Second example of a measured DC pressure profile.....	88
Figure 36: Histogram showing standard deviation between the measured DC pressure profiles over five revolutions for the second example.....	88
Figure 37: Comparison between the simulated DC pressure profile and the measured DC pressure profile for the first example’s operating conditions.	89
Figure 38: Comparison between the simulated DC pressure profile and the measured DC pressure profile for the second example’s operating conditions.....	90
Figure 39: Comparison of the simulated pump outlet flow and pump torque to the theoretical performance of the pump at 100% displacement.....	91
Figure 40: Important pump geometry factors considered in the DC Module and their comparison to the simulated DC pressure and flow profiles for the operating conditions corresponding to Figure 39 and Table 2 and where ϕ is measured CW from ϕODC	93
Figure 41: Sensitivity of the DC Module pressure calculations to external leakages.	95
Figure 42: Plots summarizing the distribution of the calculated external leakages term corresponding to an individual DC over a shaft revolution and the correlation of this leakage term to other pertinent DC parameters and DC Module outputs.....	96
Figure 43: Simulated relative sensitivity of the pump outlet flow QA to air content, fluid temperature, pump pressure levels, and pump speed.....	98
Figure 44: Simulated relative sensitivity of the internal forces $M1$ to air content, fluid temperature, pump pressure levels, and pump speed.....	99
Figure 45: Simulated relative sensitivity of both the pump outlet flow QA and the internal forces $M1$ to changes in the displacement β	100
Figure 46: Stator free body diagram used to derive the equation of motion.	101
Figure 47: Example $M1$ profile over a single shaft revolution for the operating conditions corresponding to the example simulation in Section 5.4.	102
Figure 48: Hydraulic circuit diagram for the experimental setup used for the stator dynamics validation measurement study.....	103

Figure 49: Example line pressure and eccentricity measurement data from the stator dynamics validation study.	105
Figure 50: Progressive bias spring rate as a function of β	108
Figure 51: Higher frequency, higher amplitude stator dynamics validation example.....	108
Figure 52: Lower frequency, lower amplitude stator dynamics validation example.....	109
Figure 53: Example CFD analysis results for the leakage flow across the stator pivot for a control chamber gauge pressure of 7bar with μ_{oil} of 46cP.	112
Figure 54: Pivot groove leakage CFD data and the fitted Equation (6.14) curves.	112
Figure 55: Case drain CFD data for multiple viscosities and the fitted model given by Equation (6.17).	113
Figure 56: General system model block diagram with completed modules faded out to highlight which components have been completed and discussed to this point.	114
Figure 57: Overview of the black-box representation of the case study control system.	115
Figure 58: Transfer function $G2$ steady state gain schedule.	117
Figure 59: Validation results for the transfer function $G2$ with “pump on” data.	118
Figure 60: Steady state gain schedules for transfer functions $G3A$ and $G3B$	119
Figure 61: “Pump on” validation results for the transfer function representation of $V3$	120
Figure 62: “Pump off” validation results for the transfer function representation of $V3$ for a large amplitude 0.5Hz sinusoidal command profile.	121
Figure 63: “Pump off” validation results for the transfer function representation of $V3$ for a large amplitude 0.5Hz sinusoidal command profile with the “pump off” gain schedules.	122
Figure 64: Alternate gain schedules for the $V3$ representation in “pump off” cases.	123
Figure 65: Block diagram description of the black-box representation of $V1$	124
Figure 66: Offset value schedule used in $V1$ representation.	126
Figure 67: “Pump on” validation results for the $V1$ representation.	127
Figure 68: “Pump off” validation results for the $V1$ representation at 10bar and small amplitude 5Hz sinusoidal command profile.	128
Figure 69: Block diagram reduction of the case study control system black-box model for performance analysis purposes.	129

Figure 70: Bode diagram of the case study control system representation.....	130
Figure 71: Map of the poles and zeros of GA in the complex plane.	130
Figure 72: Critical frequencies for the adjustment system dynamics model.	131
Figure 73: Typical system response to a change in regulation set point taken from vehicle measurements in the case study materials.	133
Figure 74: Comparison of the case study's current control system architecture and the proposed active electrohydraulic control system architecture.....	136
Figure 75: Example engine speed and line pressure traces taken from vehicle data using the case study system with predicted pump displacements.	137
Figure 76: Required control valve flow gain calculations for the highlighted event in Figure 75 with the leading edge highlighted here for reference.....	139
Figure 77: Proposed system block diagram showing the interconnection of the control valve, its amplifier, and the controller with the system plant consisting of the pump and load line.	140
Figure 78: Simulated performance comparison between the proposed electrohydraulic pressure compensation solution equipped with the valve identified in Section 8.1 and using the simplified nonlinear pump model against the measured system response taken from the vehicle measurements used in Section 8.1.....	145
Figure 79: Zoomed-in view of the proposed solution performance comparison presented in Figure 78 to highlight the differences in the simulated and baseline responses.	146
Figure 80: Circuit diagram for the experimental setup established for proving the proposed control system experimentally.	147
Figure 81: Measurement results from the constant reference pressure test of the proposed control system with a variable speed input and constant load restriction.	149
Figure 82: Detail view plots corresponding to Figure 81.	149
Figure 83: Measurement results from the variable reference pressure test of the proposed control system with a variable speed input and constant load restriction.	150
Figure 84: Detail view plots corresponding to Figure 83.	150
Figure 85: Comparison of the measured and simulated pump outlet pressure and displacement for a varying pump speed to the proposed control system design.	152
Figure 86: Detail view of the results presented in Figure 85.	152

- Figure 87: Block diagram of the cascaded pump control scheme for pressure compensation developed using feedback linearization and model following control techniques. 156
- Figure 88: Control valve flow tracking using the nonlinear model following controller given by Equations (9.14) through (9.16) assuming constant pressures p_A, g and p_D, g 159
- Figure 89: VDVP displacement tracking using the nonlinear model following control described by Equations (9.25) through (9.27) and assuming a constant pump speed for three valve bandwidth settings to highlight the impact of the valve dynamics. 162
- Figure 90: Simulated performance comparison of the proposed electrohydraulic solution with the advanced nonlinear controller featuring feedback linearization (FBLZ) with the results presented in Section 8.2.4. 164
- Figure 91: Zoomed in view of the results depicted in Figure 90. 165
- Figure 92: Performance comparison of the nonlinearly controlled proposed system with two different control valve bandwidths. 165
- Figure 93: Comparison of the normalized control valve spool positions for the two controller cases when a high valve bandwidth is assumed..... 166

LIST OF ABBREVIATIONS

CAD	Computer Aided Design/Drafting/Drawing
CFD	Computational Fluid Dynamics
CMD	Command
CPU	Central Processing Unit
cRIO	Real-time controller with Compact Reconfigurable Input Output and an FPGA module produced by National Instruments
CW/CCW	Clockwise/Counter-clockwise
DAQ	Data Acquisition
DC	Displacement Chamber
DOF	Degrees of Freedom
FBLZ	Feedback Linearization
FF/FB	Feedforward/Feedback
FPGA	Field Programmable Gate Array
HP/LP	High Pressure/Low Pressure
ICE	Internal Combustion Engine
IDC/ODC	(Kinematic) Inner Dead Center/Outer Dead Center
LTI	Linear Time Invariant
LVDT	Linear Variable Differential Transformer
NI	National Instruments
PID	Proportional Integral Derivative
RC	Reduction (or Control) Chamber
RMS	Root-mean-squared
SC	Spring Chamber (Case)
SMC	Sliding Mode Control
STP	Standard Temperature and Pressure (0°C and 1bar)
TF	Transfer Function
VBS	Variable Bleed Solenoid
VDVP	Variable Displacement Vane Pump

NOMENCLATURE

a_c	Circumferential acceleration where the additional subscript refers to the body in motion (see Section 3.9)	m/s ²
a_{ijk}	Internal moment fit equation coefficients (see Section 8.2.2)	-
a_r	Radial acceleration where the additional subscript refers to the body in motion (see Section 3.10)	m/s ²
a_L	LVDT triangle side length at full eccentricity (see Section 4.1.2)	mm
A	Effective orifice area with subscripts identifying the connection	m ²
b_L	Distance from O ₁ to the LVDT centerline (see Section 4.1.2)	mm
c_i	Control chamber leakage flow model coefficients (see Section 6.5)	-
c_{ijk}	Internal moment fit equation coefficients (see Section 8.2.2)	-
c_r	Model following control law parameters (see Section 9.1)	-
$C_{\beta,i}$	DC volume rate of change partial derivative term (see Section 3.4)	mm
C_S	Equivalent stator damping/friction coefficient (see Section 6.2)	kgm ² /s
d_{ijk}	Pump flow rate fit equation coefficients (see Section 8.2.2)	-
d_s	Spring wire diameter (see Section 6.3)	mm
D_S	Mean helical spring diameter (see Section 6.3)	mm
$D_{\beta,i}$	DC volume rate of change partial derivative term (see Section 3.4)	-
$D_{\phi,i}$	DC volume rate of change partial derivative term (see Section 3.4)	-
e	Distance between O ₂ and O ₃ (see Section 3.2)	mm
e_p	Pressure compensation error (see Section 8.2)	bar
f	General nonlinear state space model dynamics function (see Section 9.1)	-
f_{BW}	Bandwidth frequency (see Section 7.4)	Hz
f_{cr}	Critical or spring surge frequency (see Section 7.4)	Hz
g	General nonlinear state space model input function (see Section 9.1)	-
G	Transfer function where subscript refers to the system represented (see Chapter 7 and Section 8.2)	-
G_{steel}	Shear modulus of the spring steel (see Section 6.3)	GPa
h	General nonlinear state space model output function (see Section 9.1)	-
H	Vane height (see Section 3.2)	mm

I_S	Mass moment of inertia of the cam (see Chapter 6)	kgm^2
k	Bias spring rate (see Section 6.3)	N/mm
k_{stop}	Effective spring rate of the stator end stop (see Chapter 6)	N/mm
K	General transfer function steady state gain and where the subscript refers to the corresponding transfer function (see Chapter 7)	-
K_{mix}	Bulk modulus of the fluid air mixture (see Section 3.7)	Pa
K_{oil}	Bulk modulus of the pure hydraulic oil (see Section 3.7)	Pa
l	Distance from O_1 to O_2 (see Section 3.2)	mm
l_0	Compressed bias spring length at a zero eccentricity angle (see Chapter 6)	mm
l_f	Free, uncompressed, length of the bias spring (see Chapter 6)	mm
l_v	Length of a vane (see Section 3.9)	mm
L	Distance from O_1 to O_3 (see Section 3.2)	mm
m	Mass for determining inertial component of pump internal moments (see Sections 3.9 and 3.10)	
M	Moment where the subscript refers to the source	Nm
n	Rotational speed of the pump shaft (see Section 1.3.3)	RPM
N_a	Number of active coils in the bias spring (see Section 6.3)	-
O_1	Center of the pivot pin (see Section 3.2)	-
O_2	Center of the rotor (see Section 3.2)	-
O_3	Center of the stator's internal surface (see Section 3.2)	-
p	Absolute pressure (or gauge if subscript includes “,g”), where the subscripts refer to the specific control volume or line	Pa
P_{CF}	Power associated with the cam friction (see Section 6.2)	W
$P_{Friction}$	Total power loss of the pump from friction sources (see Section 6.2)	W
Q	Volumetric flow rate corresponding to control volume referred to by the subscript and where positive values refer to flows into the control volume	m^3/s
Q_{Comp}	Volumetric losses due to fluid compressibility (see Section 5.5)	m^3/s
Q_S	Total pump volumetric flow losses (see Section 5.5)	m^3/s
Q_{SE}	External losses of the pump (measurable leakage) corresponding to the control volume indicated by the subscript (see Section 5.5)	m^3/s
Q_{SI}	Internal losses of the pump (not measurable leakage inside the pump) (see Section 5.5)	m^3/s
Q_β	Volumetric flow rate associated with stator motion (see Section 8.1)	m^3/s

r	Radius of the rotor (see Section 3.2)	mm
r_{air}	Aeration by volume in the fluid/air mixture (see Section 3.7)	-
r_o	Centroid position vector of the oil within the DC control volume for determination of the pump internal moments (see Section 3.9)	mm
r_v	Centroid position vector of a vane for determination of the pump internal moments (see Section 3.9)	mm
R	Radius of the cam inner surface (see Section 3.2)	mm
$R_{laminar}$	Effective impedance model resistance of the stator pivot groove due to laminar effects (see Section 6.5)	kg/m ⁴ s
R_{Line}	Impedance model resistance of the pump load line (see Section 3.8)	kg/m ⁴ s
$R_{turbulent}$	Effective impedance model resistance of the stator pivot groove due to turbulent effects (see Section 6.5)	kg/m ⁷
s	Laplace variable (see Chapter 7)	-
t	Time or 10% to 90% rise time with an “r” subscript (see Section 7.4)	s
T	Temperature of the fluid/air mixture (see Section 3.7)	°C
u	General command signal input (see Section 9.1)	-
u_v	Control valve command signal in voltage (see Section 8.2.1)	V
v_c	Circumferential velocity where the additional subscript refers to the body in motion (see Section 3.9)	m/s
v_r	Radial velocity where the additional subscript refers to the body in motion (see Section 3.10)	m/s
V	Volume or size of the control volume indicated by the subscript	m ³
w	Vane width (see Section 3.3)	mm
x	General nonlinear state space variable (see Section 9.1)	-
x_s	Instantaneous LVDT position (see Section 4.1.2)	mm
x_v	Normalized control valve spool position (see Section 8.2.1)	-
x_L	LVDT position at full eccentricity (see Section 4.1.2)	mm
y	General nonlinear state space output or desired output when the subscript “d” is included (see Section 9.1)	-
α_{ci}	Circumferential acceleration function coefficients (see Section 3.9)	-
α_D	Discharge coefficient in the turbulent orifice equation (see Section 3.5)	-
α_i	Half sector angle of the i th DC defining the angular span between the vanes (see Section 3.2)	rad

α_{ri}	Radial acceleration function coefficients (see Section 3.10)	-
β	Eccentricity angle of the cam giving the geometric displacement of the pump and where subscripts refer to special eccentricities (see Section 3.2)	rad
γ	Position vector for determining pump internal moments and where subscripts refer to which points are related (see Section 3.10)	-
Γ	Cross product term for determination of the pump internal moments where subscript refers to the associated accelerating body (see Section 3.10)	m
δ_L	Offset angle used in the LVDT signal processing (see Section 4.1.2)	rad
ε	General feedback error (see Section 9.1)	-
ζ	General transfer function damping ratio or the damping ratio of the dynamic system indicated by the subscript (see Chapter 7)	-
η	Efficiency relating to the aspect indicated by the subscript and where “M” is mechanical, “T” is total, and “V” is volumetric (see Section 5.4)	-
θ	Complementary eccentricity angle (see Section 3.2)	rad
κ	Parametric variable used in the DC volume functions (see Section 3.2)	-
λ_i	Distance from O_2 to a point P on the inner surface of the stator corresponding to the i^{th} DC (see Section 3.2)	mm
λ_{ei}	Exposed vane length between the rotor and cam inner surfaces for the i^{th} DC (see Section 3.3)	mm
μ_{oil}	Dynamic viscosity of the oil (see Section 6.5)	cP
ν	Artificial control input (see Section 9.1)	-
ρ	Density where the subscript refers to the material	kg/m ³
σ	Arc length between two vane tips (see Section 3.10)	mm
τ	Stator moment influence factor corresponding to the pressure of the control volume indicated by the subscript (see Section 3.10 and Chapter 6)	m ³
τ_r	Time constant (see Section 7.4)	s
ϕ	Shaft rotation angle or the angular position of a displacement chamber and where subscripts indicate special angles as in Section 3.4	rad
χ	Collection of common terms similar to ω (see Section 3.10)	-
ψ_i	Shaft load torque influence factor for the i^{th} DC (see Section 3.9)	m ³
ω	Collection of common terms in the derivation of the pump’s internal moment, subscripts indicate variations (see Sections 3.9 and 3.10)	-
ω_n	General transfer function natural frequency or of the dynamic system indicated by the additional subscript (see Chapter 7)	rad/s

ABSTRACT

Author: Jenkins, Ryan, P. PhD

Institution: Purdue University

Degree Received: May 2019

Title: An Analysis of a Pressure Compensated Control System of an Automotive Vane Pump

Major Professor: Andrea Vacca

Pressure compensated vane pump systems are an attractive solution in many automotive applications to supply hydraulic power required for cooling, lubrication, and actuation of control elements such as transmission clutches. These systems feature variable displacement vane pumps which offer reductions in parasitic loads on the engine and in wasted hydraulic energy at high engine speeds when compared to traditional fixed displacement supply pumps. However, oscillations in a currently available pressure compensation system limits the achievable performance and therefore the application of this solution.

This dissertation presents the development and experimental validation of a lumped parameter model in MATLAB/Simulink of a current pressure compensated vane pump system for an automatic transmission oil supply application. An analysis of the performance of this system using the validated pump model and a developed black box control system model reveals that the low cost solenoid valve present in the control circuit to set the regulation pressure limits the achievable bandwidth to 1.84Hz and causes a significant time delay in the response. To address this limitation, as well as eliminate a non-minimum phase zero introduced by the case study's control circuit architecture, an actively controlled electrohydraulic pressure compensation system is proposed. This proposed system is explored both experimentally and in simulation making use of the accuracy of the presented variable displacement vane pump model. Significant improvements in the achievable system performance are shown with both a simple PI control law (47% reduction in the pressure response time) and an advanced cascaded model following controller based on feedback linearization (58% reduction in the pressure response time). An analysis of these results reveals that implementing the proposed control system with a 5(L/min)/bar proportional valve with a 20Hz at $\pm 100\%$ (60Hz at $\pm 50\%$) amplitude bandwidth and a PI control law is an economical path to achieving the best performance improvements for this automotive application.

1. INTRODUCTION

1.1 Background

Our modern lifestyle depends on machines. There are machines for transportation, construction, farming, and every kind of production. In order to increase their performance and decrease costs, engineers work tirelessly improving the total efficiencies of nearly every machine that moves us around or gets our work done. In many cases, these top-level efficiency gains are obtained through enhancement of the efficiencies of the components that are used to make the machines. Perhaps one of the best examples of this can be seen in the automotive industry.

The past few decades have seen much improvement in engine performance. As the primary power source in most vehicles, these improvements have led to significant gains in vehicle performance, lifetime, and often fuel economy. The impact of these improved engines, however, is often offset by low performance or efficiency in the subsystems which use the engine's power to run the vehicle such as the transmission, cooling systems, and lubrication circuits. Proper attention should be given to these subsystems to obtain additional improvements in vehicle efficiencies and facilitate more intelligent machines.

Hydraulic systems have historically been very popular within the mobile machinery, aerospace, and even automotive industries due to their high power density. Innumerable patents and academic publications address the design, analysis, and control of each hydraulic application. Many of these applications require that the pump supply hydraulic power at a controlled system pressure up to a given maximum volumetric flow rate to one or more "consumers". These consumers could be linear or rotary actuators, thermal management systems, or lubrication circuits. The pump in these applications would be considered pressure controlled.

Design changes occur slowly in an industrial setting. Any potential improvement or solution that could actually be adopted must be both technically correct and economically feasible. Satisfying these two conditions can be difficult, expensive, and time consuming. Because of this, proven systems are typically reused to support new product lines for several years. This can lead to problems when the engineers that designed the system move on and their replacements do not know the systems as intimately, making it harder to use the current system as a springboard to the next generation design without significant research investments.

Research and development (R&D) projects carry inherent financial risks for a company, especially in a competitive market such as the automotive industry. Having a full understanding of the hydraulic system and its components allows a company to effectively guide their R&D efforts to reach improved solutions more quickly and better capitalize on potential gains.

In an endeavor to improve performance of a typical oil supply system for an automotive transmission application, for example, is it better for developers to focus on the evolution of the pump or its control valves? How will design changes in one component affect the performance of the other components and the system as a whole? Answering these questions is especially difficult when different development teams have ownership of the various components.

Even after answering these questions to establish the technical correctness of a solution, an unavoidable question remains; is it economically feasible to make the change? While the goal of this dissertation is not to explore the economics of automotive oil supply systems, the impact of component costs as they affect the system performance is considered. Analyses such as this are invaluable tools to decision makers in determining the economic feasibility of a solution and the trade-off between cost and performance.

This dissertation provides a thorough analysis of a common type of pressure controlled pump system architecture that is used throughout the automotive sector in an effort to clearly address the main question posed above; is it better to focus on the evolution of the pump or its control valves to improve performance? A pressure compensated vane pump system for an automatic transmission oil supply is taken as a specific case study. This example is introduced in Section 1.3, and provides context for the research objectives (Section 1.4) and the organization of the document (Section 1.5) with acknowledgement of the limiting factors to its performance.

1.2 Pump Pressure Control

Pump pressure control can be effected in several ways. While the simplest method involves setting the pump pressure by throttling a portion of the pump's volumetric flow over a relief valve or regulator valve, this is an inefficient approach for moderate to high power applications such as the supply of a constant input pressure to the control valves of one or more linear actuators on a mobile machine. The throttled flow in these cases represents wasted power and results in higher oil cooling requirements. Therefore, this method is typically seen only in low-pressure cooling circuits, such as would be found in a hydrostatic transmission.

Several additional applications that exhibit this simple form of pressure control are found in the automotive sector, including power steering systems, internal combustion engine (ICE) lubrication, and transmission control. In recent years, however, many companies and researchers have looked to other forms of pressure control as part of the push towards higher component efficiencies. Typically, the answer is found in replacing the fixed displacement pump with an appropriately sized variable displacement pump to allow for controlled pump output quantities and reduced parasitic loads. These solutions promise additional fuel savings between 2-4% for some applications [1]. The control of these variable positive displacement machines fall under two broad categories: direct operated and pilot operated pressure control [2]. Example schematics of these solutions are given in Figure 1.

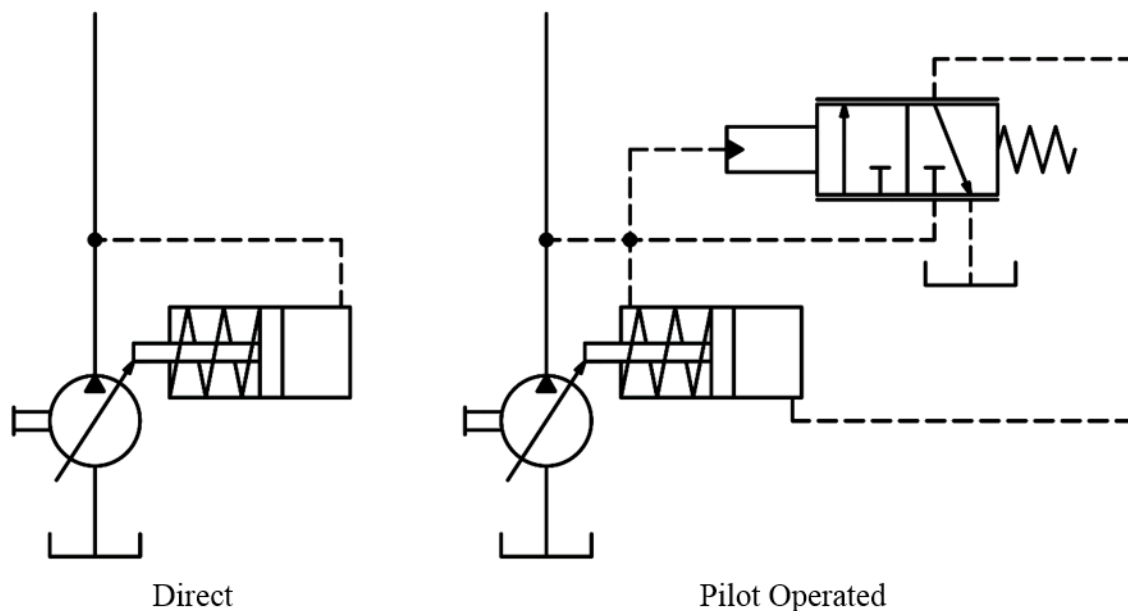


Figure 1: Schematic representations of a direct pump pressure control and a pilot operated pump pressure control.

In either case, the actual displacement level of the pump (typically an axial piston type or vane type machine) is varied to provide only the required level of flow to maintain a desired maximum pressure level at the pump outlet. In the direct pressure control system on the left in Figure 1, the pump displacement is reduced from a maximum level when the force from the outlet pressure acting on the bore side dominates the force balance of the adjustment cylinder. As the displacement decreases, the pump outlet flow decreases until a new equilibrium point is reached. This new equilibrium point corresponds to the reduced displacement level where the

Some hydromechanical pump control architectures exhibit tendencies toward oscillatory behavior. While transitioning these systems to an electrohydraulically controlled version of the control architecture can improve the performance, it can also introduce new challenges. Component selection and the configuration of multiple control valve stages, if applicable, can both affect the stability and achievable performance of the electrohydraulic control system. Understanding the limitations of any pump control system requires a comprehensive understanding of the physics of the system, including the nature of the forces generated within the pump, and typical load characteristics which determine the pump operating conditions.

1.3 A Case Study

To illustrate the impact that both the control system architecture and the component selection procedure have on the performance and stability of pressure controlled pump systems, a pressure compensated variable displacement vane pump (VDVP) for an automatic transmission is taken as a case study as mentioned previously. The pressure compensated VDVP in this application supplies the transmission with the necessary hydraulic power to actuate the various clutches while simultaneously satisfying the transmission's cooling and lubrication needs. While the specific characteristics of the transmission loading (as characterized by a flow demand at a required system pressure) differ from other automotive systems (e.g. ICE lubrication, variable valve timing, or power steering) the pumps and pump control circuits are highly similar. Thus, there is no loss of generality by taking a transmission oil supply system as a case study.

1.3.1 The Variable Displacement Vane Pump

Figure 3 provides an illustration of the pivoting-cam type VDVP analyzed as part of this case study. This VDVP has seven vanes housed in slots machined into a rotor which engages the pump shaft through a spline connection. These vanes are allowed to slide in and out of the slots in a radial fashion (with respect to the shaft) between a retaining ring and the inner surface of the stator whenever there is an eccentricity between the rotor body and the inner surface of the stator. The stator eccentricity then controls the variation of the pump displacement by controlling the maximum and minimum sizes of each displacement chamber. A displacement chamber (DC) is defined as the volume enclosed by two consecutive vanes, the stator, and the rotor from the sides and the pump case from above and below (not shown in Figure 3). As the shaft rotates

clockwise, the DC volume increases from minimum to maximum as it traverses the suction port region. This expansion of the volume draws fluid into the chamber and constitutes the suction stroke. As the shaft continues to rotate, the DC volume decreases in size back to a minimum as it passes the delivery port, expelling fluid into the port in the delivery stroke. Each DC volume experiences a 180° suction stroke and a 180° delivery stroke (kinematically) each revolution.

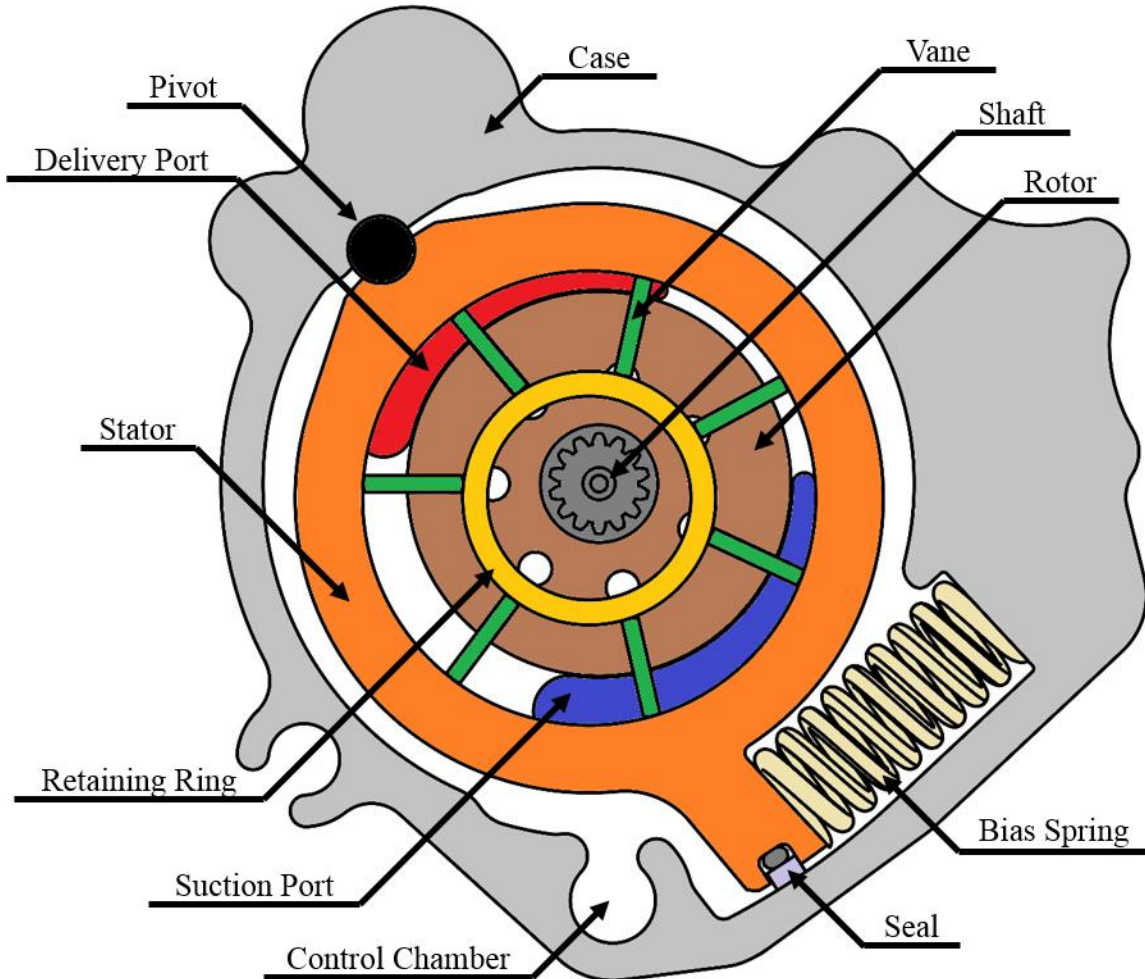


Figure 3: Component identification illustration of the 7-vane pivoting-cam type variable displacement vane pump analyzed in the case study.

The eccentricity between the rotor and the stator is nominally at a maximum due to the influence of the bias spring and internal forces acting on the stator. These internal forces are primarily comprised of DC pressure forces acting on the stator and centrifugal forces of both the vanes and the oil within the DC. When the control chamber pressure rises as a result of control valve flow into the chamber, the resulting pressure force induces a rotation of the stator about the pivot point by acting against these internal forces, thereby reducing the eccentricity.

1.3.2 The Pressure Compensation Control Circuit

The pressure compensation control system pertaining to and evaluated in the case study belongs to the category of pilot operated pump control architectures and is depicted in Figure 4.

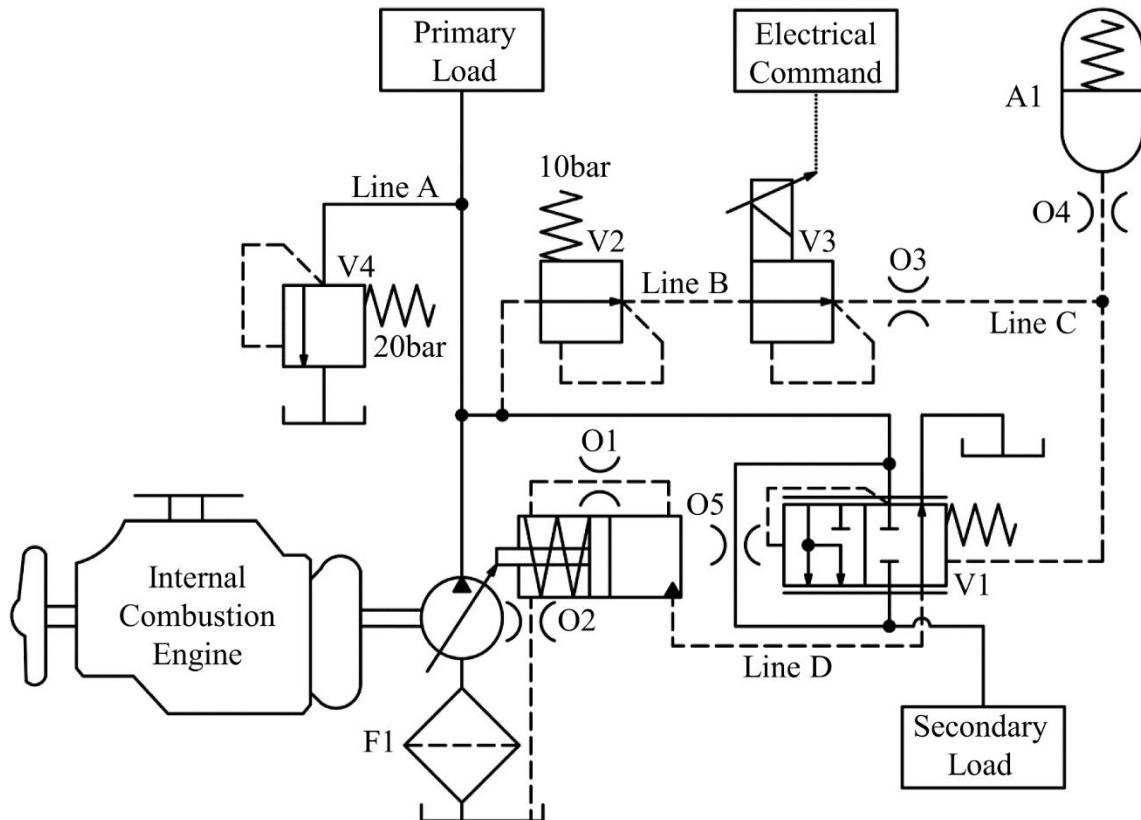


Figure 4: Baseline pressure compensation pump control system architecture for an automatic transmission supply VDVP evaluated in the case study.

In this configuration, the pressure regulation valve V1 shifts from the default position shown in Figure 4 to the second position—connecting Line A and Line D—when the pressure in Line A exceeds the level determined by the combination of the Line C pilot pressure set by an electrical command to the valve V3 and an offset determined by the V1 spring. When V1 shifts to this open position, oil flows from Line A into Line D and the stator (represented symbolically as an adjustment cylinder in Figure 4) begins to move. The resulting control chamber pressure (bore side chamber pressure in the cylinder) is then a function of the internal forces acting on the stator, the leakage flow from the chamber (orifice O1), and the controlled flow through V1. For a constant flow demand, the pump outlet pressure decreases as the pump displacement decreases. As this pressure in Line A falls, the V1 spool moves until an equilibrium condition is reached.

At this point, the metered flow through V1 will match the leakage flow through O1 for the control chamber pressure corresponding to the new, reduced eccentricity equilibrium condition for the given pump operating conditions. The system continues in this state until the system operating conditions change (i.e. in the engine speed or load's flow demand) or a new pressure regulation level in Line A is commanded via an electrical signal to the valve V3.

A dynamic Line A pressure regulation level is therefore set by a varying electrical command signal sent to the solenoid valve V3, which is the primary component regulating the pilot pressure in Line C. The orifices O3 and O4 and a small spring loaded accumulator A1 provide additional damping to Line C in an effort to stabilize this important pilot pressure.

Another factor that helps to stabilize the Line C pilot pressure is that the oil supplied to V3 is regulated to a maximum pressure of 10bar through the pressure reducing valve V2. As indicated in Figure 4, the maximum pressure in Line A is limited to 20bar by the relief valve V4 and all pressure compensation activity occurs only at lower pressures.

1.3.3 Typical Operating Conditions

The case study VDVP operates at low pressures (approximately 5-18bar) as an open-circuit unit drawing oil directly from the reservoir through a pickup filter, F1 in Figure 4. Because of this low-pressure, open-circuit operation, oil aeration and cavitation can be significant. In fact, aeration levels for the case study pump are such that 3% entrained air (undissolved as bubbles) by volume at the pump outlet is typical and can reach levels as high as 9% by volume. Aeration levels can have a significant impact on the overall system performance as they alter the fluid bulk modulus, or "stiffness", of the working fluid particularly at the lower pressures commonly found in automotive applications [3] [4].

Since automatic transmissions are required to function properly in vehicles for any weather conditions, the case study VDVP also experiences a wide range of operating temperatures between -40°C and 150°C [5]. Typical automatic transmission fluid, like all hydraulic fluids, experiences significant changes in many physical properties over this range of temperatures [6]. These changes in physical properties (*inter alia* density, viscosity, bulk modulus, and air solubility) can all affect the system performance.

Finally, since the case study VDVP is driven by the engine shaft via a chain drive at a nearly 1:1 ratio, the pump operates over a wide range of speeds from as low as 600RPM to as

high as 5500RPM. As the VDVP in this application provides the hydraulic power necessary to actuate the clutches as well as satisfy the cooling and lubrication requirements, it is helpful to understand these requirements as a function of speed. Higher system pressure requirements and flow demands accompany the actuation of clutches, which translates to an intermittently high demand on the pump. Meanwhile, cooling and lubrication both require a lower system pressure and a roughly constant flow demand independent of the engine speed. The combination these high and low load characteristics results in duty cycles such as the one depicted in Figure 5.

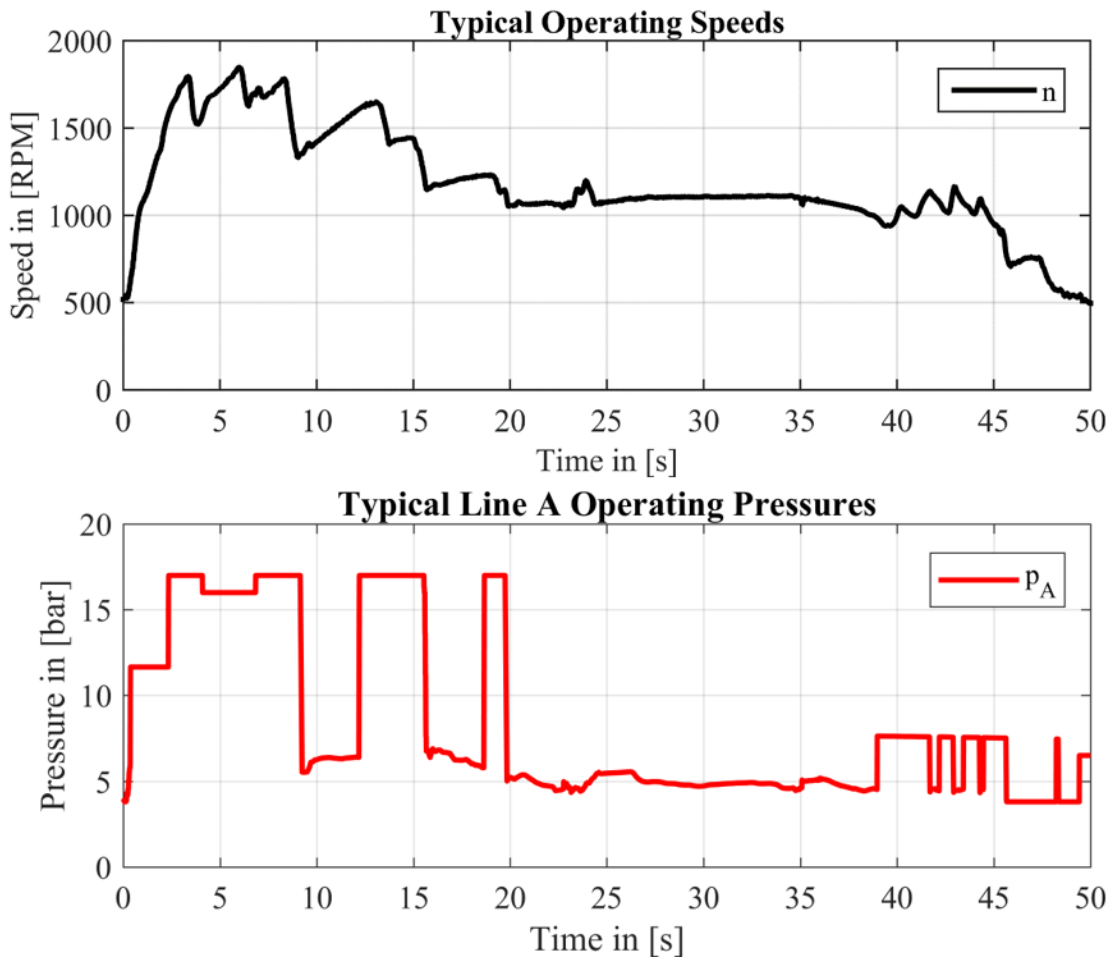


Figure 5: Duty cycle representative of the typical operation of the pressure compensated VDVP for an automatic transmission supply analyzed in the case study.

The only information regarding the pump operating conditions that is missing from Figure 5 is a trace of the VDVP displacement. This is intentional for two reasons. One is that the displacements are primarily dependent on the flow demand, which for this case study is assumed to be unknown. The pump displacement will also be affected by the oil properties, albeit to a

lesser extent, and the required displacement to meet the flow demand at a given speed will be different for different temperatures and aeration levels. Since the temperature and aeration levels are unknown for this supposed duty cycle, several assumptions would need to be made in order to estimate the pump displacements. A second reason is that the pressure and speed traces shown in Figure 5 are the essential inputs to the pressure compensated VDVP system when the pressure trace is interpreted as a commanded Line A pressure level. With this interpretation, Figure 5 represents all the required information to specify a desired operating condition of a well-designed pressure compensated pump.

1.4 Research Objectives

For many pressure controlled applications, unexplained variability in behavior or performance is fairly common. One of the most common observations is unacceptable levels of pressure or flow oscillations. This applies to the case study introduced in the previous section and leads to two key questions. What is causing the undesired behavior or performance limitations? How can these problems be eliminated or attenuated? For complex systems like the case study taken here, a detailed analysis of each component is required to address the first of these questions. Results from this analysis then guide possible solutions to the second question. The focus of the research presented in this dissertation can therefore be summarized by the following objective statements.

- Develop a numerical simulation model for a pivoting-cam type VDVP which accounts for all principally significant physical phenomena. This model must also realistically represent the dynamic performance of the pump.
- Validate the numerical simulation model by comparing simulation results to measurements collected on a custom experimental test rig and to representative data available in the established academic literature.
- Experimentally characterize the stability and dynamic performance of the pump control system using actual hardware from an automotive automatic transmission application.
- Evaluate the system stability and performance limitations and their sensitivity to various parameters such as speed and fluid properties.
- Present an electrohydraulic pressure compensation control architecture—complete with control valve sizing guidelines—that provides improved system performance.

- Validate the proposed control system both experimentally and numerically in simulation.
- Discuss and compare advanced controller concepts for pressure compensation control of variable displacement units with electrohydraulic pump control architectures.

Answering the two questions posed in this section and completion of these seven objectives represents various significant contributions to the academic community. These contributions specifically provide a greater understanding of the performance limitations of pressure compensated oil supply systems for automatic transmissions and similar automotive applications with low production costs as well as provide a framework for the evaluation of the impact of these systems on the total vehicle efficiency.

In summary, this dissertation aims to assess the performance and stability of an existing pressure compensated VDVP oil supply system and propose an alternate, superior solution.

1.5 Dissertation Organization

The remainder of this dissertation is organized as follows. Chapter 2 reviews the literature relevant to the research objectives of this dissertation. Chapter 3 briefly discusses the overall system modeling approach before presenting details on the developed lumped parameter module for calculating DC pressures, internal forces, and pump outlet conditions for the case study VDVP. Chapter 4 then presents the design and setup details for the custom experimental test rig used for system testing and validation study measurements. Chapter 5 gives details on the specific post processing required to complete the validation study of the DC pressure profile, the most critical output of the lumped parameter DC module, and presents several comparisons between simulated results and experiments. Chapter 6 completes the lumped parameter pump model by providing details of the pump adjustment system module comprised of the control chamber and stator dynamics models with corresponding experimental measurements.

Chapter 7 deals with the experimentally derived black-box model developed to study the dynamic behavior of the case study pressure-compensation pump control system while in Chapter 8 an electrohydraulic pressure compensation system is proposed and proved as a concept. Chapter 9 expands on the initial work presented in Chapter 8 by discussing advanced controller concepts with the goal of exploiting all of the potential benefits from transitioning to the proposed system from the baseline system presented in Chapter 7. Final conclusions, observations, and recommendations are then presented in Chapter 10.

2. STATE OF THE ART

The research objectives presented in Section 1.4 can be divided into the three main topics given below. This chapter presents an overview of the relevant literature in each of these three topic areas.

- Modeling the plant (i.e. the VDVP).
- Characterizing an existing control system (i.e. the baseline architecture in Figure 4).
- Development of an advanced control system for improved performance.

As the first bullet point indicates, the plant that will be studied in this dissertation is the VDVP alone and not the transmission that it supplies. While research has been done on the modeling of various transmission components and subsystems as plants [7] [8], restricting the plant definition to the VDVP only both maintains a higher degree of generality of application and allows for a more focused treatment of the research objectives.

2.1 VDVP Plant Modeling

Vane type pumps have found application in many hydraulic systems for a variety of reasons. Depending on the design, these pumps are well suited to low- and medium-pressure (below 250bar) applications due to their compactness, low cost, and generally lower flow rate pulsations and noise emissions [2]. While there are many vane pump designs available [2], the two main designs that are used in pressure controlled applications are single stroke pumps of either pivoting-cam type (such as the case study design shown in Figure 3) or sliding-cam type (see [9] for an example). Because of their wide application, many modeling approaches have been presented for various purposes including pump design and optimization, characterization of pressure or flow ripples, and analysis of the pump dynamics. As the first topic addressed in this dissertation is the creation of a VDVP plant model, the models available in the literature have been filtered based on their utility as a dynamic plant model.

2.1.1 Modeling Approaches

In general, pump models in the literature are either lumped parameter numerical models or three-dimensional (3D) computational fluid dynamics (CFD) models. In some cases, a blend

of the two approaches is taken to incorporate the typically higher realism of 3D CFD models with the low computational cost of lumped parameter models for an improved simulation tool [10]. Regardless of the approach, each model must have a well-defined purpose and encapsulate the physics necessary to achieve that purpose to an appropriate level of precision. The complexity of each model is then defined by the purpose of the model.

For example, a simple model calculating the effective flow and torque of a pump may be sufficient for analyzing the pump's impact on the overall fuel efficiency of a vehicle [8], but will be insufficient for answering the question of what aspects of the pump's design most affect the performance. In this second case, a more complex model calculating the internal pressure forces and pump friction [11] may be more suitable. This more complex model would still answer the first question, but at a much higher computational cost.

To meet the purposes of this dissertation already stated, the required model should accurately represent the internal forces acting on the stator and the outlet behavior of the pump with the lowest model complexity possible. Therefore, the models presented in the literature following the lumped parameter paradigm are of particular interest.

The lumped parameter model of a 9-vane sliding-cam type VDVP in [10] is the most recent model published in the literature and represents the state of the art in VDVP modeling. This model was created in the Simcenter AMESim environment (Siemens) with custom components representing the pump geometry and various flow paths (including leakage paths) to simulate the pump performance, including the internal pressure forces. CFD simulations were utilized to tune the parameters for the flow calculations for an overall good agreement with experimental data. The authors present an analytical vector ray approach to determine the time rate of change of the DC volume, but they do not include eccentricity rate effects in this determination and calculate the DC volume numerically through a separate approach. Additionally, the authors mention what is included in the model calculations for the internal forces acting on the stator only cursorily and do not present the underlying equations.

Similar lumped parameter models were developed in AMESim previously for modeling the performance of both sliding-cam type [9] and pivoting-cam type [12] ICE lubrication pumps. A similarity of these models with the work in [10] is an analytical, projection based evaluation of the flow areas connecting the DC with the ports. In [9], the DC volume derivative is again calculated analytically with a vector ray approach but the DC volume is calculated analytically

using the area of the DC footprint. Unlike in [10], the authors in [9] present equations for calculating the internal forces acting on the stator. However, the underlying equations used in [9] to calculate the DC pressures are left vague. Despite this, [9] has received a lot of attention as one of the first comprehensive lumped parameter models for evaluating the pump performance.

As one of the industry standard modeling programs, AMESim contains some standard components useful for creating vane pump models [13]. These components are based on work published in [14] as well as some of the formulations presented in [2] and [9]. The calculation of the internal forces acting on the stator in these models is simplified. Until 2017, these standard components only supported sliding-cam type VDVP models without significant work developing custom components. The 2017 release of the AMESim 16 platform, on the other hand, contains several new development tools (including CAD import) and better supports pivoting-cam VDVP.

In [15] a lumped parameter model of an 11-vane sliding-cam type pump was developed in MATLAB for use in noise and vibration optimization. The authors give some details on how the DC pressures are modeled, but do not specify how the DC flows exchanged with the ports are calculated. Furthermore, an analytical model of the circumferential pressure distribution associated with the DC that was developed by fitting curves to experimental measurements was also presented. This pressure distribution is divided into four principal modes.

The concept of dividing the DC pressures into four distinct modes was first presented in 1986 [16] and has been used to characterize the internal pressure forces by [17], [18], [19], and [20], to name a few. Each of these models uses a pair of cylindrical coordinates centered at the rotor and stator surfaces, respectively, with several angles corresponding to the spans of the ports to define zones for each of these modes and the relevant DC geometries. In [19] these zones even define which of four sets of differential equations is used at any given time step, necessitating smoothing functions for transitioning between zones. A more mathematically rigorous analytical model for a 13-vane sliding-cam type pump, also with a piecewise construction of the DC pressure but without the need for smoothing functions, was presented in [21]. This model, however, neglects the rotational speed of the shaft in zones of pure compression or expansion.

Others, such as [11] and [22], model the DC flows and pressures using 1D CFD models in GT-SUITE. In [11], the results from the simplified 1D CFD model were compared to results from a 3D CFD model in PumpLinX similar to models such as in [23], [24], and [25] to show that the simpler model is capable of simulating the pump performance well. An issue with the

CFD approaches is the complexity and difficulty of pairing these flow and pressure simulations with dynamic models of the stator motion.

A review of each of the models available in the literature and discussed in this section reveals the following gaps. There are no analytical models of the DC geometry (both volume and time rate of change of the volume) derived from a single coordinate system consistent with the stator dynamics equation. A model of this type is ideal for dynamic studies as it preserves more of the naturally occurring coupling effects between the resulting differential equations. Additionally, with the possible exception of [10], none of the lumped parameter models include the port geometries beyond their angular positions with respect to the stator. Nevertheless, some account for these effects by including additional terms to represent incomplete filling [26] [27]. Furthermore, the models presented in this section assume the vanes are equally spaced around the circumference of the rotor when in practice this is even avoided [28]. Unequal vane spacing affects the development of DC pressures, and subsequent forces, through timing effects.

The model presented in this dissertation will address these limitations by providing a novel approach to modeling the DC geometries and using port representations similar to those found in works such as [29] and [30].

2.1.2 Model Validation

Pump models can be validated in various ways, depending on their purpose. Because the purpose of the lumped parameter model in this dissertation is to provide realistic internal forces for evaluation of the stator dynamics and system performance, the most critical aspect of the model to validate—once a detailed geometric model is established—is the DC pressure profile.

In [31], two methods are presented for measuring a single DC pressure in an 11-vane sliding-cam unit under working conditions. The first method involves the installation of a single miniature pressure transducer in the rotor body between two vanes such that the sensing element of the transducer is in continuous direct contact with the DC volume. For this configuration, the transducer cables are threaded through ducts machined into the shaft to slip rings in a modified pump case. The signal is then transmitted via the slip rings to the data acquisition system.

An advantage of this setup is clearly the continuous and direct measurement of the DC pressure profile. However, this design is impractical in many cases, particularly for pumps in automotive applications in passenger vehicles such as the case study pump. This is due to their

compact design and the availability of appropriately sized sensors. Whenever a sensor is found that works with the pump shaft and size, there remains the difficult, and often equally impractical, task of modifying the pump shaft and pump case with ducts and slip rings. Ultimately, this method has high setup costs and can be limited in accuracy due to the slip rings.

The second method presented in [31] is a form of hydraulic telemetry instead of the electrical telemetry of the first method. The DC pressure is transmitted via ducts machined into the shaft from the rotor face to a sealed chamber in a modified pump case. A pressure transducer can then be easily installed in the case and data acquisition is straightforward from there.

An advantage of this method is the option to measure not just the DC pressure, but other pressures inside the pump as well. For example, in [31] the authors also measure the pressure behind the vanes (in the guide slot on the rotor side). This method also allows for the continuous measurement of the pressures. However, the duct and chamber transmission dynamics must be accounted for properly. A finite element model was used in [31] to analyze these effects and correct for them. This method of sensing the DC pressure has similar drawbacks to the first method in terms of pump modifications and their associated cost, but may be more practical.

A third method for sensing the DC pressure has been employed by various authors and involves the measurement of the pressure at a single location. In [9], a single pressure transducer was installed in the case of the pump near the delivery port to measure the pressure as the DC volume moved into connection with the delivery port. The purpose of these measurements was to characterize the incomplete filling of the DC. In contrast, [32] presents the results of an experimental study of a 7-vane pivoting-cam type pump for ICE lubrication applications where seven equally-spaced pressure transducers were installed in the pump case at the locations (labeled blue dots) shown in Figure 6 to measure the DC pressures plus an additional pressure transducer measuring the delivery port pressure.

A disadvantage of this setup is that the DC pressure measurement is no longer continuous and must be reconstructed in a piecewise fashion. In [32], this is done by performing a linear interpolation between consecutive sensor signals over a 2° interval of rotation corresponding to the passage of a vane over the sensor location, cutting off the connection to any of the DC. While the post-processing requirements associated with this method are more stringent than the two methods presented in [31], the physical setup is typically more tractable as the transducers can be mounted in the case. Nevertheless, packaging can be challenging with this method for some

compact VDVP designs as the sensors must not interfere with the port geometries and various surface finishes as much as possible. To reduce the effect on surfaces, and to minimize distortions of the DC pressure measurement, the transducers in [32] communicated with the DC volumes via small ducts as shown in Figure 7 [33].

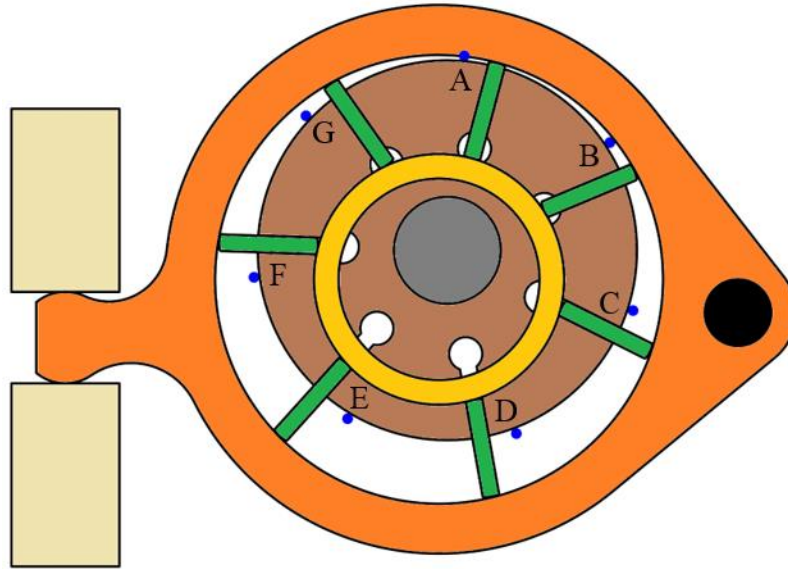


Figure 6: Transducer locations for the measurement setup described in [32].

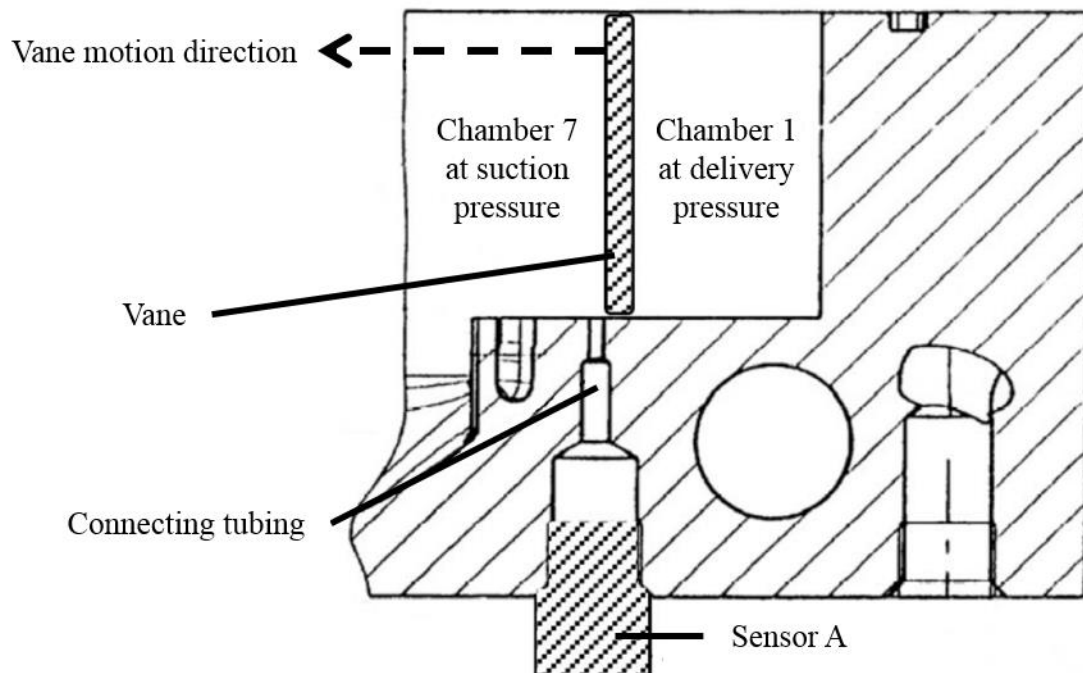


Figure 7: Pressure transducer tubing geometry, adapted from [33].

As Figure 7 indicates, these small ducts lead to a small chamber at the surface of the pressure transducer. The geometry of this connection has associated dynamics that, for high accuracy measurements, must be accounted for in post-processing as they can affect the frequency content of the DC pressure measurement [33]. However, the extent of these effects is dependent on both the connection geometry and operating conditions such as aeration levels [34]. To minimize these effects, the volume of the sensor chamber should be as small as possible with as small a diameter as possible for the connecting duct.

Due to geometric constraints in the case study VDVP, the method chosen for measuring the DC pressures in this dissertation most closely follows the third method presented here. However, a minimal number of strategically placed pressure transducers sufficient to characterize the complete profile was implemented with a novel “baton-passing” post-processing algorithm to reconstruct a continuous profile.

2.2 System Identification

Generally speaking, system identification is the blend of art and science dealing with the creation of mathematical models of dynamic systems from experimental data representing input-output relationships. It is a broad topic with a foundation in statistics and has found application in a variety of fields. Within controls, the goal of system identification is typically the development of an accurate plant model to use in controller synthesis. Depending on the type of system under investigation, the type of model to be estimated, and the ultimate purpose of the model, there are a wide range of techniques available. An overview of the state of the art in system identification, as well as an overview of some of the core principles, is available in [35].

One aspect discussed in [35] that is worth mentioning here is the distinction between black-box models, white models, and the various shades of grey between these extremes. White-box models are a product of diligent and extensive physical modeling based on the fundamental principles constituting the plant. When some parameters within a white-box model have unknown or uncertain values, the model becomes “off-white”. “Smoke-grey” models often involve finding nonlinear transformations of the measured data allowing for a better chance of finding a linear relationship to describe the system using semi-physical modeling. Models featuring compositions of local models which fit neighborhoods of the data well or that are hybrid models may be referred to as “steel-grey” or “slate-grey” and have varying actual shades

of grey. Finally, black-box models are derived from, essentially, highly flexible surface fitting functions or generic model structures and may not have any physical significance. The actual shade of the model depends on the application and on the amount of information known *a priori* to the engineer.

Characterizing the baseline control system taken in the case study, therefore, begins with a decision between pursuing a grey-box description or a black-box description. A white-box description of the control system shown in Figure 4 is outside of the scope of this dissertation, especially considering the objectives already stated. In order to characterize the stability and performance limitations of the baseline system, a simple black-box description is sufficient.

A common approach to black-box modeling is to use a least squares approach to find the coefficients of a difference equation belonging to a certain model type, such as the popular linear models ARX and ARMAX [36]. Another common approach is the identification of linear time-invariant (LTI) transfer functions in the frequency domain through either deterministic or stochastic approaches [37]. Nonlinear methods include neural networks, wavelet estimators, fuzzy models based on fuzzy set memberships, and polynomial nonlinear state space (PNLSS) models [36] [38] [39].

While each of these methods are valid approaches to characterize the complex and nonlinear behavior of V1 and V3 in Figure 4, the chosen approach presented in Chapter 7 is more of a brute force optimization of a more-or-less grey-box transfer function structure for an ad hoc representation describing the dominant dynamics instead of the formulation of a control synthesis appropriate representation. This will result in a similar approach to the state of the art analysis of regulation system stability of a pressure compensated vane pump presented in [40].

2.3 Advanced Pump Control Systems

In line with the discussion of Section 1.2, pump pressure control systems can be either passive (direct or pilot operated) or active (electrohydraulic). Most often, passive architectures are used in practice and remain the state of the art solutions, thus motivating the analysis in this dissertation of the case study system.

Within automotive VDVP applications, the case study control system is a good example of a highly adjustable system. Sometimes the adjustability of the system is limited to discrete levels associated with specific typical operating conditions [41]. For automotive applications

with passive control systems, work has also been done to optimally size the piloted control valves to facilitate packaging constraints while maintaining performance [42]. Each of these characteristics (i.e. adjustability and good performance within packaging constraints) is also achievable with electrohydraulic architectures.

Electrohydraulic architectures can be valve-centered or pump-centered solutions. For example, [43] presents several realizations of an electrohydraulic pressure compensation valve that controls the pressure and flow via throttling while [44] features control of the motion of a VDVP cam using an electrohydraulic servovalve to control the pressure by changing the effective pump flow. This dissertation will focus on the latter solution.

A distinct advantage of controlling pump output quantities by electrohydraulically actuating the pump adjustment system is that many controller architectures are available with their respective benefits. For VDVP systems in particular, [44] presents a Quantitative Feedback Theory (QFT) controller design ideally suited for systems with large parameter uncertainties that may be operating-point dependent. Meanwhile, in [45] a nonlinear volume flow controller for a VDVP based on input-output linearization of a minimal mathematical model developed in [21] is presented and compared to feedforward linearizing approach with PI output feedback. Finally, [46] and [47] present several configurations with high bandwidth for turbine engine “fueldraulic” applications in aerospace including a Wheatstone controller. While these three examples adequately sum up the literature on electrohydraulic VDVP systems, additional examples of electrohydraulic pressure control are available in other applications.

An overview of control methods used in fluid power applications is given in [48]. In this survey of the state of the art, it is clear that, in addition to the industry staple of PID control, optimal state feedback controls [49], various adaptive controls [50] [51], robust sliding mode controls (SMC) [52], and both fuzzy-logic [53] and neural control [54] schemes have all been successfully applied. Thus, careful application of any control methodology capable of stable tracking of a reference signal can be used to effect pressure control of a variable displacement pump and will open the door to improved performance and improved efficiencies.

This dissertation will investigate two different control approaches that may find application in environments similar to the case study where controller economy in terms of computational effort is also important. As the “bread and butter” of control engineers, PID controllers in various forms solve between 90-95% of all control problems [55]. Selecting a

proper form of this common controller is therefore one of the first tasks in the design procedure and should be based on the application at hand [56]. For the case study system, a relatively first order process dynamics and a line pressure set point that is normally constant (and low) with periodic high plateaus precludes the use of a derivative term. Meanwhile, reducing steady-state errors to assure sufficient pressures are maintained for proper transmission operation prompts the inclusion of an integral term. Thus, the first approach (Chapter 8) will be a common, basic PI controller that is fairly intuitive to tune. This approach is contrasted by a cascaded nonlinear controller design in Chapter 9 which has similarities to [45].

2.4 Intended Contributions

In light of this review of the relevant literature and considering the research objectives put forth in Section 1.4, the goals of this dissertation can be summarized as follows.

- Provide a model for a pivoting-cam type vane pump accurate enough to both assess the dynamics of the pump in the current solution and serve as a realistic plant for the development of new pump control methodologies. At this point in time, this type of model for direct use in MATLAB/Simulink has not been presented in the literature. Furthermore, no clear discussion of the mathematical foundations of the internal forces acting on the stator within a pivoting-cam type VDVP presently exists. This dissertation aims to address both these limitations in the current state-of-the-art literature.
- Present and demonstrate a novel methodology for the measurement of the displacement chamber pressures within a small pivoting-cam type VDVP for automotive applications. This is an area with only a few contributions presented in the literature which are not feasible for all pumps. Reliable measurements of these pressures are critical in both the evaluation of model validity and the assessment of the impact of various design features on the internal forces and noise emissions of a pump in the development and optimization of these pumps.
- Clearly assess the dominant dynamics of an existing low-cost pressure compensation control system for an automatic transmission application to identify the limiting components and their impact on the system performance. Very little research is available on the low-cost valves used in these control systems [57] [58] and no evaluation of the system performance as a whole is presently available.

- Propose and evaluate an actively controlled electrohydraulic pressure compensation system for the case study application complete with an intelligent and modern controller design. This is also an area with very little published research.

In addition to these four goals, this dissertation will also contribute to the current state of the art by illuminating a few areas where additional research is necessary. These future topics will be discussed after the body of this dissertation in the concluding remarks of Chapter 10.

3. LUMPED PARAMETER VDVP DC MODULE

The numerical simulation model developed in this dissertation is comprised of three primary components as illustrated in Figure 8. The main component is an off-white lumped parameter VDVP model with two modules. The VDVP subsystem communicates flow to a simple load simulator module which returns line pressures. These line pressures are also fed into the third component, a pump control system model, which simulates the control system valves V1, V2, and V3 in Figure 4 to generate a flow used to control the stator motion. Based on the forces acting on the stator, the stator moves to a position where the new pump displacement results in a pump flow and outlet pressure that matches the commanded operating condition.

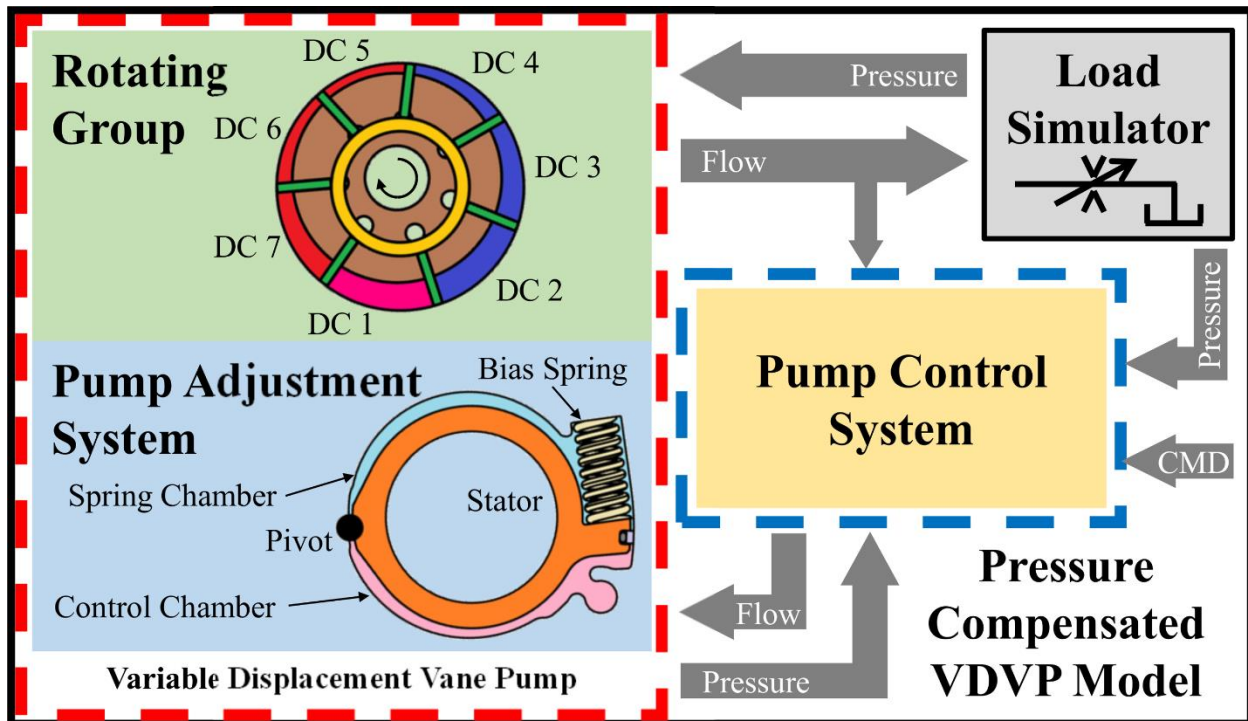


Figure 8: Overview of modeling approach illustrating major system model components.

This chapter presents the development of the seven displacement chamber (DC) models comprising the rotating group module. These models, as Figure 9 illustrates, contain a dynamic pressure build up equation for the DC control volume coupled to orifice flow equations communicating with the ports. The resulting DC pressure, along with the pump speed and displacement, determines the internal moments (including pressure and centrifugal forces) applied to the stator using the detailed pump geometry information contained in each DC model.

Chapter 6 will present the development of the Adjustment System Dynamics Module elements shown in Figure 9 and Chapter 7 will discuss the regulation system module for the case study. Due to the similarity of the load simulator module with the DC Module and their more highly coupled nature, the load simulator development will also be presented in this chapter.

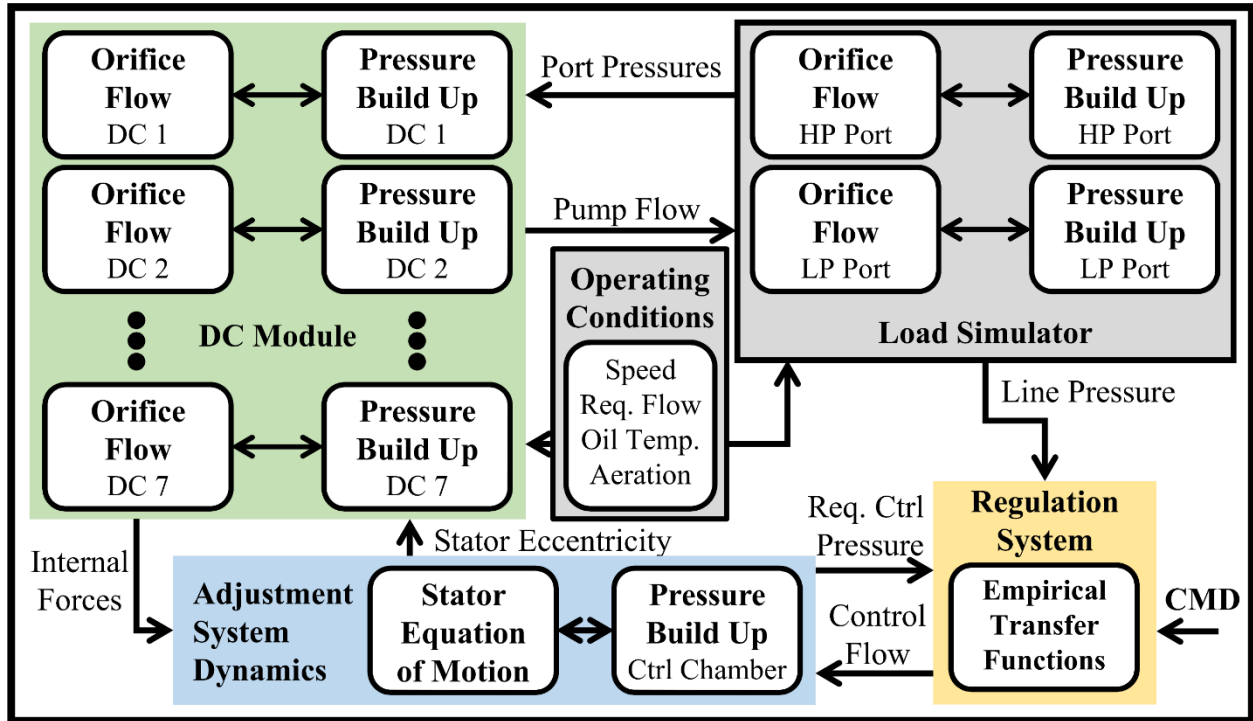


Figure 9: General system model block diagram highlighting the degree of complexity in each module of the overview presented in Figure 8.

While the MATLAB/Simulink environment was used for this dissertation, the model presented here can be implemented in other simulation tools capable of solving systems of differential equations.

3.1 DC Pressure Build Up Equation

At the heart of the DC Module is the pressure build up equation given by Equation (3.1). The solution of Equation (3.1) gives the instantaneous absolute pressure p_{DCi} in the i^{th} chamber's control volume V_{DCi} . The pressure build up equation is derived from the conservation of mass law and is widely used in the literature (e.g. [10] [12] [15] [16] [19] [21]).

$$\frac{dp_{DCi}}{dt} = \frac{K_{mix}}{V_{DCi}} \left(Q_{rHPi} + Q_{rLPi} + Q_{SE,DCi} - \frac{dV_{DCi}}{dt} \right) \quad (3.1)$$

The variables Q_{rHPi} , Q_{rLPi} , and $Q_{SE,DCi}$ in Equation (3.1) represent the flow exchanged with the delivery port, suction port, and case (i.e. external leakage flow), respectively and K_{mix} is the effective bulk modulus of the fluid/air mixture filling the chamber completely. Each of these variables will be discussed in more detail in later sections. However, with regards to the leakage, the term $Q_{SE,DCi}$ can be estimated from measurements (as will be shown later) or calculated using physically based models of the tribological interfaces. A sensitivity study in Chapter 5 will show that this term has a negligible impact on the DC pressure profile, so $Q_{SE,DCi}$ will be neglected unless otherwise specified and no tribological interface models are included in this work. Nevertheless, some internal leakage phenomena and volumetric compression effects are included in the formulation of the DC Modules as will be shown.

3.2 Pump Geometry

A critical first step in defining the geometric parameters used in Equation (3.1), and throughout the lumped parameter VDVP model as a whole, is the establishment of a consistent and convenient coordinate system. Figure 10 depicts this coordinate system and several basic geometric parameters required to define both the DC geometry and its location.

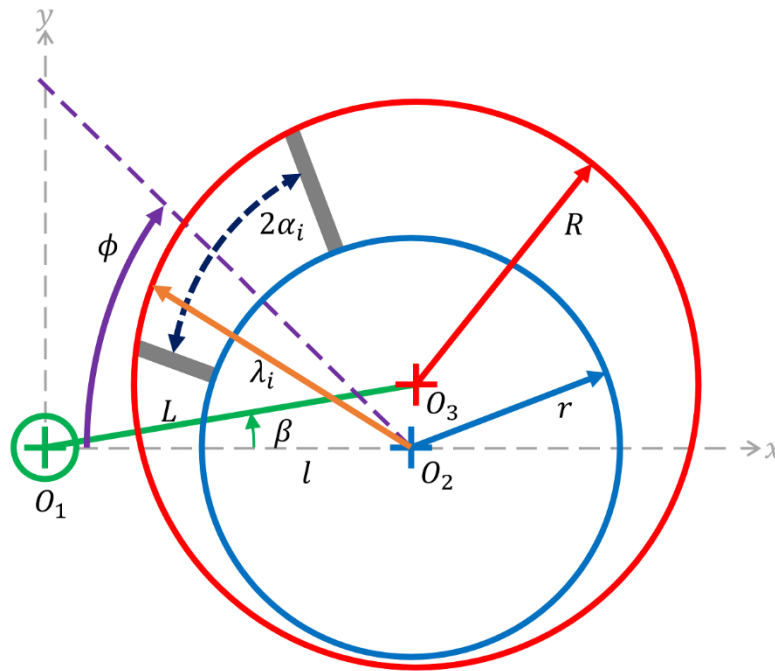


Figure 10: Coordinate system used in the VDVP model along with some basic geometric parameters.

As Figure 10 illustrates, this coordinate system is centered at the pivot point O_1 with the rotor center O_2 along the horizontal axis at a distance l from the pivot. The center O_3 of the inner surface of the stator is then located, in a polar sense, a distance L from this origin at an angle β measured counterclockwise from the horizontal axis. This angle β defines the eccentricity between the rotor and stator and therefore the displacement of the pump. As such, β will be referred to as both the eccentricity angle and the displacement throughout this dissertation.

Another key aspect of this coordinate system is the definition of ϕ , or the shaft rotation angle. This angle is measured clockwise from the horizontal axis to a vector ray with an origin O_2 . DC locations are given with respect to the centroid of the DC volume between two vanes enclosing an angle $2\alpha_i$, the rotor with radius r , the stator with radius R , the top case, and the port plate (separated by a distance equal to the vane height H).

Each DC is characterized by a unique size defined by its sector half-angle α_i . These angular sizes, as well as the naming convention for the seven DC, are given in Figure 11. The angular spans assumed in the DC Module are taken from the 3D CAD model of the case study pump and are similar to angular spans reported in [28].

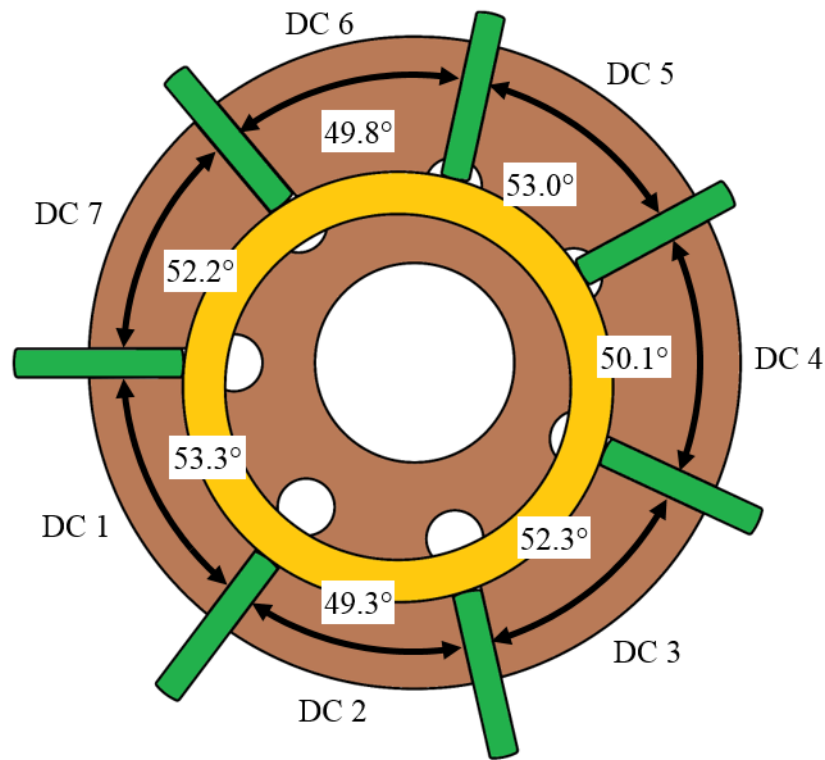


Figure 11: Naming convention of the individual DC with their respective angular spans from the case study 3D CAD model.

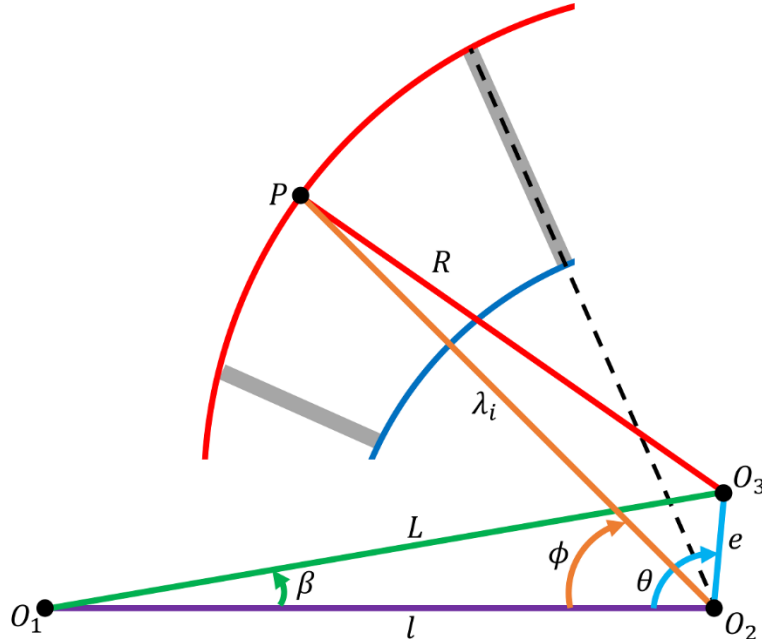


Figure 12: Triangles used to define λ_i .

The vector λ_i shown in Figure 10 defines the position of an arbitrary point P on the stator with respect to O_2 within the i^{th} DC. Figure 12 illustrates the geometry needed to describe λ_i . The common side to the two triangles is the line segment connecting O_2 and O_3 with a length e equal to the linear eccentricity between the rotor and stator centers as calculated by Equation (3.2). This line segment is oriented at an angle θ clockwise from the horizontal axis which is found using the law of cosines in Equation (3.3). This angle θ will be referred to as the complementary eccentricity angle and has a one-to-one relationship with β .

$$e = \sqrt{l^2 + L^2 - 2lL \cos(\beta)} \quad (3.2)$$

$$\theta = \cos^{-1}\left(\frac{l - L \cos(\beta)}{e}\right) \quad (3.3)$$

Applying the law of cosines to the O_2O_3P triangle with e and θ defined by Equation (3.2) and Equation (3.3), respectively, then gives the expression given by Equation (3.4). This expression can be simplified through the application of trigonometric shift and reflection properties to Equation (3.5). Solving Equation (3.5) for λ_i with the quadratic formula and taking only positive lengths gives the expression for λ_i in Equation (3.6).

$$R^2 = \begin{cases} e^2 + \lambda_i^2 - 2e\lambda_i \cos(\theta - \phi) & \text{if } 0 \leq \phi \leq \theta \\ e^2 + \lambda_i^2 - 2e\lambda_i \cos(\phi - \theta) & \text{if } \theta < \phi < \theta + \pi \\ e^2 + \lambda_i^2 - 2e\lambda_i \cos(\theta + 2\pi - \phi) & \text{if } \theta + \pi \leq \phi < 2\pi \end{cases} \quad (3.4)$$

$$R^2 = e^2 + \lambda_i^2 - 2e\lambda_i \cos(\theta - \phi) \quad (3.5)$$

$$\lambda_i = e \cos(\theta - \phi) + \sqrt{R^2 - e^2 \sin^2(\theta - \phi)} \quad (3.6)$$

Equation (3.6) actually gives the distance between O_2 and the arbitrary point P for a given angular position ϕ and eccentricity β . Recasting this formula as a parametric function of κ defined on the interval $[-1,1]$ for a given DC provides a useful expression, Equation (3.7), for defining infinitesimal slices of that DC where the curly bracket notation is used to indicate that λ_i is a function. This curly bracket notation is used throughout this thesis.

$$\lambda_i\{\kappa\} = e \cos(\theta - \phi - \kappa\alpha_i) + \sqrt{R^2 - e^2 \sin^2(\theta - \phi - \kappa\alpha_i)} \quad \kappa \in [-1,1] \quad (3.7)$$

3.3 DC Volume Calculation

Equation (3.7) can be used to calculate an interesting length λ_{ei} with Equation (3.8). For $\kappa = 1$, Equation (3.8) gives the exposed length of the leading vane for the i^{th} DC, or the distance along the line through the vane centroid from O_2 between the rotor and stator surfaces, at a given DC position ϕ and eccentricity β . Defining w to be the width of a vane, V_{DCi} can then be found using the integral in Equation (3.9) and subtracting the approximate volumes inside the $2\alpha_i$ sector of both the leading and trailing vanes. In reality, the vane tips are slightly curved and the line of contact between the vane and the stator changes as the rotation angle changes. This effect is assumed to be negligible relative to the terms included in Equation (3.9).

$$\lambda_{ei}\{\kappa\} = \lambda_i\{\kappa\} - r \quad (3.8)$$

$$V_{DCi}\{\phi, \beta\} = \int_{-1}^1 \frac{\alpha_i H}{2} ([\lambda_i\{\kappa\}]^2 - r^2) d\kappa - \frac{wH}{2} \lambda_{ei}\{-1\} - \frac{wH}{2} \lambda_{ei}\{1\} \quad (3.9)$$

The nature of the integrand in Equation (3.9) necessitates the use of numerical methods to solve for V_{DCi} at a particular ϕ and β . Therefore, a custom MATLAB script applied the trapezoidal method to solve Equation (3.9) on a grid of ϕ and β to generate a 2D lookup table of pre-calculated volumes for each DC. This grid was defined as the product space of a vector of

values of ϕ spanning one complete shaft revolution at a resolution $\Delta\phi$ of 0.5° with a vector of β values ranging from 0° to a maximum of 5.6° at a resolution $\Delta\beta$ of 0.056° . Following this procedure results in volumes that differ from those measured directly in the 3D CAD model by less than 0.5% typically. At each simulation time step, V_{DCi} in Equation (3.1) is then found by linearly interpolating between points of the lookup table using the simulated ϕ and β .

3.4 DC Volume Rate of Change

The time rate of change of V_{DCi} is found deriving Equation (3.9) with respect to time to get the expression given by Equation (3.10). The partial derivatives in Equation (3.10) are rather tedious to derive and are given in Equation (3.11) and Equation (3.13) with terms defined by Equations (3.12), (3.14), and (3.15). These partial derivative terms are handled in much the same way as V_{DCi} in that they are pre-calculated on the same grid of ϕ and β using the trapezoidal method to generate 2D lookup tables for each DC. Linear interpolation between the points in the tables then gives accurate coefficients for use in Equation (3.10).

$$\frac{dV_{DCi}}{dt} = \frac{\partial V_{DCi}}{\partial \phi} \frac{d\phi}{dt} + \frac{\partial V_{DCi}}{\partial \beta} \frac{d\beta}{dt} \quad (3.10)$$

$$\frac{\partial V_{DCi}}{\partial \phi} = \int_{-1}^1 \alpha_i H \lambda_i \{\kappa\} D_{\phi i} \{\kappa\} d\kappa - \frac{wH}{2} D_{\phi i} \{-1\} - \frac{wH}{2} D_{\phi i} \{1\} \quad (3.11)$$

$$D_{\phi i} \{\kappa\} = e \sin(\theta - \phi - \kappa \alpha_i) - \frac{e^2 \sin(\theta - \phi - \kappa \alpha_i) \cos(\theta - \phi - \kappa \alpha_i)}{\sqrt{R^2 - e^2 \sin^2(\theta - \phi - \kappa \alpha_i)}} \quad (3.12)$$

$$\frac{\partial V_{DCi}}{\partial \beta} = \int_{-1}^1 \alpha_i H \lambda_i \{\kappa\} D_{\beta i} \{\kappa\} d\kappa - \frac{wH}{2} D_{\beta i} \{-1\} - \frac{wH}{2} D_{\beta i} \{1\} \quad (3.13)$$

$$D_{\beta i} \{\kappa\} = C_{\beta i} \{\kappa\} - D_{\phi i} \{\kappa\} \frac{lL \cos(\beta) - L^2}{e^2} \quad (3.14)$$

$$C_{\beta i} \{\kappa\} = \frac{lL \sin(\beta)}{e} \left(\cos(\theta - \phi - \kappa \alpha_i) - \frac{e \sin^2(\theta - \phi - \kappa \alpha_i)}{\sqrt{R^2 - e^2 \sin^2(\theta - \phi - \kappa \alpha_i)}} \right) \quad (3.15)$$

For a given constant eccentricity, Equation (3.10) can be simplified by neglecting the second term on the right hand side of the equality. Analyzing this new expression, Equation

(3.16), can provide some useful insights. For a non-zero shaft speed (i.e. the time rate of change of ϕ is some positive real number), the time rate of change of V_{DCi} will only be zero when the partial derivative term given by Equation (3.11) is zero. This occurs at two key angular positions.

$$\frac{dV_{DCi}}{dt} = \frac{\partial V_{DCi}}{\partial \phi} \frac{d\phi}{dt} \quad (3.16)$$

The first of these is given by Equation (3.17) and corresponds to the kinematic outer-dead-center position of the DC volume, or the ODC angle ϕ_{ODC} . When the DC is in the ODC position, its volume is at a maximum. The ODC angle then marks the transition point from the pumping chamber's suction stroke to its delivery stroke. The second angle, by no surprise, occurs at an offset of 180° from ϕ_{ODC} and represents the inner-dead-center (IDC) position corresponding to the minimum DC volume, or the dead volume [2]. Taking the difference between V_{DCi} at ϕ_{ODC} and ϕ_{IDC} then gives the displaced volume of the i^{th} DC at the assumed β .

$$\phi_{ODC} = \theta \quad (3.17)$$

$$\phi_{IDC} = \theta + \pi \quad (3.18)$$

Summing the displaced volume contributions of all seven DC at a maximum β gives the geometric displacement, or nominal size, of the pump. Meanwhile, superimposing the volumetric rate of change, during the delivery stroke only, of each DC upon each other gives the pump's kinematic flowrate. The geometric displacement V_p and kinematic flowrate Q_{kin} are useful in evaluating the steady-state performance of the pump and will be revisited later in Chapter 5.

The angles ϕ_{ODC} and ϕ_{IDC} are also useful in displaying information about the pump performance or state variables over a single revolution of the shaft. Therefore, unless otherwise specified, plots showing pump flows, pressures, and forces as a function of the angular position of the shaft will report a ϕ measured clockwise from ϕ_{ODC} at a maximum eccentricity condition. Reasons for this will become more apparent in the context of the instantaneous DC flowrates.

3.5 DC Flow Equations

These instantaneous flowrates, Q_{rHPi} and Q_{rLPi} in Equation (3.1), are calculated using the orifice equation for turbulent flow as given by Equation (3.19) and Equation (3.20). As Figure 13 illustrates, these equations describe the pressure driven flow through an equivalent orifice

connection between the i^{th} DC control volume and the delivery port or suction port, respectively. The “size” of this orifice connection is determined by the constant discharge coefficient α_D of 0.6 and an area parameter A_{rHPi} or A_{rLPi} which will be defined in Section 3.6.

The hyperbolic tangents in Equation (3.19) and Equation (3.20) behave as smooth sign functions and result in better numerical conditioning for the solver in Simulink. Using a hyperbolic tangent instead of a sign function only distorts the magnitude of the flow when the pressures are nearly equal (i.e. a differential pressure less than 3Pa) and thus has a negligible impact on the overall performance predictions in terms of both flowrates and pressures. A more significant effect is captured by using the effective density of the fluid/air mixture ρ_{mix} which will be defined in Section 3.7.

$$Q_{rHPi} = \alpha_D A_{rHPi} \tanh(p_{HP} - p_{DCi}) \sqrt{\frac{2|p_{HP} - p_{DCi}|}{\rho_{mix}}} \quad (3.19)$$

$$Q_{rLPi} = \alpha_D A_{rLPi} \tanh(p_{LP} - p_{DCi}) \sqrt{\frac{2|p_{LP} - p_{DCi}|}{\rho_{mix}}} \quad (3.20)$$

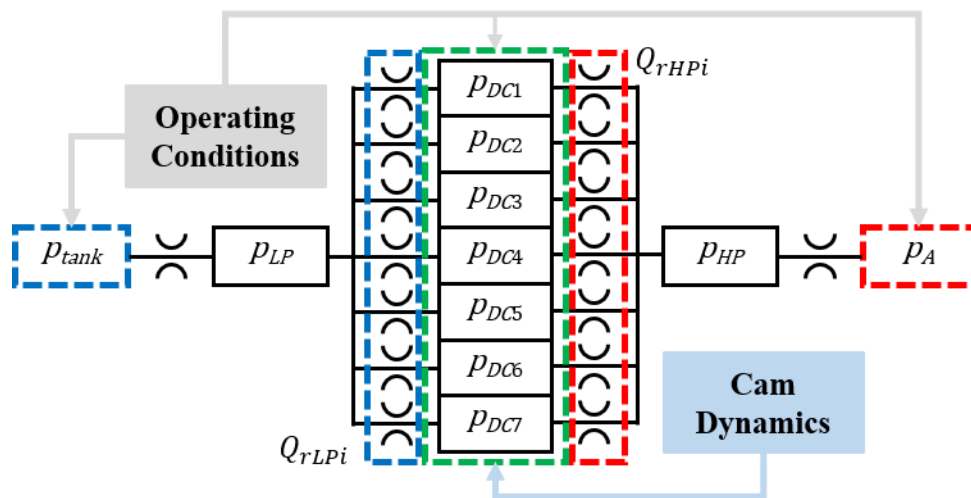


Figure 13: Network of orifice connections between the various control volumes considered in the lumped parameter pump model.

3.6 Equivalent Area Files

The most critical components, by far, of Equations (3.19) and (3.20) are the equivalent areas A_{rHPi} and A_{rLPi} . These parameters vary with the rotation of both the shaft and the stator.

For any given combination of ϕ and β , A_{rHPi} and A_{rLPi} contain information about the port and relief groove geometries and their intersection with the unique DC control volume geometry for that orientation. Ultimately, the value of A_{rHPi} , or A_{rLPi} , at a given ϕ and β represents the minimum cross-sectional area of the flow passage between the i^{th} DC and the delivery port, or suction port, perpendicular to the streamlines of the flow. This information is contained in the DC Module in the form of 2D lookup tables called area files.

This area file approach is in line with previous work conducted at the Maha Fluid Power Research Center such as in [30] and therefore allows for the simulation of realistic cross-port flows that contribute to the unmeasurable internal leakages of the pump. Generation of these area files is a several step process that starts with defining the realistic control volume geometries. This is accomplished by a Boolean subtraction operation using the 3D CAD model of the pump and an arbitrarily larger solid cube. The solid bodies that remain after the pump geometry is removed represent the various control volumes filled with fluid. Figure 14 illustrates these fluid bodies for an example case of a DC near ϕ_{ODC} at a maximum eccentricity condition. Once generated, these bodies are fixed in space relative to each other and analyzed.

While the DC control volume may be generated in this fashion, it is more convenient to build a parametric 3D model that provides the accurate geometry based on inputs of the current angular position ϕ , the sector size $2\alpha_i$, and the current eccentricity β . This is not done for the port volumes on account of their more complex geometries and in an effort to reduce the number of analyses required. A critical aspect of the parametric DC model is that the definitions of ϕ and β coincide with the coordinate system established in Figure 10. This ensures proper alignment of the area files in Equations (3.19) and (3.20) with the geometric information considered in Equation (3.1) for a consistent geometric model that captures timing effects arising from the non-uniform vane spacing shown in Figure 11.

The fluid bodies are analyzed in the next step of the area file generation process at each of the lookup-table grid points for each of the seven DC. If the same grid of ϕ and β used for the DC volume lookup tables is used, 509,040 fluid geometry configurations would need to be analyzed. In each analysis, a minimum of three areas must be measured to fully characterize A_{rHPi} and A_{rLPi} (one for the delivery port and one for each branch of the suction port). Thus, over one and half million area measurements would need to be made.

To reduce the size of this problem to a more manageable scope, only three eccentricity levels corresponding to 20%, 50%, and 100% pump displacements were used. This reduces the number of area analyses needed to only 45,360 (3% of the original problem size). Ideally, each of these area analyses would be supported by 3D CFD simulations to characterize the streamlines. However, since each DC is sufficiently similar to the others and the streamlines are trivial to find once the DC is completely over the port opening, CFD simulations for a few configurations can give insight into the streamline trends over a range of ϕ values. Simple section cuts in the 3D CAD model can then reveal the relevant cross sections for measurement.

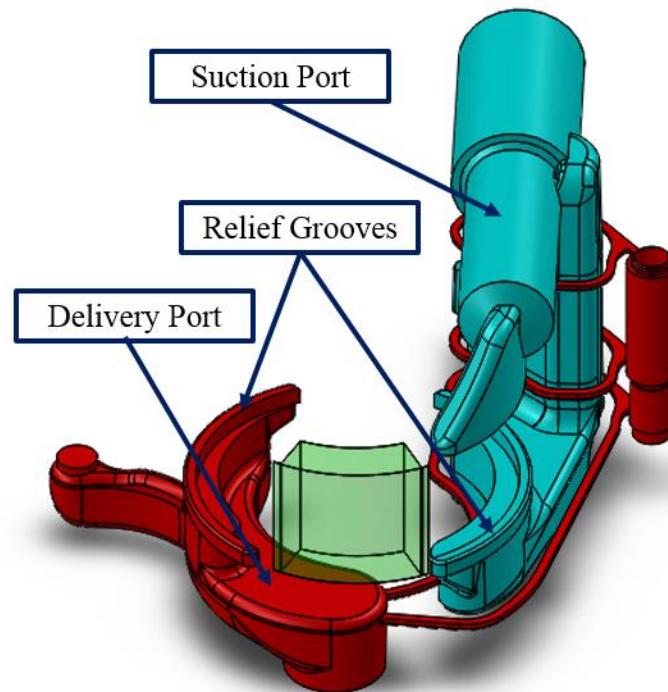


Figure 14: Example control volume geometries extracted from the 3D CAD model of the pump representing the suction port (blue), delivery port (red), and a single DC at an arbitrary position close to ϕ_{ODC} at maximum β .

Figure 15 provides an illustration of this procedure. Starting in images A and B, the overall fluid geometry configuration is examined and the streamlines are visualized (either based on experience and knowledge of the fundamental fluid dynamics or using CFD simulations). At this step, trivial area file values can be assigned. For the configuration shown in Figure 15 this means assigning a zero value to the A_{rLPi} tables for this grid point. With the streamlines visualized, a section cut, such as in image C, reveals the perpendicular cross sections such as in

image D. In many cases, however, multiple cross sections may need to be checked to find the minimum value to store in the area file.

For the example illustrated by Figure 15, this procedure results in a cross section of the relief groove machined into the stator with an area of 6.073mm^2 . This is the value assigned to A_{rHPi} for the grid point even though the area does not belong any shared face between the DC volume and the delivery port. As Figure 15 reveals, this shared face has a larger area of 10.223mm^2 . This is roughly 68% larger than the downstream value along the relief groove in addition to being a face at an angle with respect to the streamlines.

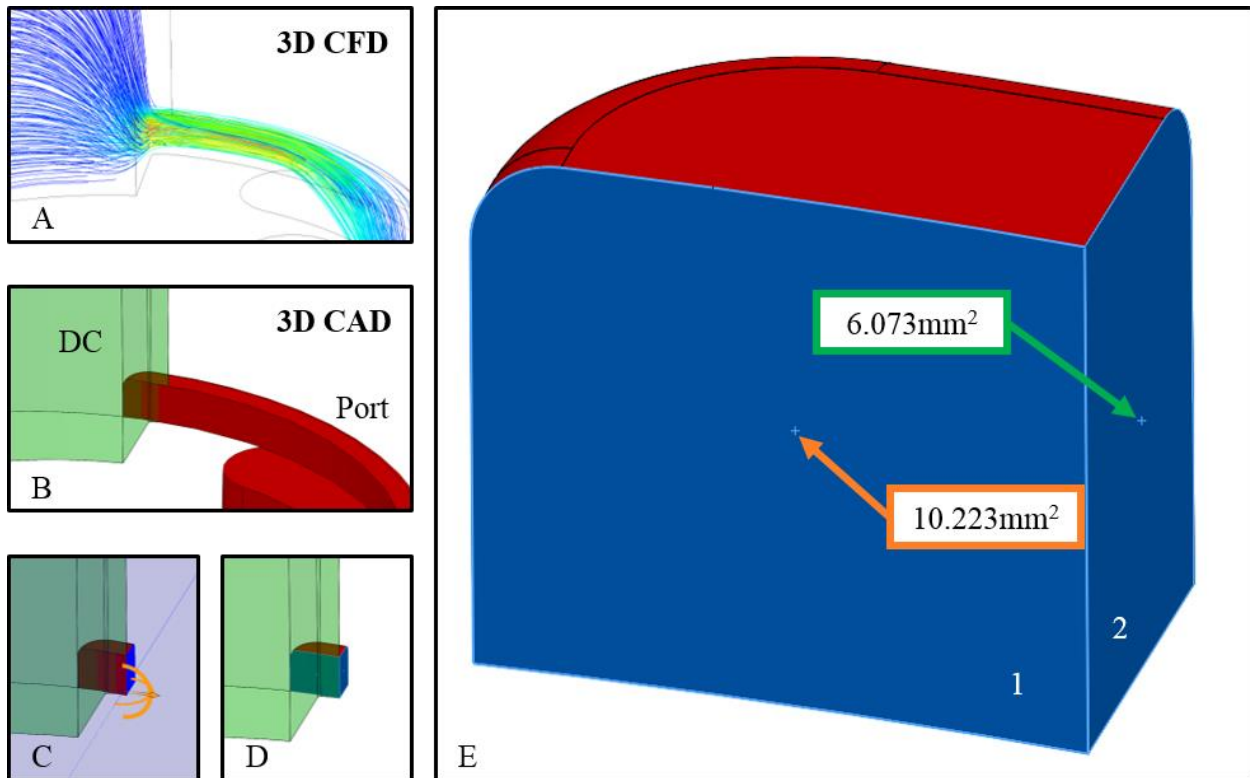


Figure 15: Illustrative example of the procedure of analyzing section cuts in the 3D CAD model to evaluate the area file value for a given fluid geometry configuration. Image A: Streamlines from 3D CFD simulation. Image B: 3D CAD model at the same position. Image C: Section cut using the DC geometry. Image D: Resulting fluid geometry of the port. Image E: Comparison of the measured areas of faces 1 and 2, with face 2 being the minimum perpendicular area along the streamlines indicated by the CFD simulation results shown in Image A.

This evaluation procedure is most critical in the regions near ϕ_{ODC} and ϕ_{IDC} where the DC volume is transitioning into, or out of, connection with the ports and restriction of the flow passage is highest. These regions have the highest impact on the shape of the resulting flow and pressure profiles calculated by the set of Equations (3.1), (3.19), and (3.20). Figure 16 illustrates

the final results of this careful analysis by presenting area file for DC 2 for both 20% and 100% displacements. The detail view in Figure 16 shows typical shapes for these restricted area regions near IDC. The restricted area regions near ODC are similar in shape and magnitude.

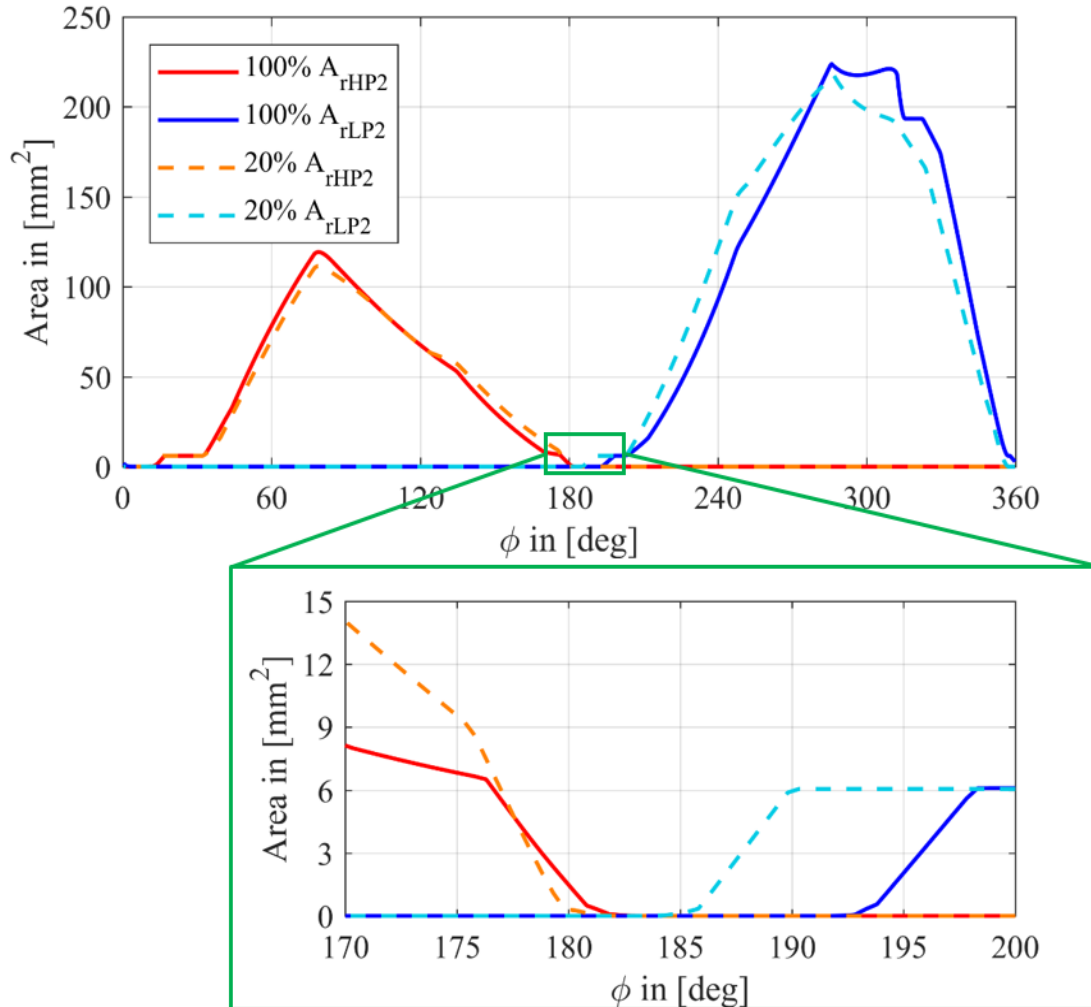


Figure 16: Example DC 2 area file results showing the IDC transition region in detail to illustrate the timing effects and relative magnitude of the restricted area regions. The ϕ angles here are measured clockwise from ϕ_{ODC} at maximum eccentricity.

The detail view in Figure 16 also illustrates how the relative timing of the port connections changes with displacement. As the eccentricity changes, the relief grooves in the stator move relative to the port geometry resulting in a shorter effective angular distance that the DC volume must travel between the ports. A comparison between the area files at a maximum eccentricity condition for DC 1 and DC 2 in Figure 17 for this same IDC region reveals a similar difference in timing effected by their difference in angular spans. In fact, the larger α_i of DC 1

actually closes the gap between the delivery and suction ports near IDC at low eccentricities, resulting in a brief cross-port connection and is the only such instance for the case study pump.

Comparing the area files at different displacement levels for a single DC reveals that a linear interpolation between the values at different displacement levels for a given ϕ is both possible and results in a sufficient level of accuracy. Figure 16 illustrates this observation.

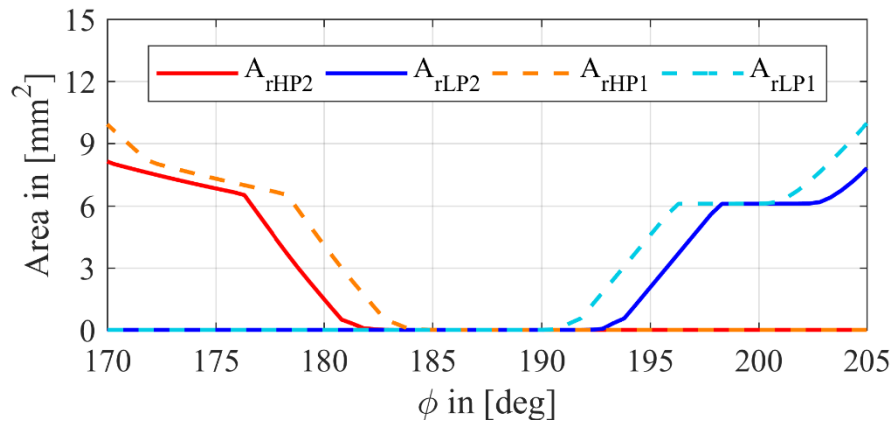


Figure 17: Detail view of the IDC region comparing the DC 1 and DC 2 area files at full displacement to show timing effects with ϕ again measured clockwise from ϕ_{ODC} .

Following this area file generation procedure, and its implementation in the model, results in accurate flow passage geometries and therefore instantaneous flowrates as evidenced by the correlation of the DC pressure profiles that will be shown in Chapter 5. Other state of the art VDVP models do not include this level of detail. In fact, many of them only consider the area of the shared face between the DC volume and the port geometry [9] [10] [14].

3.7 Oil Model

The simulation model calculates the fluid properties used in the pressure and flow calculations with an empirical model developed in the Maha Fluid Power Research Center for an ISO 32 hydraulic oil giving the pure fluid's dynamic viscosity μ_{oil} , density ρ_{oil} , and bulk modulus K_{oil} as functions of both pressure and the fluid temperature T_{oil} [59]. To account for aeration effects, these parameters were used to find the effective density and bulk modulus of the fluid/air mixture p_{mix} and K_{mix} , respectively, using Equation (3.21) and Equation (3.22) where r_{air} is the percentage by volume of entrained air. In Equation (3.22), the density of air at STP ρ_{air} was assumed. These equations can be applied to any alternate oil model, depending on the

purpose of the simulation, such as the one presented in [6]. However, only the ISO 32 hydraulic oil model will be used in this work.

For this dissertation, the value r_{air} is held constant even though models in the literature allow this quantity to vary as the pressure changes [3]. This simplification arises from the assumption that cavitation effects are negligible in an evaluation of the overall pump dynamics.

$$K_{mix} = \frac{K_{oil}p_{DCi}}{p_{DCi} + r_{air}K_{oil}} \quad (3.21)$$

$$\rho_{mix} = \frac{(1 - r_{air})V_{DCi}\rho_{oil} + r_{air}V_{DCi}\rho_{air}}{V_{DCi}} \quad (3.22)$$

3.8 Port Modules

In order to calculate the instantaneous DC flowrates with Equation (3.19) and Equation (3.20), the port pressures p_{HP} and p_{LP} are required. As Figure 9 indicates, the load simulator has a similar construction to the DC Module, i.e. coupled flow and pressure build up equations. Equations (3.23) and (3.24), therefore, describe the delivery port pressure and flow characteristics while Equations (3.26) and (3.27) describe the suction port characteristics.

$$\frac{dp_{HP}}{dt} = \frac{K_{mix}}{V_{HP}} \left(\sum_{i=1}^7 Q_{rHPi} - Q_A \right) \quad (3.23)$$

$$Q_A = \alpha_D A_{load} \tanh(p_A - p_{HP}) \sqrt{\frac{2|p_A - p_{HP}|}{\rho_{mix}}} \quad (3.24)$$

$$p_A = R_{Line} Q_A \quad (3.25)$$

$$\frac{dp_{LP}}{dt} = \frac{K_{mix}}{V_{LP}} \left(Q_{in} - \sum_{i=1}^7 Q_{rLPi} \right) \quad (3.26)$$

$$Q_{in} = \alpha_D A_{filter} \tanh(p_{tank} - p_{LP}) \sqrt{\frac{2|p_{tank} - p_{LP}|}{\rho_{mix}}} \quad (3.27)$$

Equation (3.25) represents a simple way to calculate the line pressure where the resistance R_{Line} is selected to result in a desired pressure level for a given flow demand and is

used when the entire VDVP system is simulated. When focusing on the behavior of the DC Module at a specific set of operating conditions, p_A is set constant and the parameters A_{load} and A_{filter} in Equation (3.24) and Equation (3.27), respectively, determine the loading conditions of the pump. Modeling the ports in this manner allows for the simulation of port pressure ripples and includes the effects of fluid compressibility on the pump outlet flow.

3.9 Internal Forces: Rotor Torque

For a given set of operating conditions, i.e. pump speed and outlet pressure, Equation (3.1) can now be completely solved and a discussion of the dynamic forces acting on various pump components is possible. Returning to Equations (3.7) and (3.8) and observing Figure 18, the rotor torque, or shaft load M_p , can be found. Neglecting friction, this torque is a combination of inertial loads coming from both the vanes and the mass of the oil trapped in the DC and the forces generated by the DC pressures.

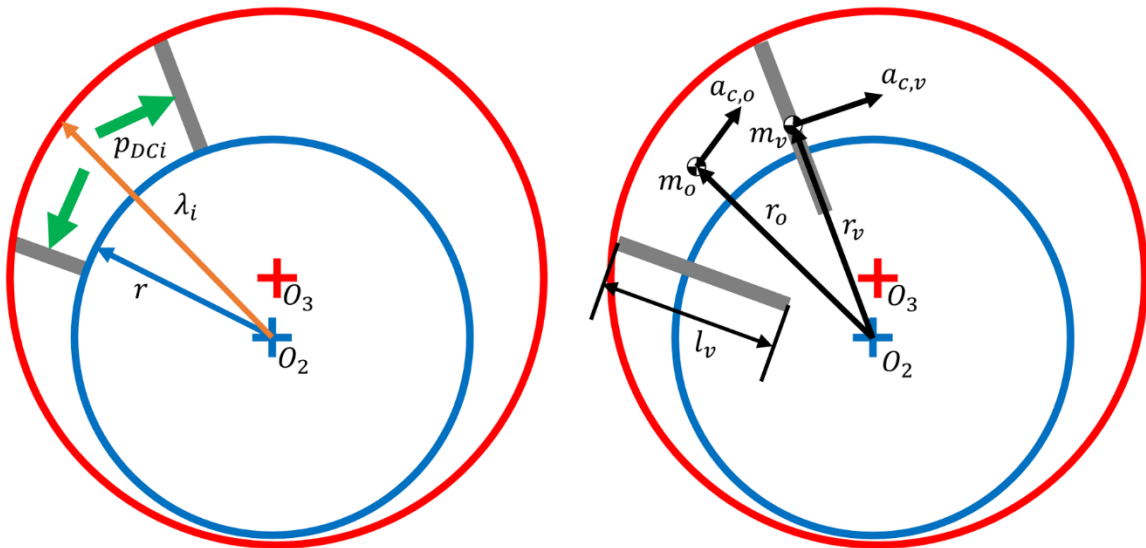


Figure 18: Diagrams used to determine expressions to calculate rotor torque.

Assuming the pressure force on a vane is equal in magnitude to the product of the instantaneous DC pressure and the exposed area of that vane and acts through the centroid of that area, the torque contribution of a single DC can be found by multiplying the pressure by a geometric parameter ψ_i given by Equation (3.28). These parameter values are stored in 2D lookup tables for each DC based on the same grid of ϕ and β values used in the V_{DCi} lookup

tables. The net moment generated by the DC pressures can then be simply calculated as the sum of the contributions from each DC.

$$\psi_i\{\phi, \beta\} = \frac{H}{2} ([\lambda_i\{-1\}]^2 - [\lambda_i\{1\}]^2) \quad (3.28)$$

The inertial load component, on the other hand, is found by analyzing the curvilinear path traversed by the centers of mass of both the oil within a chamber and the vanes themselves. This begins with the definition of the position vectors r_o and r_v which give the radial locations of the centroid of the DC control volume and leading vane, respectively, in a polar coordinate system where ϕ defines the angular position. These radial locations are given by Equations (3.29) and (3.30), where l_v is the length of the vane.

$$r_o = \frac{\lambda_i\{0\} + r}{2} \quad (3.29)$$

$$r_v = \lambda_i\{1\} - \frac{l_v}{2} \quad (3.30)$$

Equations (3.29) and (3.30) are then used to define the circumferential velocity of both centers of mass as in Equations (3.31) and (3.32). Deriving these expressions for the circumferential velocity, which requires finding the partial derivatives of Equation (3.7) with respect to both ϕ and β , results in Equations (3.33) and (3.34) where the partial derivative coefficients functions of both ϕ and β and are listed as Equations (3.35) through (3.38).

$$v_{c,o} = r_o \frac{d\phi}{dt} \quad (3.31)$$

$$v_{c,v} = r_v \frac{d\phi}{dt} \quad (3.32)$$

$$a_{c,o} = \alpha_{c1,o} \left(\frac{d\phi}{dt}\right)^2 + \alpha_{c2,o} \frac{d\phi}{dt} \frac{d\beta}{dt} + r_o \frac{d^2\phi}{dt^2} \quad (3.33)$$

$$a_{c,v} = \alpha_{c1,v} \left(\frac{d\phi}{dt}\right)^2 + \alpha_{c2,v} \frac{d\phi}{dt} \frac{d\beta}{dt} + r_v \frac{d^2\phi}{dt^2} \quad (3.34)$$

$$\alpha_{c1,o}\{\phi, \beta\} = \frac{e^2 \sin(\theta - \phi) \cos(\theta - \phi)}{\sqrt{R^2 - e^2 \sin^2(\theta - \phi)}} - e \sin(\theta - \phi) \quad (3.35)$$

$$\alpha_{c2,o}\{\phi, \beta\} = \frac{\omega_s\{0\}}{e} + \frac{\omega\{0\} \sin(\theta - \phi)}{\sqrt{R^2 - e^2 \sin^2(\theta - \phi)}} \quad (3.36)$$

$$\alpha_{c1,v}\{\phi, \beta\} = \frac{2e^2 \sin(\theta - \phi - \alpha_i) \cos(\theta - \phi - \alpha_i)}{\sqrt{R^2 - e^2 \sin^2(\theta - \phi - \alpha_i)}} - e \sin(\theta - \phi - \alpha_i) \quad (3.37)$$

$$\alpha_{c2,v}\{\phi, \beta\} = \frac{2\omega_s\{1\}}{e} + \frac{2\omega\{1\} \sin(\theta - \phi - \alpha_i)}{\sqrt{R^2 - e^2 \sin^2(\theta - \phi - \alpha_i)}} \quad (3.38)$$

The terms ω_s and ω in Equations (3.36) and (3.38) are collections of common terms that arise during the derivation process. They are parametric functions similar to Equation (3.7) and are given by Equations (3.39) and (3.40).

$$\omega\{\kappa\} = lL \cos(\beta + \theta - \phi - \kappa\alpha_i) - (l^2 - e^2) \cos(\theta - \phi - \kappa\alpha_i) \quad (3.39)$$

$$\omega_s\{\kappa\} = lL \sin(\beta + \theta - \phi - \kappa\alpha_i) - (l^2 - e^2) \sin(\theta - \phi - \kappa\alpha_i) \quad (3.40)$$

With the circumferential accelerations defined by Equations (3.33) and (3.34), the resulting inertial loads applied to the rotor body are assumed to be equal to the negative product of the mass (concentrated at its center of mass), the circumferential acceleration, and the radial position given by either Equation (3.29) or (3.30) as indicated by the term inside the second summation in Equation (3.41). As Equation (3.41) indicates, the net inertial load applied to the rotor body is found by summing the contribution of each DC and its leading vane.

$$M_p\{\phi, \beta\} = \sum_{i=1}^7 \psi_i p_{DCi} - \sum_{i=1}^7 (\rho_{mix} V_{DCi} r_o a_{c,o} + m_v r_v a_{c,v}) \quad (3.41)$$

While the expression for the shaft load M_p given by Equation (3.41) does not include any friction effects, it does include torque losses arising from the compressibility of the fluid/air mixture via the pressure build up equation, Equation (3.1), and non-ideal timing arising from the port designs via the area files in Equations (3.19) and (3.20). In Chapter 5 it will be shown that these effects account for most of the torque losses in the pump. Furthermore, an exact calculation of the pump torque is not necessary in the evaluation of the pump dynamics and their interaction with a pressure control system architecture. For these reasons, Equation (3.41) is sufficient to calculate realistic pump torques for this dissertation.

3.10 Internal Forces: Moment Applied to Stator

Calculation of the dynamic forces acting on the stator is not as straightforward analytically even though it is simple conceptually. Conceptually, the pressure force has a magnitude equal to the product of the DC pressure and the surface area of the stator bounding the DC and acts along a unit vector starting at O_3 and piercing the surface area's centroid. Referring to Figure 19, this force would then be acting along the vector $\vec{\gamma}_{3P}$ and the resulting moment can be found by taking the cross product of $\vec{\gamma}_{1P}$ with this force vector. Meanwhile, the inertial loads are equal to the cross product of $\vec{\gamma}_{1P}$ with the centrifugal forces of both the oil within the DC and the vanes acting in a radial direction.

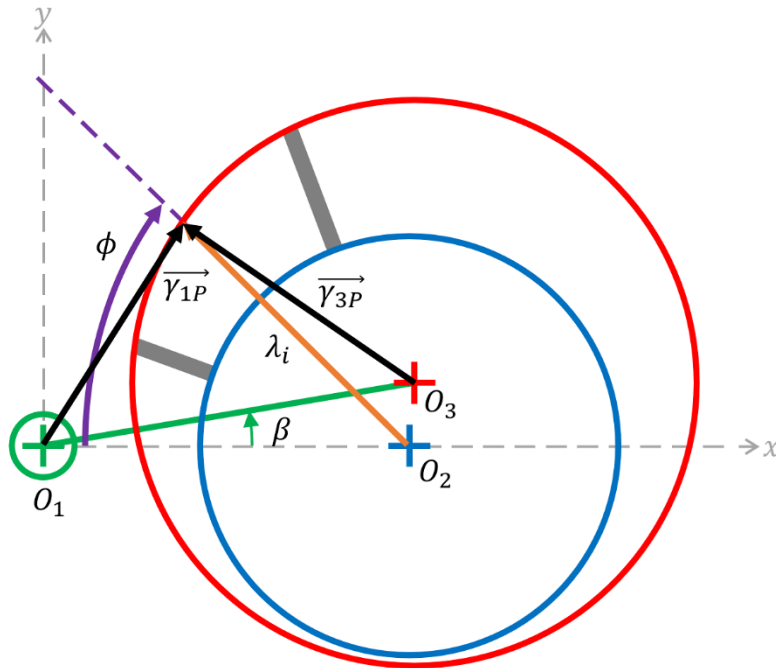


Figure 19: Diagram showing vector definitions used in determining the DC pressure induced stator moment.

In general, the vectors $\vec{\gamma}_{1P}$ and $\vec{\gamma}_{3P}$ in Figure 19 terminate at a point P identical to the endpoint of the vector with length λ_i and can thus be defined by Equation (3.42) through Equation (3.47) parametrically in terms of κ . Just as Equation (3.7) is valid for any combination of ϕ and β , these expressions are also valid for any combination of ϕ and β . Furthermore, it can be shown that the length of $\vec{\gamma}_{3P}$ is always equal to the radius of the inner surface of the stator R .

$$\vec{\gamma}_{3P}\{\phi, \beta, \kappa\} = [\gamma_{3Px}\{\kappa} \quad \gamma_{3Py}\{\kappa}] \quad (3.42)$$

$$\gamma_{3Px}\{\kappa\} = l - L \cos(\beta) - \lambda_i\{\kappa\} \cos(\phi + \kappa\alpha_i) \quad (3.43)$$

$$\gamma_{3Py}\{\kappa\} = \lambda_i\{\kappa\} \sin(\phi + \kappa\alpha_i) - L \sin(\beta) \quad (3.44)$$

$$\overrightarrow{\gamma_{1P}}\{\phi, \beta, \kappa\} = [\gamma_{1Px}\{\kappa\} \quad \gamma_{1Py}\{\kappa\}] \quad (3.45)$$

$$\gamma_{1Px}\{\kappa\} = l - \lambda_i\{\kappa\} \cos(\phi + \kappa\alpha_i) \quad (3.46)$$

$$\gamma_{1Py}\{\kappa\} = \lambda_i\{\kappa\} \sin(\phi + \kappa\alpha_i) \quad (3.47)$$

Using the parametric definition of the arc along the stator surface between the vanes given by Equation (3.45), the arc length can be found by integrating the differential element defined by Equation (3.48) over the range of κ values. Note that the prime notation here does not refer to derivatives with respect to time but partial derivatives with respect to κ . Using Equations (3.49) through (3.51) allows for the surface area σ can be found through numerical integration.

$$d\sigma = H \sqrt{[\gamma'_{1Px}\{\kappa\}]^2 + [\gamma'_{1Py}\{\kappa\}]^2} d\kappa \quad (3.48)$$

$$\gamma'_{1Px}\{\kappa\} = -\lambda'_i\{\kappa\} \cos(\phi + \kappa\alpha_i) + \alpha_i \lambda_i\{\kappa\} \sin(\phi + \kappa\alpha_i) \quad (3.49)$$

$$\gamma'_{1Py}\{\kappa\} = \lambda'_i\{\kappa\} \sin(\phi + \kappa\alpha_i) + \alpha_i \lambda_i\{\kappa\} \cos(\phi + \kappa\alpha_i) \quad (3.50)$$

$$\lambda'_i\{\kappa\} = e\alpha_i \sin(\theta - \phi - \kappa\alpha_i) + \frac{2e^2\alpha_i \cos(\theta - \phi - \kappa\alpha_i) \sin(\theta - \phi - \kappa\alpha_i)}{\sqrt{R^2 - e^2 \sin^2(\theta - \phi - \kappa\alpha_i)}} \quad (3.51)$$

If, instead of integrating to find σ at this point, the differential surface area is used as the area to find the pressure force, then Equation (3.52) can be written to describe a geometric parameter τ_{DCi} . Equation (3.53) gives the expression that is found by substituting the definitions of $\overrightarrow{\gamma_{1P}}$, $\overrightarrow{\gamma_{3P}}$, and $d\sigma$ into Equation (3.52) and performing the cross product operation. A custom MATLAB script was used to solve Equation (3.53) numerically using the trapezoidal method for each of the grid points used in the V_{DCi} calculations to generate 2D lookup tables of τ_{DCi} for each DC. The accuracy of these calculations was checked against the 3D CAD model of the pump using a projected areas method for several combinations of ϕ and β . This comparison indicated a typical error less than 1% for Equation (3.53). Therefore, an accurate net pressure moment acting on the stator can then be found by summing the contribution of each DC using Equation (3.54).

$$\tau_{DCi}\{\phi, \beta\} = \int_s \left(\vec{\gamma}_{1P} \times \frac{\vec{\gamma}_{3P}}{\|\vec{\gamma}_{3P}\|} \right) d\sigma \quad (3.52)$$

$$\tau_{DCi}\{\phi, \beta\} = \int_{-1}^1 H \sqrt{[\gamma'_{1Px}]^2 + [\gamma'_{1Py}]^2} \frac{\gamma_{1Px}\gamma_{3Py} - \gamma_{1Py}\gamma_{3Px}}{R} d\kappa \quad (3.53)$$

$$M_{DC}\{\phi, \beta\} = \sum_{i=1}^7 \tau_{DCi} p_{DCi} \quad (3.54)$$

While many authors have included centrifugal forces acting on the stator from both the vanes and the oil in the DC [9] [10] [20] [24] [60], others neglect these components and consider only the DC pressure force contribution to the internal forces acting on the stator [11] [16] [19] [21]. For many operating conditions, these centrifugal forces are small compared to the dominant pressure forces. However, at high speeds they can represent as high as half the magnitude of the pressure force [60]. To calculate these centrifugal forces and the moment they exert on the stator, Equations (3.29) and (3.30) must first be used to define the velocity of the centers of mass in the radial direction as given by Equations (3.55) and (3.56).

$$v_{r,o} = \frac{1}{2} \left(\frac{\partial \lambda_i\{0\}}{\partial \phi} \frac{d\phi}{dt} + \frac{\partial \lambda_i\{0\}}{\partial \beta} \frac{d\beta}{dt} \right) \quad (3.55)$$

$$v_{r,v} = \frac{\partial \lambda_i\{1\}}{\partial \phi} \frac{d\phi}{dt} + \frac{\partial \lambda_i\{1\}}{\partial \beta} \frac{d\beta}{dt} \quad (3.56)$$

Following the mathematical description of the curvilinear motion of a point, the radial component of the total acceleration of the centers of mass shown in Figure 18 is found by deriving the expressions given by Equations (3.55) and (3.56) and including the centrifugal acceleration term. Grouping similar terms, these accelerations can then be expressed by Equations (3.57) and (3.58) and where the several coefficients are given by Equation (3.59) through Equation (3.76).

$$a_{r,o} = \alpha_{r1,o} \left(\frac{d\phi}{dt} \right)^2 + \alpha_{r2,o} \left(\frac{d\beta}{dt} \right)^2 + \alpha_{r3,o} \frac{d\phi}{dt} \frac{d\beta}{dt} + \alpha_{r4,o} \frac{d^2\phi}{dt^2} + \alpha_{r5,o} \frac{d^2\beta}{dt^2} \quad (3.57)$$

$$a_{r,v} = \alpha_{r1,v} \left(\frac{d\phi}{dt} \right)^2 + \alpha_{r2,v} \left(\frac{d\beta}{dt} \right)^2 + \alpha_{r3,v} \frac{d\phi}{dt} \frac{d\beta}{dt} + \alpha_{r4,v} \frac{d^2\phi}{dt^2} + \alpha_{r5,v} \frac{d^2\beta}{dt^2} \quad (3.58)$$

$$\alpha_{r1,o}\{\phi, \beta\} = -\frac{r}{2} - \frac{R^2 + e^2 R^2 (2 \cos(2[\theta - \phi]) - 1)}{2(R^2 - e^2 \sin^2(\theta - \phi))^{3/2}} \quad (3.59)$$

$$\alpha_{r2,o}\{\phi, \beta\} = b_{r,o1} + b_{r,o2} + b_{r,o3} + b_{r,o4} \quad (3.60)$$

$$b_{r,o1}\{\phi, \beta\} = \frac{e^2 \chi\{0\} + \omega\{0\}(l^2 - lL \cos(\beta))}{2e^3} \quad (3.61)$$

$$b_{r,o2}\{\phi, \beta\} = \frac{lL[\sin(\beta) \sin(\beta + \theta - \phi) - 2 \cos(\beta + 2[\theta - \phi])]}{2\sqrt{R^2 - e^2 \sin^2(\theta - \phi)}} \quad (3.62)$$

$$b_{r,o3}\{\phi, \beta\} = \frac{\omega_2\{0\}(l^2 - lL \cos(\beta) + e^2)}{2e^2 \sqrt{R^2 - e^2 \sin^2(\theta - \phi)}} \quad (3.63)$$

$$b_{r,o4}\{\phi, \beta\} = -\frac{[\omega\{0\}]^2 \sin^2(\theta - \phi)}{2(R^2 - e^2 \sin^2(\theta - \phi))^{3/2}} \quad (3.64)$$

$$\alpha_{r3,o}\{\phi, \beta\} = \frac{\omega_2\{0\} + L^2 - lL \cos(\beta)}{2\sqrt{R^2 - e^2 \sin^2(\theta - \phi)}} \quad (3.65)$$

$$\alpha_{r4,o}\{\phi, \beta\} = \frac{e^2 \sin(\theta - \phi) \cos(\theta - \phi)}{2\sqrt{R^2 - e^2 \sin^2(\theta - \phi)}} - \frac{e \sin(\theta - \phi)}{2} \quad (3.66)$$

$$\alpha_{r5,o}\{\phi, \beta\} = \frac{\omega_s\{0\}}{2e} + \frac{\omega\{0\} \sin(\theta - \phi)}{2\sqrt{R^2 - e^2 \sin^2(\theta - \phi)}} \quad (3.67)$$

$$\alpha_{r1,v}\{\phi, \beta\} = \frac{l_v}{2} - \frac{2R^2 + e^2 R^2 (3 \cos(2[\theta - \phi - \alpha_i]) - 1)}{2(R^2 - e^2 \sin^2(\theta - \phi - \alpha_i))^{3/2}} \quad (3.68)$$

$$\alpha_{r2,v}\{\phi, \beta\} = b_{r,v1} + b_{r,v2} + b_{r,v3} + b_{r,v4} \quad (3.69)$$

$$b_{r,v1}\{\phi, \beta\} = \frac{e^2 \chi\{1\} + \omega\{1\}(l^2 - lL \cos(\beta))}{e^3} \quad (3.70)$$

$$b_{r,v2}\{\phi, \beta\} = \frac{lL[\sin(\beta) \sin(\beta + \theta - \phi - \alpha_i) - 2 \cos(\beta + 2[\theta - \phi - \alpha_i])]}{\sqrt{R^2 - e^2 \sin^2(\theta - \phi - \alpha_i)}} \quad (3.71)$$

$$b_{r,v3}\{\phi, \beta\} = \frac{\omega_2\{1\}(l^2 - lL \cos(\beta) + e^2)}{e^2 \sqrt{R^2 - e^2 \sin^2(\theta - \phi - \alpha_i)}} \quad (3.72)$$

$$b_{r,v4}\{\phi, \beta\} = -\frac{[\omega\{1\}]^2 \sin^2(\theta - \phi - \alpha_i)}{(R^2 - e^2 \sin^2(\theta - \phi - \alpha_i))^{3/2}} \quad (3.73)$$

$$\alpha_{r3,v}\{\phi, \beta\} = \frac{\omega_2\{1\} + L^2 - lL \cos(\beta)}{\sqrt{R^2 - e^2 \sin^2(\theta - \phi - \alpha_i)}} \quad (3.74)$$

$$\alpha_{r4,v}\{\phi, \beta\} = \frac{e^2 \sin(\theta - \phi - \alpha_i) \cos(\theta - \phi - \alpha_i)}{\sqrt{R^2 - e^2 \sin^2(\theta - \phi - \alpha_i)}} - e \sin(\theta - \phi - \alpha_i) \quad (3.75)$$

$$\alpha_{r5,v}\{\phi, \beta\} = \frac{\omega_s\{1\}}{e} + \frac{\omega\{1\} \sin(\theta - \phi - \alpha_i)}{\sqrt{R^2 - e^2 \sin^2(\theta - \phi - \alpha_i)}} \quad (3.76)$$

These expressions contain two additional term groupings, ω_2 and χ , similar to ω and ω_s which are defined by Equations (3.39) and (3.40) and are given by Equations (3.77) and (3.78).

$$\omega_2\{\kappa\} = lL \cos(\beta + 2[\theta - \phi - \kappa\alpha_i]) - (l^2 - e^2) \cos(2[\theta - \phi - \kappa\alpha_i]) \quad (3.77)$$

$$\chi\{\kappa\} = 2lL \sin(\beta) \sin(\theta - \phi - \kappa\alpha_i) - (l^2 - e^2) \cos(\theta - \phi - \kappa\alpha_i) \quad (3.78)$$

As previously mentioned, the moment generated by these accelerations, as calculated by Equations (3.57) and (3.58), is found by taking the cross product of the vector $\overrightarrow{\gamma_{1P}}$ with an endpoint P on the inner surface of the stator along the unit vector describing the direction of acceleration. The direction of acceleration for the oil within a DC is assumed to be identical to the unit vector associated with $\overrightarrow{\gamma_{3P}}$ while the direction for the vane acceleration is assumed to be identical to the unit vector associated with $\lambda_i\{1\}$. Knowing these directions, the cross product operation can be performed and the results can be tabulated in a manner similar the lookup tables discussed previously. These cross product operations result in Equations (3.79) and (3.80).

$$\Gamma_o\{\phi, \beta\} = \frac{L[e \cos(\theta - \phi) + \sqrt{R^2 - e^2 \sin^2(\theta - \phi)}] \sin(\beta + \phi) - lL \sin(\beta)}{R} \quad (3.79)$$

$$\Gamma_v\{\phi, \beta\} = l \sin(\phi + \alpha_i) \quad (3.80)$$

With the accelerations given by Equations (3.57) and (3.58) and the cross products given by Equations (3.79) and (3.80), the net inertial load imposed on the stator by the vanes and the oil within the DC can be expressed as M_{vo} using Equation (3.81).

$$M_{vo}\{\phi, \beta\} = \sum_{i=1}^7 (\rho_{mix} V_{DCi} a_{r,o} \Gamma_o + m_v a_{r,v} \Gamma_v) \quad (3.81)$$

Solving Equation (3.81) in simulation is done similarly to Equation (3.54) where the cross product terms, DC Volumes, and acceleration equation coefficients are all pre-calculated and stored in 2D lookup tables to then be used with the current values of the time derivatives of both ϕ (given as inputs) and β (calculated with the stator equation of motion). Combining the resulting M_{vo} and the M_{DC} calculated with Equation (3.54) results in the total moment exerted by the rotating group on the stator, neglecting friction, that must be overcome by the control chamber pressure moment and is written simply as M_1 using Equation (3.82).

$$M_1\{\phi, \beta\} = M_{DC} + M_{vo} \quad (3.82)$$

The model described in this chapter can be used, considering the fluid properties of automatic transmission fluid at 70°C, to compare M_{vo} and M_{DC} at several operating conditions to reveal the significance of the inertial loads with respect to the pressure loads for this case study design at a maximum eccentricity position. At low pressures and low speeds, the mean value of M_{vo} is approximately 1.5% of the mean value of M_{DC} with a ratio of the peak-to-peak values at about 2%. At low pressures and high speeds, however, the mean value of M_{vo} increases to roughly 37.5% of the mean value of M_{DC} with a peak-to-peak value ratio of less than 1%. For a more extreme case of both high pressures and maximum pump speed, the ratio of M_{vo} to M_{DC} is just over 9% with a peak-to-peak ratio again less than 1%. Referring back to the typical duty cycle depicted in Figure 5, the ratio of M_{vo} to M_{DC} varies between about 2% and almost 5% with peak-to-peak ratios around 1%.

While the inertial loads captured by M_{vo} are not dominant, they are significant at higher speeds and lower pressures and non-negligible in general. Their significance is also dependent on the pump displacement level. For the low pressure and high speed scenario at a 50% displacement, the ratio of M_{vo} to M_{DC} actually increases to about 81% while the peak-to-peak ratio remains close to 1%. At a 20% displacement, however, the ratio of M_{vo} to M_{DC} for the low pressure at high speed scenario drops to nearly 19% with a peak-to-peak ratio of about 1.6%.

The main reason for this dependence on the displacement level arises from the fact that the mean M_{DC} acts to decrease β at full displacement but changes signs such that the mean M_{DC} acts to increase β as the displacement reduces. Meanwhile, the mean M_{vo} always acts to decrease β regardless of the displacement. Thus, depending on the operating pressure and speed, there will be an eccentricity where the pressure and inertial loads balance and the net internal forces from the rotating group goes to zero. The nature of these loads will be explored more in detail in both Chapter 6 and Chapter 9.

3.11 Summary

In summary, Chapter 3 as a whole describes a semi-empirical and physics based pump model designed to calculate the following quantities as continuous variables.

- Instantaneous displacement chamber pressures, p_{DCi}
- Instantaneous displacement chamber flowrates, Q_{rHPi} and Q_{rLPi}
- Internal moments imposed by the rotating group on the pivoting stator, M_1
- Effective pump outlet flow and pressure, Q_A and p_A
- Effective pump load torque, M_p

Each of these variables considers realistic physical properties of the working fluid (a mixture of oil and entrained air), realistic geometries, and time-varying stator eccentricities that will be calculated in the module described by Chapter 6. On the other hand, both the leakages across the lubricating interfaces of the rotating group and any friction (viscous or not) at these interfaces are neglected in the calculation of these variables.

Of the variables on this list, M_1 , Q_A and p_A are the most important quantities to describe in order to both quantify and qualify the behavior of a pressure compensated pump from the perspective of the rotating group. M_1 is critical as the primary moment, in addition to the bias spring moment in Chapter 6, that must be overcome to change β for a given operating condition. The pressure p_A is critical as it is the process variable in a pressure compensated system and will match the set point only when the flow demand of the connected load is satisfied by Q_A .

Using the complex model derived in this chapter, these critical parameters can be simulated with a sufficient level of detail to be useful later in both exploring the effects of and determining the origin of parametric sensitivities, resonant behavior, and system instabilities.

V5 in Figure 20 and represents the servovalve used to generate the load conditions on the pump in combination with the filter F2, return line flowmeter, and the heat exchanger. Another critical component of the test rig, not depicted in Figure 20, is the data acquisition (DAQ) and control system, which will be discussed in Section 4.6.

4.1 Modified Case Study Pump

The case study pump installed on the custom test rig was modified in three ways. For each modification, care was taken to modify the stock pump components in ways that would minimize the effect of the modifications on the pump performance. The remainder of the test rig was designed around this modified unit to preserve its natural environment as much as possible.

4.1.1 Top Case Modifications

As mentioned in Section 2.1.2, the geometry and size of the case study pump presents various challenges preventing a direct and continuous measurement of the DC pressures over a complete revolution of the shaft. In order to capture the DC pressures, four dynamic pressure transducers were installed in the top case of the pump as in Figure 21 (see Drawing 1 in APPENDIX B for more details) and additional transducers were installed at the inlet and outlet of the pump. The DC pressure profile was then extracted from these six pressure signals using a novel “baton-passing” post-processing algorithm that will be presented in Chapter 5.

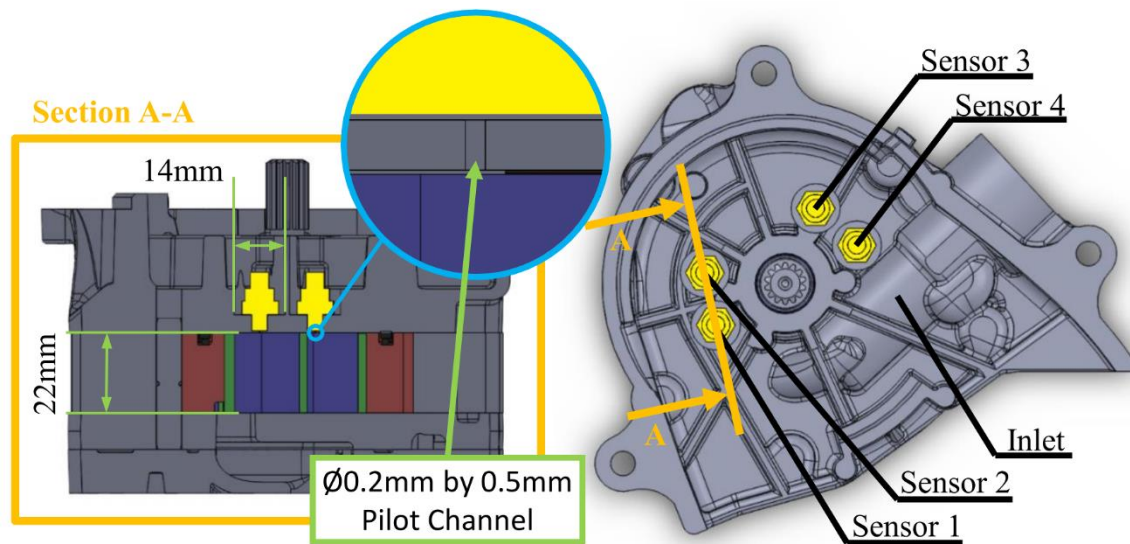


Figure 21: DC pressure transducer locations and orientation relative to other pump components as shown by the 3D CAD model.

As Figure 21 illustrates, the DC pressure transducers were installed in the top case of the pump “above” the DC volumes. These transducers communicate with the DC volumes through small pilot holes similar to the geometry shown in Figure 7 and analyzed in [33] [34]. The location of these pilot holes, depicted as yellow dots in Figure 22, allow them to be in contact with the DC volumes regardless of the stator eccentricity. They are circumferentially spaced so that DC 2, the smallest chamber, spans the gap between Sensor 1 and Sensor 2 near ODC and between Sensor 3 and Sensor 4 near IDC. These pilot holes are also located so that at least one sensor is in direct contact with the DC volume whenever that chamber is in transition from one port to the other so that the principal gradients in the pressure profile are directly measured.

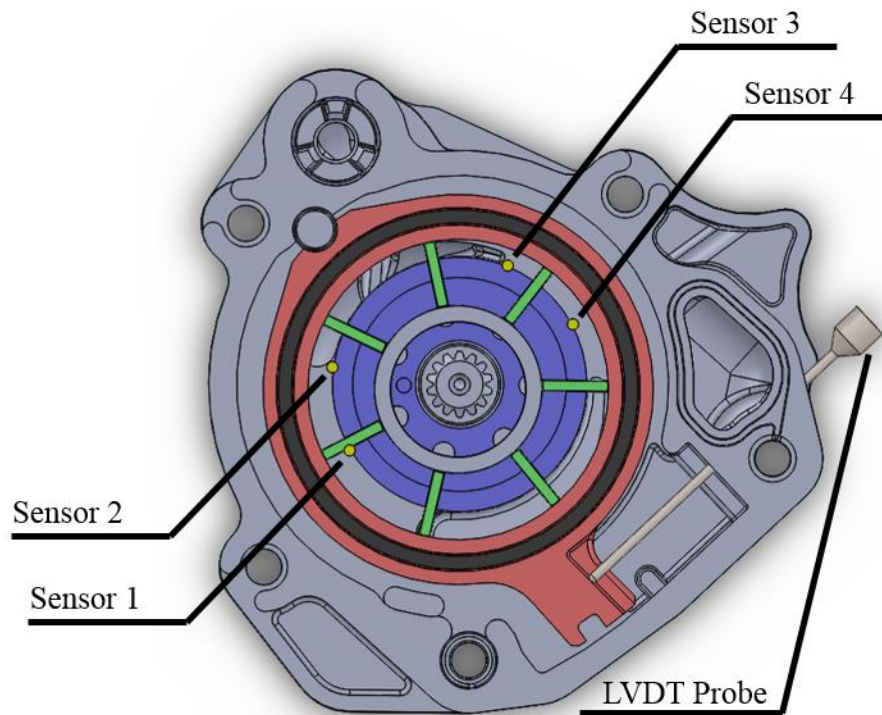


Figure 22: 3D CAD image showing location of the DC pressure transducer pilot holes relative to the rotor and stator bodies.

Figure 23 further illustrates this principle by presenting the target viewing windows, or angular regions where each sensor’s pilot hole is in contact with the DC volume. The detail view included in Figure 23 shows that the location of Sensor 2 allows for several degrees of overlap with Sensor 1 even for the smallest DC while still remaining in contact with the chamber until the pressure in the chamber converges to the delivery, or HP, port pressure. In a similar fashion,

Sensor 1 first enters into contact with the DC before the chamber has fully left the suction, or LP, port as evidenced by the small cyan region from about 350° to 360° in Figure 23. Sensor 3 and Sensor 4 are, however, somewhat sub-optimally located to completely bridge the gap on the IDC side due to the physical constraint of not interfering with the inlet geometry as can be seen in Figure 21. Nevertheless, Sensor 4 remains in contact with the DC volume until the pressure has nearly converged to the LP port pressure.

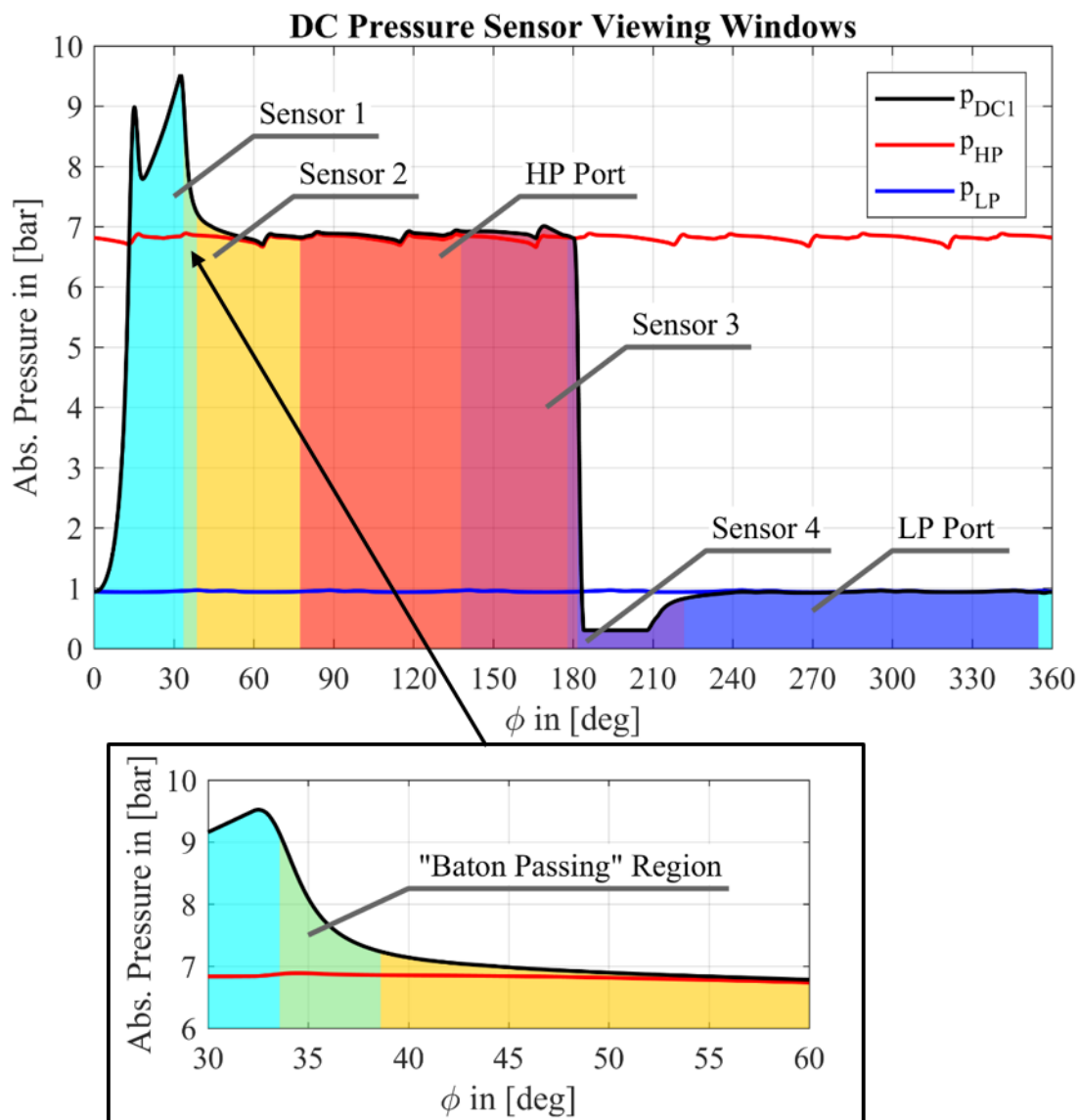


Figure 23: Target viewing windows for the six pressure transducers installed in the case study pump to measure the DC pressure profile.

Each of the four DC sensors and the HP port sensor were fast piezo-resistive, sealed-gauge pressure transducers from the Kulite XTL-123C-190 model line. In order to achieve a high

enough resolution of the profile, these sensors, along with a trigger pulse signal occurring once per revolution in the rotary encoder installed on the electric motor, were sampled at a 20kHz rate. (A Keller Valueline piezo-resistive pressure transducer sampled at 200Hz was used at the pump inlet to capture the mean value of the suction port pressure.) This, in addition to the fact that the rotary encoder is of quadrature type with a resolution of 1024 pulses per revolution, allows for precise and repeatable measurements of the DC pressure profile.

4.1.2 Pump Wall Modification

In addition to illustrating the locations of the DC pressure sensor pilot holes, Figure 22 also shows the orientation of a custom LVDT probe with respect to the pump. This location and orientation of the LVDT probe allow for the highest sensitivity measurement possible with the case study pump. This leads to better quality measurements with a higher accuracy that are critical in the validation of the pump model for two reasons. Simulated results generated at the same eccentricity level as the pump during operation on the test rig can be compared to the measured data for a fairer comparison and ultimately a better correlation. These measurements can also be used to validate the stator dynamics model that will be presented in Chapter 6.

As Figure 22 illustrates, the probe enters the pump through a hole drilled into the pump wall between the suction port geometry and a bolt hole (see Drawing 2 in APPENDIX B). The probe extends along the centerline of the bias spring (suppressed in Figure 22 for clarity) to make contact with the stator on the spring landing. In this way, the LVDT measures the linear motion of the stator along the centerline of the spring and a simple geometric relationship, Equation (4.1), can be used to convert the linear position x_s back to an angular eccentricity.

$$\beta = \tan^{-1} \left(\frac{a_L - (X_L - x_s)}{b_L} \right) - \delta_L \quad (4.1)$$

Figure 24 shows the definitions of the geometric parameters used in Equation (4.1). As Figure 24 indicates, b_L represents the distance from the pivot to the LVDT centerline and a_L represents the distance along the LVDT centerline from the 0° eccentricity reference line to the contact point on the stator when the stator is at a maximum eccentricity. Similarly, X_L represents the measured extension of the LVDT when the stator is at maximum eccentricity while δ_L is the angular offset between the plane connecting the pivot and stator centerlines and the plane connecting the pivot centerline and the LVDT probe contact point.

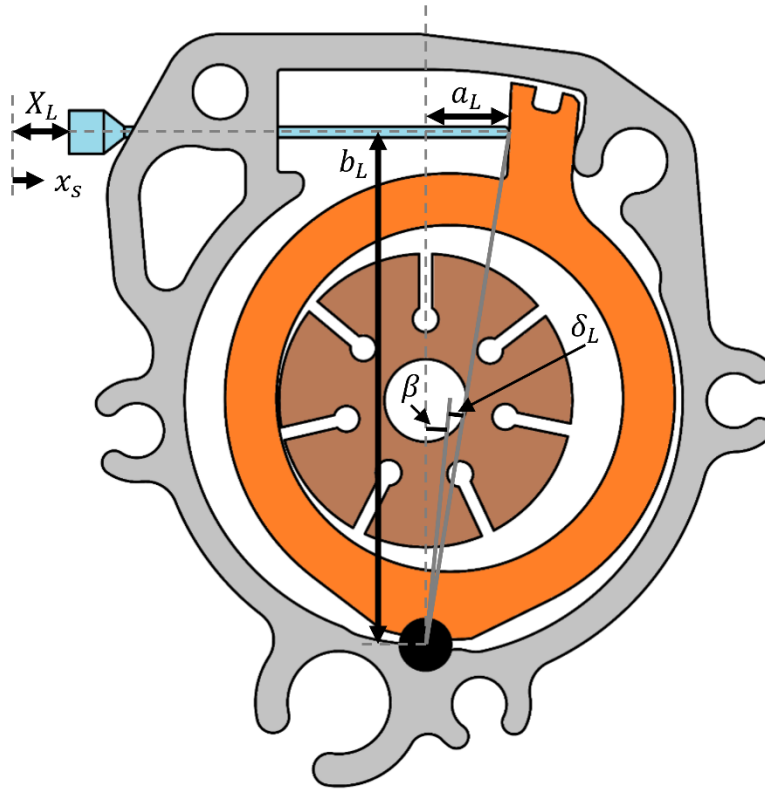


Figure 24: Parameter definitions used in converting the linear displacement of the stator measured by the LVDT to angular displacement in terms of β .

The LVDT used in this case is manufactured by RDP Electrosense, has a measurement range of 10mm, and is spring loaded. For this application, however, the LVDT spring was insufficient to maintain contact between the probe and the stator, so an additional spring was installed to assist it and ensure a higher degree of accuracy in the measurements. This additional return spring is visible in the detail view of Figure 25 and acts between a washer that interfaces with the probe tip to create a land and part of the body of the LVDT.

This design allows the 10mm range of motion for the LVDT to occur outside of the pump near its mounting location in an inlet adapter block. In order to meet these requirements and to prevent any buckling or deterioration, the custom probe tip was 3D printed in stainless steel according to Drawing 5 in APPENDIX B and then polished to reduce friction.

To correctly orient the LVDT and secure it in place, the inlet adapter block was designed and manufactured according to Drawing 8 in APPENDIX B to both house the LVDT and relocate and reorient the pickup filter F1 (see Figure 4 and Circuit 1). Relocation and reorientation of F1 was necessary to prevent interference with both the LVDT and other test rig

features such as the pump mounting flange discussed in Section 4.2. The inlet adapter block also provides instrumentation ports to measure both the temperature and pressure of the working fluid at the pump inlet. Because one of the primary purposes of this block is the correct orientation of the LVDT, it is mounted directly to the pump casing with a custom bracket detailed by Drawing 9 in APPENDIX B. Figure 25 shows the complete subassembly of this block, the modified case study pump, and inlet instrumentation.

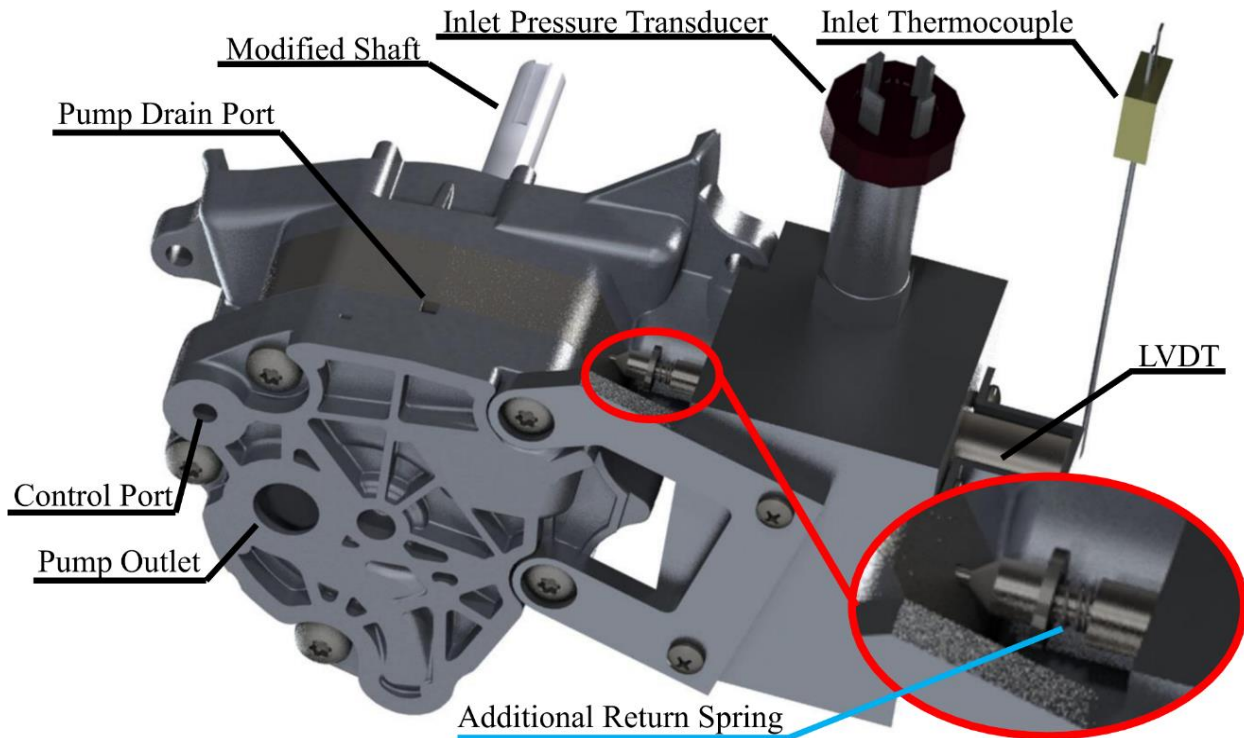


Figure 25: 3D CAD rendering of the modified pump assembly complete with the inlet adapter block, LVDT, and pump inlet instrumentation.

4.1.3 Pump Shaft Extension

In order to drive the pump with an available electric motor, the pump shaft was modified according to the engineering drawings (Drawing 6 and Drawing 7) in APPENDIX B and can be seen in Figure 25. As the pump is typically submerged in oil, this modification extended the pump shaft a sufficient distance to allow for a shaft seal assembly to be included on the pump mounting flange, which forms one wall of the reservoir enclosing the pump, and still have room to align and couple the shaft to an electric motor shaft using a Lovejoy L110 jaw-type coupling.

4.2 Pump Mounting Flange

A custom mounting flange was designed and manufactured according to the drawings (Drawing 10 to Drawing 15) included in APPENDIX B. This custom flange, depicted in Figure 26, has several key features. First, a bolt pattern designed to work with existing mounting rails on the steel structure supporting the electric motor. The pump centerline's location above the surface of this steel structure and between the two mounting rails aligns the pump and electric motor shaft centerlines such that fine tuning with shims was possible.

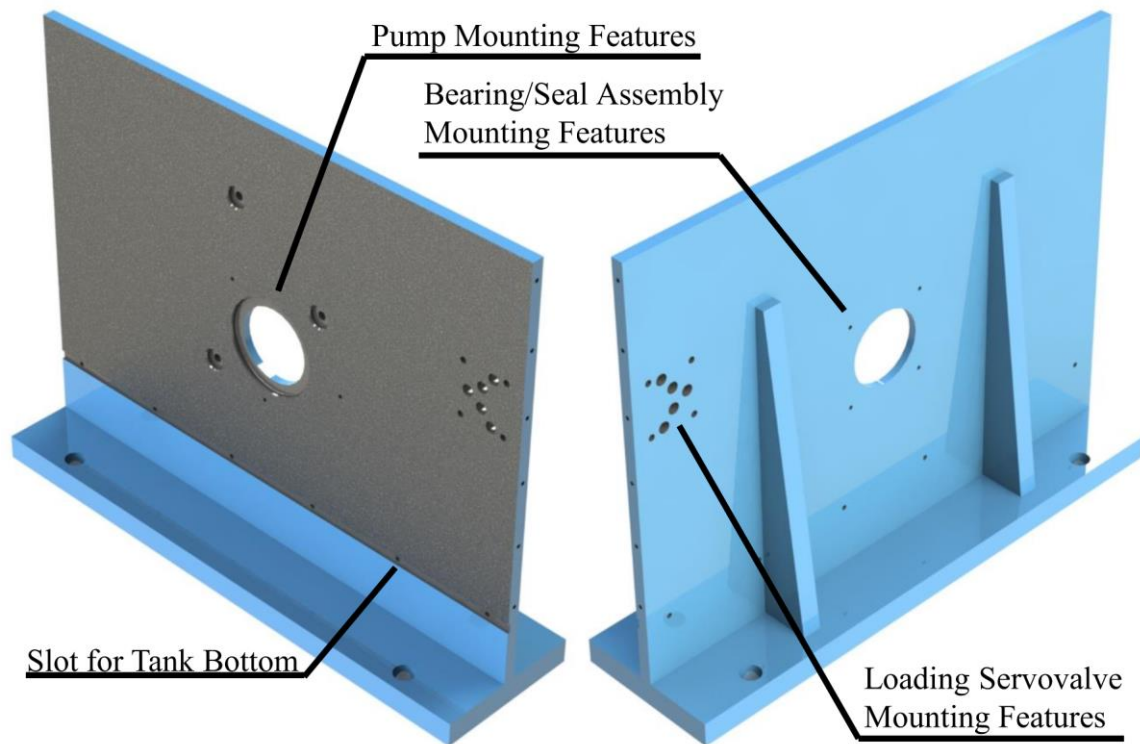


Figure 26: 3D CAD rendering of the custom pump mounting flange.

The pump is located and oriented with a centering ring feature and three mounting screw holes, which can be seen in the view on the left-hand side of Figure 26. The orientation of the pump by these features ensures a proper mating with a pump adapter block that accompanied the custom valve block. This adapter block mounts to the flange via three bolts with spacers that ensure appropriate compression of seals surrounding the pump outlet and control port features visible in Figure 25. The block also provides a usable port geometry for the Line A connection to the loading servovalve in Figure 20 as well as the interface required by the valve block.

As previously mentioned, this mounting flange serves as one wall of a tank to preserve the submerged environment of the pump. The flange therefore includes a slot for installing the

tank bottom and screw holes along the sides for attaching the tank walls. Both of these features are also visible in the left-hand side view of Figure 26. Meanwhile, the mounting bolt pattern for the roller bearing and shaft seal assembly for both supporting the extended shaft and sealing the tank wall around it can also be seen surrounding the centering ring hole on the right-hand side view in Figure 26. Details regarding this assembly and the custom aluminum block housing the bearing and seal are included in APPENDIX B with Drawing 20 through Drawing 22.

The final important feature of the mounting flange that is visible in Figure 26 is the mounting pattern for the loading servovalve. More details on how the servovalve is mounted to the flange will be provided in Section 4.4.

4.3 Reservoir Design

To complete the tank, an aluminum plate formed the bottom of the tank and a sheet of transparent polycarbonate bent into shape formed the walls. A silicone-based epoxy sealant was applied along the edges of the mounting flange and bottom plate before the polycarbonate wall was bolted on. A ruler was attached to the wall to provide a rough measurement of the oil level within the tank which was designed to contain approximately 30L of oil for an oil level of 18cm. This oil level results in a typical inlet pressure for comparable conditions to those found in an automatic transmission.

Another feature of the tank is a polycarbonate dividing wall that separates the return flow from the inlet to the pump's pickup filter, essentially acting as a baffle. To prevent contamination of the oil within the tank and to contain oil sprays from the pump case drain, a polycarbonate lid was manufactured and installed to cover the test rig.

These components can be seen in the 3D CAD rendering in Figure 27. Additional details can be found in the engineering drawings for these components included in APPENDIX B.

4.4 Port Adapter Blocks

In addition to the pump and inlet adapter blocks, two other adapter blocks were designed and manufactured to complete the hydraulic circuit depicted in Figure 20. The first of these provides SAE port features inside and outside the tank to connect the pump outlet to the return line through the loading servovalve. This external connection is labeled "Line A Port" in Figure

27. Hydraulic lines connect this port to the “Tank Return” adapter block on the other side of the tank through a flowmeter and a heat exchanger. This “Tank Return” adapter block provides SAE port features on the outside of the tank and a simple hole inside the tank.

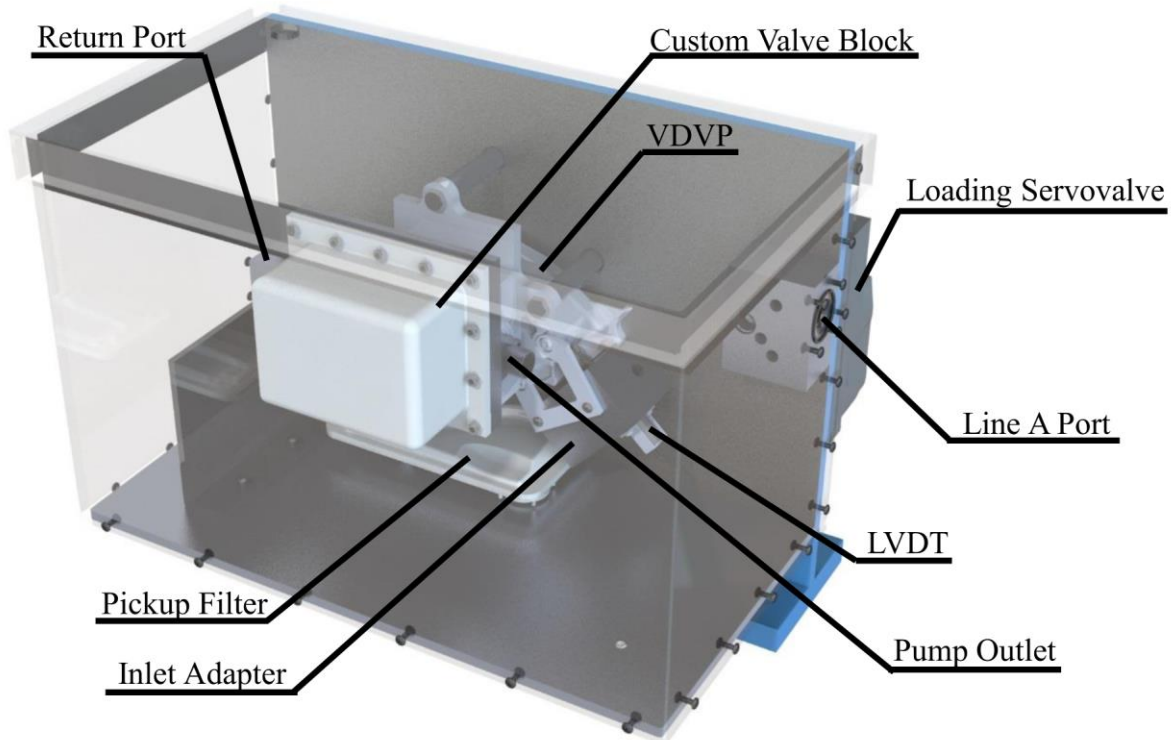


Figure 27: 3D CAD rendering of the test rig assembly to illustrate the general spatial orientation of the components relative to one another and their relative sizes.

4.5 Additional Test Rig Hardware

The completed test stand is shown in Figure 28 with the exception of the DAQ/Control system components which were installed in an adjacent room. Being the completed test rig assembly, Figure 28 also shows the filter F2, return line flowmeter, heat exchanger, and electric motor discussed in the introduction to this chapter and depicted schematically in Circuit 1 (Figure 20). The only component not shown is the polycarbonate cover discussed in Section 4.3.

In addition to the components discussed here, several other adapter blocks were designed and manufactured to conduct valve studies and in the course of characterizing the stator dynamics. These additional components will be discussed at later points. Drawings for all of the components designed and built for the test rig are included in APPENDIX B while details regarding the loading servovalve specifications are available in APPENDIX C.

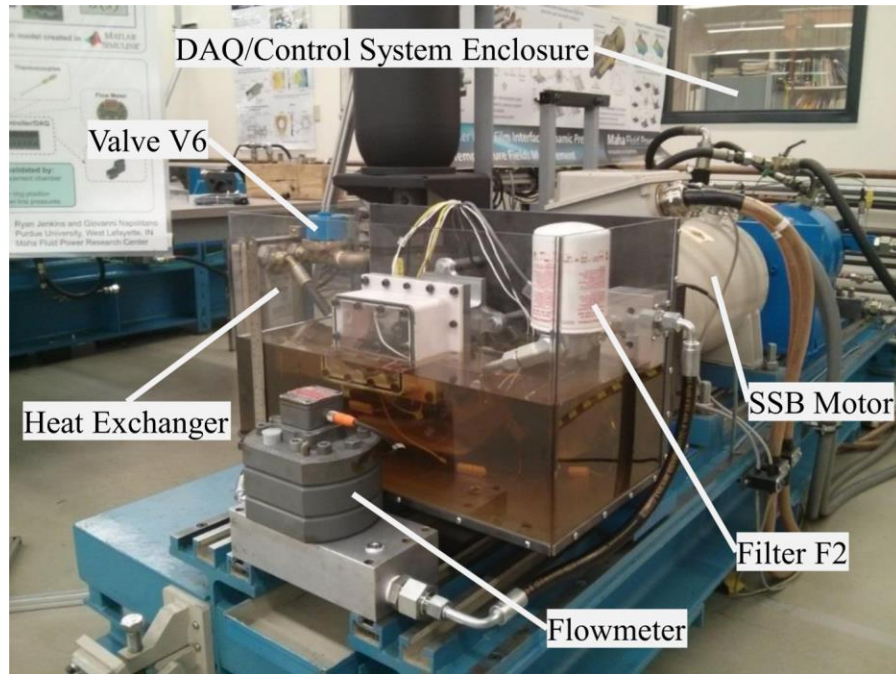


Figure 28: Picture taken of the completed experimental setup in April of 2016 with the polycarbonate cover removed.

4.6 Data Acquisition and Control System

Data acquisition and control of the test rig was handled with a National Instruments compact RIO (NI cRIO) setup running NI software products. The NI cRIO platform is highly modular and configurable, allowing multiple sampling rates and control loop rates within the same DAQ/Control program running on the controller CPU. Figure 29 lists these rates for each module as set for the DC pressure measurement study and provides an overview of this setup.

Another feature of this setup is afforded by the internal memory available to the controller coupled with the chassis' reconfigurable FPGA which allows for the creation of virtual sensors. An example of this is the virtual speed sensor that processes the quadrature pulse train signal coming from the electric motor's rotary encoder. This virtual sensor operates at a rate of 80MHz and outputs a trigger signal at 20kHz and the shaft speed in RPM at 200Hz.

The NI products referred to in Figure 29, along with other electrical components for providing power to both this system and the various sensors, were housed in a custom built DAQ/Control box. This enclosure also housed a proportional valve driver (Lynch LEPDX) for controlling the solenoid valve V3 included in the custom valve block and discussed in Section

1.3.2 along with Figure 4. Additional details for selected components may be found in APPENDIX C while a complete wiring diagram of the DAQ/Control system enclosure is available in APPENDIX D.

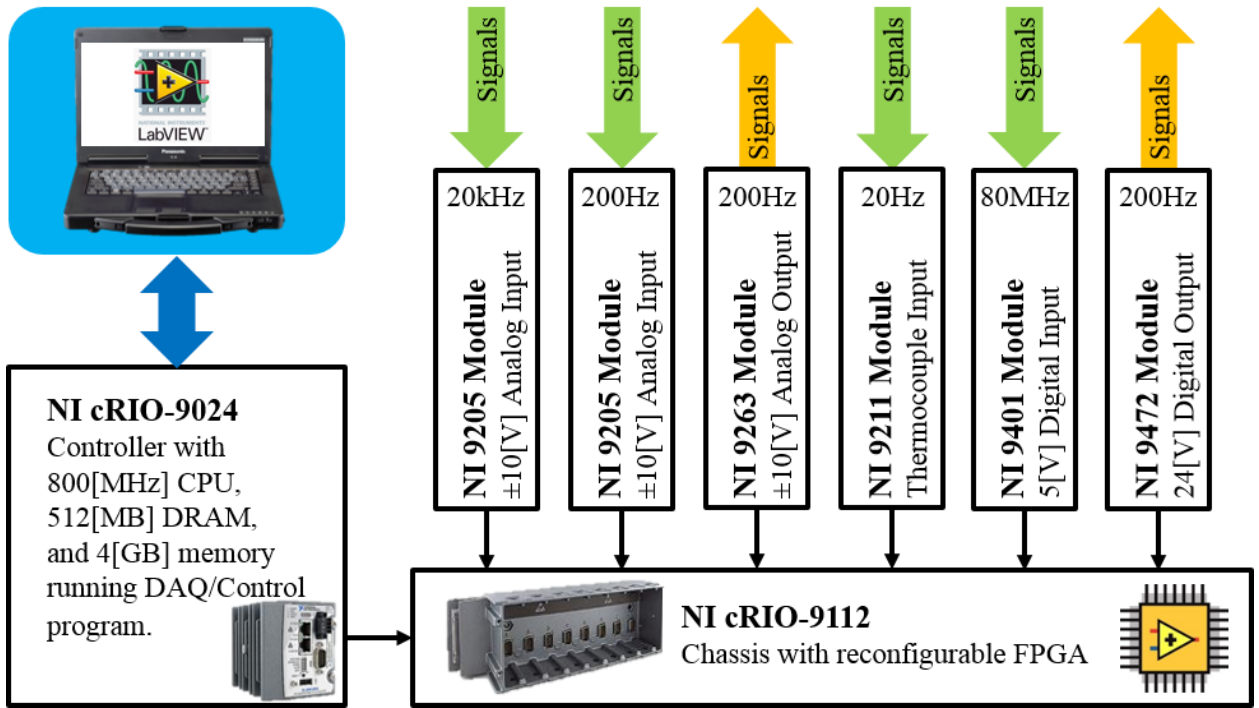


Figure 29: Overview of the DAQ/Control setup showing the NI cRIO products used and the sampling rates set for each of the modules for the DC pressure measurement study.

5. DC MODULE VALIDATION STUDY

As mentioned in Chapter 4, the four DC pressure transducers, Line A pressure transducer, and shaft trigger signal were all sampled at a rate of 20kHz for the DC Module validation measurement study. The remaining sensor signals, including the Line E and valve block pressure transducers (see Figure 20) and the shaft speed, were sampled at 200Hz. The DAQ/Control program for this measurement study was created in LabVIEW and measurements taken over 30s to 60s time intervals were saved simultaneously for both sampling rates, allowing the signals to be aligned properly in post processing. Measurements were conducted at several operating conditions as defined by the pump speed, displacement level, and outlet pressure following the procedure outlined below.

- Step 1. Start the DAQ/Control program on the cRIO, load the user interface on the connected laptop, and power on the sensors and other electronic components.
- Step 2. Command the loading servovalve to a fully open position.
- Step 3. Start the electric motor and set to the desired speed.
- Step 4. Use the solenoid valve V3 (see Figure 20) to set the Line A pressure command.
- Step 5. Check the stator displacement measurement. If the pump is at the desired displacement level, skip to Step 9. Otherwise, continue to Step 6.
- Step 6. Adjust the opening of the loading servovalve incrementally to change the flow demand seen by the pump.
- Step 7. Adjust the V3 command, if necessary, to refine the commanded Line A pressure.
- Step 8. Check the stator displacement measurement. If the pump is now operating at the desired conditions, continue to Step 9. Otherwise, return to Step 6.
- Step 9. Save data for a 30-60s measurement sample.
- Step 10. Return the loading servovalve to the fully open position and, if necessary, adjust pump speed to the desired speed for the next operating condition.
- Step 11. Repeat Step 4 through Step 9 for the next operating condition. If no more measurements are required, continue to Step 12.
- Step 12. Command the loading servovalve to a fully open position.
- Step 13. Command V3 to set the lowest Line A pressure setting.
- Step 14. Stop electric motor and turn off DAQ/Control electronics.

5.1 DC Pressure Profile Post-Processing Algorithm

Figure 30 presents example measurement data for the six pressure transducer signals required to recreate the DC pressure profile as part of the DC Module validation study. These signals represent just over one and half revolutions of the shaft as evidenced by the eleven discontinuities easily visible in the Sensor 4 trace. These discontinuities occur each time a vane passes below a sensor pilot hole and similar discontinuities are detectable in the signal traces for the other three DC pressure sensors.

Referring back to Figure 23 in Section 4.1.1 and observing the signals in Figure 30 around 40ms in the traces for Sensor 3 and Sensor 4, it can be seen that the pressures in these nearby sensors match for a brief period of time during the “baton passing” region where both sensors are in contact with the same DC volume. Observing the traces for Sensor 2, or alternatively Sensor 3, and the Line A pressure transducer (which was positioned very close to the pump outlet) also reveals clear periods of time when the pressures measured by these two sensors match very closely. This observation can also be made comparing the traces for Sensor 1, or Sensor 4, and the Line E pressure transducer.

These observations validate the design objectives behind the pump modifications described in Section 4.1.1 by subjectively showing that the “baton passing” regions exist in the measured signals. Therefore, it is possible to recreate a continuous pressure profile by stitching together data from contiguous sensors corresponding to a single chamber. To accomplish this, a custom MATLAB post-processing script was written that follows the algorithm outlined below.

- Step 1. Start with the index of the data point corresponding to the start of a new rotation of the shaft as indicated by a pulse in the trigger signal.
- Step 2. Search forward through the data for Sensor 1 (S1) to find the first discontinuity in the pressure signal after the index found in Step 1. This corresponds to the passing of a vane and the beginning of what will be temporarily called Chamber 1 (C1). Record the index at which this discontinuity occurs as the beginning of C1 in S1.
- Step 3. Continue forward through the data until the next discontinuity occurs. Record this index as the end of C1 in S1 and the beginning of C2 in S1.
- Step 4. Continue searching forward through the data for S1 in this manner to identify the beginnings and endings of the remaining chambers for this revolution. Note that the end of C7 in S1 will typically belong to the beginning of the next revolution.

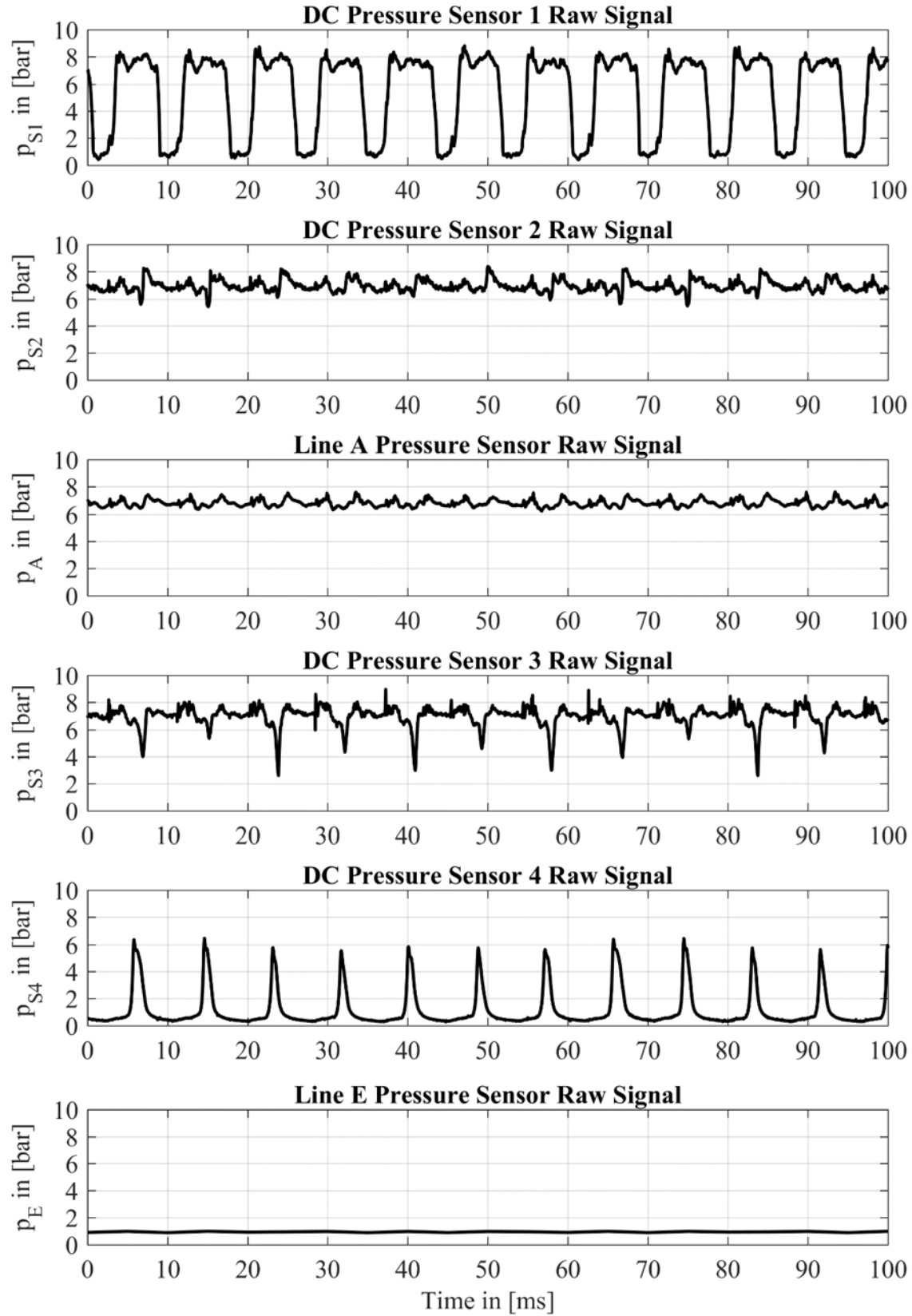


Figure 30: Raw DC pressure profile measurements from the DC Module validation study.

- Step 5. Repeat Steps 2 through 4 for five complete revolutions of the shaft.
- Step 6. Parse out of the raw S1 data the signal pertaining to C1 over the five revolutions using the indices recorded for the beginnings and endings of C1 in S1. Pad this new data vector with zeros wherever C1 is not connected to S1 so that this new vector is the same length as the raw S1 data vector for five shaft revolutions.
- Step 7. Repeat Step 6 for the remaining chambers.
- Step 8. Repeat Steps 2 through 7 for the Sensor 2 (S2) signal labeling C1 as the first complete chamber encountered after the index corresponding to the first beginning of C1 in S1.
- Step 9. Repeat Steps 2 through 7 for the signal from Sensor 3 (S3). To determine which chamber to label C1, use the measured speed and the angles depicted in Figure 30 to determine the approximate time offset between the beginning of C1 in S1 and the beginning of C1 in S3 as well as the approximate time offset between the beginning of C1 in S2 and the beginning of C1 in S3. The discontinuity in the S3 signal closest to both of these offset values will be the beginning of C1 in S3.

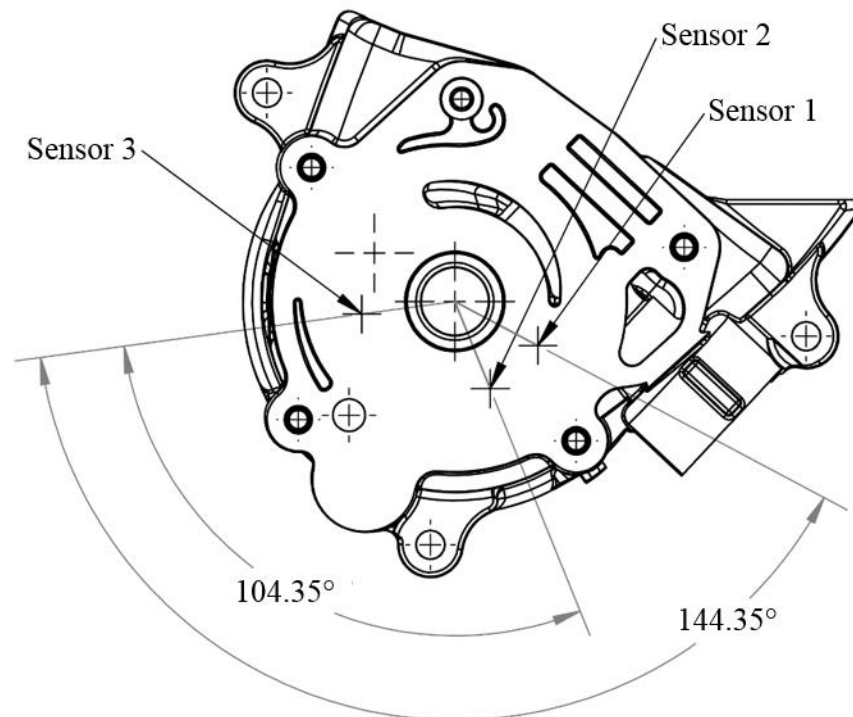


Figure 31: Angular distances between pilot hole locations for Sensor 3 and Sensors 1 and 2 for use in determining offsets.

- Step 10. Repeat Steps 2 through 7 for the signal from Sensor 4 (S4) labeling C1 as the first complete chamber encountered after the index corresponding to the beginning of C1 in S3 identified in Step 9.
- Step 11. Parse out of the raw Line A data vector the signal pertaining to C1 using the indices corresponding to the endings of C1 in S2 and the beginnings of C1 in S3. Pad this new vector with zeros similar to the other vectors.
- Step 12. Create a new vector of zeros the same length as the others and fill the indices between the endings of C1 in S4 and the beginnings of C1 in S1 with the mean value of the Line E pressure signal.
- Step 13. Repeat Steps 11 and 12 for the remaining chambers.
- Step 14. Add the new signal vectors corresponding to C1 from all six sensors together. Whenever two of these vectors are non-zero at the same index, use the average value for that index. The resulting composite vector will represent a continuous pressure profile measurement over five revolutions of the shaft.
- Step 15. Using the indices corresponding to each beginning of C1 in S1, separate the profiles from each of the five revolutions and align them with one another. Find the average profile over the five revolutions and the standard deviation of the profile between revolutions to fully characterize the pressure profile for C1.
- Step 16. Repeat Steps 14 and 15 for the remaining chambers.
- Step 17. Using the time values at the indices corresponding to the beginnings and endings of C1 in each of the four DC pressure sensors (S1, S2, S3, and S4), determine the mean and standard deviation of the time between vane events for C1. Convert this time to an angular span for C1 using the measured speed.
- Step 18. Repeat Step 17 for the remaining chambers.
- Step 19. Compare the measured angular spans of each chamber to identify the largest and smallest chambers, statistically. These two chambers should be sequential as indicated in Figure 11. Rename the composite pressure profiles for each chamber (C1 through C7) according to the naming convention established in Figure 11.
- Step 20. Store the resulting profiles in a secure location with a record of the operating conditions associated with the measurement set.

Figure 32 illustrates this algorithm for a single DC over a single shaft revolution.

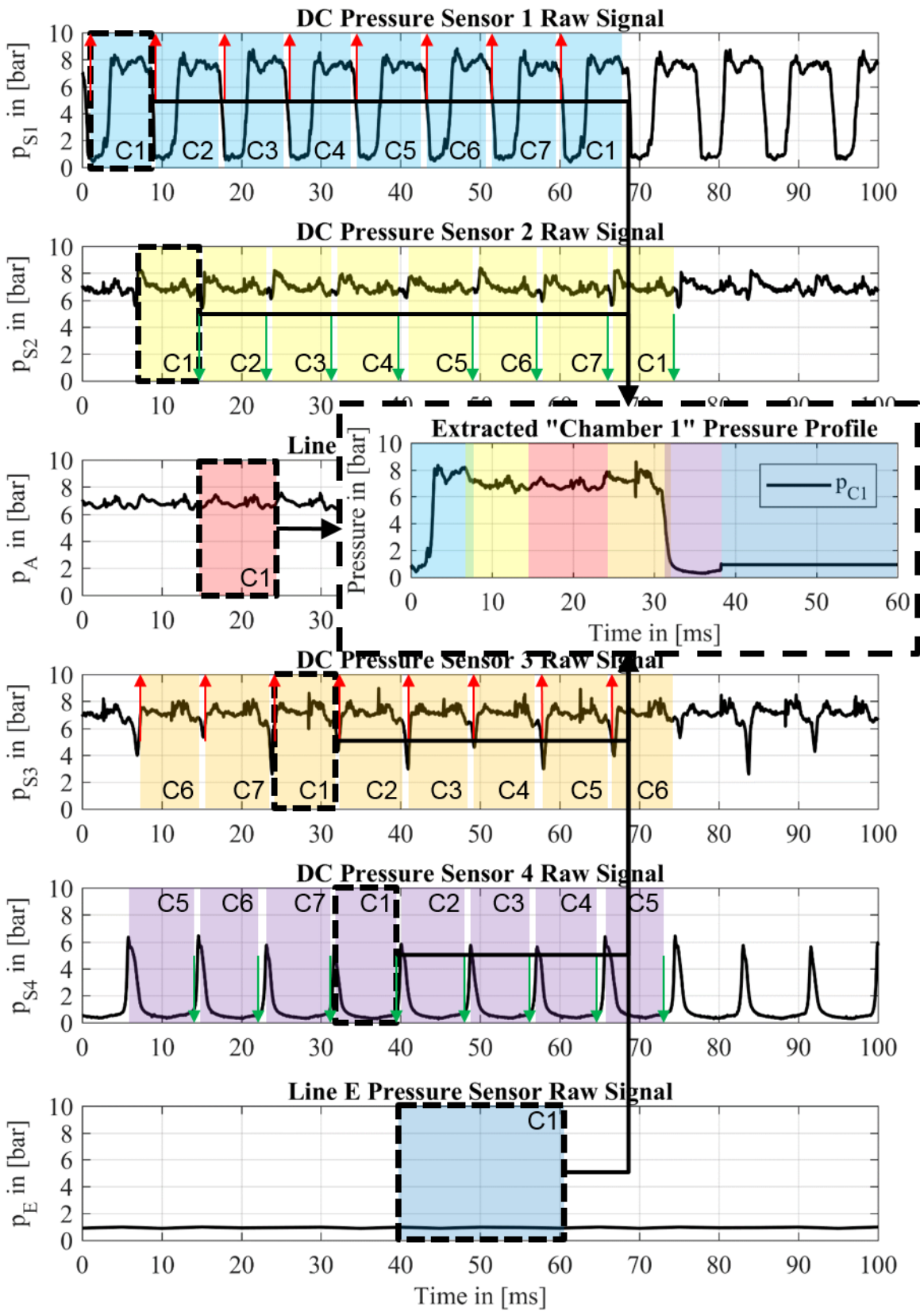


Figure 32: Illustration of the “baton passing” post-processing algorithm.

Table 1 provides a comparison of the mean angular span measured in this validation study as calculated by Step 19 for each DC with the nominal angular span for that DC. The nominal values were measured in the 3D CAD model and are the values assumed in the DC Module. Therefore, for higher accuracy and better validation plots, there should be a low percent difference %D between the measured and nominal spans as calculated by Equation (5.1).

As Table 1 indicates, the measured and nominal spans agree well and the average difference is less than half a percent (absolute).

$$\%D = 100 \frac{(2\alpha_i)_{measured} - (2\alpha_i)_{nominal}}{(2\alpha_i)_{nominal}} \quad (5.1)$$

Table 1: Comparison of the measured and nominal (from CAD and assumed in the DC Module) angular spans for each DC in the case study pump.

Chamber	Measured Span	Nominal Span	%D
1	53.3°	53.3°	0.00%
2	49.5°	49.3°	0.41%
3	52.4°	52.3°	0.19%
4	50.3°	50.1°	0.40%
5	52.5°	53.0°	-0.94%
6	50.2°	49.8°	0.80%
7	52.2°	52.2°	0.00%

5.2 Measured DC Pressure Profile

Figure 33 and Figure 35 give examples of the measured DC pressure profile extracted from the raw measured data using the algorithm established in Section 5.1. These measured profiles match well with published measurement profiles available in the literature [31] [32].

Furthermore, Figure 34 and Figure 36 help illustrate the accuracy of the experimental setup described in Chapter 4 in terms of capturing the DC pressures. These two figures represent the standard deviation between the profiles for five consecutive revolutions of the shaft using unfiltered pressure transducer data. Quantitatively, the standard deviation between the measured profiles from different revolutions is less than 0.1bar for over 90% of the time. This implies that the mean profiles depicted in Figure 33 and Figure 35 represent the true profiles, statistically speaking, to a high degree of confidence. This degree of measurement accuracy and repeatability was typical for other measurements taken during this experimental validation study.

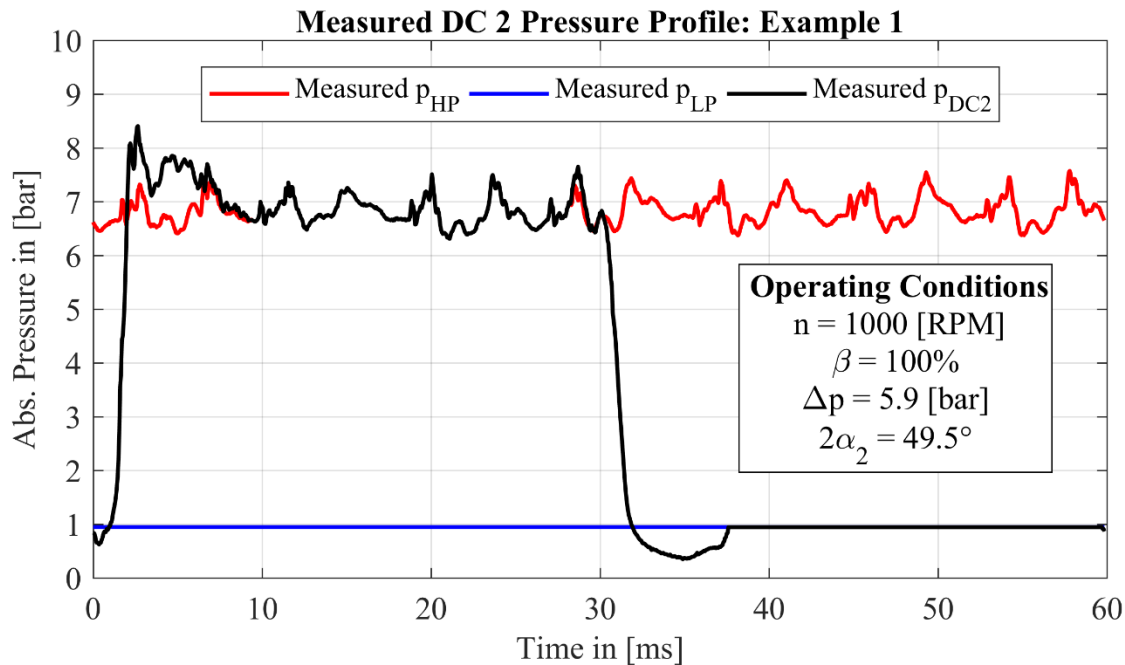


Figure 33: First example of a measured DC pressure profile.

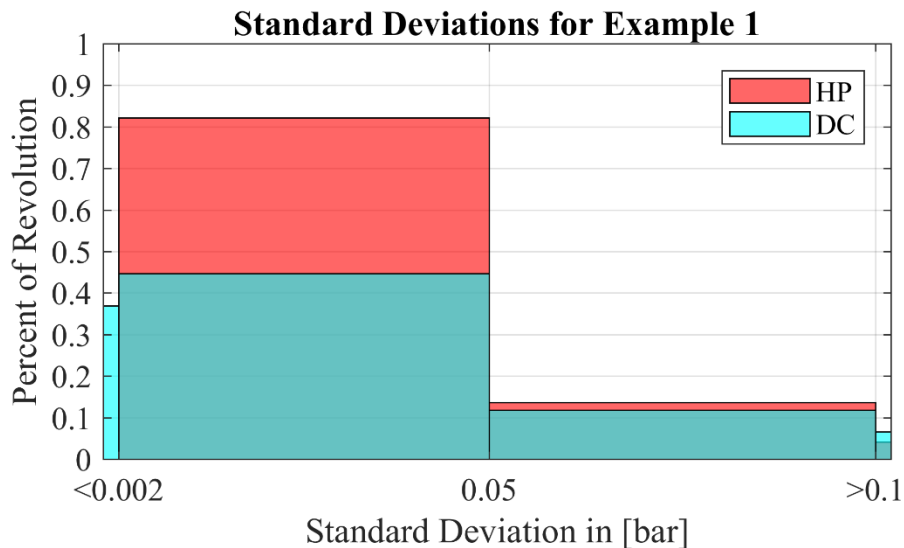


Figure 34: Histogram showing standard deviation between the measured DC pressure profiles over five revolutions for the first example.

As the notes in Figure 33 and Figure 35 indicate, the example measurements shown here represent DC 2 at different operating conditions. These two conditions were chosen to include in this dissertation to show the difference in the measured pressure profile at different pump displacements. These results are typical of measurements taken at other speeds and pressures.

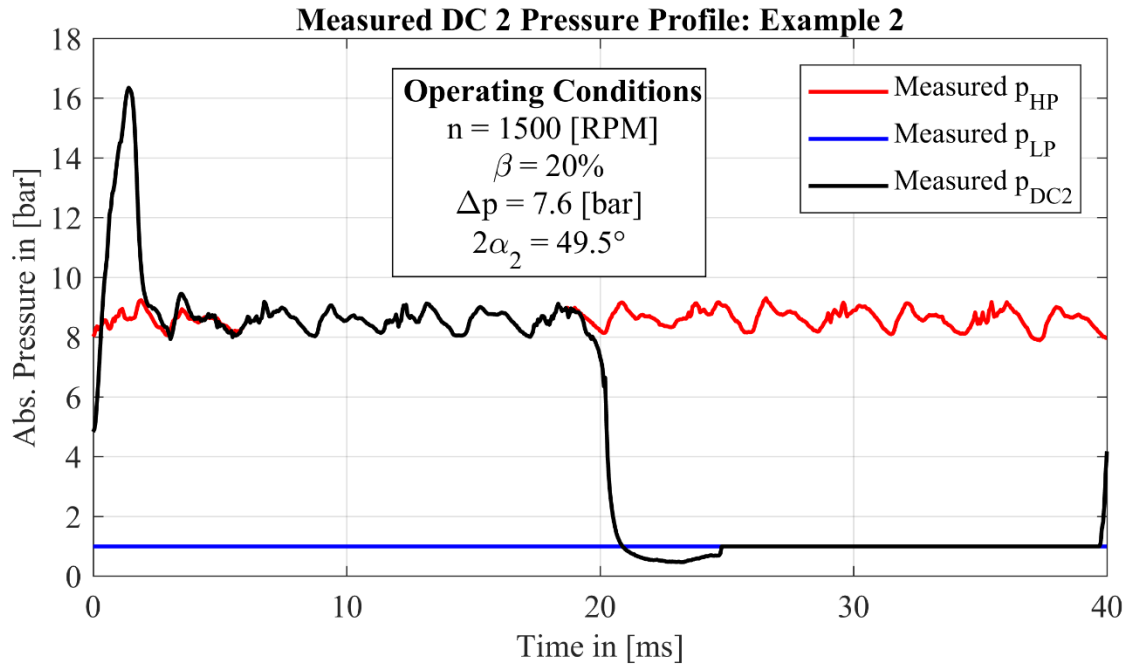


Figure 35: Second example of a measured DC pressure profile.

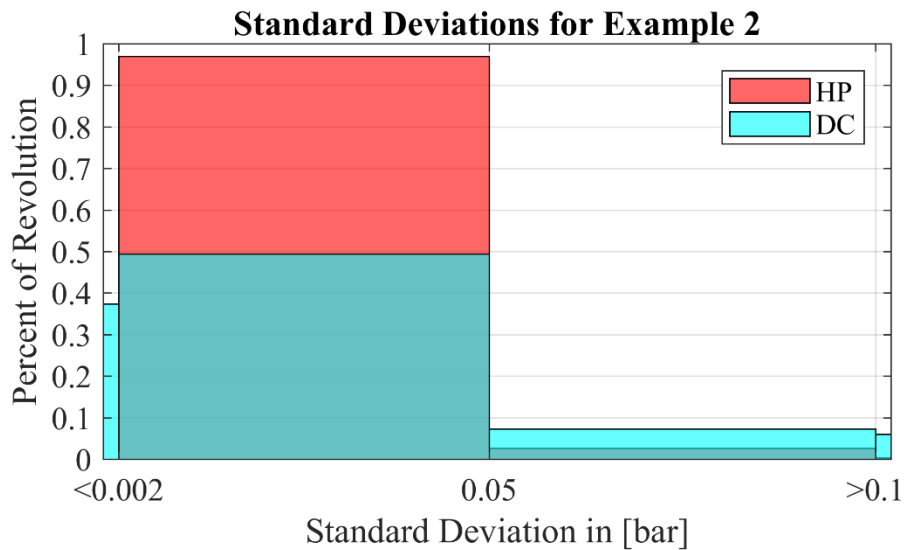


Figure 36: Histogram showing standard deviation between the measured DC pressure profiles over five revolutions for the second example.

5.3 Validation Comparison

Figure 37 and Figure 38 show comparisons between the simulated DC pressure profile using the lumped parameter model established in Chapter 3 and the two example measured

profiles given by Figure 33 and Figure 35. It should be noted here that the only operating condition not known for the measured data is the aeration level. Therefore, the aeration levels indicated in the notes on Figure 37 and Figure 38 represent the values (reported in percent by volume) that gave the best agreement between the simulated and measured profiles.

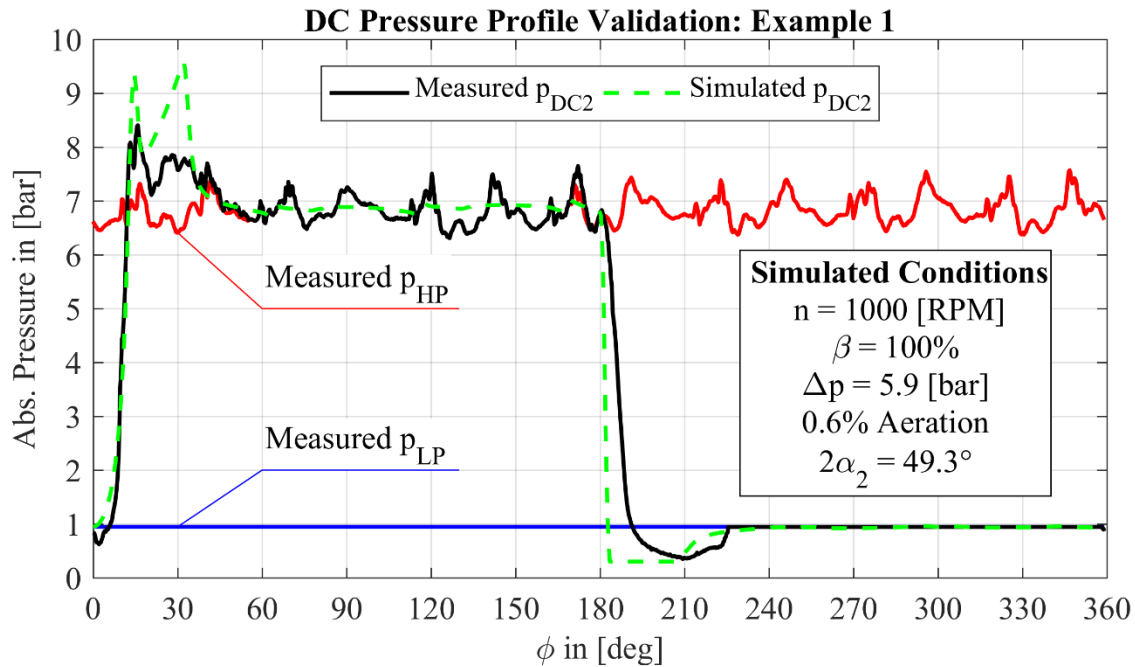


Figure 37: Comparison between the simulated DC pressure profile and the measured DC pressure profile for the first example's operating conditions.

As Figure 37 indicates, the agreement between the simulated and the measured profiles is good. Nevertheless, a few key discrepancies exist. First, the discrepancies between 0° and 30° in the figure depend on the entrained air content of the fluid and on the external leakages. Since the simulated profile here neglects external leakages, the second pressure peak is slightly more pronounced. Another source for the discrepancies in this section is numerical solver errors. These were reduced as much as possible by using a variable-step solver method designed for stiff systems of differential equations with a small maximum step length.

The discrepancies between 180° and 220° are similar to those between 0° and 30° . However, an additional source of error comes from the fact that the DC Module does not model cavitation effects or the solubility of the entrained air in the hydraulic oil. As cavitation and varying air content is most likely in this region, these effects are likely the prominent sources of error between the model and the real profile. Additionally, to avoid negative absolute pressure values (which have no physical meaning) the simulated DC pressures have a lower saturation

bound of 0.3bar. This is the reason for the discontinuity in the simulated profile in Figure 37 at 185° . Unfortunately, this saturation obscures the shape of the profile in this region.

The discrepancies between 60° and 180° in Figure 37 are attributed to the simplified port and line load models. The simulated Line A pressure does oscillate (i.e. there is a port pressure ripple simulated), but to a lesser extent than the measurements.

The agreement in this portion of the profile could be improved with additional tuning of parameters and development of the Port Modules or by the inclusion of the dynamics of the pressure transducer connection geometries as was done in [33] and [34]. Another effect that could be included, based on the physical design of the pump adapter block, deals with wave propagation and resonance arising from the non-uniform diameter of the Line A channels cut into the pump adapter block. Transmission line models such as the ones developed in [61] and [62] can be used to incorporate this type of line dynamics. Nevertheless, the profile as a whole is already quite representative.

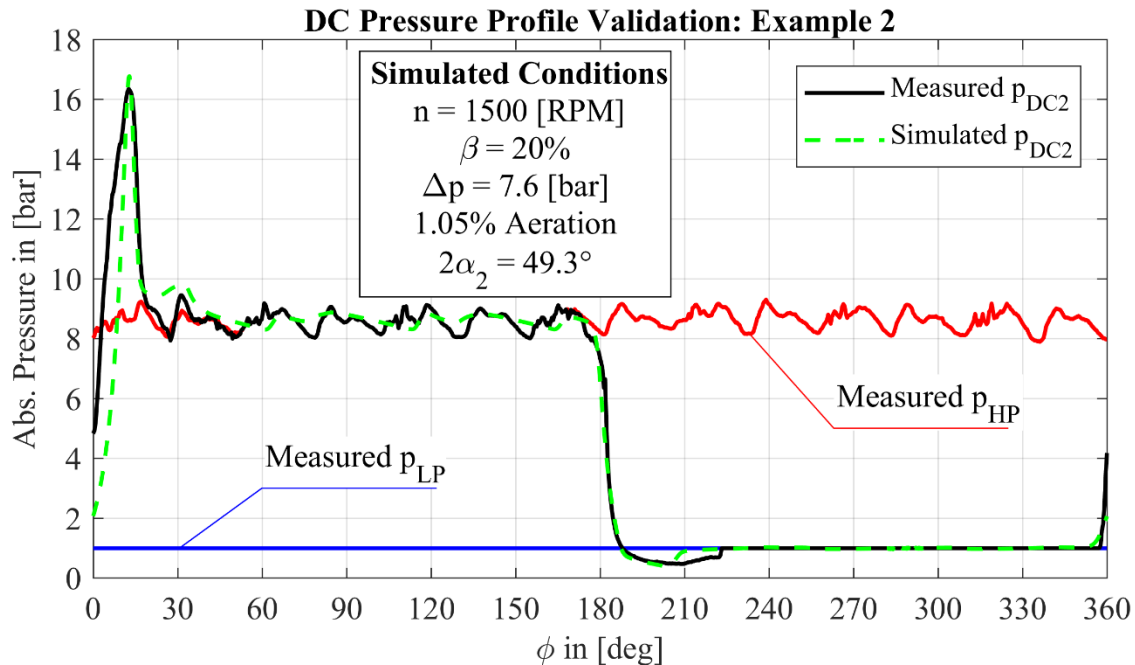


Figure 38: Comparison between the simulated DC pressure profile and the measured DC pressure profile for the second example's operating conditions.

Figure 38 also shows a good agreement between simulation and measurement. In both cases, Figure 37 and Figure 38, the simulated results are representative. These realistic pressure profiles come at a relatively low computational cost and are sufficiently validated to be used with confidence to generate the internal forces required for an analysis of the pump dynamics.

5.4 Additional Simulation Results and Comparisons

As an additional verification of the validity of the DC Module, Figure 39 provides a comparison of the simulated pump performance to a set of available steady-state measurements for the pump that were provided by the case study's sponsor. Figure 39 includes the kinematic flowrate $Q_{A,kin}$ which is the sum of the delivery stroke portions of Equation (3.10) for each DC and the theoretical flowrate $Q_{A,th}$ which is a product of the pump speed and displacement at 100% efficiency. Similarly, the theoretical torque $M_{P,th}$ is a product of the differential pressure and the pump displacement at 100% efficiency.

This illustrates that the model is producing reasonable, and expected, system level results. A fact which is best summarized numerically in Table 2 which uses the efficiency definitions given by Equations (5.2) through (5.4) where n is the pump speed and the pump size V_p is 25cc/rev. These definitions were also used for the measured data.

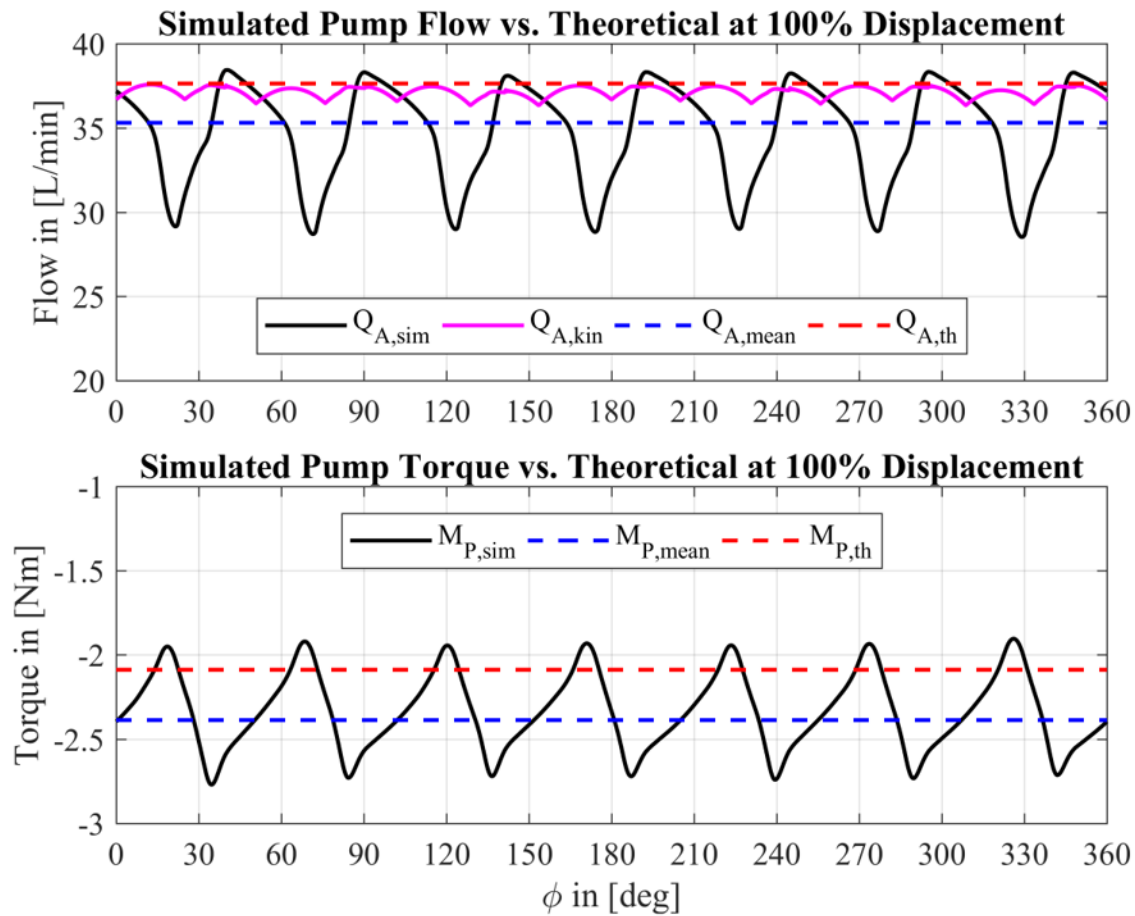


Figure 39: Comparison of the simulated pump outlet flow and pump torque to the theoretical performance of the pump at 100% displacement.

$$\eta_V = \frac{Q_A}{nV_P} \quad (5.2)$$

$$\eta_T = \frac{Q_A(p_{HP} - p_{LP})}{nM_P} \quad (5.3)$$

$$\eta_M = \frac{\eta_T}{\eta_V} \quad (5.4)$$

Table 2: Comparison of simulated and measured pump efficiencies.

Case	Flow [L/min]	Torque [Nm]	η_V	η_M	η_T
Measured	34.5	2.44	0.92	0.84	0.78
Simulated	35.3	2.42	0.94	0.85	0.80
Theoretical	37.5	2.06	N/A	N/A	N/A

Table 2 is very informative and indicates that the DC Module, which neglects external leakages and shaft friction, gives reasonable results that lie perfectly between the measured steady-state and theoretical pump performances. This means that the simulated volumetric efficiency η_V represents the maximum attainable “best case” efficiency as it is only a result of oil compressibility and pump design features. The total efficiency η_T and mechanical efficiency η_M are similar in nature and thus provide additional upper limits on the pump efficiency.

Figure 39 shows a high degree of flow non-uniformity (see [2] for a definition) in the simulated flow. This is largely due to the design of the pump as illustrated by Figure 40. These plots illustrate how the port geometry contained in the area file combines with the DC volume rate of change to result in a region near ϕ_{ODC} where the DC volume is unconnected to either port while in the delivery stroke and thus experiences pure compression. The DC pressure rises in this isolated region (“isolated” as in “not connected”), but not completely to the port pressure level. As the DC continues through the revolution and begins to make contact with the delivery port around 15° , a backflow from the delivery port into the DC is required to bring up the pressure around 20° . As the connection is still restricted and the DC volume rate of change is non-negligible (already roughly a third of its maximum absolute value) between about 20° and 35° , the pressure in the chamber spikes. This pressure spike results in a delivery flow spike around 40° . Both the backflow spike and the delivery flow spike contribute to the fluctuations and non-uniformity of the simulated pump flow in Figure 39. This is a typical behavior for VDVP [12].

Furthermore, these effects are exaggerated at lower eccentricities as ϕ_{ODC} moves into the suction port region. Close inspection of Figure 40 around 0° and 360° reveals that even for 100% displacement, or maximum eccentricity, there is a slight connection between the DC and the suction port when the DC begins its delivery stroke. At a 20% displacement, the DC spends approximately 25° or almost 14% of its delivery stroke in connection to the suction port.

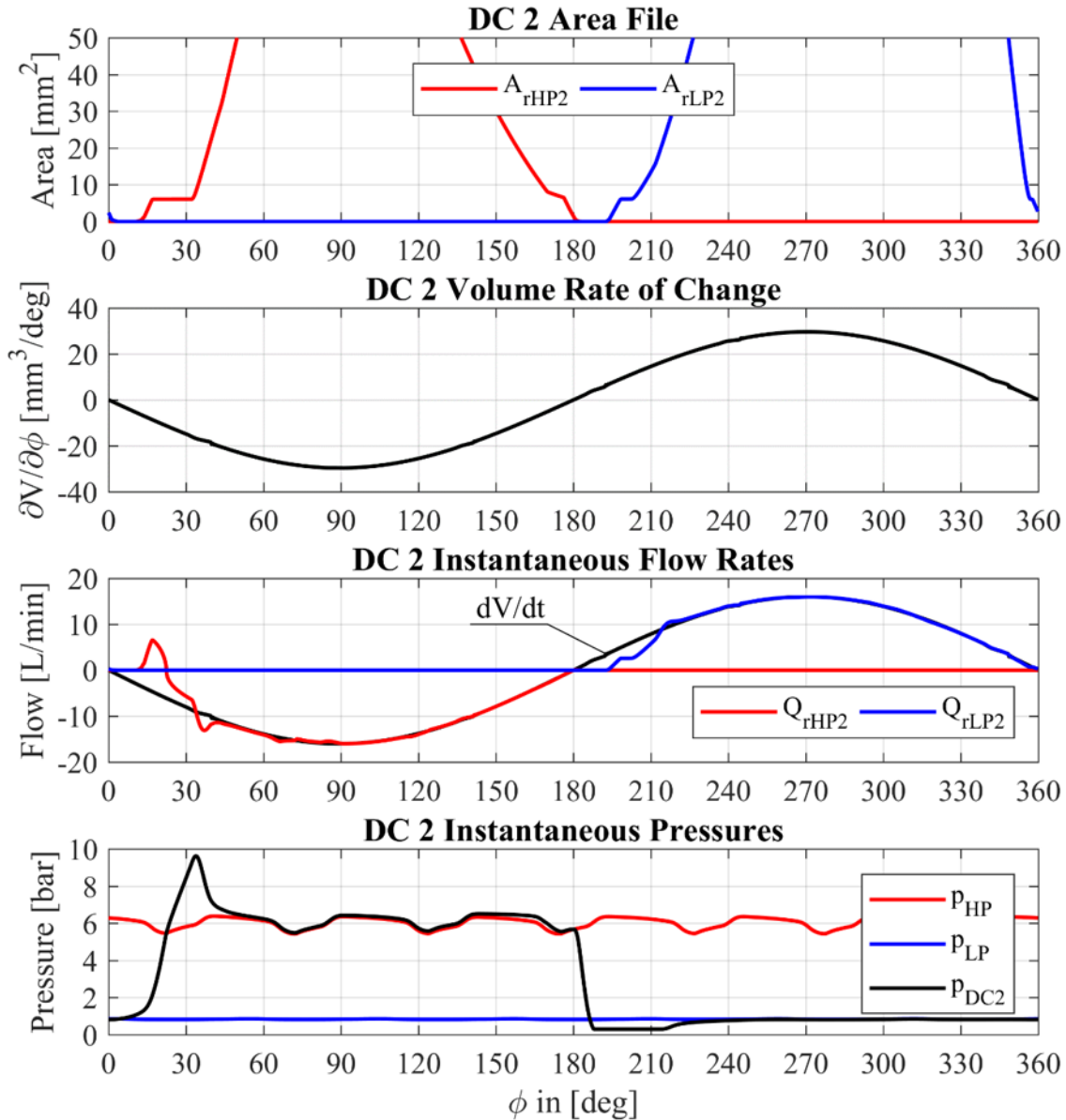


Figure 40: Important pump geometry factors considered in the DC Module and their comparison to the simulated DC pressure and flow profiles for the operating conditions corresponding to Figure 39 and Table 2 and where ϕ is measured CW from ϕ_{ODC} .

This also means that roughly 14% of the suction stroke at 20% displacement is spent in connection to the delivery port. An effect that somewhat counters this is the change in the angular size of the isolated regions at lower eccentricities, giving additional time for the pressure to build up [63]. This illustrates the impact that port design can have on the pump performance.

Because these flow effects are included in the DC Module, the pressure profiles are sufficiently validated and the overall performance agrees well at 100% displacement. The DC Module can then be considered to produce realistic performance throughout its operating range.

5.5 Effect of External Leakages

Using the information contained in Table 2, the net external leakages for the pump Q_{SE} at that selected operating condition can be determined using Equations (5.5) and (5.6).

$$Q_S = nV_P - Q_{Eff} \quad (5.5)$$

$$Q_{SE} = Q_S - Q_{SI} - Q_{Comp} \quad (5.6)$$

The term Q_{Eff} in Equation (5.5) refers to the effective flow rate of the pump measured under steady-state conditions. Equation (5.6) then gives the breakdown of the volumetric losses Q_S into its constituent components. These are the external leakages Q_{SE} , internal leakages Q_{SI} , and compressibility losses Q_{Comp} . While the internal leakages and compression losses are not directly measureable, the net external leakages from the DC can be determined from measured case drain flows provided the control chamber leakage portion of this flow is known. Thus, Equations (5.5) and (5.6) can only be used to determine the external leakages if the effects of the internal leakages and compression losses are known from a detailed simulation model.

Because Q_{SI} represents the flow between DC volumes through the lubricating gaps surrounding the vanes as well as cross-port flow, the effect of these leakages can be modeled. Compression losses can also be modeled. Therefore, even though the DC Module does not include models of the lubricating gaps to calculate gap flows, the simulated pump flow still represents, to a large degree, the theoretical pump flow minus compression losses and internal leakages and thus Equation (5.7) holds for this case study.

$$Q_{SI} + Q_{Comp} = nV_P - Q_{A,sim} \quad (5.7)$$

$$Q_{SE,DCi} = \frac{Q_{SE}}{3.5} \quad (5.8)$$

Once Q_{SE} is known, Equation (5.8) can be used to determine the net contribution of each DC to the total external leakages per revolution. This value, $Q_{SE,DCi}$, can be distributed throughout the revolution as depicted in Figure 42. As Figure 42 illustrates, this distribution is characterized by leakage flow out of the DC and into the case whenever the DC pressure is high. Additionally, a small amount of flow is considered to leak into the chamber (positive flows in the third plot of Figure 42) from neighboring high-pressure DC when the pressure in the chamber is low. Nevertheless, the integral of this distribution over a revolution still results in $Q_{SE,DCi}$.

Including this leakage term in Equation (3.1) and re-running the DC Module simulation for a similar set of operating conditions (in fact the operating conditions of the second measurement example presented in this chapter), and comparing the resulting pressure profiles gives a good sense of the sensitivity of the DC Module to these leakages. Figure 41 shows this comparison and indicates that the effect of external leakages on p_{DCi} is negligible. In fact, the absolute difference between the two profiles shown in Figure 41 is less than 0.1bar for over 95% of the revolution. Thus, neglecting external leakages in the simulation model has no negative effects with respect to the purpose of this model, i.e. the evaluation of the pump dynamics.

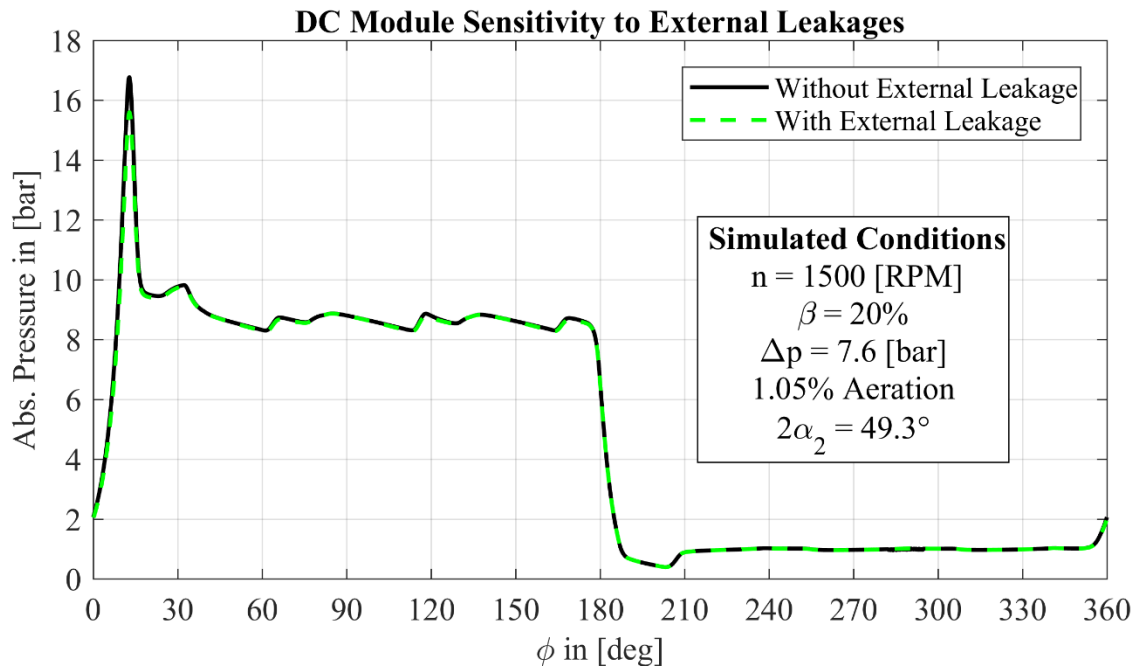


Figure 41: Sensitivity of the DC Module pressure calculations to external leakages.

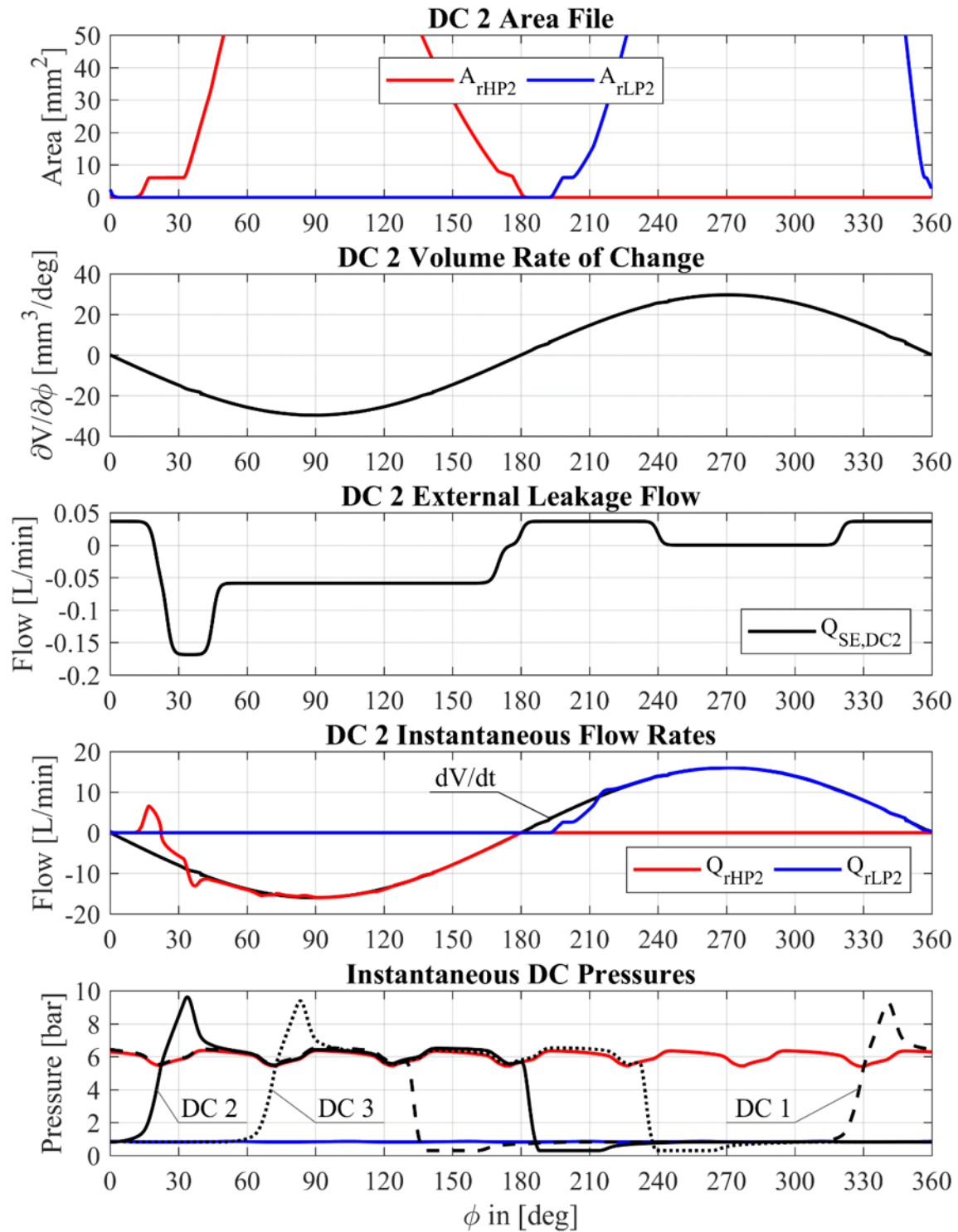


Figure 42: Plots summarizing the distribution of the calculated external leakages term corresponding to an individual DC over a shaft revolution and the correlation of this leakage term to other pertinent DC parameters and DC Module outputs.

As the largest difference between the two profiles shown in Figure 41 occurs around 15° at the zenith of the pressure spike, one additional comment about the effect of external leakages can be made. The primary effect of external leakages is the attenuation of the magnitude of the spikes in the DC pressure profile. This is directly correlated to a reduction in the magnitude of the internal pressure force spikes. Thus, from a dynamics standpoint, neglecting the external leakages results in a worst case scenario that is better for isolating the limitations of the system. This observation provides additional, and strong, support for not developing complex fluid-structure-interaction models to describe the tribological interfaces of the pump for a model sufficiently accurate to perform an analysis of the system dynamics.

5.6 Takeaways

In conjunction with the observations of Section 5.5 and considering the validation plots presented throughout this chapter as sufficient evidence that the DC Module presented in Chapter 3 is a good representation of the case study pump's hydraulic behavior, several takeaways can now be highlighted. As stated in Section 1.4, the goal of this research is to characterize the performance of the case study system. While the pump dynamics will be explored in Chapter 6, several aspects of the system performance as it pertains to the pump's hydraulic behavior can be explored with the validated model.

The pump interacts hydraulically with the pressure compensated system as a whole in two principle ways. First, the pump acts as a flow source to the system. Second, the pump generates internal forces that act on the adjustment system components and therefore define the required control effort.

While some of the flow characteristics of the pump were discussed in Section 5.4, the DC Module also reveals the relative impact of some of the fluid properties on these flow characteristics. Figure 43 illustrates how aeration levels, temperature, pressure, and pump speed all affect the outlet flow Q_A .

As the two plots on the left-hand side of Figure 43 reveal, a large part of the flow non-uniformity is also due to the compressibility of the working fluid. Compression losses Q_{Comp} increase with increasing air content and pump outlet pressures, so differences in the upper limit on the pump's volumetric and total efficiencies can also be seen between the cases plotted. Table 3 summarizes these differences in efficiency as well as the mean flow rates for each of the cases

plotted in Figure 43. In both Figure 43 and Table 3, only one parameter varies between cases so its impact on the performance relative to a common baseline case can be more easily evaluated.

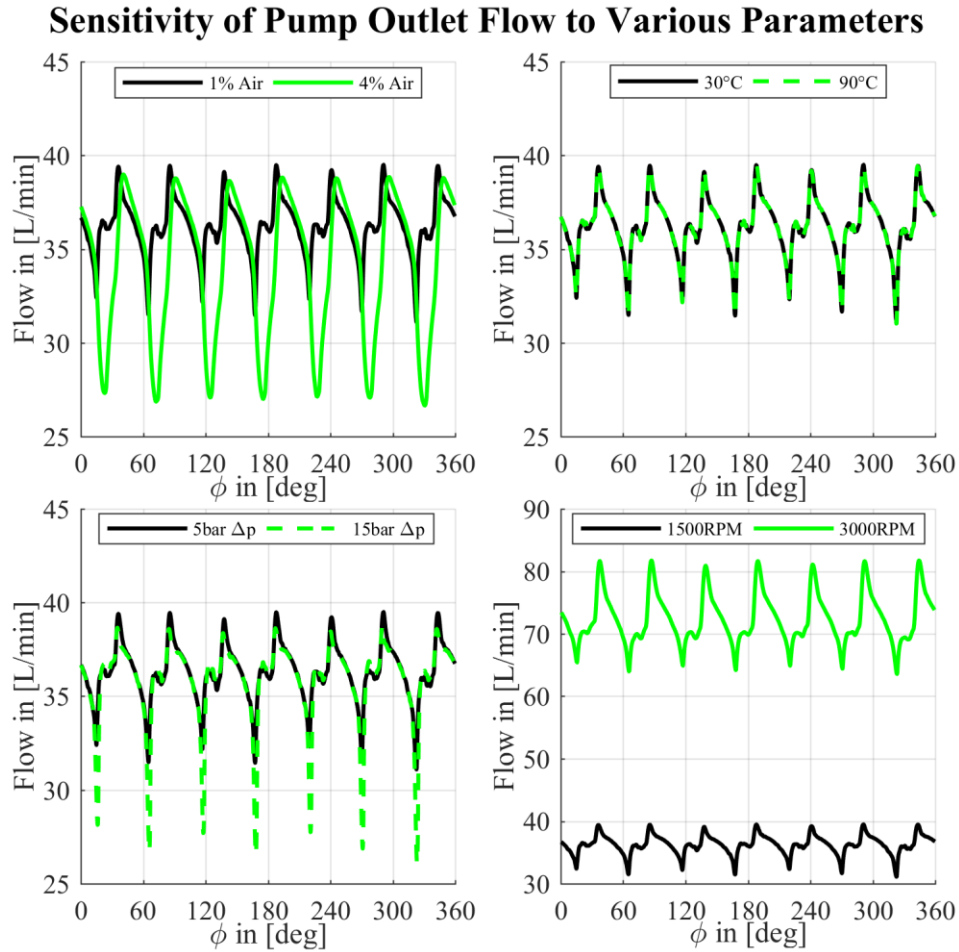


Figure 43: Simulated relative sensitivity of the pump outlet flow Q_A to air content, fluid temperature, pump pressure levels, and pump speed.

Table 3: Summary of the relative sensitivity of various pump performance parameters to changes (one at a time) in air content, fluid temperature, pump pressure levels, and pump speed.

Simulation Case	Mean Q_A [L/min]	Mean M_1 [Nm]	Max η_V	Max η_M	Max η_T
Baseline	36.36	5.63	0.969	0.826	0.800
Higher Air Content	34.33	2.14	0.915	0.875	0.801
Higher Temperature	36.35	5.04	0.969	0.835	0.809
Higher Pressure	35.63	3.41	0.950	0.909	0.863
Higher Pump Speed	72.01	16.81	0.960	0.613	0.588
Lower Displacement	18.71	3.87	0.972	0.884	0.859

Table 3 also includes mean values for the internal forces of the pump, M_1 , and their relative sensitivity to changes in operating conditions. Figure 44 provides plots of M_1 for each of these sensitivity cases. As these plots illustrate, the internal forces generated by both the DC pressures and centrifugal forces associated with the rotating group are complex and dynamic. Depending on the frequency response characteristics of the pump adjustment system, these dynamic loads can be a driving source of undesirable oscillatory behavior.

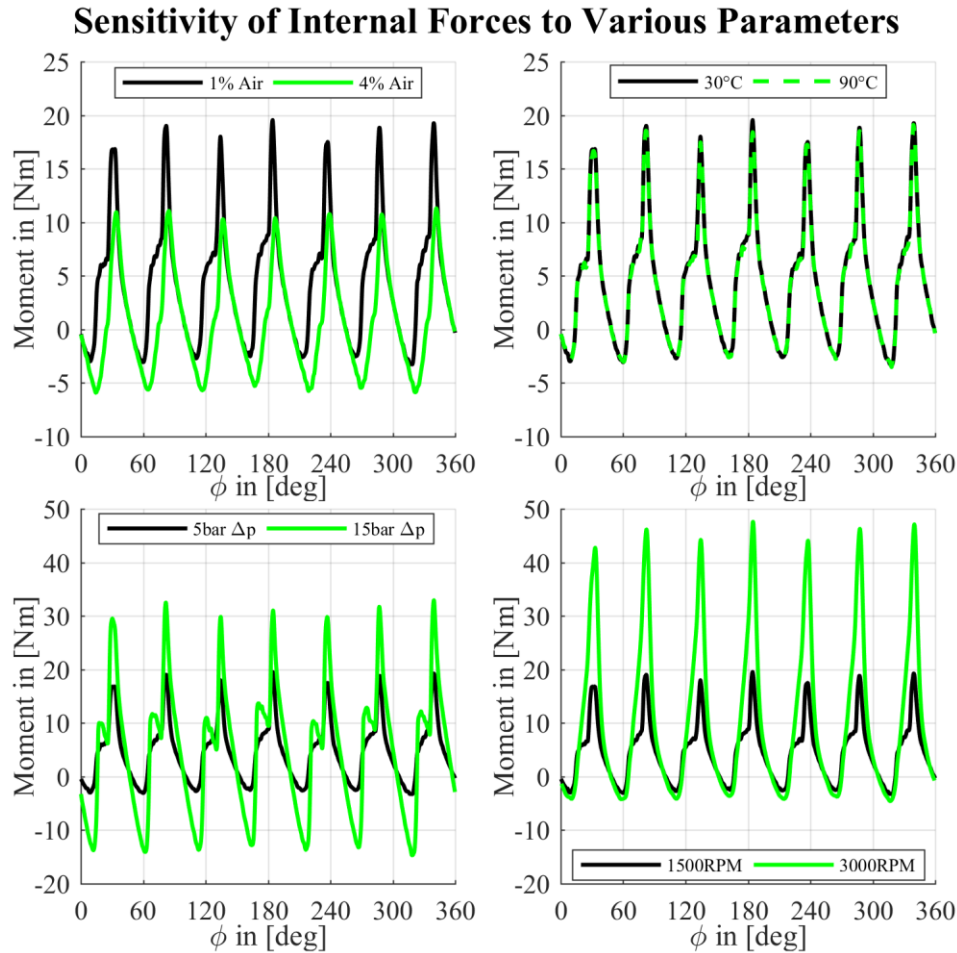


Figure 44: Simulated relative sensitivity of the internal forces M_1 to air content, fluid temperature, pump pressure levels, and pump speed.

As these forces impact the stator eccentricity, their nature changes as a function of the pump displacement. Figure 45 illustrates the stator eccentricity's impact on both the pump outlet flow and the internal forces acting on the stator. The flow plot reveals that the magnitude of the flow peaks decrease at reduced displacements while the moment plot reveals that the shape of the internal forces begin to approach a typical saw-tooth shape.

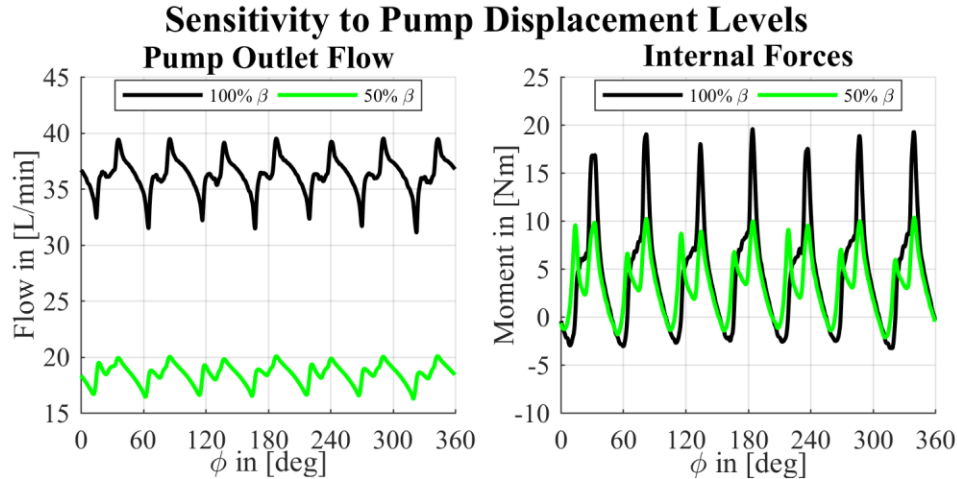


Figure 45: Simulated relative sensitivity of both the pump outlet flow Q_A and the internal forces M_1 to changes in the displacement β .

The final row in Table 3 provides the mean values associated with the traces given in Figure 45 as well as the maximum efficiencies for the reduced displacement case. For the baseline case operating condition (defined by the pump pressure and speed) reducing the displacement appears to improve the efficiency of the pump. However, it must be remembered that the model neglects external leakages and friction, so the true efficiency may not improve. Nevertheless, this example highlights the complex and nonlinear nature of both Q_A and M_1 as system variables. In terms of the system performance, the following takeaways are now clear.

- The mean value and shape of Q_A and M_1 vary with changes in the pump operating conditions, resulting in the transmission of complex and nonlinear signals to the rest of the system.
- These periodic signals can excite oscillatory responses in the pump adjustment system, load, and pressure compensation control valves which can develop into undesirable resonant behavior or instabilities depending on the dynamics of these connected systems.
- Based on the example duty cycle presented in Section 1.3.3, the nature of these excitation signals, and their potential to induce undesirable oscillatory behavior, is constantly changing throughout normal operation.
- While not perfect, the DC Module presented in Chapter 3 is accurate enough to sufficiently represent the pump's behavior for a more in depth analysis of the system performance to identify the source of limitations.

6. ADJUSTMENT SYSTEM DYNAMICS MODULE

As Figure 9 indicates, the adjustment system module in Figure 8 that completes the lumped parameter vane pump model is comprised of a set of coupled dynamic equations. The first of these is the stator equation of motion and the second describes the pressure build-up of the control chamber. Figure 46 illustrates the several sources of forces acting on the stator, which has an inertia I_S , and an equivalent free body diagram that is useful in defining the stator equation of motion given by Equation (6.1).

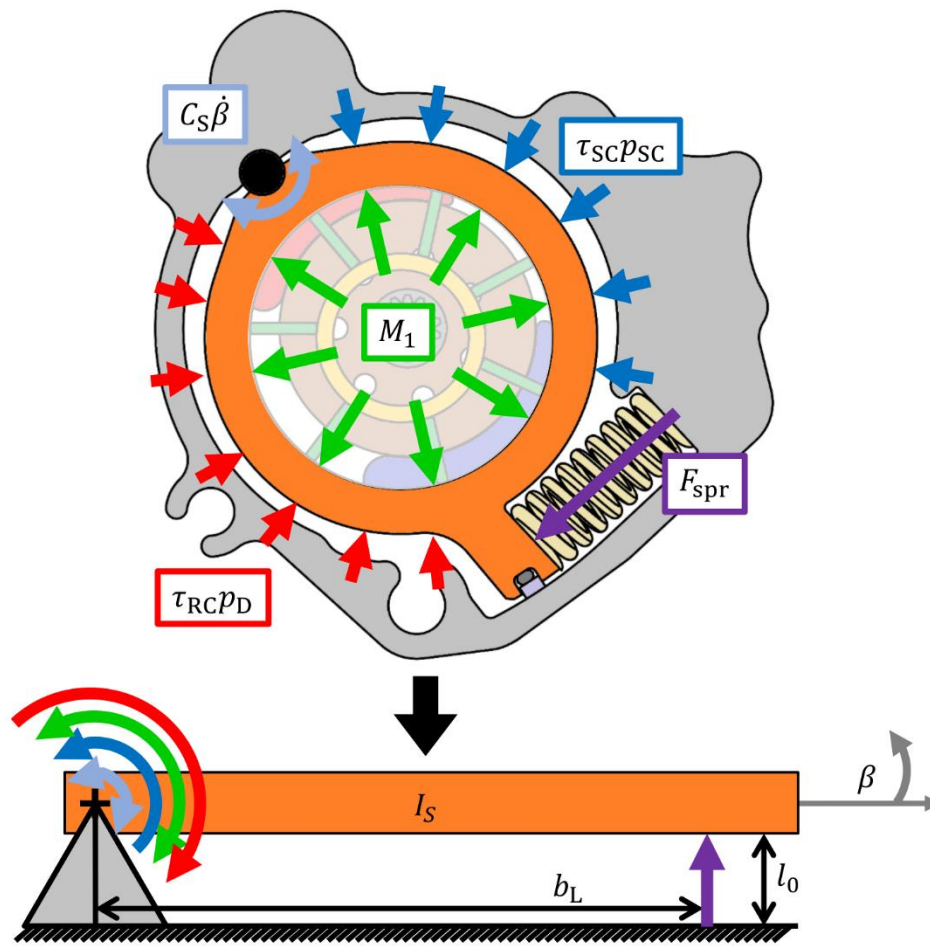


Figure 46: Stator free body diagram used to derive the equation of motion.

$$I_S \frac{d^2\beta}{dt^2} = kb_L (l_f - (b_L \sin(\beta) + l_0)) - C_S \frac{d\beta}{dt} + M_1 + \tau_{RC} p_D + \tau_{SC} p_{SC} + M_{st} \quad (6.1)$$

As Figure 46 indicates, the spring force acts at a moment arm of length b_L identical to the definition of b_L given in Figure 24 for the LVDT signal to eccentricity angle conversion. This

force, F_{spr} , is therefore defined by the bias spring rate k and the linear compression of the spring along its centerline. This compression depends on the free length of the spring l_f , the eccentricity angle β , and the length of the spring at a zero eccentricity angle l_0 as indicated in Equation (6.1). Meanwhile, the damping term $C_S \frac{d\beta}{dt}$ represents the net effect of all viscous friction and seal friction terms defined in [11]. Determining the spring rate k and the lumped damping coefficient C_S from measured data makes this pump adjustment system module a semi-empirical lumped parameter model.

The third term on the right-hand side of Equation (6.1) comes from Equation (3.82) and represents the internal forces acting on the stator discussed previously. Figure 47 depicts an additional example of this moment. As should be apparent, positive moments here tend to increase the stator eccentricity.

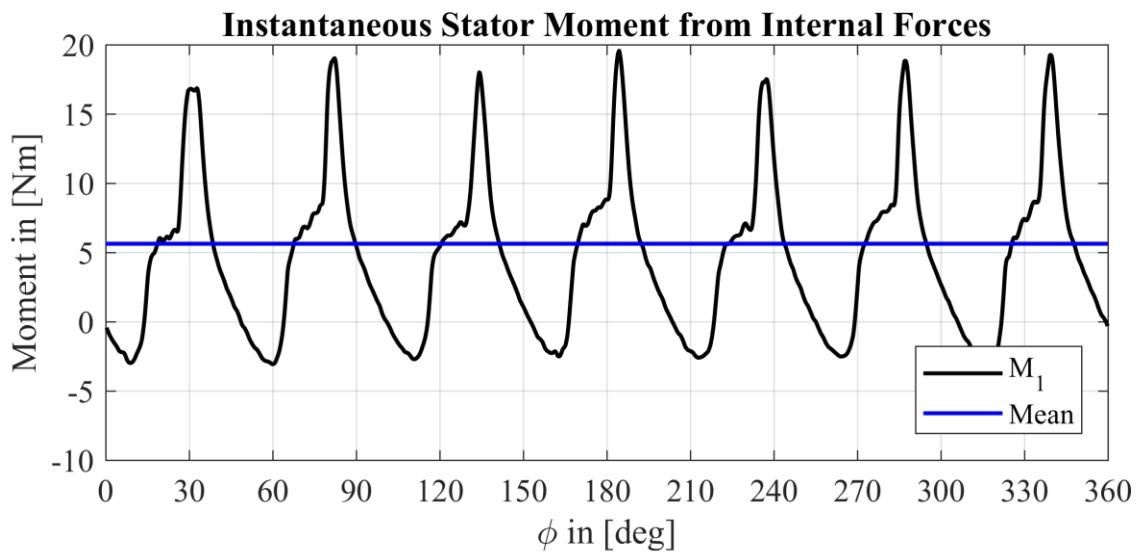


Figure 47: Example M_1 profile over a single shaft revolution for the operating conditions corresponding to the example simulation in Section 5.4.

As Figure 46 indicates, the fourth and fifth terms on the right-hand side of Equation (6.1) represent the pressure force moments from the control chamber and spring chamber, respectively. The parameters τ_{RC} and τ_{SC} are geometric parameters similar to τ_{DCi} in meaning and were defined using projected areas taken from the 3D CAD model of the stator. These two chambers are connected via a groove machined into the circumference of the pivot pin. Any flow across the pivot, or leaked into the spring chamber from the delivery port or DC, then drains to the tank through a large hole in the case near the spring which maintains the spring chamber

pressure at atmospheric levels. The control chamber pressure, therefore, must overcome the sum of the internal force, spring, damping, and spring chamber pressure terms to effect stator motion.

The final term in Equation (6.1) is a nonlinear representation of the additional force encountered when the stator reaches the ends of the permissible travel and either comes into contact with the pump case or compresses the bias spring fully. This term is given by Equation (6.2) and effectively maintains the simulated stator eccentricity within physically significant bounds while also providing a slight cushioning force as the stator approaches contact with the case. The parameter k_{stop} is simply taken to be a constant representing an arbitrarily stiff spring.

$$M_{st} = \begin{cases} k_{stop}(\beta_{max} - \beta) - 3C_s \frac{d\beta}{dt}, & \beta > \beta_{max} \\ -0.8C_s \frac{d\beta}{dt}, & 0.97\beta_{max} < \beta < \beta_{max} \\ k_{stop}(\beta_{min} - \beta), & \beta < \beta_{min} \\ 0, & otherwise \end{cases} \quad (6.2)$$

6.1 Experimental Setup

In order to measure the stator dynamics, the custom test rig described in Chapter 4 was modified according to the diagram depicted in Figure 48 (see also Circuit 2 in APPENDIX A).

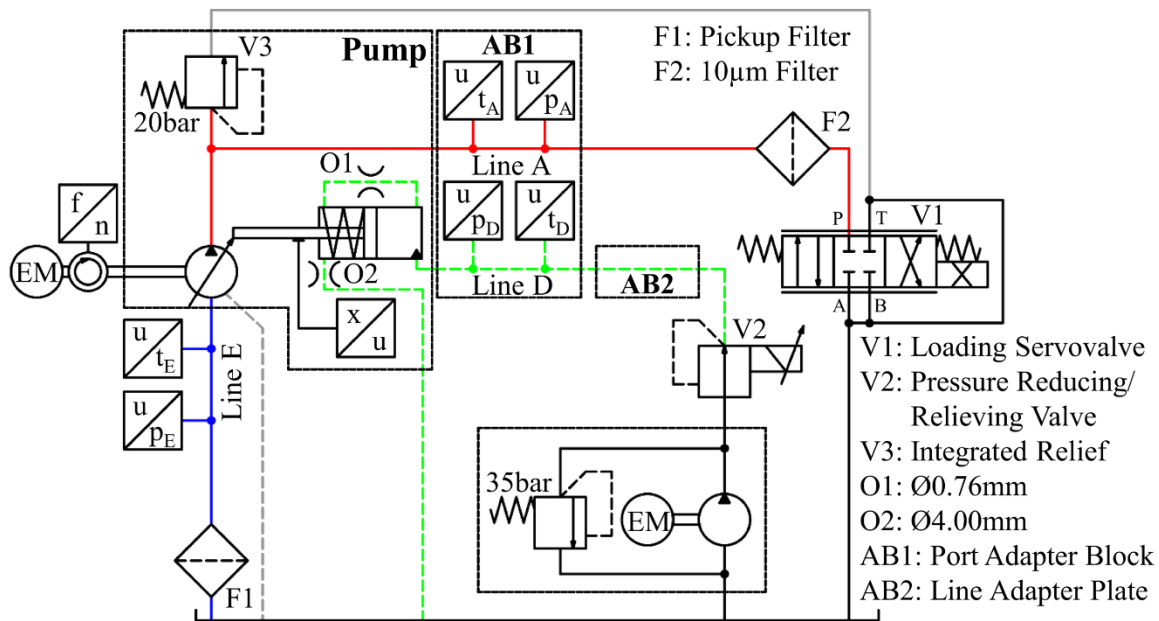


Figure 48: Hydraulic circuit diagram for the experimental setup used for the stator dynamics validation measurement study.

For the stator dynamics measurements, the DC pressure transducers were no longer monitored. Instead, the LVDT, Line A pressure, and Line D pressure signals were of primary interest and therefore sampled at a 2kHz rate. As Figure 48 indicates, the control chamber pressure was regulated using an independent pressure source and a separate valve which interfaced with the pump adapter block via a custom plate manufactured for this setup and described by Drawing 25 in APPENDIX B. Valve details are available in APPENDIX C.

The test procedure associated with this setup is outlined below and an example of the resulting measurement data is given by Figure 49.

- Step 1. Start the DAQ/Control program on the cRIO, load the user interface on the connected laptop, and power on the sensors and other electronic components.
- Step 2. Command the loading servovalve to a fully open position.
- Step 3. Start the auxiliary pressure supply.
- Step 4. Start the electric motor and set to the desired speed.
- Step 5. Command valve V2 in Figure 48 to regulate the control chamber pressure to follow a square wave reference profile.
- Step 6. Record the line pressures and stator displacements for multiple square wave frequencies and amplitudes.
- Step 7. Repeat Steps 6 and 7 for a sinusoidal reference profile.
- Step 8. Turn off the auxiliary pressure supply.
- Step 9. Turn off the electric motor.
- Step 10. Power down the DAQ/Control system.

Post-processing the data from this study is straightforward and does not require any additional discussion beyond the procedure to convert the LVDT signal to eccentricity angle outlined in Section 4.1.2. The unfiltered result of this conversion is shown in Figure 49 while a zero-lag low-pass filter was applied to the pressure signals to eliminate high frequency noise.

The drop of the Line A pressure below the Line D pressure occurs here due to a constant loading valve position and the reduction in pump outlet flow as a result of the reduced eccentricity. Normally, the pressure in Line A would never drop below the Line D pressure even for a constant loading valve position and a decreasing β because they are connected through the regulation valve V1 in Figure 4. However, since these pressures are decoupled in this experimental setup, the constant loading valve position and reduction in β produces these results.

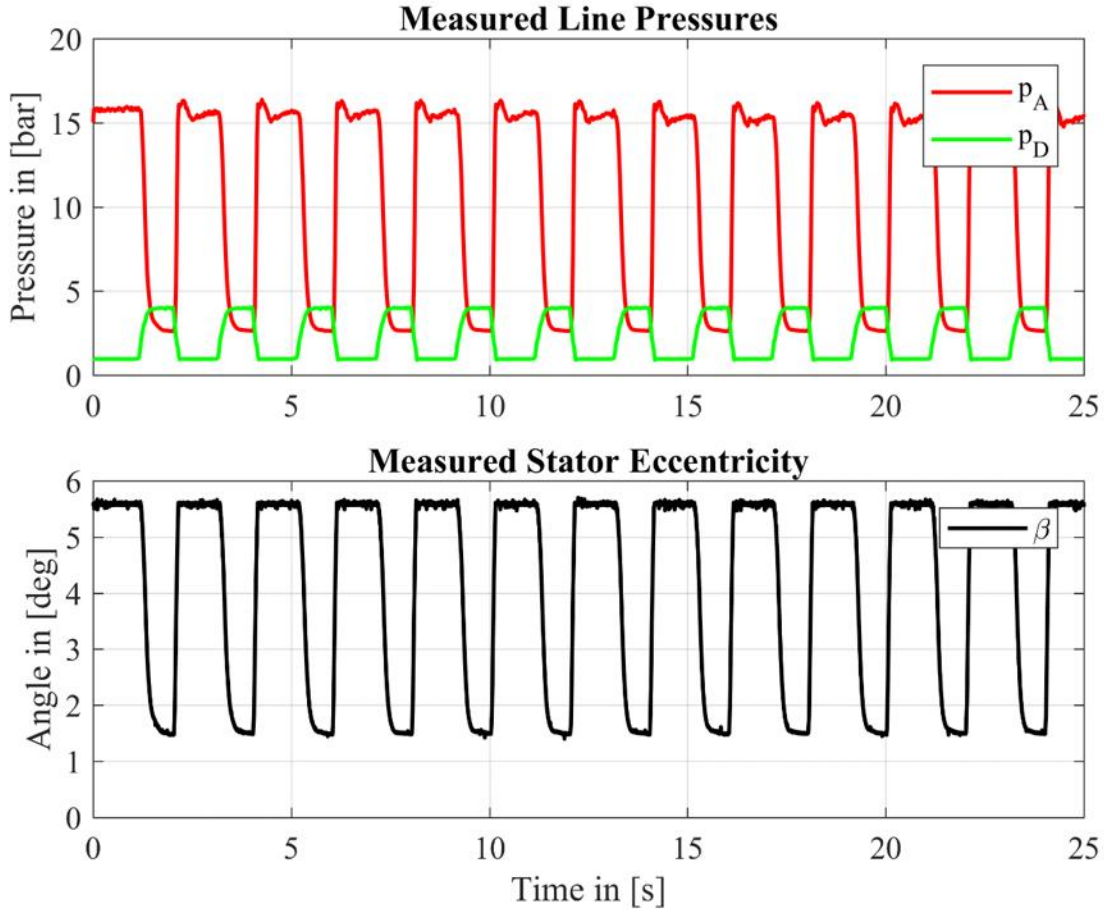


Figure 49: Example line pressure and eccentricity measurement data from the stator dynamics validation study.

6.2 Damping Coefficient C_S

Analyzing the step response of the stator as shown in Figure 49 and other similar measurements indicated a fairly first-order response type. To recreate this effect, the value of C_S given by Equation (6.3) was chosen. This value results in an overdamped second-order system behavior for Equation (6.1) when using the nominal bias spring rate (taken from the spring data sheet) with a similar rise time to the measured data.

$$C_S = 7.66 \left[\frac{kgm^2}{s} \right] \quad (6.3)$$

This parameter choice was further validated by comparing the resulting power loss due to stator friction effects with published results in [11]. This power was calculated using the RMS (root-mean-squared) stator velocity from measured data by Equation (6.4). An estimate of the

total power losses due to all pump friction sources is gleaned from Table 2 by applying Equation (6.5) which has a similar interpretation to that of Equation (5.7) when M_P is given by Equation (3.41) in the DC Module. Taking the ratio of the stator friction power P_{SF} and the total friction power losses $P_{Friction}$ reveals that the power losses associated with the stator friction represent approximately 20% of the total friction power. This agrees well with the results published for a similar pump design in [11] for similar oil conditions.

$$P_{SF} = C_S \left(\frac{d\beta}{dt} \right)_{RMS}^2 \quad (6.4)$$

$$P_{Friction} = n(M_{Eff} - M_P) \quad (6.5)$$

6.3 Nonlinear Spring Rate k

As the bias spring is a helical compression spring, it exerts a force on the stator proportional to the compression it experiences between the stator and case lands. This force results in a positive pivoting moment that biases the stator to a maximum eccentricity position and is one of the primary forces the control chamber pressure must overcome to reduce the pump displacement. As Equation (6.1) indicates, the compression of the spring is nonlinear as a function of β and all that remains is to define the spring rate k .

A data sheet was supplied with the case study pump giving the nominal bias spring rate. In reality, the actual spring rate varies from unit to unit due to manufacturing tolerances and normal variations in material properties. Equation (6.6), taken from [64], reveals that these variations can be as large as 17% of the nominal rate of 28.59N/mm as shown in Table 4.

$$k = \frac{G_{steel} d_s^4}{8N_a D_s^3} \quad (6.6)$$

Table 4: Calculated bias spring rates for various combinations of spring parameters.

Case	$(\underline{d}_s, \underline{D}_s)$	$(\underline{d}_s, \overline{D}_s)$	$(\overline{d}_s, \underline{D}_s)$	$(\overline{d}_s, \overline{D}_s)$
$N_a = 8.25$	27.7 $\left[\frac{N}{mm} \right]$	25.9 $\left[\frac{N}{mm} \right]$	33.5 $\left[\frac{N}{mm} \right]$	31.3 $\left[\frac{N}{mm} \right]$
$N_a = 8.50$	26.9 $\left[\frac{N}{mm} \right]$	25.1 $\left[\frac{N}{mm} \right]$	32.5 $\left[\frac{N}{mm} \right]$	30.4 $\left[\frac{N}{mm} \right]$
$N_a = 8.75$	26.1 $\left[\frac{N}{mm} \right]$	24.4 $\left[\frac{N}{mm} \right]$	31.6 $\left[\frac{N}{mm} \right]$	29.5 $\left[\frac{N}{mm} \right]$

This variation of 17% occurs even when the dimensional tolerances specified in the data sheet are kept. The symbols \underline{d}_s and \underline{D}_s represent the minimum wire diameter and mean coil diameter values, respectively, within the manufacturing tolerance bounds. The symbols \overline{d}_s and \overline{D}_s , on the other hand, represent the maximum allowable values within these bounds. Meanwhile, the parameter N_a represents the number of active coils. The shear modulus G_{steel} was kept constant at the nominal value for this class of spring steel for the comparison given in Table 4.

When comparing simulated eccentricity profiles to measured profiles from various tests, different spring rates (most within this range of variability) were required to get reasonable model agreement. These various tests represented different amplitude square waves at different frequencies. Because the internal forces calculated by the DC Module were validated through validating the DC pressure profile, a linear spring rate was therefore deemed insufficient.

Due to the pump geometry and the pivoting motion of the stator, the bias spring does not experience compression between two parallel surfaces but a combination of a linear compression and bending as the angle between the two lands varies linearly with the eccentricity angle. Under these conditions, the internal shear and torsional stresses developed in the spring and discussed in [64] would be different for a given centerline length than in the case of pure linear compression between two parallel surfaces for the same spring. This obviously changes the force required to compress the spring.

In order to represent the true spring force acting at a point on the stator land, a nonlinearly progressive spring rate model was created to capture the added effort of bending the spring. This model is depicted in Figure 50 and is given by Equation (6.7) where β is in radians.

$$k = 34.5 - 3.5 \tanh(60\beta - 4.08) \quad (6.7)$$

The spring rate resulting from Equation (6.7) increases nonlinearly from a nominal spring rate within the range of variability represented by Table 4 to a value almost 23% greater at a minimum compressed length for a maximum increase of 33% over the nominal spring rate reported on the data sheet. This model was created by determining the constant k with the best agreement at certain points in several measurements then finding a function fitting these points.

This empirical spring rate model, together with the C_S defined by Equation (6.3), completes the semi-empirical equation of motion describing the stator dynamics within the pump adjustment system module.

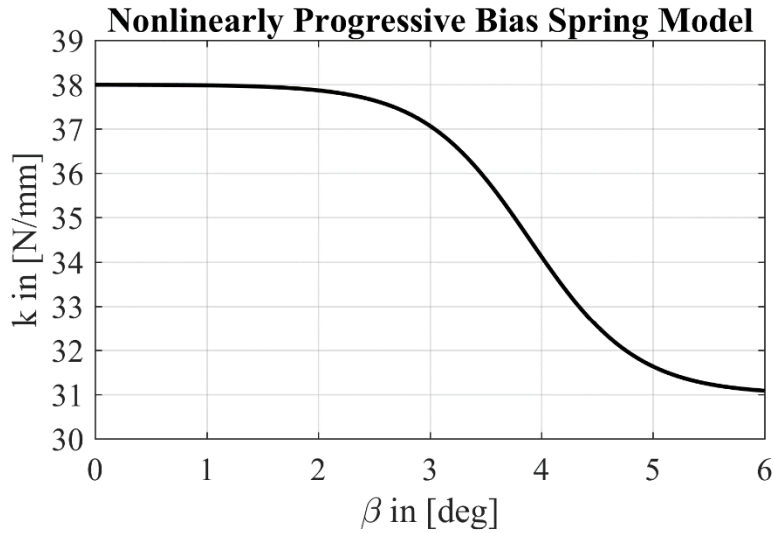


Figure 50: Progressive bias spring rate as a function of β .

6.4 Model Validation of the Stator Equation of Motion

Figure 51 shows an example validation comparison that highlight the accuracy of the stator equation of motion with the nonlinear bias spring rate given by Equation (6.7). As is apparent here, the modeling error is highest during the reduction transients due to several factors.

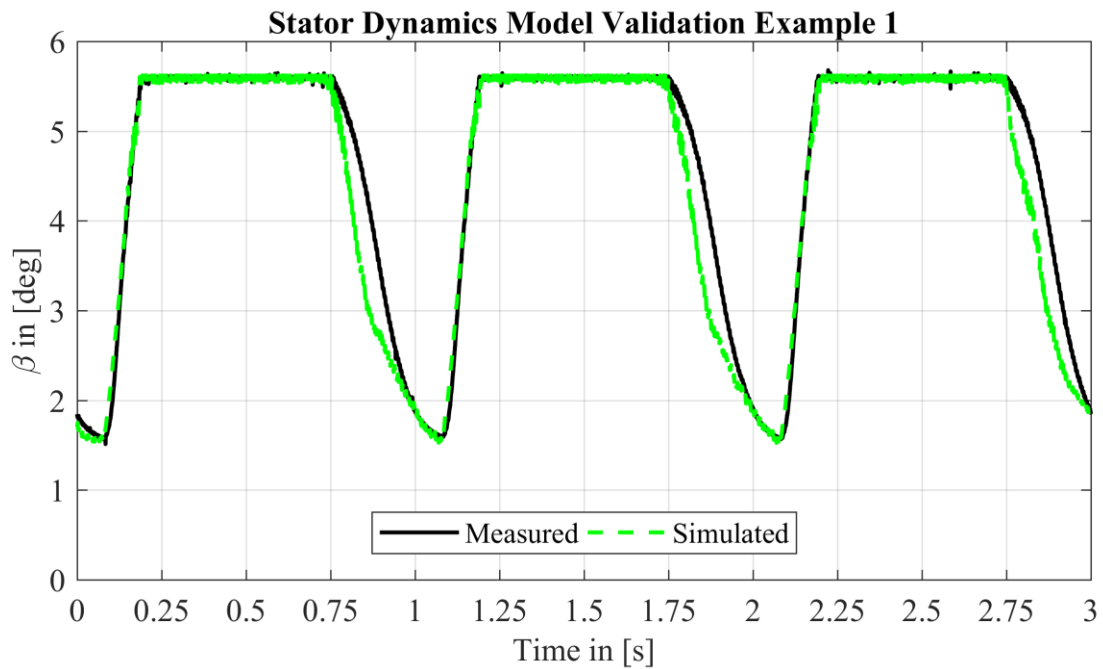


Figure 51: Higher frequency, higher amplitude stator dynamics validation example.

The first of these factors is the difference between the actual geometry of the case study pump installed on the test rig and the nominal geometry assumed from the 3D CAD in the lumped parameter model. While the variations in the DC geometries are small, as indicated by Table 1, and the model represents the pump geometry well, as indicated in Sections 3.3 and 3.10, they can still have a significant impact on the internal forces. This impact is manifested by changes in both the magnitude and shape of the internal forces as well as in the frequency content through altering the moment arms, exposed areas, and DC pressure dynamics. Therefore, the overall agreement between the simulated and measured profiles is fairly representative of the behavioral differences between units due to production tolerances.

The second factor is the simplified approach of a lumped linear damping term. Including models of the various friction sources presented in [11] would allow for a more realistic and nonlinear damping term. However, the net effect would be an increase in the damping and change the damping profile slightly. This lumped, linear approach is then valuable in that it provides representative stator dynamics at a low computational price for a dynamics analysis.

A possible third factor is that the real pump exhibits some form of hysteresis in both the effective spring and damping forces due to the design of the seal depicted in Figure 3. This type of effect is likely to be minor in impact relative to the other two factors presented above.

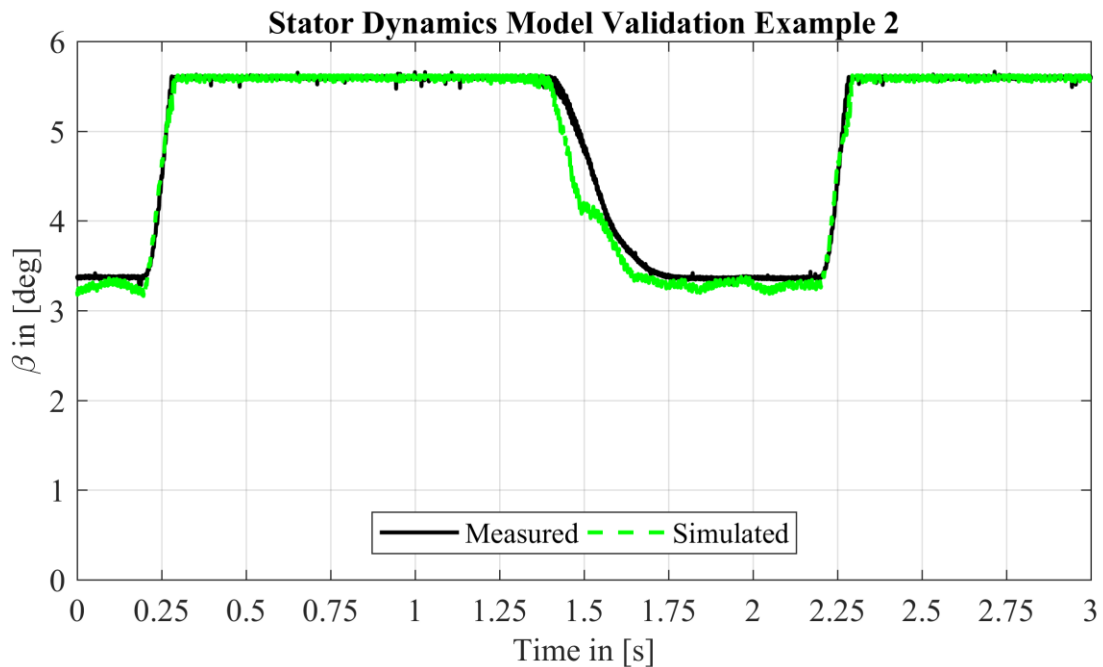


Figure 52: Lower frequency, lower amplitude stator dynamics validation example.

Figure 52 presents an additional validation example with a similar quality of performance. In fact, the mean error between the simulated and measured eccentricity profiles is less than a thousandth of a degree for the two examples presented here plus three other cases not included here. This degree of accuracy translates to an average error less than a hundredth of a percent in the displacement of the pump during a dynamic cycle. The maximum (on average) error during the reduction transients across the five validation examples examined is just over a degree (or roughly 19% displacement). While this is definitely a mark against the model presented in this dissertation, Figure 51 and Figure 52 illustrate that the behavioral trends are still captured well and indicate that the general dynamic interactions are preserved.

Based on these observations, the stator equation of motion is valid and representative of realistic pump performance. This validated second-order dynamics model exhibits a range of natural frequencies between 78.8Hz and 87.2Hz for the nominal inertia assumed. With the high damping coefficient, the stator is overdamped and has a rise time less than 74ms. Additional and neglected high frequency dynamics and nonlinearities in the true system (such as spring surge [64]), so this model is only valid for frequencies below about 200Hz.

6.5 Control Chamber Pressure Model

The other half of the adjustment system module, referring back to Figure 9, is the dynamic description of the control chamber pressure. This is accomplished by the solution of the system of equations represented by Equations (6.8) and (6.9) with β and $\frac{d\beta}{dt}$ taken from Equation (6.1). The spring chamber pressure is similarly modeled with Equations (6.10) and (6.11).

$$p_D = \frac{K_{mix}}{V_D} \int \left(Q_D - Q_{SE,D} - \frac{\partial V_D}{\partial \beta} \frac{d\beta}{dt} \right) dt \quad (6.8)$$

$$V_D = \frac{\partial V_D}{\partial \beta} \beta + V_{D,0} \quad (6.9)$$

$$p_{SC} = \frac{K_{mix}}{V_{SC}} \int \left(Q_{SE,D} - Q_{case} - \frac{\partial V_{SC}}{\partial \beta} \frac{d\beta}{dt} \right) dt \quad (6.10)$$

$$V_{SC} = \frac{\partial V_{SC}}{\partial \beta} \beta + V_{SC,0} \quad (6.11)$$

The geometric parameters describing the chamber volumes and how they change with β were found using the 3D CAD model of the pump and are constants. The term Q_D in Equation (6.8) refers to the controlled flow through the regulation valve V1 in Figure 4 or, alternatively, through the control valve when the VDVP is employed with a different pressure compensation control system architecture. As this flow comes from a different part of the overall system model, its characteristics will be discussed more in Chapters 7 and 8. The terms $Q_{SE,D}$ and Q_{case} , on the other hand, are, respectively, the leakage flow out of the control chamber across the pivot and the case drain flow out of the spring chamber.

Models for these leakage flows were created from 3D CFD analyses using Fluent in ANSYS to generate pressure drop versus flow data. Figure 53 provides an example of this analysis and shows more clearly the pivot geometry. For each interface, the pivot and the case drain holes, the geometry was imported from the 3D CAD model of the pump and isolated to simplify the domain of the problem to something similar to what is shown in Figure 53. This geometry was then used to run several CFD simulations for different known differential pressures to calculate the flow rate through the passage.

Once the simplified geometry was imported into ANSYS, the automatic mesh generation tool was utilized before refining the mesh slightly in the area of the pivot pin groove. A multiphase mixture model with laminar flow was then used for these simulations to represent the oil/air mixture present in the pump. The density of the oil was programmed to reflect the mathematical model describing the ISO 32 oil used in this research for several realistic and commonly encountered constant viscosities while the default properties of air stored in Fluent were used for the air. Beyond these customizations, the default solver parameters were used with second order accuracy in the spatial discretization of the density and momentum calculations and a Green-Gauss cell based approach to the gradient calculations. As the Fluent solver in ANSYS has been shown to perform well in benchmark tests [65], the default settings here are assumed to result in sufficiently accurate simulations of the flow through these leakage paths.

Figure 54 presents the data points from this analysis for the pivot. As the flow through the pivot pin groove was assumed to be a combination of laminar channel flow and turbulent orifice flow, a model derived from a linear combination of resistance terms from the general impedance model for transmission lines was fit to the points. Equation (6.12) gives the impedance model relationship between the differential pressure across a hydraulic resistance and

the flow through that resistance. Equation (6.13) is derived from Equation (6.12) by simply completing the square and solving for the flow as a function of the differential pressure.

$$\Delta p = R_{turbulent}Q^2 + R_{laminar}Q \quad (6.12)$$

$$Q = \sqrt{\frac{|\Delta p|}{R_{turbulent}} + \left(\frac{R_{laminar}}{2R_{turbulent}}\right)^2} - \frac{R_{laminar}}{2R_{turbulent}} \quad (6.13)$$

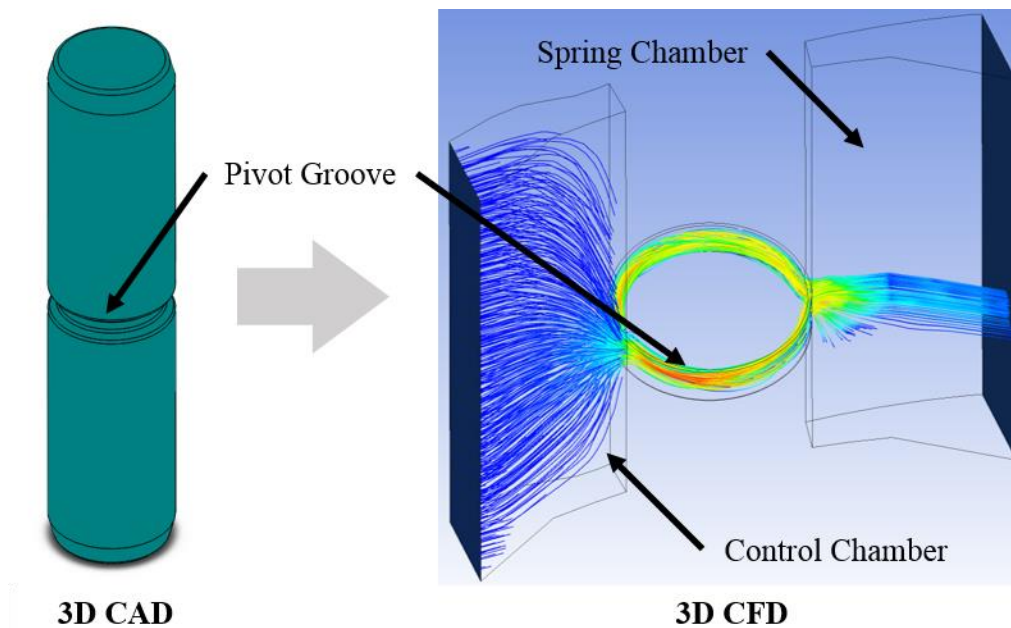


Figure 53: Example CFD analysis results for the leakage flow across the stator pivot for a control chamber gauge pressure of 7bar with μ_{oil} of 46cP.

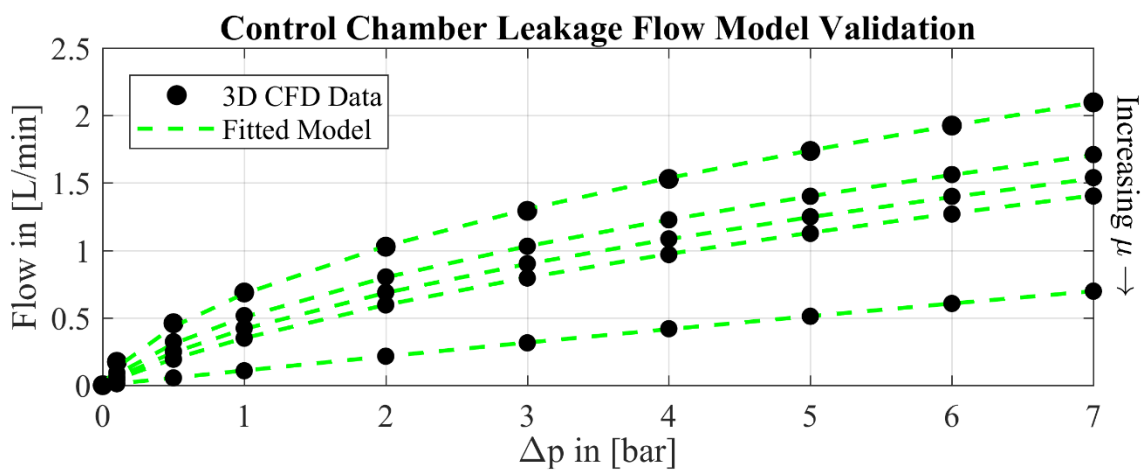


Figure 54: Pivot groove leakage CFD data and the fitted Equation (6.14) curves.

Using the coefficients of the impedance model regression lines for the CFD data at each simulated dynamic viscosity, the coefficients in Equation (6.14) can be defined as functions of the fluid viscosity μ_{oil} to calculate a realistic $Q_{SE,D}$ for use in Equations (6.8) and (6.10). Utilizing Equations (6.15) and (6.16), the model described by Equation (6.14) fits the CFD generated data well and exhibits an average R^2 value of 0.9998. Equation (6.14) returns values for $Q_{SE,D}$ in units of L/min for input pressures in bar and μ_{oil} in cP.

$$Q_{SE,D} = \sqrt{c_1\{\mu_{oil}\}|p_D - p_{SC}| + (c_2\{\mu_{oil}\})^2} - c_2\{\mu_{oil}\} \quad (6.14)$$

$$c_1\{\mu_{oil}\} = 0.217(\log_{10}(\mu_{oil}))^3 - 0.62(\log_{10}(\mu_{oil}))^2 + 0.22 \log_{10}(\mu_{oil}) + 0.83 \quad (6.15)$$

$$c_2\{\mu_{oil}\} = (6.73 \times 10^{-5})(\mu_{oil})^2 + (4.37 \times 10^{-3})\mu_{oil} + 0.196 \quad (6.16)$$

This model is valid for values of μ_{oil} ranging from 5cP to 180cP and pressures spanning the measured control chamber pressures taken from vehicle tests. The reason for this large range of viscosities arises from the fact that the viscosity of a typical automatic transmission fluid (ATF) spans a similar range of values for operating temperatures between roughly 3°C and 107°C [6]. While this range may not cover all possible operating conditions that the case study pump may see in a vehicle application, it does include the operating conditions of the example cases studied in this dissertation.

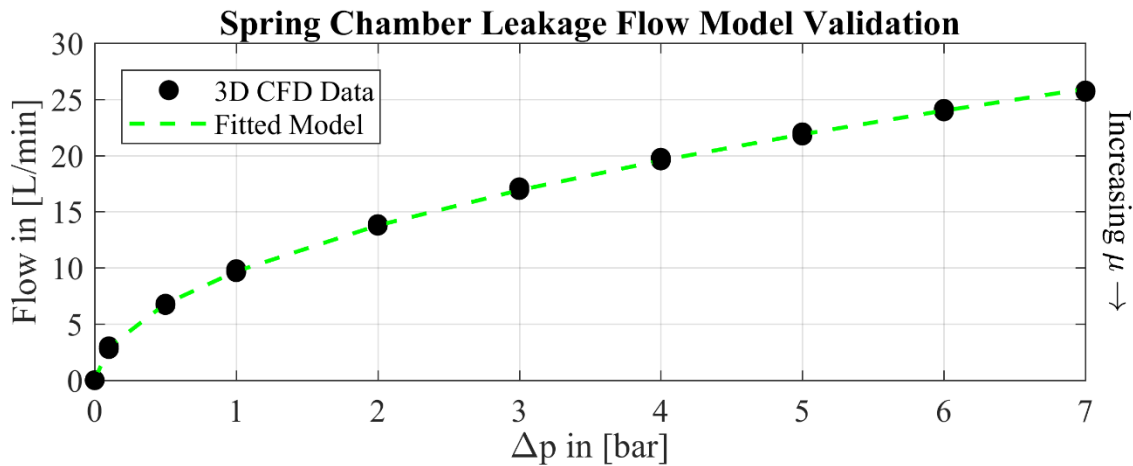


Figure 55: Case drain CFD data for multiple viscosities and the fitted model given by Equation (6.17).

The case drain term Q_{case} is similarly modeled by Equations (6.17) through (6.19) and shown Figure 55. As Figure 55 illustrates, this interface proved insensitive to changes in μ_{oil} .

This leads to constant model coefficients and a R^2 value of 0.9998. Like Equation (6.14), Equation (6.17) takes pressures in bar and returns values for Q_{case} in L/min.

$$Q_{case} = \sqrt{c_3 |p_{SC} - p_{tank}| + (c_4)^2} - c_4 \quad (6.17)$$

$$c_3 = 97.42 \quad (6.18)$$

$$c_4 = 0.19 \quad (6.19)$$

6.6 Summary

In summary and as Figure 56 illustrates, the completion of the adjustment system dynamics module with the control chamber pressure model results in a complete, and validated, model of the case study VDVP. All that remains to describe and analyze the case study system is then to define a set of empirical transfer functions to represent the pressure regulation system valves, which is the topic of Chapter 7. As Figure 56 indicates, the pump model which has been presented can recreate both the main line and required control pressures and can therefore be employed with models of new system architectures as will be done in Chapters 8 and 9.

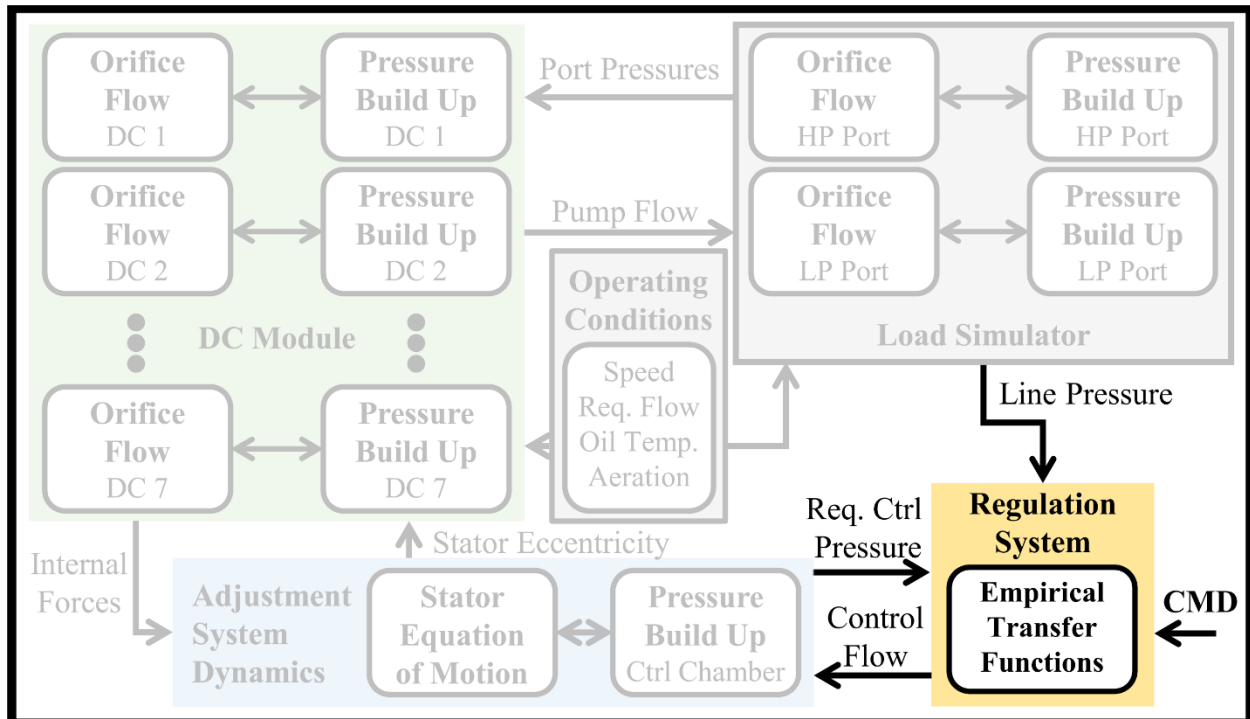


Figure 56: General system model block diagram with completed modules faded out to highlight which components have been completed and discussed to this point.

7. BASELINE PUMP CONTROL SYSTEM

The performance and stability of a pressure controlled pump system, in general, depends on both the dynamics of the pump with its adjustment system and the control system valves. Sometimes the control system valves are lumped into the term “adjustment system” or the adjustment mechanism in the pump is lumped into the generic “control system”. Here, however, the two systems will remain differentiated as follows. The “adjustment system” will be comprised everything in Chapter 6 and is limited to those displacement regulation elements within the pump case. The “control system” will then refer to all components outside the pump case, *inter alia* the control valve and—in the case of electrohydraulic control systems—the automatic control law and microcontroller. It should be noted that the capacitance of the line connecting the pump to the control valve, which technically belongs to the control system with this classification, was added to the control chamber capacitance within the adjustment system.

For the case study VDVP system depicted in Figure 4, the control system is comprised of three valves, two orifices, a spring loaded accumulator, and three pilot lines. As Section 2.2 states, a transfer function (TF) structure will be determined experimentally for an ad-hoc black-box model of this control system instead of building a physically based white or off-white model. This empirical model will represent the dynamics of the case study system primarily for an analysis of its associated dynamics and less for a predictive model of future behavior.

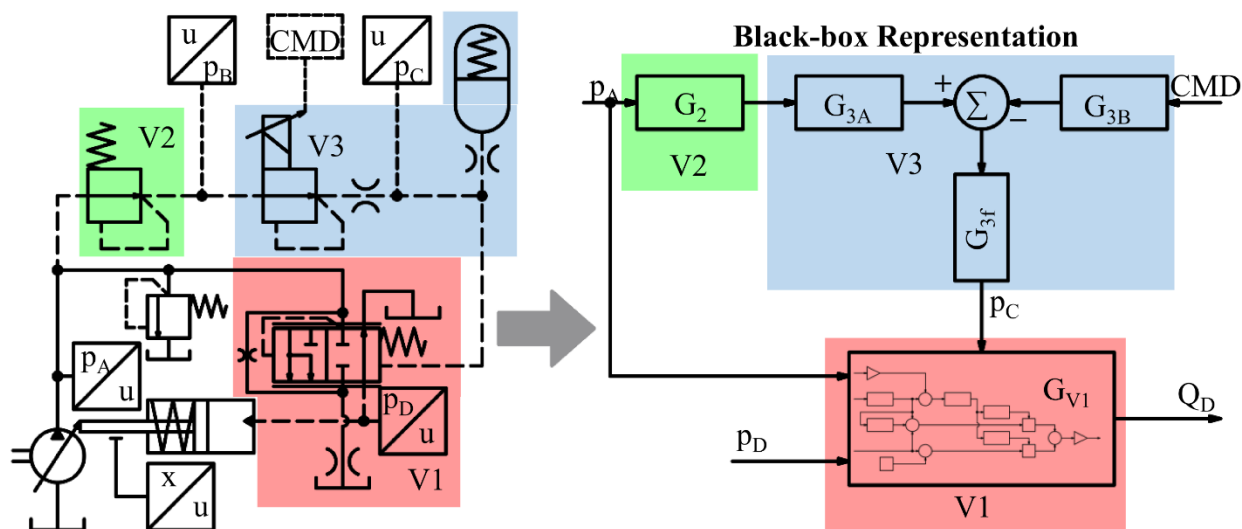


Figure 57: Overview of the black-box representation of the case study control system.

Figure 57 depicts the overall model structure for this black-box representation of the case study valve block. As Figure 57 indicates, the components of the valve block were grouped into three primary subsystems corresponding to the three valves. The first, and simplest, of these is the V2 subsystem which represents the pressure reducing valve V2 with a transfer function based on the generic transfer function given by Equation (7.1) that is discussed in Section 7.1.

$$G = \frac{K\omega_n^2}{s^2 + 2\zeta\omega_n s + \omega_n^2} \quad (7.1)$$

The second subsystem in Figure 57 is the V3 subsystem representing the solenoid valve V3, the spring loaded accumulator, and the regulation setting pilot line (Line C) dynamics. Because the solenoid valve takes in two inputs, p_B and CMD , separate transfer functions are utilized. In this way, one transfer function represents the electromechanical dynamics of V3 while the other represents the hydromechanical dynamics of the valve. The sum of the output signals of these two transfer functions are then passed through a filter representing the pilot line dynamics. This subsystem is also based on the generic second-order transfer function given by Equation (7.1) and is the subject of Section 7.2.

The final subsystem in Figure 57 is the V1 subsystem representing the dynamics of the regulation valve V1. This subsystem differs from the other two in that it represents the input-output relationship between three pressures (Line A, Line C, and the Line D feedback pressure) and the flow Q_D through the valve into Line D. While the structure of this representation is given by Figure 65 and discussed in Section 7.3, it can be conceptualized as a single three-input-single-output transfer function as depicted in Figure 57.

This chapter concludes with a performance analysis using the composite black-box representation of the valve block achieved by the interconnection of these three subsystems as shown in the right-hand side of Figure 57.

Measurements used to develop and test each subsystem were collected on the experimental setup described in Chapter 4 using Circuit 1 in APPENDIX A (see also Figure 20). Additional measurements were collected using Circuit 3 with the pump outlet blocked using a custom plug described by Drawing 26 in APPENDIX B and the Line A pressure was supplied by the external source used in the stator dynamics validation measurements collected with Circuit 2.

To distinguish between these two circuits, Circuit 1 and Circuit 3, throughout this chapter, measurements will be identified as data collected with the “pump on” or the “pump off”,

respectively. “Pump off” data was primarily used to double check the dynamics and refine the structure of the black-box representation. The final model, however, was tuned to give a better agreement with the more relevant “pump on” data. While not perfect, this approach has yielded various valuable insights.

7.1 V2 Representation

The starting point for the V2 representation was the 3D CAD model of the valve provided with the case study materials. This revealed that the pressure reducing valve V2 is a spool valve by design and should thus have second-order dynamics dictated by the spool’s inertia, some viscous friction, and the spring rate of the valve spring. Based on the spool’s inertia and the nominal spring rate on the data sheet, the natural frequency of the valve is close to 76Hz.

This nominal natural frequency was used as ω_n in Equation (7.1) with a value of 0.6 for ζ to generate the base dynamics of the transfer function G_2 given by Equation (7.2).

$$G_2 = \frac{K_2(2.28027 \times 10^5)}{s^2 + 573.026s + (2.28027 \times 10^5)} \quad (7.2)$$

Comparing the output of G_2 , for a unity steady-state gain K , and the measured Line B pressure p_B when the measured Line A pressure p_A was used as the input revealed that these dynamics gave a good agreement in terms of the frequency content and signal to noise ratio. Matching the mean values, however, required a non-unity steady-state gain for higher p_A .

Since pressure reducing valves typically maintain a near constant down-stream pressure, which for this value was determined to be about 10bar, the steady-state gain K_2 was represented as a function of p_A and is shown in Figure 58. The decreasing gain value simulates the ratio of the reduction in pressure from Line A to 10bar in Line B when Line A is above 10bar.

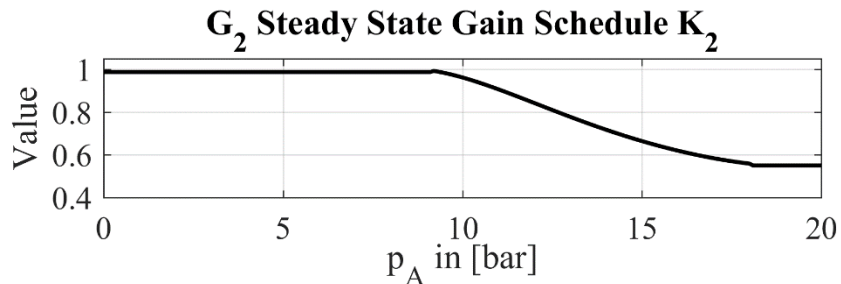


Figure 58: Transfer function G_2 steady state gain schedule.

Using Equation (7.2) with the gain schedule for K_2 given by Figure 58 gives the simulated p_B in Figure 59 along with the measured p_B to show the validity of this model.

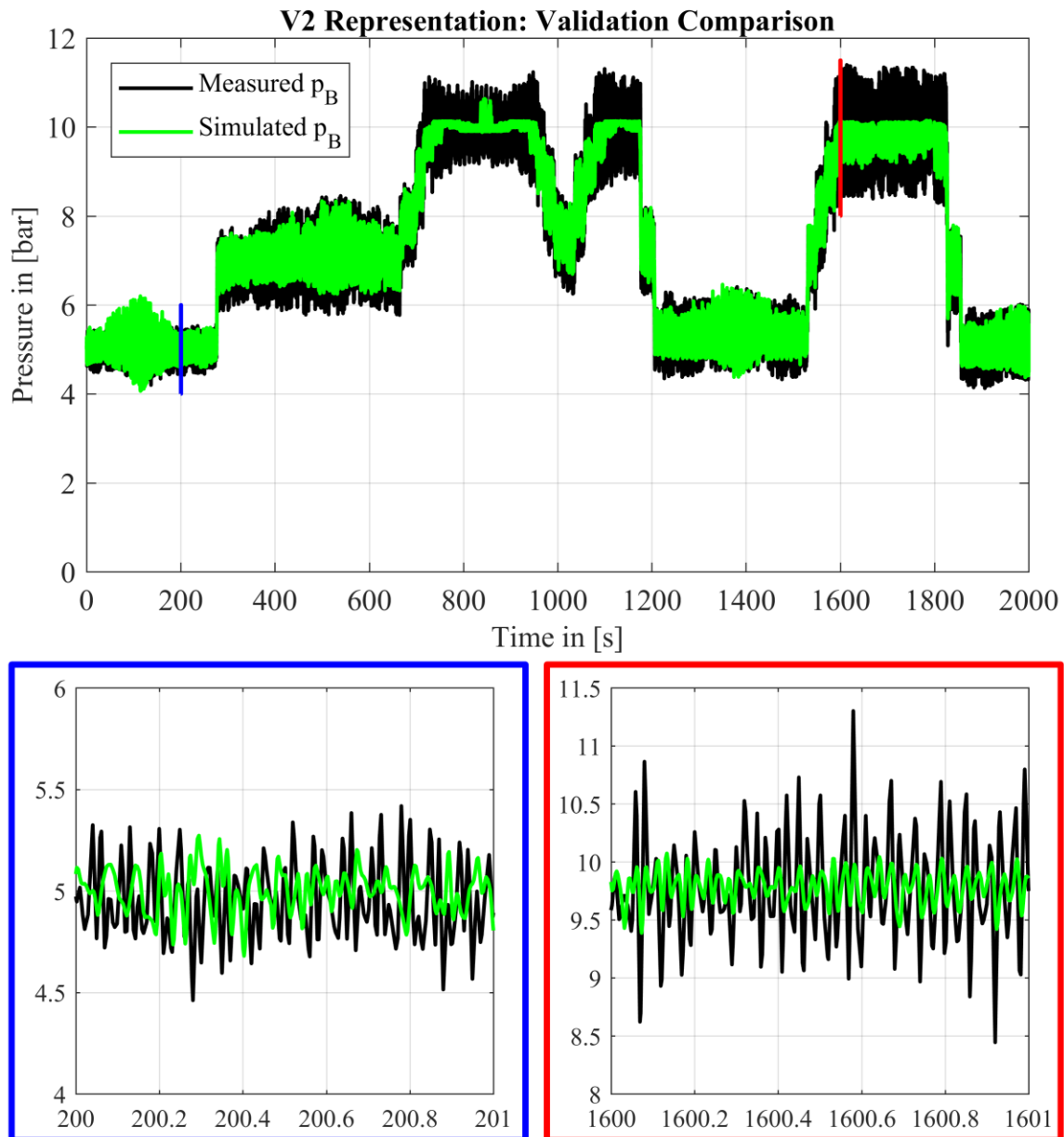


Figure 59: Validation results for the transfer function G_2 with “pump on” data.

As Figure 59 indicates, the model is representative of the overall trends and the quality of the measured pilot pressure in Line B. Additional comparisons using “pump off” data revealed a similar quality of agreement. Therefore, the model comprised of Equation (7.2) and Figure 58, while simple, provides a good, representative estimation of the dynamics of the valve V2 and is sufficient for a performance analysis.

7.2 V3 Representation

As Figure 57 indicates, the solenoid valve V3 and its associated subsystem is represented by the three transfer functions which are given below by Equations (7.3) through (7.5).

$$G_{3A} = \frac{K_{3A}(2.2207 \times 10^5)}{s^2 + 659.7339s + (2.2207 \times 10^5)} \quad (7.3)$$

$$G_{3B} = e^{-0.03s} \frac{K_{3B}(246.7397)}{s^2 + 28.2743s + (246.7397)} \quad (7.4)$$

$$G_{3f} = \frac{94.2478}{s + 94.2478} \quad (7.5)$$

As the simplified model presented for G_2 is a logical representation of a pressure reducing valve, it was the starting point for the hydromechanical component of V3 described by G_{3A} in Equation (7.3). Initial comparisons between simulation and measurement, however, indicated that an ω_n of 75Hz with a ζ of 0.7 resulted in better matching. As was the case with G_2 , the steady state gain varies as a function of the input p_B and is given by the K_{3A} schedule depicted in Figure 60.

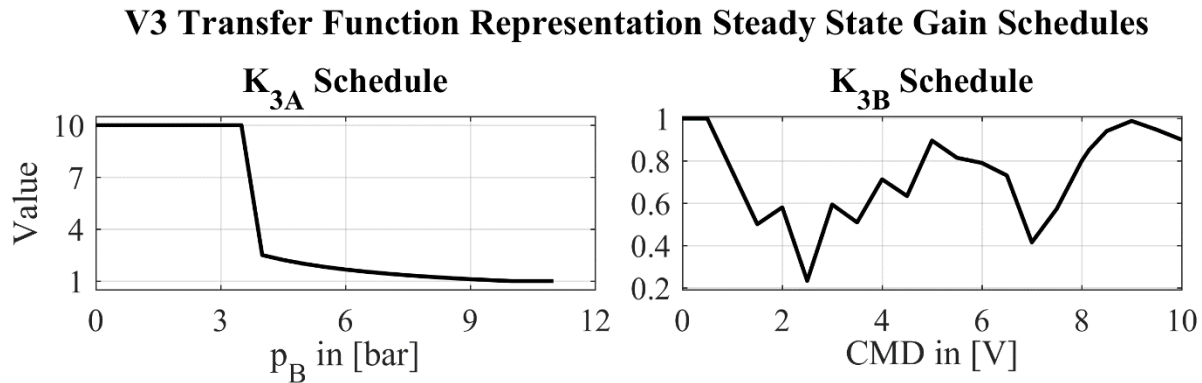


Figure 60: Steady state gain schedules for transfer functions G_{3A} and G_{3B} .

The second transfer function, G_{3B} , represents the electromechanical dynamics of the solenoid and their effect on the Line C pilot pressure signal. These dynamics, contained in Equation (7.4), are characterized by an ω_n of 2.5Hz, a ζ of 0.9, and a pure time delay of 30ms. Furthermore, the steady state gain schedule for K_{3B} given in Figure 60 was required to match the mean values of the pressure. These parameters are the result of extensive comparisons between measured data and simulations using the structure outlined in Figure 57. This study indicated that the time delay was required to match the phase of the measured data.

Essentially, G_{3A} gives the starting point for the mean value of p_C and G_{3B} gives the reduction from this “maximum” based on the electrical command CMD . Additionally, the time delay in G_{3B} approximates the net effect of the conversion from a CMD in volts to a proportional current signal via the valve driver. Together, these two transfer functions give a representative p_C profile when measured p_B and CMD profiles are used as inputs. The noise content of this simulated p_C profile is improved by the additional filter G_{3f} given by Equation (7.5) representing the pilot line dynamics. Figure 61 provides an example validation comparison.

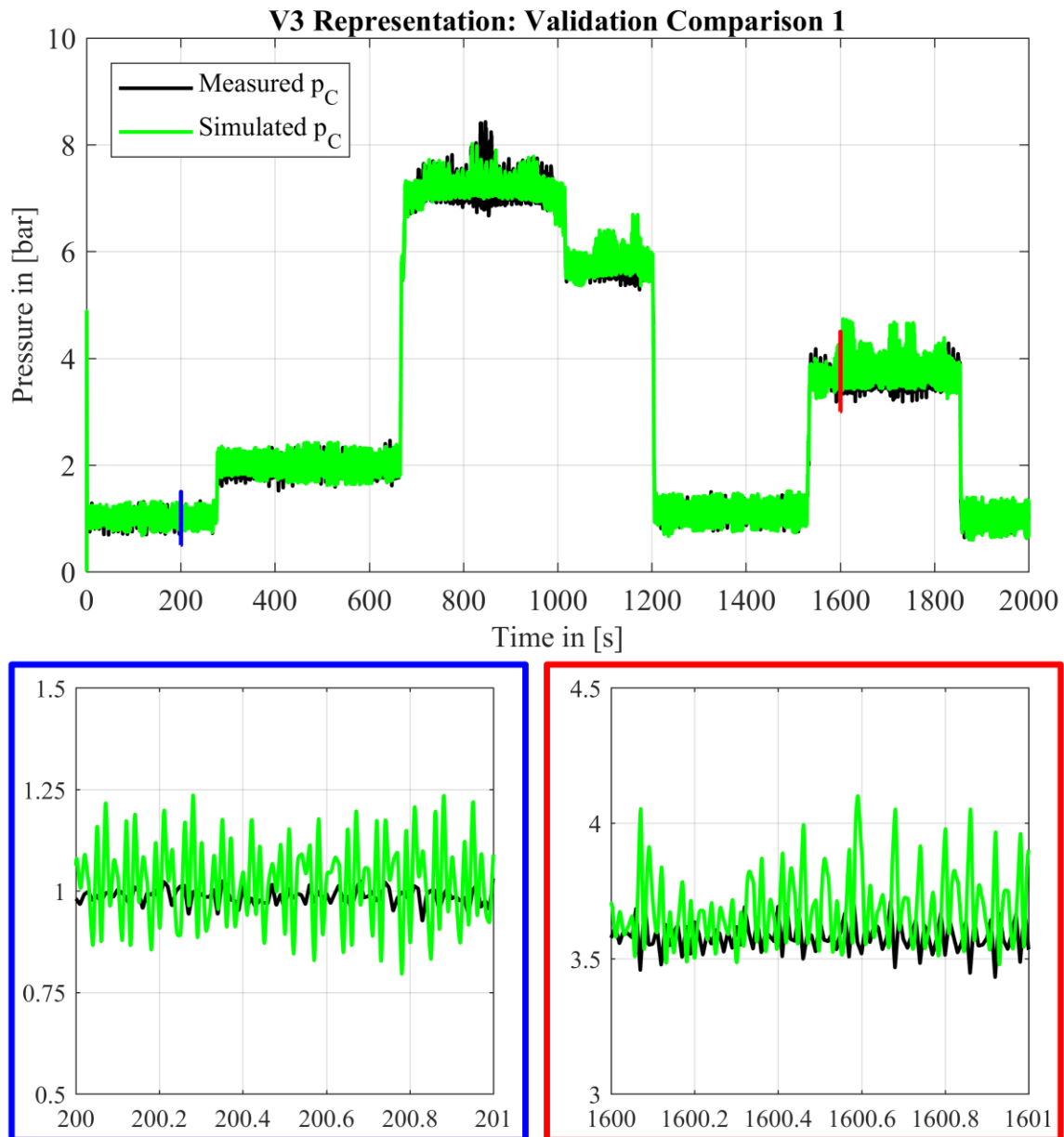


Figure 61: “Pump on” validation results for the transfer function representation of V3.

While Figure 61 shows good model agreement for a “pump on” case, Figure 62 and Figure 63 show that the model represented by Equations (7.3) through (7.5) and Figure 60 does not agree as well with “pump off” data. This is likely due to undefined coupling between p_C and p_A , and somewhat p_D , through the regulator valve V1. Nevertheless, these figures clarify that the selected dynamics are valid and the influence of any potential coupling effects are assumed to be negligible, especially in light of the good agreement shown for the “pump on” case.

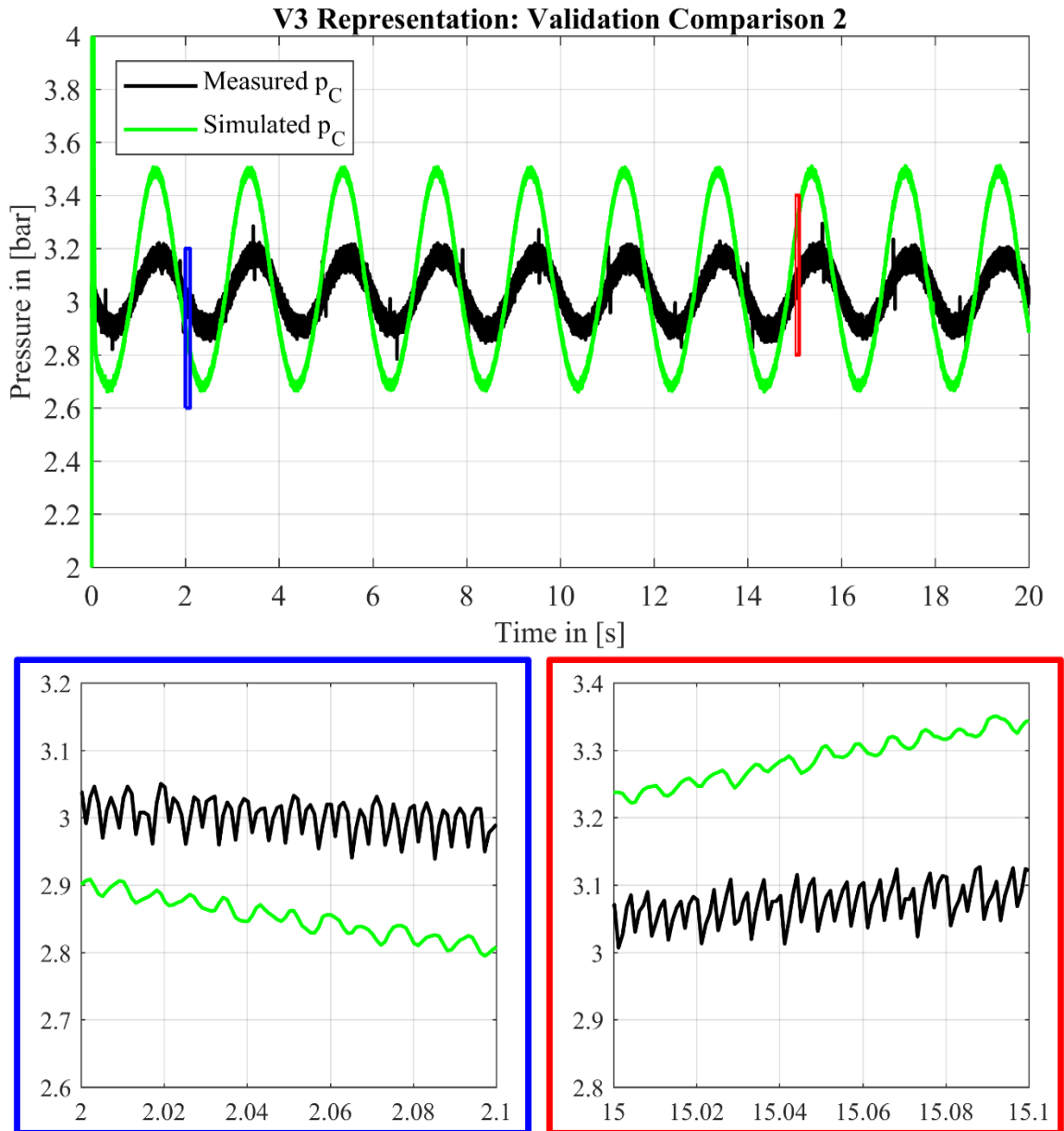


Figure 62: “Pump off” validation results for the transfer function representation of V3 for a large amplitude 0.5Hz sinusoidal command profile.

The agreement in Figure 62 can be drastically improved by essentially scaling the steady state gains presented in Figure 60 to those shown in Figure 64 (58% for K_{3A} and 40% for K_{3B}) as Figure 63 indicates. This result further strengthens the claim that the relevant dynamics are captured by Equations (7.3) through (7.5). This model can therefore be taken as representative of the case study components to a reasonable degree of accuracy for a performance analysis even though this model is still an approximation and should be interpreted in that light.

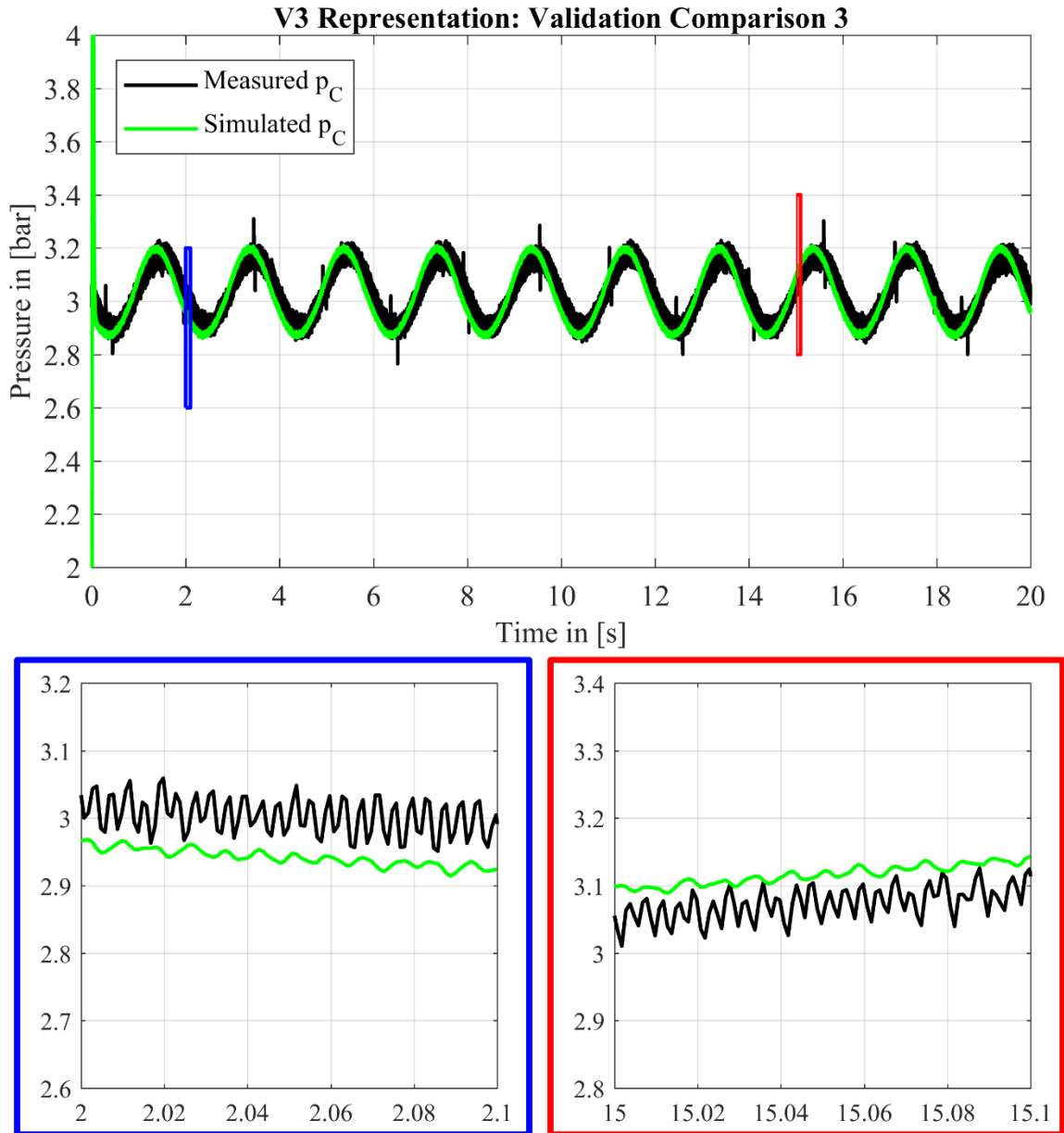


Figure 63: “Pump off” validation results for the transfer function representation of V3 for a large amplitude 0.5Hz sinusoidal command profile with the “pump off” gain schedules.

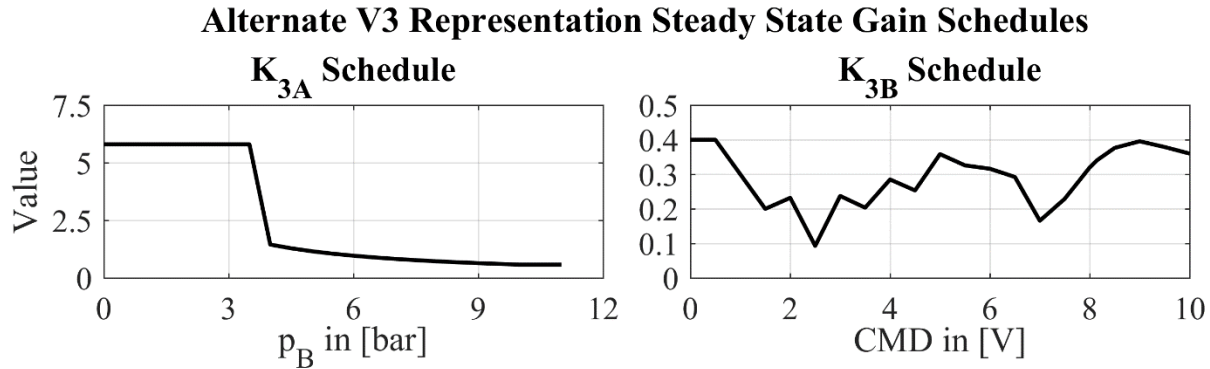


Figure 64: Alternate gain schedules for the V3 representation in “pump off” cases.

For example, although an ω_n of 2.5Hz is used in Equation (7.4) and throughout this study, an analysis of the measurements taken using Circuit 3 representing various sinusoidal commands of differing frequencies and amplitudes indicated that the overall bandwidth of V3 from CMD to p_C may be closer to 1.5Hz. This value is higher than the damped natural frequency of G_{3B} equal to 1.09Hz. This is most likely due to nonlinear effects, the impact of the valve driver dynamics, and the specifics of the dithering in CMD . Variable bleed solenoid (VBS) valves such as V3 have been shown to exhibit nonlinear effects such as hysteresis in addition to other variations in performance due to fluctuations in temperature [5].

Even with these neglected nonlinearities, the model presented in this section can provide insights into the general impact of V3 on the control system performance as a whole because it does contain representative dynamics. In studies available in the literature, others have used system identification techniques to characterize solenoid valves for automatic transmissions similar to V3 [57] [58]. These studies report ω_n nearly four times higher for the electromechanical dynamics than what is used here for similar values of ζ (0.93-0.98). One reason for this discrepancy arises from the fact that none of the internal feedback within the valve is included in the model presented here. According to [57], this internal feedback improves the bandwidth of the valve. Differences in the valve sizes, and thus the component masses, also contributes to the discrepancy. Finally, the ISO 32 hydraulic oil used in the experimental measurements for this chapter has a dynamic viscosity nearly half of the value reported for ATF in [6] at the same temperature. Regardless of the reasons and even considering the higher ω_n available in the literature, its low bandwidth makes the solenoid valve V3 the limiting component of the case study control system as will be shown in more detail later.

One final point regarding the V3 representation as an approximation has to do with hardware limitations of the experimental setup. In the real automatic transmission, the solenoid valve V3 is driven with a current signal possessing very specific dithering characteristics. Due to the limitations of available valve drivers, these dithering characteristics were not reproduced exactly. While this may seem like a small matter, this difference in the electrical command signal results in a different solenoid performance in the laboratory experiments than the true performance in the case study transmission. When optimized, dynamic driving signals for electromechanical control valves can reduce hysteresis and improve dynamic behavior [66].

The heuristic model presented in this section is then the best representation of the V3 subsystem in a laboratory environment and may not accurately represent the dynamic performance of the subsystem onboard a vehicle. Fortunately, this difference should be slight and the model is still a useful characterization. In this regard, the goal stated in Section 1.4 of identifying the source of performance limitations can be achieved so that the first step can be taken in the development of advanced pressure compensation control systems.

7.3 V1 Representation

The structure of the black-box representation of the V1 subsystem is given by Figure 65.

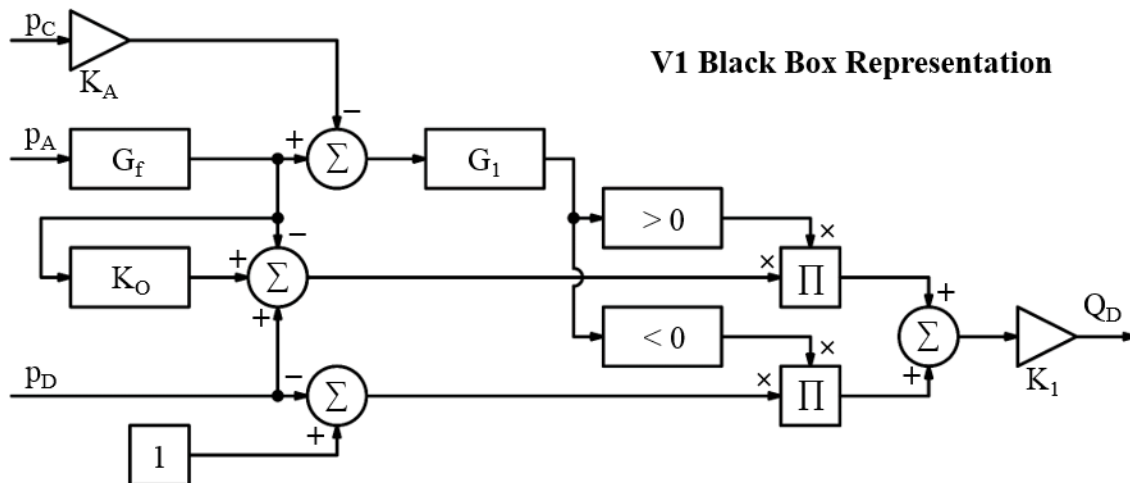


Figure 65: Block diagram description of the black-box representation of V1.

As this block diagram indicates, the model switches dynamically between two differential pressures as the input to a constant flow gain K_1 . In this way, the dynamics of the spool and valve spring are captured in the transfer function G_1 and recreate the force balance acting on the

spool. Therefore, the gain K_A represents the pilot area ratio between the surfaces exposed to the pilot pressure p_C and the line pressure hydraulically fed back to the other side of the spool and simulated by a filtered p_A . The initial dynamics for G_1 and the value for K_A were estimated from the 3D CAD model and the data sheet for the regulator valve spring and then adjusted using the measured data.

In order to perform this characterization of the V1 subsystem, however, the flow Q_D through the valve is required. Since this flow was not measured on the test rig, this signal was reconstructed from the measurements of p_D and β and the leakage model presented in Section 6.5. The basis of this reconstruction is the control chamber's pressure build-up equation given by Equation (6.8). If the differential form of Equation (6.8) is solved for Q_D as in Equation (7.6), the reconstruction is straightforward using the measured signals and their numerical derivatives.

$$Q_D \cong \frac{V_D}{K_{mix}} \frac{dp_D}{dt} + Q_{SE,D} + \frac{\partial V_D}{\partial \beta} \frac{d\beta}{dt} \quad (7.6)$$

Although imperfect, Equation (7.6) still provides a fairly accurate “measurement” of Q_D that can be used with the measured data for p_A , p_C , and p_D to tune the various gains and transfer functions that make up this V1 representation. This procedure results in the transfer functions given by Equations (7.7) and (7.8).

The first of these, G_f , represents a first-order low-pass filter with a 50Hz break frequency. The second, G_1 , starts with the estimated valve dynamics characterized by a natural frequency of 70Hz and a low damping ratio of 0.05, but includes an additional fast pole equivalent to a first-order low-pass filter with a 150Hz break frequency. This low damping ratio and additional fast pole showed good agreement for many measurement cases.

$$G_f = \frac{314.159}{s + 314.159} \quad (7.7)$$

$$G_1 = \frac{(1.823 \times 10^8)}{s^3 + 986.5s^2 + (2.349 \times 10^5)s + (1.823 \times 10^8)} \quad (7.8)$$

$$Q_D = K_1 \left[\frac{1 + \tanh(10G_1\{G_f\{p_A\} - K_A p_C\})}{2} (K_O\{p_A\} + p_D - G_f\{p_A\}) + \frac{1 - \tanh(10G_1\{G_f\{p_A\} - K_A p_C\})}{2} (p_D - 1) \right] \quad (7.9)$$

Using these transfer functions and values of 2.819 and 0.114 for K_A and K_1 , respectively, the flow Q_D can then be represented by Equation (7.9), where the offset K_O is given by Figure 66. The use of hyperbolic tangent constructions in lieu of the Boolean “greater than” and “less than” operators results in better numerical conditioning and more favorable solver conditions in the model by removing discontinuities.

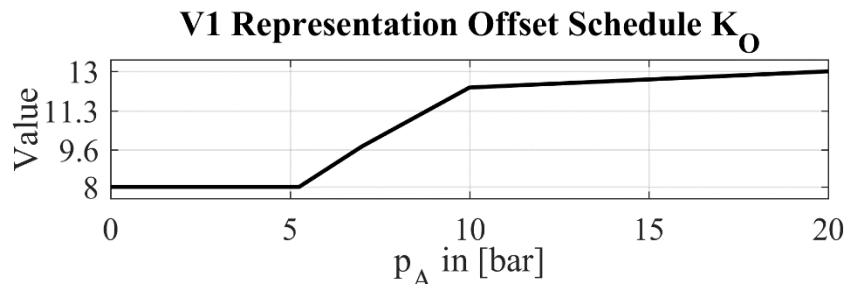


Figure 66: Offset value schedule used in V1 representation.

Figure 67 provides a comparison of this V1 representation and the “measured” Q_D for the same “pump on” case presented in Sections 7.1 and 7.2. As Figure 67 indicates, this model captures the trends of the “measured” flow fairly well with the primary discrepancies being in the high-frequency content. This is expected because the “measured” Q_D was generated using numerical derivatives which tend to amplify measurement noise. Nevertheless, higher-order numerical derivative formulas were used to reduce any noise amplification as much as possible and to provide a more accurate derivative for the “measurement”.

While the trends are captured well, the detail views in Figure 67 show that the mean values are slightly off. While additional tuning could bring the model into closer agreement, this discrepancy can also be attributed to inaccuracies in the leakage flow model given by Equation (6.14) and the fact that Equation (6.8) neglects external leakage sources other than the pivot pin groove. Furthermore, the “measured” Q_D used here contains multiple sources of measurement error were not quantified. The agreement is therefore deemed sufficient and representative.

As the detail view on the right-hand side of Figure 67 shows, even with the improved numerical conditioning provided by the continuous hyperbolic tangent constructions, the model exhibits some instabilities. This is largely due to the switching aspect of Equation (7.9) which results in discontinuities. The effect of these discontinuities is amplified between 1600-1800s due to the pressure levels in p_A and p_C resulting in a hyperbolic tangent argument near zero. This effect might be reduced with a different solver routine or controlled step sizes.

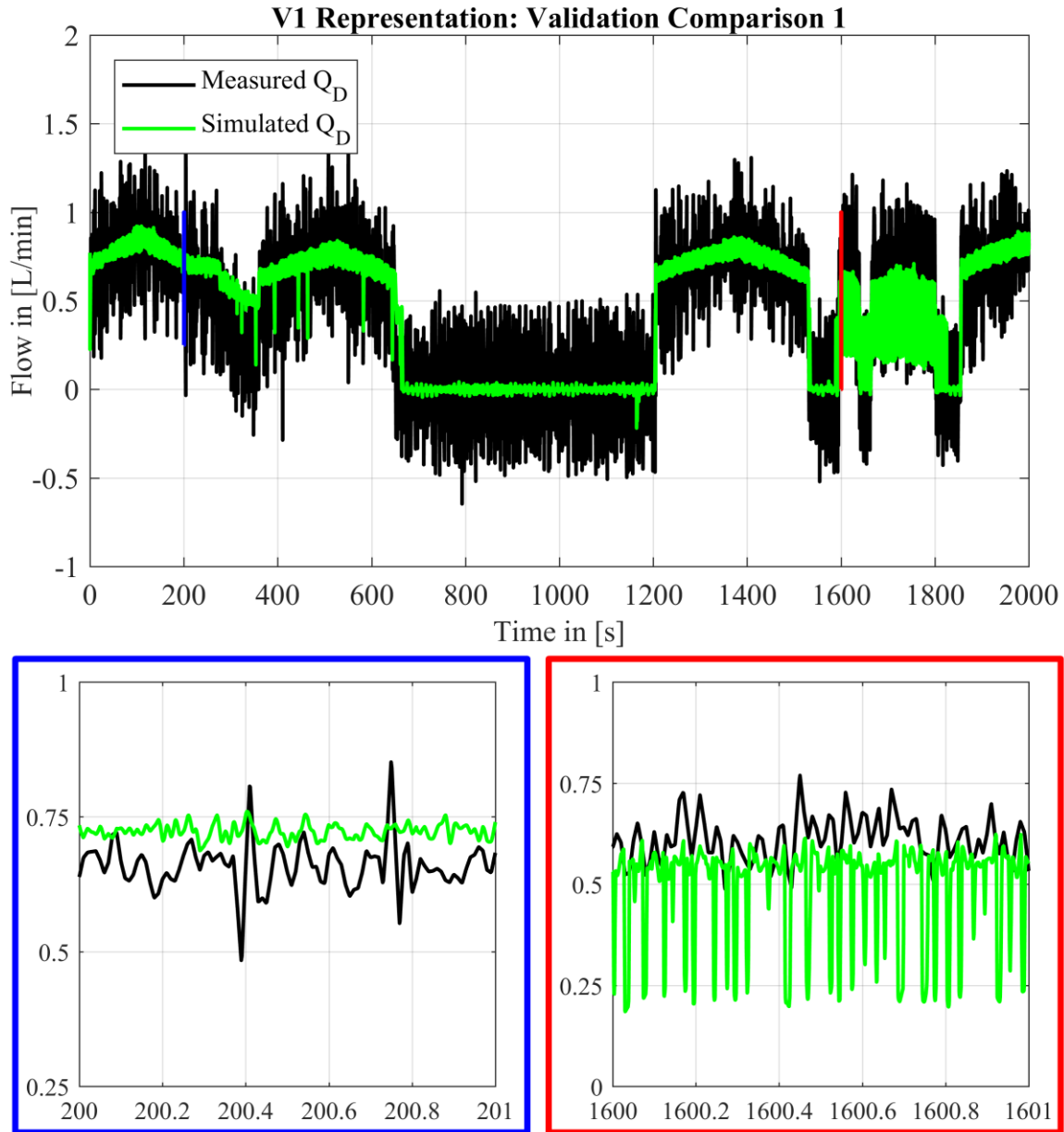


Figure 67: “Pump on” validation results for the V1 representation.

Nevertheless, as both Figure 67 and Figure 68 show, the model is still representative of the switching dynamics of the regulator valve. Furthermore, as was the case with the V3 representation, the gains and offset schedule presented earlier in this section provide a better agreement with the “pump on” than with the “pump off”, as illustrated by Figure 68. Therefore, Figure 68 is primarily intended to serve as an additional verification that the switching dynamics of the valve are captured by G_1 when given by Equation (7.8).

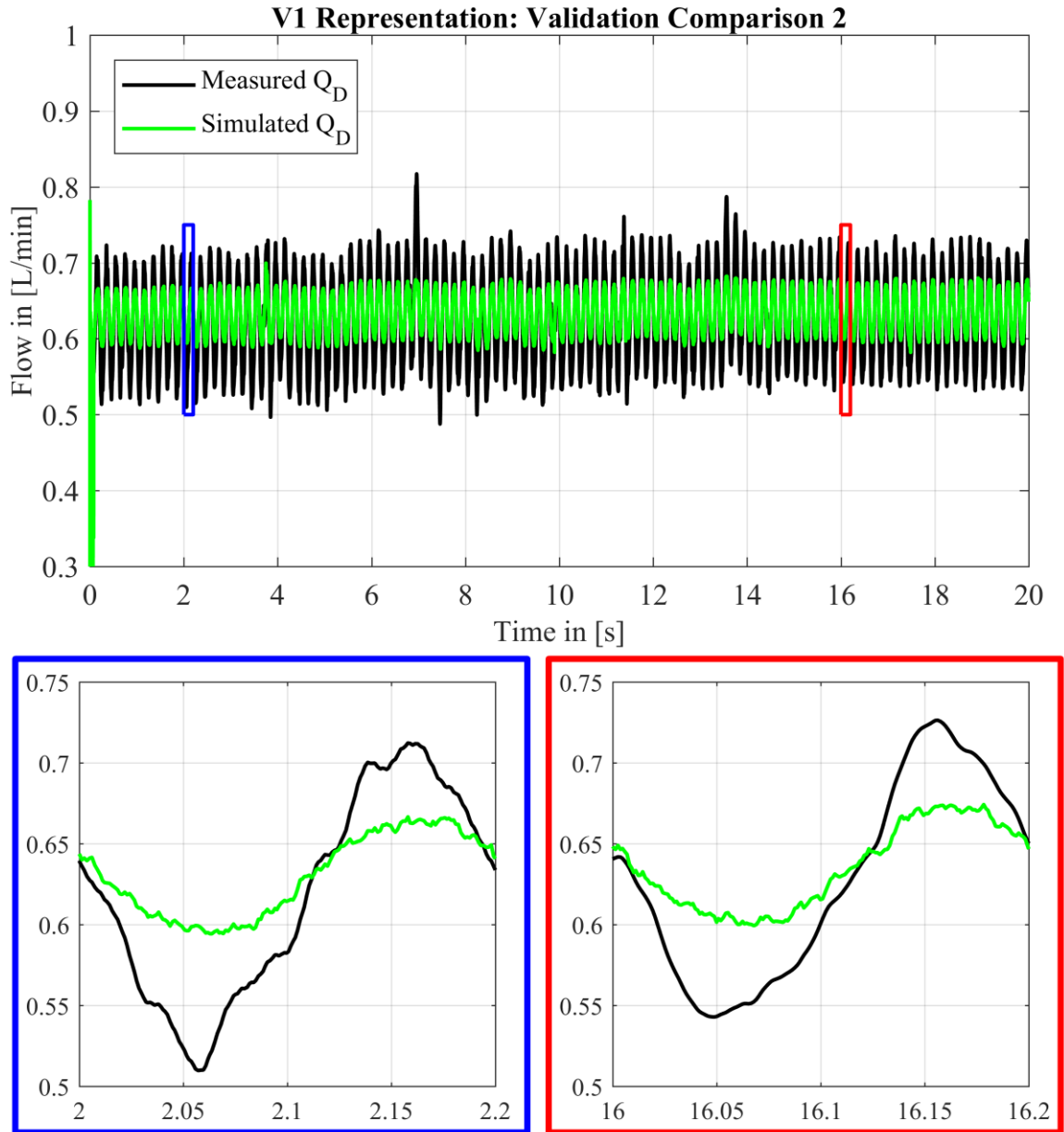


Figure 68: “Pump off” validation results for the V1 representation at 10bar and small amplitude 5Hz sinusoidal command profile.

7.4 Performance Analysis

While the actual Q_D depends on the differential pressure across the valve V1 and the flow gain K_1 , the control chamber pressure dynamics, and thus the differential pressure, has a strong dependence on the stator motion. Thus, analyzing the V1 switching dynamics gives a feeling for both the extent to which the control system can affect p_D and how quickly. This is the rationale

behind the overall model reduction depicted in Figure 57 to arrive at a series of LTI TF for an analysis of the control system performance. The first step in this reduction is to “break” the block diagram for the V1 representation depicted in Figure 65 at the output of G_1 and apply the flow gain K_1 to give the approximation contained in the red box in Figure 69.

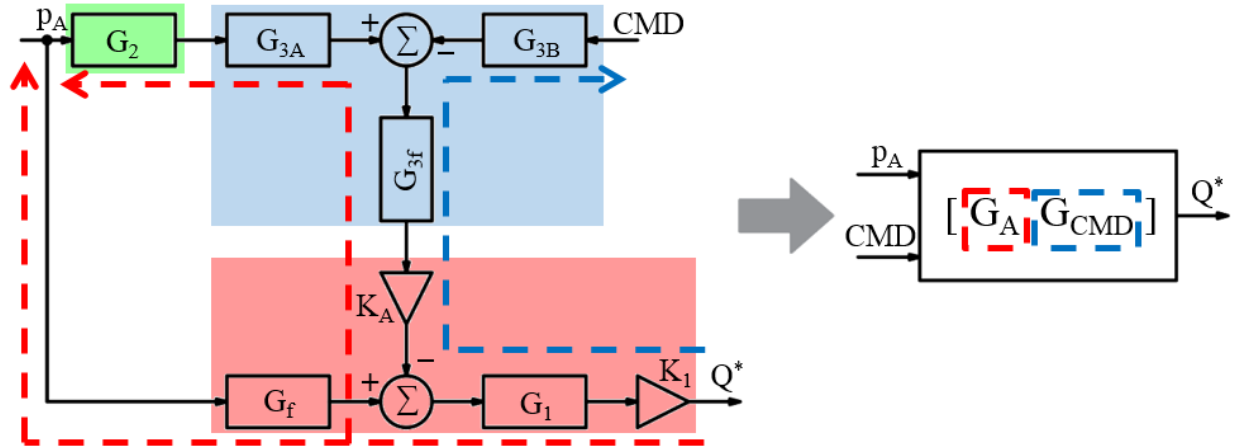


Figure 69: Block diagram reduction of the case study control system black-box model for performance analysis purposes.

Figure 69 illustrates how this approximation of V1 can be used along with the representations of V2 and V3 to reduce the case study control system to a single two-input-single-output transfer function matrix. This transfer function matrix G_{sys} is given by Equation (7.10) and relates the pump outlet pressure p_A and the solenoid command signal CMD to the effective flow gain Q^* . The two elements of G_{sys} , G_A and G_{CMD} , are given by Equations (7.11) and (7.12) and represent the input-output relationships between Q^* and p_A or CMD , respectively.

$$G_{sys} = [G_A \quad G_{CMD}] \quad (7.10)$$

$$G_A = K_1 G_1 (G_f - K_A G_{3f} G_{3A} G_2) \quad (7.11)$$

$$G_{CMD} = K_1 K_A G_1 G_{3f} G_{3B} \quad (7.12)$$

This G_A then contains the K_2 and K_{3A} gain schedules as well as the low damping of G_1 . The control system architecture, represented by the difference contained in Equation (7.11), results in a non-minimum phase zero in the G_A transfer function. These two characteristics are illustrated in the Bode diagram for this element of G_{sys} shown on the left-hand side of Figure 70 and the pole-zero map of G_A in Figure 71.

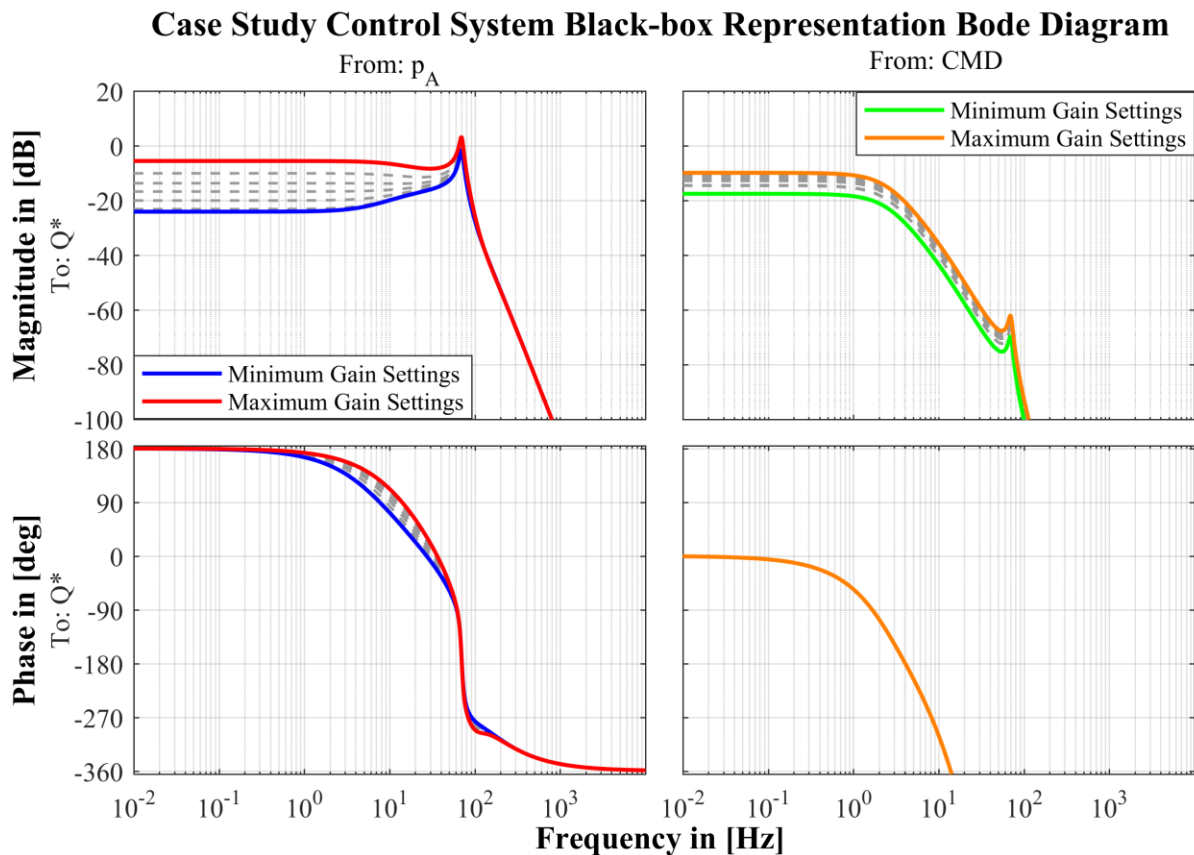


Figure 70: Bode diagram of the case study control system representation.

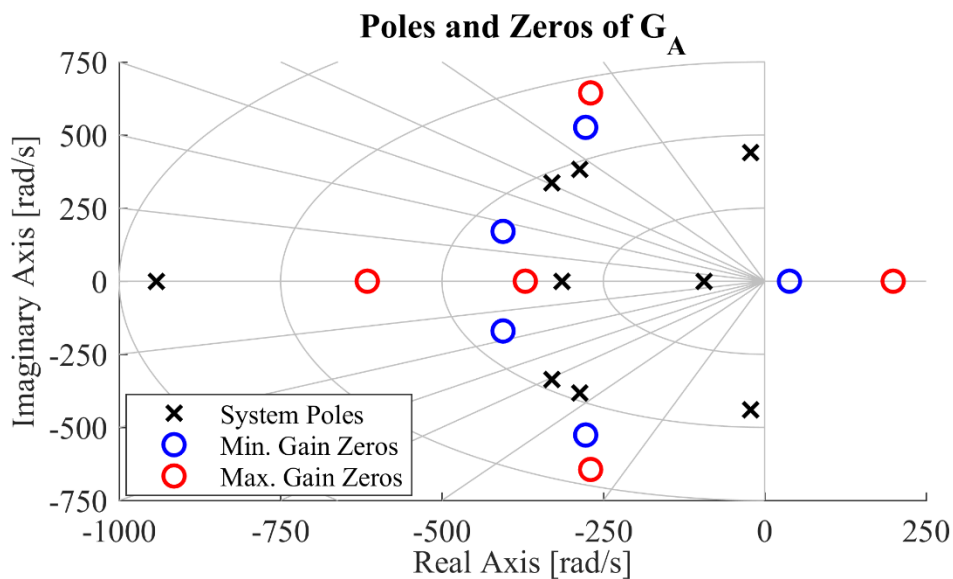


Figure 71: Map of the poles and zeros of G_A in the complex plane.

The right-hand side of Figure 70 illustrates that G_{CMD} , on the other hand, retains all of the dynamics of G_{3B} with their accompanying limitations in addition to the effects of the low

damping in G_1 as evidenced by the resonance peak at 70Hz. While the effect of this resonance in G_{CMD} is minimal, its effect in G_A is such that any frequency content of p_A in the band between 17.6Hz and 84.4Hz is amplified by at least a factor of two over the steady state gain value (with the minimum gain settings for K_2 and K_{3A}) in the effective flow gain. This can be a destabilizing effect as frequency content is transmitted through the pump because G_A is unstable (negative phase margin) at 72.8Hz for the maximum gain settings and the resonance band shrinks to include frequencies between 65.6Hz and 72.5Hz.

Figure 72 illustrates several of the critical frequencies for the pump model, including the first ten harmonic frequencies of the shaft. Pressure ripples at the outlet of the pump typically correspond to the second harmonic frequency of the shaft. In this case, the frequency of these ripples varies between 117Hz and 1283Hz as the engine speed increases. Since these frequencies are always higher than the upper limit of the G_A resonance band, they do not present a large concern as a source of instabilities. However, frequency content in p_A arising from the load dynamics imposed by either the transmission clutches or by the torque converter can lie in this resonance band. These oscillations would then be amplified by G_A and could potentially result in a degradation of the system performance.

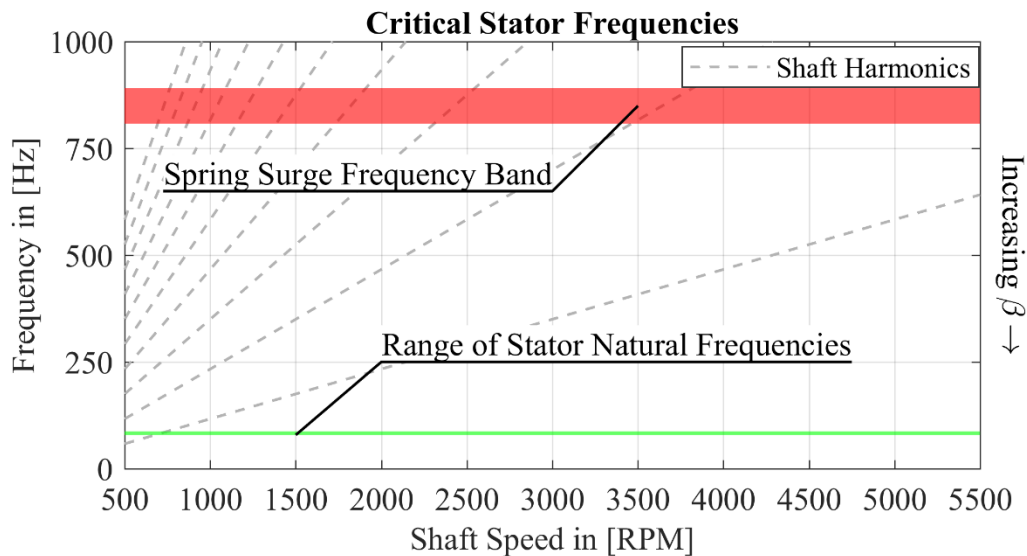


Figure 72: Critical frequencies for the adjustment system dynamics model.

Figure 72 also reveals how this performance degradation may occur. The green band in the lower half of Figure 72 represents the range of stator natural frequencies between 79Hz and 87Hz that is a result of the nonlinear bias spring model presented in Section 6.3 and falls within

the upper portion of the G_A resonance band. For the typically high damping due to friction, the stator dynamics are not particularly sensitive to these excitation frequencies. Nevertheless, for some operating temperatures the friction may be reduced to the point that the stator equation of motion represented by Equation (6.1) can become slightly underdamped. In this scenario, the damped natural frequencies still fall in the resonance band for the maximum gain settings (assuming a damping ratio as low as 0.95). This sensitivity at certain operating temperatures, or even for the different fluid properties associated with a working fluid different from the ISO 32 oil used in this dissertation, can result in an undesirable feedback effect as the stator transmits these frequencies to the rest of the pump and ultimately back into the transmission lines.

The Bode diagram in Figure 70 also illustrates that the overall bandwidth of the case study control system from the solenoid command CMD to the effective flow gain Q^* is predicted to be 1.84Hz, regardless of the gain settings. This bandwidth is defined here as the frequency corresponding to a 3dB drop in the magnitude response from the steady state gain. However, the transfer function G_{CMD} does have a gain margin of approximately 10.5 or greater at a frequency of 4.1Hz, which indicates that with an appropriate control law the bandwidth may be pushed higher. Fortunately, G_{CMD} is generally stable (i.e. has an infinite phase margin) for the range of gains depicted in Figure 70. Nevertheless, in the best case scenario the bandwidth would still be below 5Hz. Developing the control law that pushes the bandwidth toward a maximum, however, is difficult with classical controller designs in light of the pure time delay. This reiterates the point made in Section 7.2 that V3 is the limiting component in the case study control system.

For comparison, the minimum bandwidth of the pump adjustment system, as described in Chapter 6, is around 30Hz while the minimum bandwidth of G_A can be taken as 70Hz, neglecting instabilities due to resonance effects. Thus, the bandwidth of G_{CMD} is roughly a decade lower than the next most restrictive bandwidth. Exchanging the low-cost solenoid valve currently implemented for a higher quality or more advanced solenoid valve would marginally alleviate this issue but not eliminate it. In fact, borrowing the valve dynamics reported in [58] for the electromechanical dynamics contained in G_{3B} results in a hypothetical system with a final bandwidth of 6.31Hz and a gain margin of 5 or more at a frequency of 7.3Hz. Thus, even with improved electromechanical dynamics of the VBS valve, it remains the limiting factor.

Because the limitations to the system performance are so closely tied to the V3 subsystem, which ultimately determines the pilot line pressure dynamics, and p_C acts on the

regulation valve spool, the actual stability of the control system may be closer to the stability of the spool valve and governed by G_A .

Furthermore, because Q_D depends on both Q^* and the differential pressure across the valve, and because the control chamber pressure dynamics will be stiff due to the incompressibility of the hydraulic oil, the actual response time of the pressure compensated VDVP to changes in the regulation set point should only be limited to the 190ms rise time associated with the 1.84Hz bandwidth as long as the system pressure remains sufficiently high. This rise time t_r is calculated using Equations (7.13) and (7.14) from classical linear control theory where f_{BW} refers to the bandwidth frequency and τ_r is a time constant.

Equation (7.14) here is derived from the solution of a first order ordinary differential equation with a time constant τ_r and is reached by evaluating the resulting exponential to find the time elapsed between when the response reaches 10% and 90% of its steady-state value. While the actual response of the case study system is not first order, it is close to first order in appearance. This point is validated by reviewing a typical duty cycle such as the one depicted in Figure 5 and evaluating the rise time of the system in its native environment. Figure 73 provides such a comparison. Because of this similarity to a first order response, Equation (7.14) is an acceptable approximation for a quick comparison and avoids more complicated analyses.

$$\tau_r = \frac{1}{2\pi f_{BW}} \quad (7.13)$$

$$t_r = \ln(9) \tau_r \quad (7.14)$$

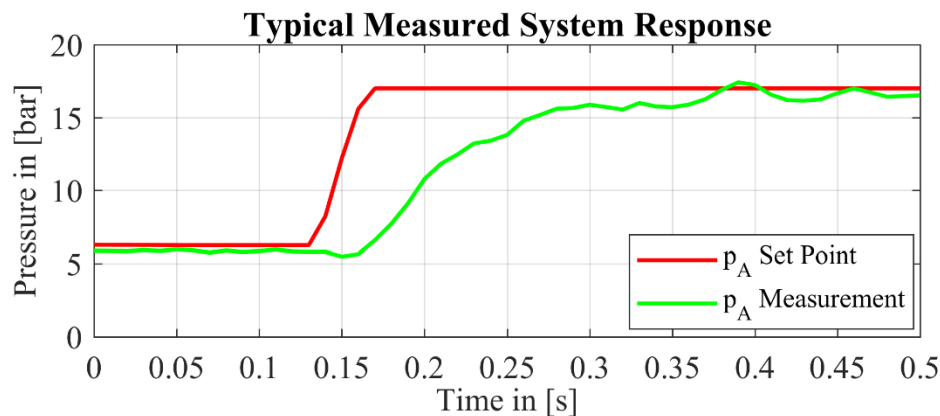


Figure 73: Typical system response to a change in regulation set point taken from vehicle measurements in the case study materials.

As Figure 73 reveals, the system exhibits a 10% to 90% rise time of 190ms and a time delay of approximately 40ms to what is essentially a step change in the regulation set point. Thus, the model presented in this chapter appears to accurately describe the performance of the case study control system. Furthermore, the matching of the approximate rise time calculated using Equations (7.13) and (7.14) indicate that the dominant dynamics are approximately first order in nature.

Another potential performance limitation illustrated by Figure 72 is the approximate range of the neglected bias spring dynamics. These neglected dynamics correspond to critical excitation frequencies f_{cr} where spring surge may occur and the bias spring may temporarily “jump” off of its lands. This behavior would result in nonlinearities in the bias spring force as well as impact forces on the stator. Both of these are clearly undesirable effects.

An approximate range of these critical frequencies can be calculated using Equation (7.15) (taken from [64]) and is between 808Hz and 892Hz. This is only an approximate range, however, as the formula contained in Equation (7.15) is for a helical compression spring between two parallel surfaces and the bias spring in the case study pump does not meet this criterion. Nevertheless, as Figure 72 illustrates, various shaft harmonic frequencies enter this range.

$$f_{cr} = \frac{1}{\pi d_s} \sqrt{\frac{k}{D_s N_a \rho_{steel}}} \quad (7.15)$$

While the primary frequency content of the internal pressure forces acting on the stator is with the second harmonic frequency of the shaft, the higher order harmonics are not negligible. These higher harmonics can be transmitted to the bias spring through these pressure forces as well as through mechanical vibrations originating in the shaft bearings. It is therefore conceivable that the bias spring would experience excitation forces in this frequency band and negatively affect the stator dynamics. Further research would be required to evaluate the severity and true nature of these effects. For this dissertation, these effects are assumed to be negligible on the grounds that they occur at frequencies roughly 27 times higher than the stator bandwidth.

In light of this analysis of the pump dynamics, the answer to the question posed at the end of Section 1.1 is now apparent; it is better to focus on the evolution of the pump’s control valves to improve performance.

7.5 Summary

In summary, the performance limitations in the pressure compensated vane pump system taken as the case study in this dissertation are a product of both the control system architecture depicted in Figure 4 and the low-cost VBS valve V3. These aspects of the case study control system result in a non-minimum phase plant with a nominal controllable bandwidth of 1.84Hz, maximum bandwidth below 5Hz, and a 30ms time delay. Nevertheless, due to the incompressibility of the oil, the control chamber pressure may respond at a higher bandwidth as only small changes in Q_D can be significantly amplified in Equation (6.8). Even so, the predicted rise time using the model matches measured rise times from a vehicle application, signifying that the limitations discussed here will appear in an actual implementation of this case study system.

Therefore, while the analysis presented in this chapter does not capture all of the dynamics of the case study system, this heuristic approach does reveal the principal limitations from a general standpoint and identifies a direction for the research that will distinctly improve the overall performance of the pressure compensated vane pump system.

While improving the dynamics of the regulation set point control valve, i.e. the VBS valve V3, by transitioning to a more expensive valve with better characteristics, the improvement in performance is likely to be marginal only. In many cases, cost is a key factor and should be minimized with any design changes. With this in mind, alternate architectures that can reduce the number and complexity of the required components is an attractive route to investigate. Even if the components used in the new architecture may cost more per unit than components in the original architecture, the overall benefits in terms of both simplification and performance improvement potential will likely justify the change.

This conclusion begins to address the questions posed at the beginning of Section 1.4. What is causing the undesired behavior or performance limitations of the baseline system? The control system architecture and components. Sensitivities to harmonic content near the resonance bands discussed in Section 7.4 contribute to pressure and flow oscillations by affecting Q_D which in turn causes oscillatory motion of the stator within the pump. This is difficult to correct for because of the phase lead seen in Figure 70.

8. PROPOSED PUMP CONTROL SYSTEM

To address the limitations of the current control system architecture in the pressure compensated VDVP analyzed in the case study, an active electrohydraulic pressure control solution is proposed here. Figure 74 compares these two architectures.

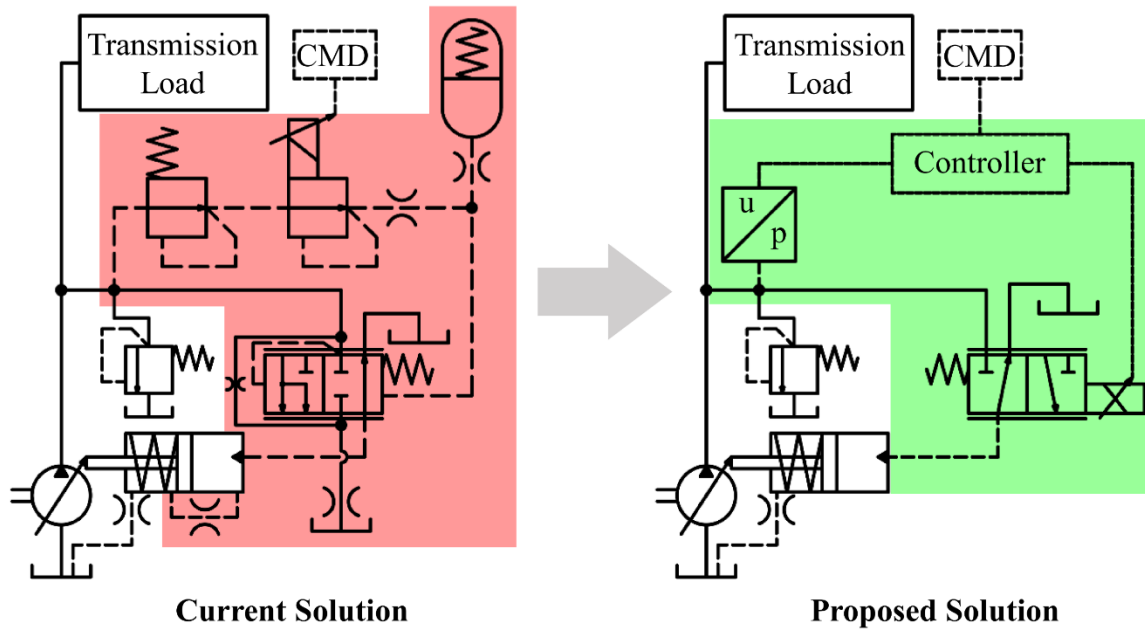


Figure 74: Comparison of the case study's current control system architecture and the proposed active electrohydraulic control system architecture.

As this figure indicates, the proposed solution consists of a 3/2 proportional directional control valve paired with a microcontroller that receives the command signal (a reference pressure) from the primary transmission controller and the pump outlet pressure via a miniature pressure transducer. This configuration is simpler than the current solution and would ultimately take up less space in the vehicle once developed. Another distinction between these two control systems is a reduction in the control chamber leakage (effected by exchanging the grooved pivot pin for a solid one). This results in stiffer adjustment system dynamics and reduces the magnitude of Q_D required to effect a given displacement change.

In addition to the benefits listed here, this proposed control system also possesses the general benefits, and challenges, accompanying all electrohydraulic pump control systems. These benefits include the possibility of using advanced control laws, as mentioned in Section

2.3, and increased system flexibility as programming can incorporate multiple features. A frequent challenge is the need for models to use in developing control laws and finding appropriately sized control valves that are fast enough for the given application.

8.1 Required Valve Characteristics

The first step in implementing an electrohydraulic control system is the selection of an appropriate valve. This requires knowledge of the dynamically changing flow demands and desired system response times. For the case study application, Figure 75 shows measured engine speeds and line pressures from vehicle data provided with the pump. The stator eccentricity, in the bottom plot, was calculated using this data and the validated lumped parameter pump model to provide an estimate of the unavailable flow demand data. Analyzing the leading edge of the highlighted event in Figure 75 gives insight into the required valve size.

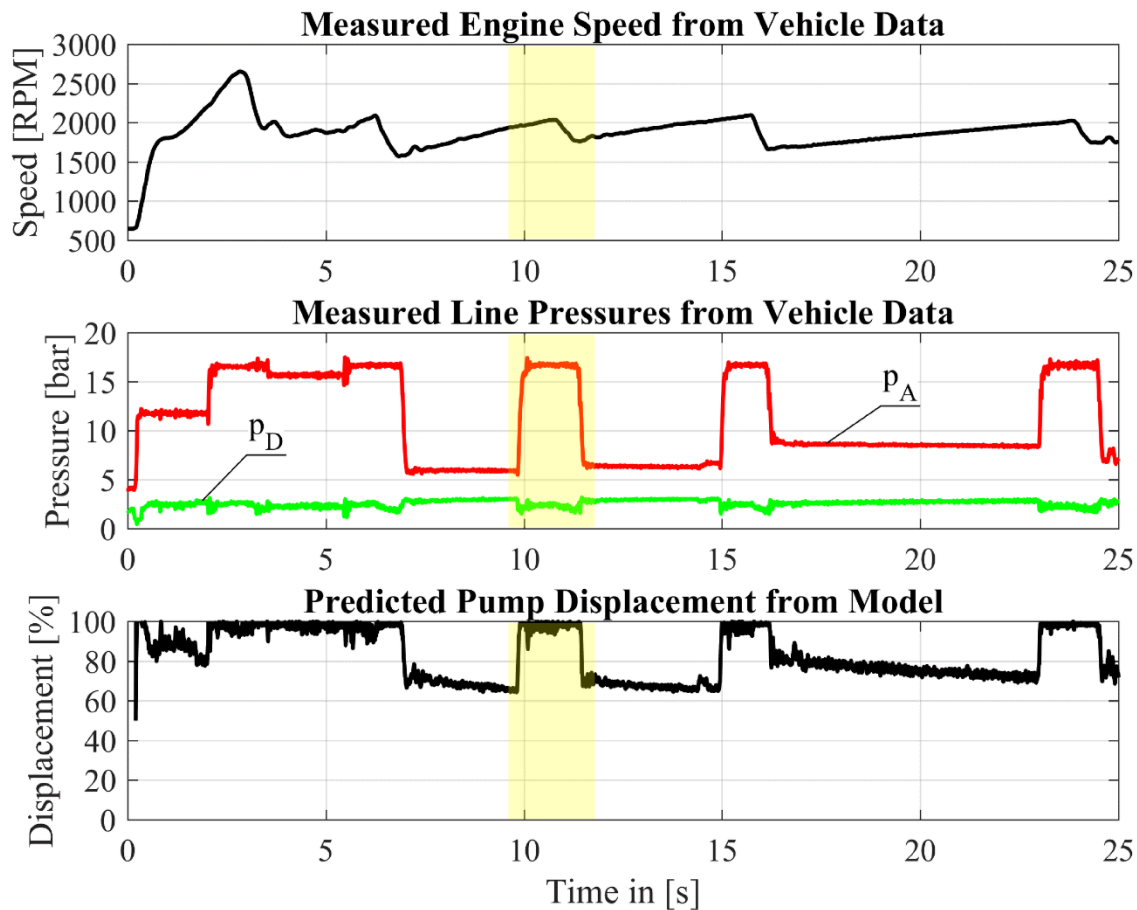


Figure 75: Example engine speed and line pressure traces taken from vehicle data using the case study system with predicted pump displacements.

This event is characterized by a 30% increase in β over an interval of about 100ms. Increasing β requires the 3/2 proportional valve in the proposed architecture (right-hand side of Figure 74) to be in the default position shown, which corresponds to low differential pressures across the valve as the control chamber pressure is dissipated over the valve back to tank. In the current architecture, this change in β starts with a differential pressure Δp across the regulation valve of approximately 2bar and ends with a Δp closer to 1bar as the control chamber pressure falls with the change in stator position. In fact, when the stator reaches a maximum eccentricity position and the control valve remains in a position connecting the control chamber to the tank, the control chamber pressure will fall to a minimum value. Since this control chamber pressure is affected by the higher control chamber leakage present in the current architecture, an estimate of the control chamber pressure, and therefore the Δp , is needed for the proposed system.

This Δp is given by Equation (8.1) and depends on the desired motion of the stator. Because the valve controls the stator motion through regulating the control chamber pressure, Equation (6.1) can be manipulated to give an accurate estimate p_D^* by Equation (8.2). Equation (8.2) is arrived at by neglecting the inertial and end stop terms in Equation (6.1) and then solving for the control chamber pressure. Since the stator eccentricity profile and M_1 are both known for this example event from the validated pump model and the information contained in Figure 75, Δp can be easily calculated.

$$\Delta p = \begin{cases} p_A - p_D, & \left(\frac{d\beta}{dt}\right)_{des} < 0 \\ p_D - p_{tank}, & \left(\frac{d\beta}{dt}\right)_{des} \geq 0 \end{cases} \quad (8.1)$$

$$p_D^* = \frac{-M_1 - kb_L(l_f - (b_L \sin(\beta) + l_0)) + C_S \left(\frac{d\beta}{dt}\right)_{des} - \tau_{SC} p_{SC}}{\tau_{RC}} \quad (8.2)$$

Assuming no control chamber leakage and no damping to slow down the motion of the stator, the required control valve flow can be calculated by Equation (8.3) for the highlighted event in Figure 75. This Q_β , associated with the motion of the stator, can be added to a leakage flow profile if the control chamber leakage properties are known for the new system.

$$Q_\beta = \left(\frac{\partial V_D}{\partial \beta}\right) \left(\frac{d\beta}{dt}\right)_{des} \quad (8.3)$$

The required valve size can then be determined using Equation (8.4), where the denominator given by Equation (8.1) using the p_D^* determined by Equation (8.2). Equation (8.4) provides a flow gain K_v requirement for this example which can be plotted as a function of time over the course of the event to identify the maximum value that will correspond to the minimum valve size capable of satisfying the duty cycle. Figure 76 provides an example of this plot for the highlighted duty cycle event depicted in Figure 75.

$$K_v = \frac{Q_\beta}{\Delta p} \quad (8.4)$$

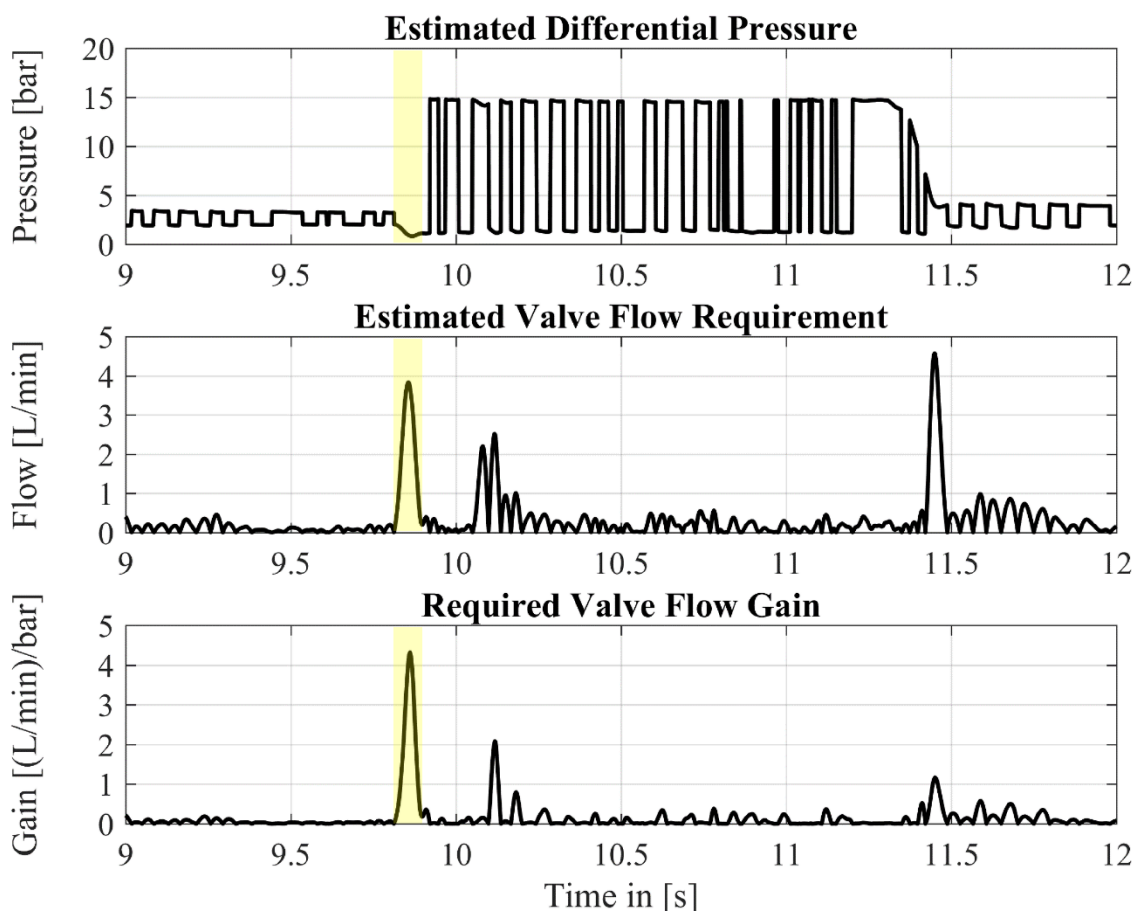


Figure 76: Required control valve flow gain calculations for the highlighted event in Figure 75 with the leading edge highlighted here for reference.

In this case, Figure 76 indicates that a valve with a flow gain of 5(L/min)/bar would meet the requirements with an acceptable margin for error in the calculations. This translates to a proportional valve sized to deliver about 25L/min of flow with a 5bar Δp per metering edge.

Simply selecting a valve with an appropriate flow gain, however, is necessary but not sufficient to guarantee the desired performance. The desired valve must also meet certain dynamic requirements to ensure the valve position can be controlled at a high enough bandwidth that the desired stator response times can be met. If the valve must shift to a fully open position within half the reference response time of the event identified in Figure 75 (40ms), the valve is assumed to need a bandwidth of 20Hz at $\pm 100\%$ displacement. This assumption can be met with available valve technologies (see [67]) and must be tested to refine this recommendation by simulating the pump response with various valve dynamics. This is done by starting with a 20Hz at $\pm 100\%$ valve (sized for 25L/min at 5bar Δp per metering edge) and incrementally changing the bandwidth to find the minimum bandwidth valve capable of meeting the duty cycle.

8.2 Proof of Concept in Simulation

As an initial proof of concept of this proposed architecture with the valve sizing indicated in the previous section, a simple PI control law was paired in simulation with a lumped parameter control valve model and a simplified form of the pump model presented in Chapters 3 and 6 using the engine speed and reference pressure inputs for the cycle described by Figure 75. These simulation results, given in Section 8.2.4 provides a useful performance prediction and a baseline for comparison with the results of simulations utilizing more advanced control laws in Chapter 9.

8.2.1 Control Valve Model

Figure 77 provides a simplified block diagram of the proposed system. As this figure illustrates, the control valve model generates a proportional flow Q_D in response to a current i_v proportional to the voltage command u_v which is output from the controller.

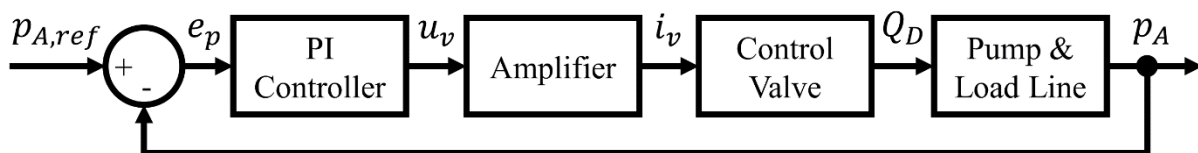


Figure 77: Proposed system block diagram showing the interconnection of the control valve, its amplifier, and the controller with the system plant consisting of the pump and load line.

Both the amplifier and control valve models are based on the typical second order transfer function given by Equation (7.1). If the electrical dynamics of the amplifier are fast enough, the current can be assumed to follow the voltage command perfectly and the amplifier transfer function can be taken as a unity gain. Conversely, the amplifier and control valve transfer functions—Equations (8.5) and (8.6), respectively—can be multiplied together to result in a fourth order transfer function as given by Equation (8.7) that relates the proportional position of the valve's spool to u_v directly as indicated by Equation (8.8).

The dynamics represented by G_v as given by Equation (8.7) are dominated by the control valve transfer function natural frequency $\omega_{n,CV}$ equal to 20Hz as indicated in Section 8.1. The amplifier natural frequency $\omega_{n,amp}$ is five times higher than $\omega_{n,CV}$ at 100Hz. Meanwhile, both ζ_{amp} and ζ_{CV} are assumed to be 0.7 for this study.

$$G_{amp} = \frac{\omega_{n,amp}^2}{s^2 + 2\zeta_{amp}\omega_{n,amp}s + \omega_{n,amp}^2} \quad (8.5)$$

$$G_{CV} = \frac{\omega_{n,CV}^2}{s^2 + 2\zeta_{CV}\omega_{n,CV}s + \omega_{n,CV}^2} \quad (8.6)$$

$$G_v = \frac{(6.234 \times 10^9)}{s^4 + 1056s^3 + (5.653 \times 10^5)s^2 + (8.334 \times 10^7)s + (6.234 \times 10^9)} \quad (8.7)$$

$$x_v^* = G_v u_v \quad (8.8)$$

This proportional spool position x_v^* is modified by Equation (8.9) to incorporate a deadband to represent an overlapped spool and saturation limits. The flow Q_D can then be calculated with this x_v and the K_v determined by Figure 76 using Equations (8.12). Equations (8.10) and (8.11) are based on the orifice equation for turbulent flow and make use of hyperbolic tangent constructions to represent the appropriate internal connections of the two positions for the control valve depicted in Figure 74. Thus, summing $Q_{D,A}$ and $Q_{D,T}$ in Equation (8.12) gives a continuous model of Q_D including the appropriate switching behavior of the valve.

$$x_v = \begin{cases} -1, & x_v^* \leq -1 \\ 0, & -0.015 \leq x_v^* \leq 0.015 \\ 1, & x_v^* \geq 1 \\ x_v^*, & \text{otherwise} \end{cases} \quad (8.9)$$

$$Q_{D,A} = K_v |x_v| \frac{(1 - \tanh(100x_v)) \tanh(p_A - p_D)}{2} \sqrt{\frac{2|p_A - p_D|}{\rho_{mix}}} \quad (8.10)$$

$$Q_{D,T} = K_v |x_v| \frac{(1 + \tanh(100x_v)) \tanh(p_{tank} - p_D)}{2} \sqrt{\frac{2|p_{tank} - p_D|}{\rho_{mix}}} \quad (8.11)$$

$$Q_D = Q_{D,A} + Q_{D,T} \quad (8.12)$$

This model, given by Equations (8.7) through (8.12), is nearly complete as a pump control system (excluding the control law) and thus fits nicely into the modeling overview depicted by Figure 8 and aligns with the definitions given at the beginning of Chapter 7.

8.2.2 Simplified Plant

To facilitate the design and evaluation of a pressure compensation control law in this application, it is helpful to consider a simplified model for the pump as a plant. From a control design perspective, the pump model developed in this dissertation converts information about the operating conditions (namely the pump speed and outlet pressure) and control efforts (or control flow Q_D) into information regarding the flow and internal forces generated by the pump. A simplified model can therefore be described by the set of expressions given below by Equations (8.13) through (8.15).

$$p_{D,g} = \frac{K_{mix}}{V_D} \int \left(Q_D - \frac{\partial V_D}{\partial \beta} \frac{d\beta}{dt} \right) dt \quad (8.13)$$

$$I_S \frac{d^2 \beta}{dt^2} = kb_L \left(l_f - (b_L \sin(\beta) + l_0) \right) - C_S \frac{d\beta}{dt} - M_1^* + \tau_{RC} p_{D,g} + M_{st} \quad (8.14)$$

$$p_{A,g} = R_{Line} Q_A^* \quad (8.15)$$

The first of these, Equation (8.13), is taken from Equation (6.8) assuming $Q_{SE,D}$ to be zero or negligible and results in the gauge pressure of the control chamber $p_{D,g}$ for a Q_D given by Equation (8.12). Equation (8.14) is a modified form of Equation (6.1) and includes a representation of the internal forces acting on the stator M_1^* given by Equation (8.16). Referring back to Figure 44 in Section 5.6, it can be seen that the moment M_1 has a form similar to a sinusoidal signal with a nonzero mean value. For this reason, M_1^* as given by Equation (8.16) can

be viewed as a simplification of the M_1 calculated using the full model presented in Chapter 3 as long as the mean value M_{1M} , amplitude M_{1A} , and frequency of this M_1^* signal correspond to the mean value, amplitude, and dominant frequency of M_1 for a given set of operating conditions.

To ensure this relationship between M_1^* and M_1 , M_{1M} and M_{1A} are given by Equations (8.17) and (8.18), respectively. The coefficients in these two equations (c_{ijk} and a_{ijk}) were calculated by fitting the nested polynomials to results from 64 simulations conducted with the full model presented in Chapter 3 using a constant oil temperature and aeration level. The operating conditions for these 64 simulations were taken from a full factorial design of experiments using four pump speeds, four outlet pressures, and four fixed pump displacements.

$$M_1^*\{n, p_{A,g}, \beta, t\} = M_{1M}\{n, p_{A,g}, \beta\} + M_{1A}\{n, p_{A,g}, \beta\} \sin\left(\frac{7\pi nt}{30}\right) \quad (8.16)$$

$$M_{1M}\{n, p_{A,g}, \beta\} = \sum_{i=0}^3 \left[\sum_{j=0}^3 \left(\sum_{k=0}^3 c_{ijk} \beta^k \right) (p_{A,g})^j \right] n^i \quad (8.17)$$

$$M_{1A}\{n, p_{A,g}, \beta\} = \sum_{i=0}^2 \left[\sum_{j=0}^2 \left(\sum_{k=0}^2 a_{ijk} \beta^k \right) (p_{A,g})^j \right] n^i \quad (8.18)$$

After determining the coefficients for the fitted models of M_{1M} and M_{1A} , the models were evaluated using the results from 32 additional simulations at other randomly selected combinations of the operating conditions. In each case, the fitted models of M_{1M} and M_{1A} recreated the mean values and amplitudes of M_1 to within a 5% mean error for a coefficient of determination greater than 0.95 for both Equation (8.17) and Equation (8.18). Considering results from all 96 simulations, these coefficients of determination are greater than 0.99. Thus, while using M_1^* instead of M_1 does result in a loss of information, it is a helpful simplification because it condenses the highly nonlinear and complicated model presented in Chapter 3 to a fast model that can be used to evaluate the trends in the internal forces within the context of evaluating controller designs. However, this is only half of the picture.

The third expression in our simplified model, Equation (8.15), provides the other half of the picture by giving the gauge pressure at the outlet of the pump $p_{A,g}$ for an effective flow rate Q_A^* at the pump outlet. This Q_A^* , Equation (8.19), is a fitted model given by a quadratic polynomial surface of β and n with coefficients given by cubic polynomials of $p_{A,g}$. The

coefficients d_{ijk} used in Equation (8.19) were also found using results from the 64 simulations described above and the goodness of the model's fit was again evaluated against results from the additional 32 simulations. The fitted model here recreates the mean Q_A calculated by Equation (3.24) to within a 0.5% mean error for a coefficient of determination over 0.99.

$$Q_A^*\{n, p_{A,g}, \beta\} = \left\langle \sum_{i=0}^2 \left[\sum_{j=0}^2 \left(\sum_{k=0}^3 d_{ijk} (p_{A,g})^k \right) \beta^j \right] n^i \mid i + j < 3 \right\rangle \quad (8.19)$$

Equation (8.19) is also a useful simplification in that it captures the effects of the volumetric losses included in the full pump model that allow it to predict upper limits to the volumetric efficiency as discussed in Section 5.4 to provide a more realistic effective flow rate (as compared to the theoretical flow rate) without having to simulate the DC pressures and flows. Because of this, the simplified nonlinear pump model presented in this section can be used for the ‘‘Pump & Load Line’’ block in Figure 77 without a major loss in model integrity.

8.2.3 Initial Controller Design

As indicated in Section 2.3, a basic PI controller was chosen as a starting approach. This control law, given by Equation (8.20), generates a command voltage u_v in response to the error e_p defined in the block diagram of Figure 77. The proportional and integral gains in Equation (8.20) were found using manual tuning and result in a satisfactory response.

$$u_v = \frac{5s + 10}{s} e_p \quad (8.20)$$

Furthermore, if the control chamber pressure dynamics in the simplified nonlinear model are assumed to be much faster than the stator dynamics and that the control chamber pressure moment perfectly balances the mean value of M_1^* and the preload moment of the spring, the pump can be assumed to behave like a second order system with a velocity input. In other words, the linear model given by Equation (8.21), where \bar{k} is the mean value of the spring rate calculated by Equation (6.7), gives a linearized model of the stator's dynamic response to changes in the control flow Q_D^* . This Q_D^* can be approximated by Equation (8.22) where the nominal differential pressure across the valve is taken to be 3bar and x_v^* is given by Equation (8.8). Since the β^* output by Equation (8.21) will be proportional to changes in the pump outlet pressure for a given pump speed, Equations (8.7), (8.8), (8.21), and (8.22) can be combined to form a simplified linear model of the proposed solution.

$$\beta^* = \frac{\left(\frac{\partial V_D}{\partial \beta}\right)^{-1} \left(s + \frac{C_S}{I_S}\right)}{s^2 + \frac{C_S}{I_S}s + \frac{(b_L)^2 \bar{k}}{I_S}} Q_D^* \quad (8.21)$$

$$Q_D^* = -K_v \sqrt{\frac{2(\Delta p)_{nominal}}{\rho_{mix}}} x_v^* \quad (8.22)$$

This greatly simplified model can be used to get an estimate of the “optimal” PI controller gains for a minimum closed loop response time using SISO system tuning tools in MATLAB. Performing this automatic tuning in MATLAB with this simplified linear model and a target response time less than 20ms results in “optimal” gains that are nearly identical (to within two decimal places) to the manually tuned gains given in Equation (8.20).

8.2.4 Results

Figure 78 provides a comparison between the simulation results using the controller given by Equation (8.20) with the measured system response from vehicle data as a baseline.

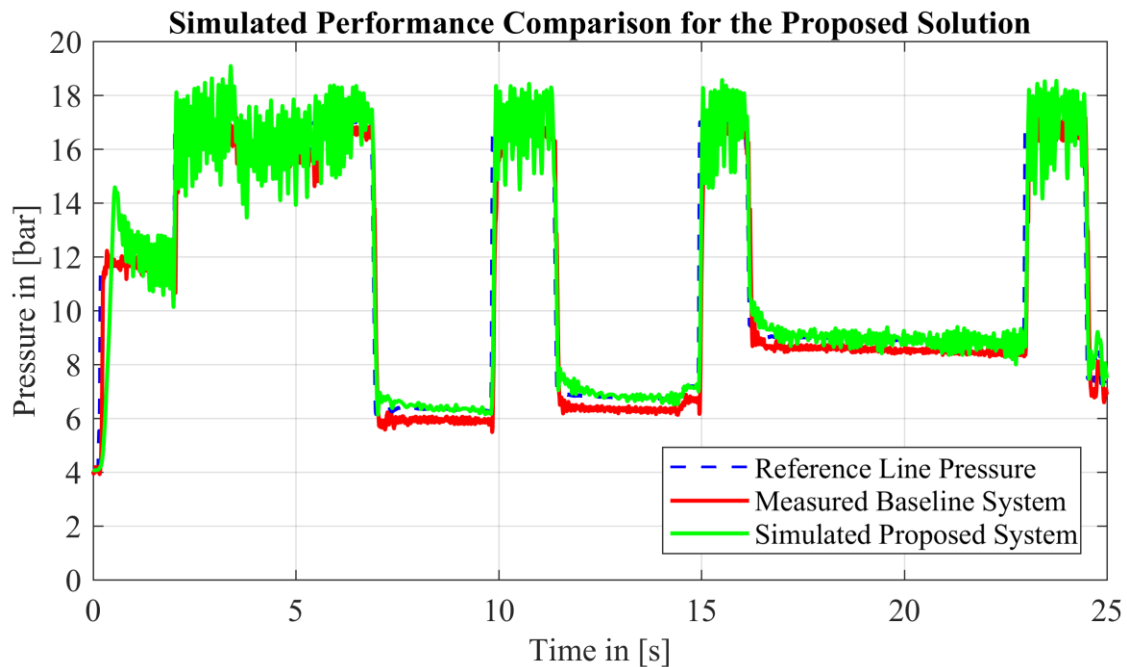


Figure 78: Simulated performance comparison between the proposed electrohydraulic pressure compensation solution equipped with the valve identified in Section 8.1 and using the simplified nonlinear pump model against the measured system response taken from the vehicle measurements used in Section 8.1.

As Figure 78 illustrates, the proposed pump control system discussed in this chapter behaves similarly to the baseline pump control system, qualitatively speaking. If the time scale of this response is reduced to show the segment corresponding to the highlighted event in Figure 75, as in Figure 79, it is easier to see that the proposed electrohydraulic control system results in a faster response time. Based on the results depicted here, the response time is predicted to be roughly 100ms (compared to the 190ms rise time of the baseline system). This means that the proposed solution should reach the desired line pressure in response to a step change in the reference in less than half the time that it takes the baseline system for the same step.

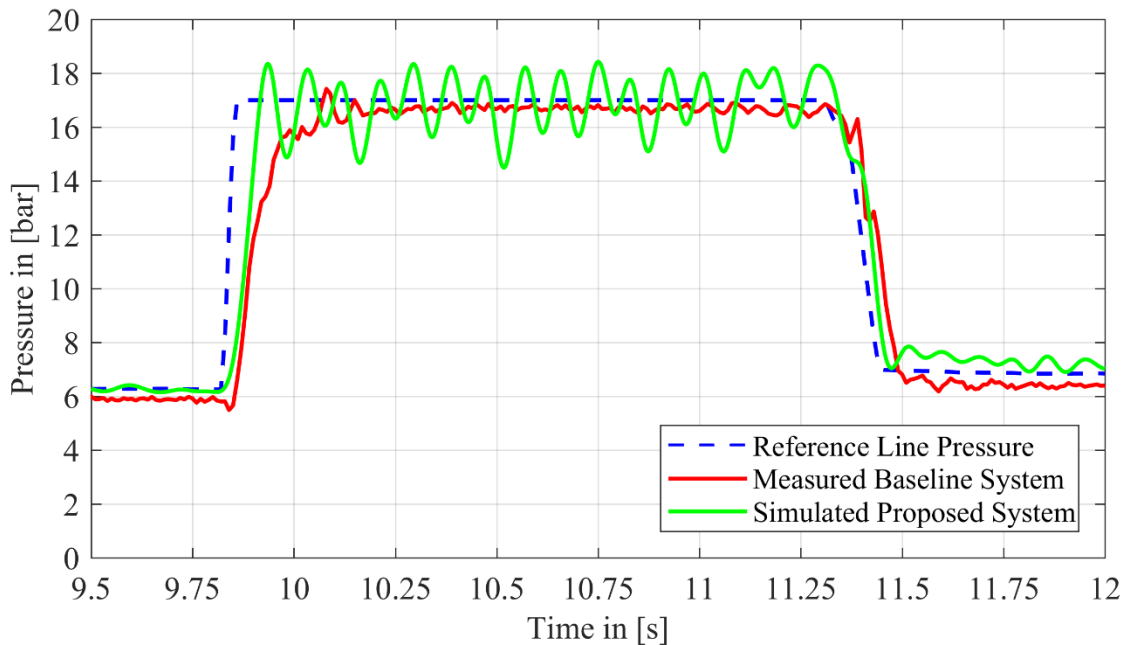


Figure 79: Zoomed-in view of the proposed solution performance comparison presented in Figure 78 to highlight the differences in the simulated and baseline responses.

8.3 Experimental Proof of Concept

As a further proof of concept and to accompany the simulation results presented in the previous section, the experimental setup described in Chapter 4 was again modified to reflect the circuit diagram given by Figure 80 (a larger version is available as Circuit 4 in APPENDIX A) and makes use of a custom adapter plate manufactured for this study according to Drawing 27 in APPENDIX B. This custom plate provides mounting holes and channels to interface with the valve port pattern for an available servovalve described by the “Control Servovalve

- Step 3. Command the control valve to fully open from A to T to ensure that the pump will start at a maximum displacement.
- Step 4. Start the electric motor and set the speed to the desired nominal value.
- Step 5. Adjust the loading servovalve until the highest desired line pressure for the experiment is reached.
- Step 6. Provide a constant reference pressure to the controller and activate the controller.
- Step 7. Vary the speed of the electric motor to simulate changes in the engine speed as the vehicle accelerates and decelerates, recording sensor signals.
- Step 8. Return the speed to the desired nominal value.
- Step 9. Reset the controller and provide a square-wave reference pressure.
- Step 10. Repeat Steps 7 and 8.
- Step 11. Command the loading servovalve to the fully open position and the control servovalve to fully open A to T.
- Step 12. Turn off the electric motor and DAQ/Control system.

This test setup mimics each aspect of the typical duty cycle of the VDVP in the case study application (refer back to Figure 5 in Chapter 1) and can therefore prove the pressure compensation abilities of the proposed control system presented in this chapter.

8.3.2 Measurement Results

Figure 81 shows measurements with a constant reference pressure signal and a varying speed input. As can be seen in the figure, the line pressure p_A is kept nearly constant despite changes in the flow capacity of the pump and a constant load restriction. Figure 82 provides a more detailed view of this behavior during the transients in the pump speed.

As the pressure plots in Figure 82 show, p_A remains within 1bar of the reference value at lower speeds and within about 1.5bar of the reference value at higher speeds with the PI controller given by Equation (8.20). This same setup handles reference pressure profiles such as a square wave as indicated by Figure 83 and Figure 84. As the detail views in Figure 84 show, the system also responds quickly to changes in the reference pressure. The measurements in this case exhibited a typical response time in the range of 50-65ms, even with a valve operating in flow saturation. Figure 84 also shows a similar deviation of p_A from the reference value as can be seen in Figure 82.

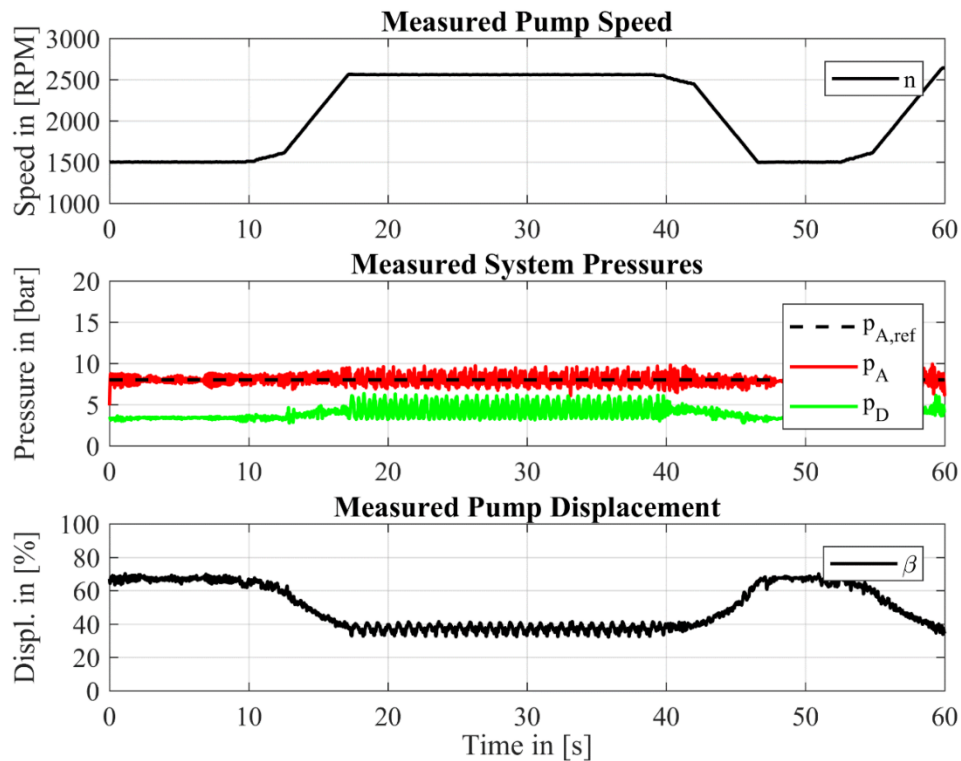


Figure 81: Measurement results from the constant reference pressure test of the proposed control system with a variable speed input and constant load restriction.

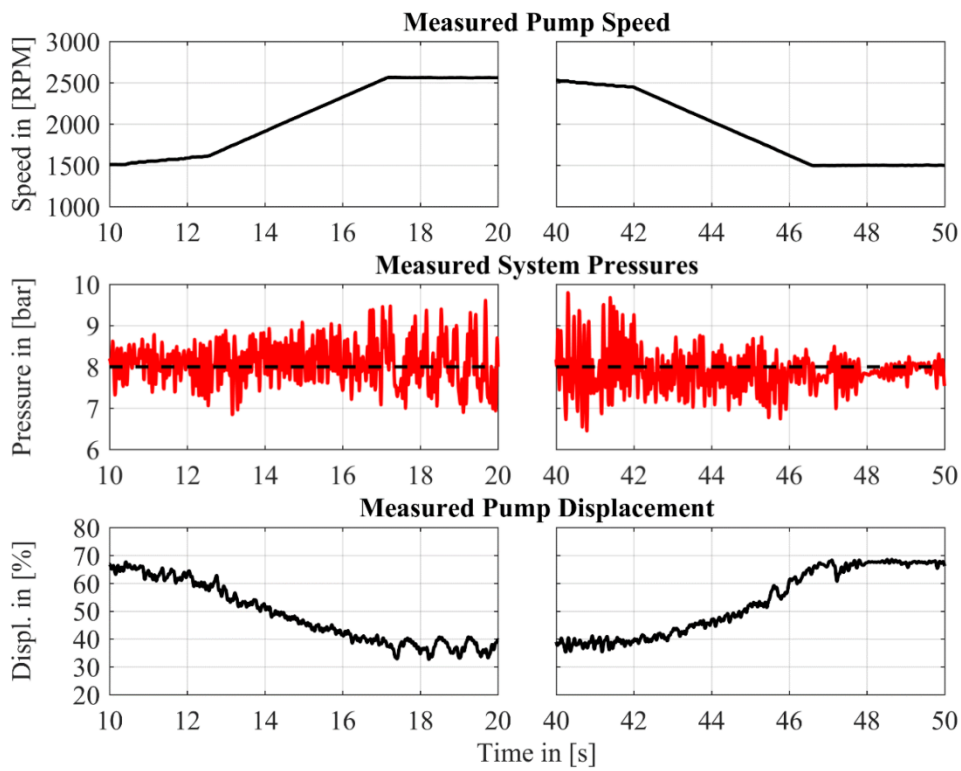


Figure 82: Detail view plots corresponding to Figure 81.

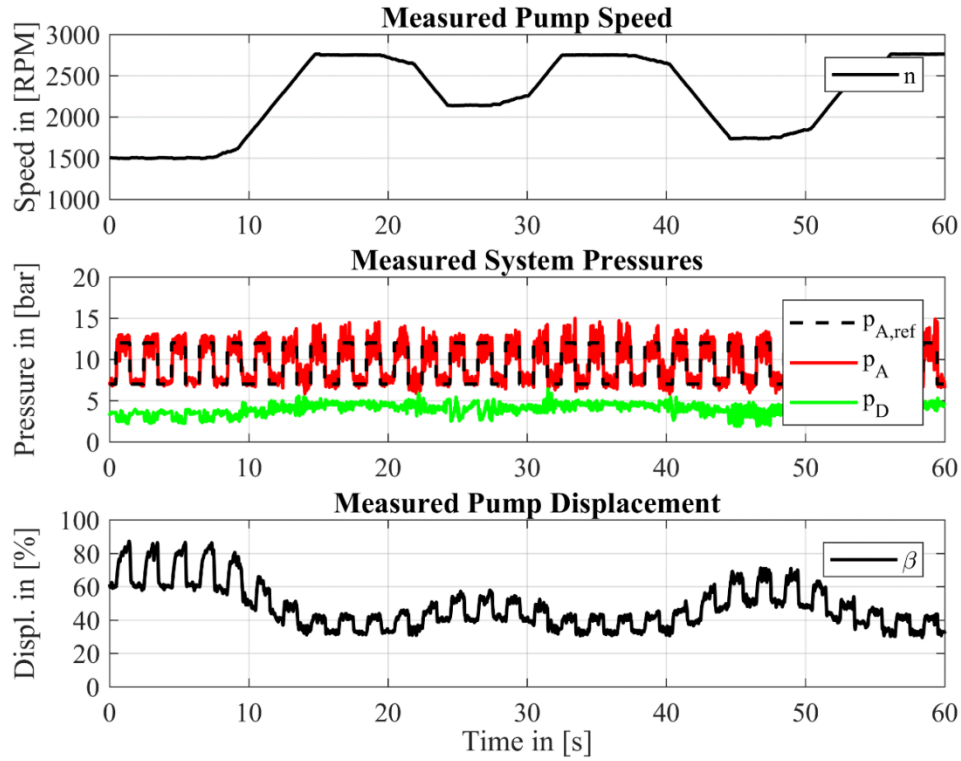


Figure 83: Measurement results from the variable reference pressure test of the proposed control system with a variable speed input and constant load restriction.

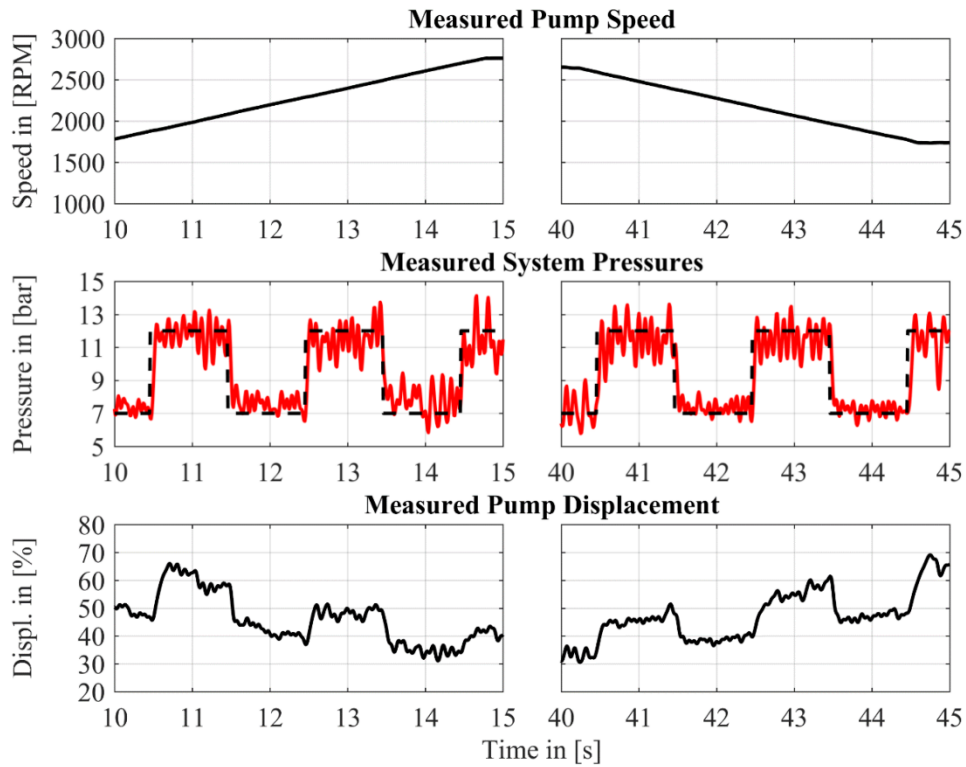


Figure 84: Detail view plots corresponding to Figure 83.

While this degree of accuracy and the general performance of the system may be improved with more advanced control laws, these results are sufficient to conclude that an adequate pressure compensated behavior can be reached with a simple controller. These results also indicate the presence of a large margin for error on the control valve flow characteristics without a major loss in performance since the control valve used in the experimental setup is quite different from the recommended size in Section 8.1.

8.3.3 Model Validation

The measured results depicted in Figure 83 can also be used to validate the simplified nonlinear simulation model provided the parameters defining G_{CV} and the value of the control valve flow gain K_v are altered to match the specifications of the valve used in the experiments. However, because the loading servovalve in the measurements was set to a constant position and the flow over the valve varied, using a simple gain to convert from Q_A^* to $p_{A,g}$ is not as accurate as in a steady-state case. While Equation (8.15) is still a good way to represent the transmission load in general, a more advanced impedance model better captures the load dynamics on the experimental setup. This relationship, Equation (8.23), gives a more accurate $p_{A,g}$ in bar for Q_A^* in L/min and is derived from the measured pressure and flow data associated with Figure 83.

$$p_{A,g} = 0.01(Q_A^*)^2 + 0.11Q_A^* \quad (8.23)$$

Replacing Equation (8.15) with Equation (8.23) in the simplified nonlinear model discussed in Section 8.2, the model can be validated for use in developing additional control strategies (the subject of Chapter 9) when the measured pump speed and reference pressure profile from the experimental data are used as inputs to the model.

Figure 85 compares the simulated p_A and β (as a percentage of its maximum) with the measurements from Figure 83. As these plots indicate, the simulation model agrees well with the measured data and accurately captures the displacement trends. Furthermore, by inspecting the detail views provided in Figure 86, it is easy to see that the magnitudes of each signal matches well. The main deviation between the simulation and the measured data is in the displacement transients as the stator returns to a higher displacement. Notwithstanding this discrepancy, the simulated performance is both realistic and representative and validates the model sufficiently to be used with confidence for control design work in Chapter 9.

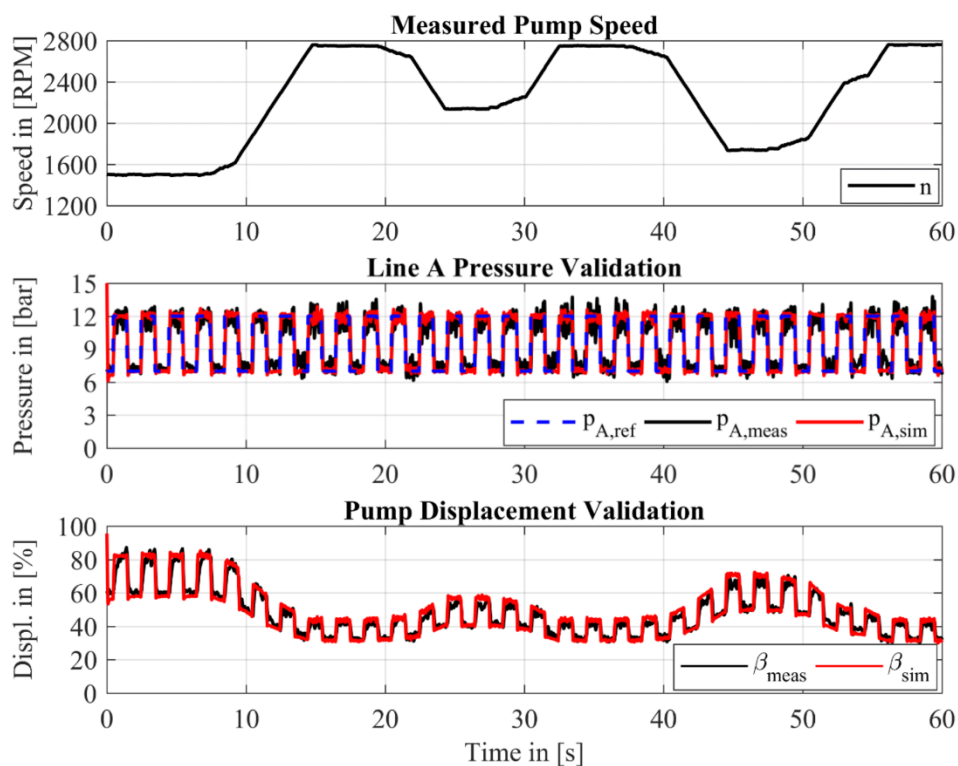


Figure 85: Comparison of the measured and simulated pump outlet pressure and displacement for a varying pump speed to the proposed control system design.

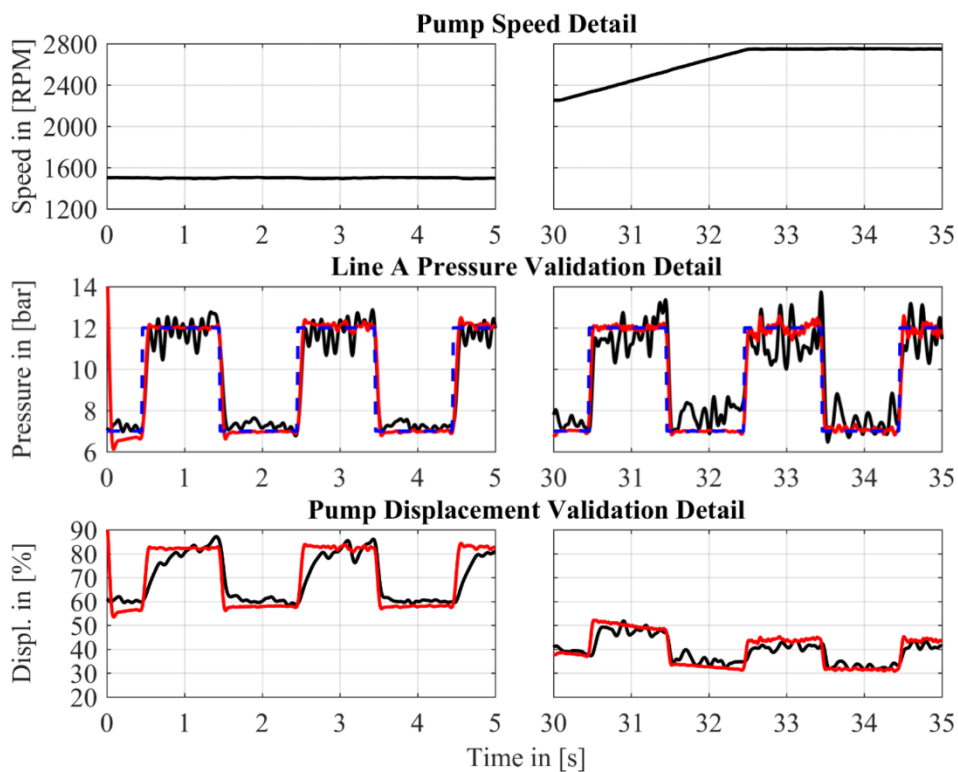


Figure 86: Detail view of the results presented in Figure 85.

8.4 Summary

Referring back to the research objectives stated in Section 1.4, this chapter has addressed aspects relating to the second, fifth, and sixth bullet points. More specifically, details are presented at the beginning of Chapter 8 for an electrohydraulic pressure compensation control architecture featuring a 3/2 proportional directional control valve while Section 8.1 outlines a procedure for determining an appropriate set of valve characteristics to assure a given performance. Section 8.1 also proposes an initial set of valve specifications for the automatic transmission application of the case study system that can be refined with additional information regarding the transmission demands and through experimentation.

Without any refinement, however, Section 8.2 establishes a simplified nonlinear simulation model with the valve specifications given in Section 8.1 and based on the lumped parameter VDVP model presented in Chapters 3 and 6 and then shows predictions of the proposed system's performance. As Section 8.2.4 indicates, the proposed system architecture cuts the pressure response time considerably (by 47%) and stably with only a simple PI control law. Section 8.3 continues to show that the proposed system provides improved performance experimentally, even when the control valve is sub-optimally sized with respect to the flow gain. Together, Sections 8.2 and 8.3 form a compelling proof of concept for the proposed architecture and set the stage for discussing additional performance gains that can be achieved through more sophisticated control concepts.

One reason the direct-drive valve used in the experimental setup was selected lies in the fact that it uses a permanent magnet linear force motor to actuate the spool. This is a technology that has been developed since the 1980's and offers good dynamic response characteristics without the need for a two-stage servovalve design. Comparatively, these valves are capable of better dynamics than valves with proportional solenoids and closed-loop position control for a similar component size and slight increase in cost [67]. Of the available valve technologies, this style of valve design is the most likely candidate for satisfying the required valve characteristics identified in Section 8.1 at higher bandwidths to take full advantage of any additional gains available by using more sophisticated control concepts. Nevertheless, further research is required to refine the bandwidth requirements of the valve and assess if proportional solenoids with closed-loop position control are sufficient for automotive pressure compensation applications.

While the control valve required for this proposed architecture may certainly be more expensive than—or at least equivalent in cost to—the baseline pressure compensation system valves, this alternative requires simpler valve block channels, fewer components, and a minimal increase in electronic controller complexity. Perhaps more importantly, this new solution promises improved performance without requiring an expensive redesign of the VDVP. Considering each of these points and without a more in-depth cost evaluation, the architecture proposed in this chapter is an economical way to both improve system performance and facilitate a more intelligent and synergistic operation of the pressure compensated pump with its environment.

Although improved performance has been achieved, in a response time sense, a second look at Figure 79 and the problem statement at the opening of Section 1.4 that unacceptable levels of pressure or flow oscillations were observed in the case study system, further justification of the proposed system is warranted. The pressure profile in Figure 79 displays significant pressure oscillations. This is primarily due to the mismatch between the real loading conditions, capacitance, and dynamic properties of the transmission which convert the flow generated by the pump into pressure and the simple impedance models given by Equation (8.15). This mismatch amplifies variations in the flow generated by the pump, which are then translated into oscillatory stator motion. The simplified stator friction model, which results in an overdamped dynamics, is not enough to counter these variations completely.

Even the experimental setup of the proposed system has challenges with these pressure oscillations, as Figure 84 shows, because the real loading of the pump in that setup does not match the real transmission driving the measured baseline system results depicted in Figure 79. A true test of the performance improvements in terms of oscillation reduction would therefore require implementation of the proposed system on a vehicle or more complex experimental setup with a full transmission. As this is outside the scope of this dissertation, it is left to the work of future researchers as they continue to focus on the evolution of the pump control system to improve performance. Until then, and looking past the pressure oscillations in current simulations, it is clear that the proposed control system is simpler than the baseline and has the clear potential for a faster response which will allow designers to tackle oscillation reductions more easily through automatic controls.

9. ADVANCED PRESSURE COMPENSATION CONTROL

Considering the electrohydraulic system proposed in Chapter 8, advanced pressure compensation controls can now be explored to satisfy the final research objective presented in Section 1.4. There are several methods that can be used to effect pressure compensation in general. However, the stiffness and nonlinearities of this system (as with many other electrohydraulic systems) can make synthesizing a controller challenging.

One way to address this is to employ feedback linearization to transform the system model into a more amenable form. While this is only one approach, it is a valuable one within the context of this dissertation for several reasons. First, feedback linearization can be used as a first step in the synthesis of a robust controller using a wide range of techniques founded in linear control theory for LTI systems. Second, it results in a relatively simple nonlinear controller that can be compared with the simple PI control law discussed in Section 8.2.3 to provide an initial evaluation of the benefits of exploring advanced control concepts in future work. And third, this more advanced controller provides an excellent framework for a continuation of the discussion on the required control valve bandwidth started in Section 8.1. The remainder of this chapter, therefore, will present the synthesis of a pressure compensation control law using feedback linearization.

9.1 Cascaded Control Scheme

Figure 87 provides a block diagram of the pressure compensation control scheme that is the subject of this chapter. As this diagram illustrates, a cascaded control approach was adopted where the pressure compensation task is accomplished by determining an appropriate reference for a pump displacement control law which, in turn, provides a reference control flow profile to a flow control law developed for the control valve.

Figure 87 also illustrates that both the VDVP displacement and control valve flow control laws consist of two parts: a model following control element and a feedback linearization element. Section 9.2 presents the synthesis of these two elements for the control valve along with simulation results to illustrate the tracking performance when the line pressures are assumed constant and the recommended valve characteristics from Section 8.1 are utilized.

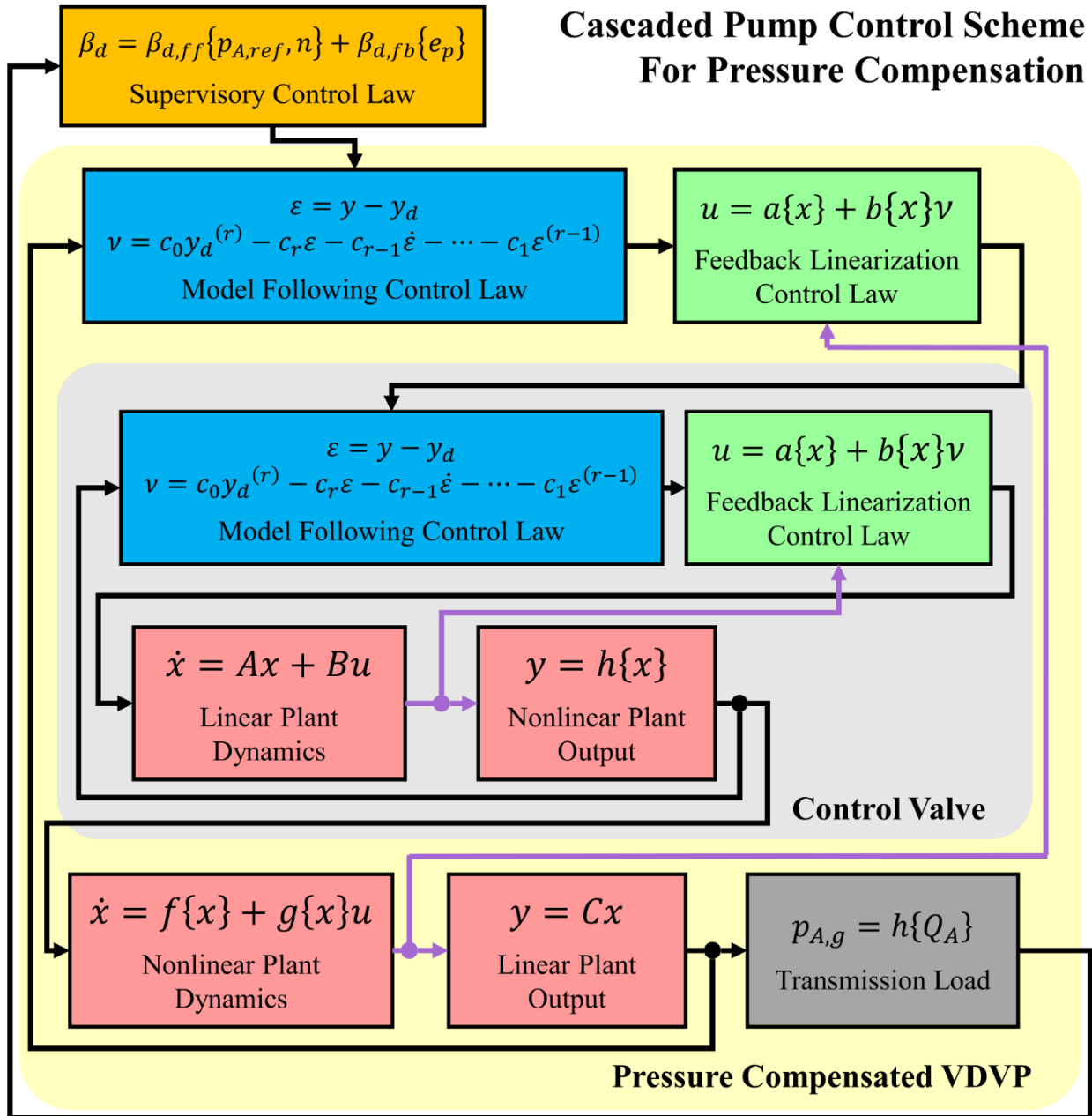


Figure 87: Block diagram of the cascaded pump control scheme for pressure compensation developed using feedback linearization and model following control techniques.

Section 9.3 addresses the synthesis of the displacement control law for the VDVP along with simulation results to illustrate the tracking performance for a few different valve bandwidths and assuming a constant pump speed. The following section presents the supervisory pressure control law that ties everything together and then Section 9.5 gives a comparison of the predicted performance with the results presented in Section 8.2.

9.2 Control Valve Flow Control

Section 8.2.1 presents the control valve model used in this study. For the controller synthesis presented in this section, however, the amplifier dynamics are neglected as they are significantly faster than the valve spool dynamics. The deadband and saturation included in Equation (8.9) is also neglected in the controller. With these simplifications, the state space representation of the valve can be expressed by Equations (9.1) through (9.3) and where Equation (9.3) is a slightly modified form of Q_D as given by Equation (8.12).

$$x = \begin{bmatrix} x_v \\ \frac{dx_v}{dt} \end{bmatrix} \quad (9.1)$$

$$\frac{dx}{dt} = \begin{bmatrix} 0 & 1 \\ -\omega_{n,CV}^2 & 2\zeta_{CV}\omega_{n,CV} \end{bmatrix} x + \begin{bmatrix} 0 \\ \omega_{n,CV}^2 \end{bmatrix} u \quad (9.2)$$

$$y = K_v |x_1| \left(\frac{(1 - \text{sgn}(x_1))}{2} \tanh(p_{A,g} - p_{D,g}) \sqrt{\frac{2|p_{A,g} - p_{D,g}|}{\rho_{mix}}} - \frac{(1 + \text{sgn}(x_1))}{2} \tanh(p_{D,g}) \sqrt{\frac{2|p_{D,g}|}{\rho_{mix}}} \right) \quad (9.3)$$

The procedure for finding a feedback linearization control law begins with finding the derivatives of the output function with respect to time. Equation (9.4) expresses the first derivative using the Lie derivatives $L_f h\{x\}$ and $L_g h\{x\}$, or the derivatives of $h\{x\}$ (or y) along $f\{x\}$ and $g\{x\}$ respectively [68], and are given by Equations (9.5) and (9.6) with the partial derivatives given by Equations (9.7) and (9.8).

$$\frac{dy}{dt} = L_f h\{x\} + L_g h\{x\}u \quad (9.4)$$

$$L_f h\{x\} = \left[\frac{\partial h}{\partial x_1} \quad \frac{\partial h}{\partial x_2} \right] f\{x\} \quad (9.5)$$

$$L_g h\{x\} = \left[\frac{\partial h}{\partial x_1} \quad \frac{\partial h}{\partial x_2} \right] g\{x\} \quad (9.6)$$

$$\frac{\partial h}{\partial x_1} = K_v \operatorname{sgn}(x_1) \left(\frac{(1 - \operatorname{sgn}(x_1))}{2} \tanh(p_{A,g} - p_{D,g}) \sqrt{\frac{2|p_{A,g} - p_{D,g}|}{\rho_{mix}}} - \frac{(1 + \operatorname{sgn}(x_1))}{2} \tanh(p_{D,g}) \sqrt{\frac{2|p_{D,g}|}{\rho_{mix}}} \right) \quad (9.7)$$

$$\frac{\partial h}{\partial x_2} = 0 \quad (9.8)$$

Note that the derivative of the sign function here is taken to be zero everywhere, simplifying Equation (9.7), although in reality the derivative is undefined for a zero argument. Also note that a second derivative of the output is required because $L_g h\{x\}$ is zero. This second derivative is given by Equation (9.9), again using the Lie derivative notation.

$$\frac{d^2 y}{dt^2} = L_f^2 h\{x\} + L_g L_f h\{x\} u \quad (9.9)$$

$$L_f^2 h\{x\} = \left[\frac{\partial L_f h}{\partial x_1} \quad \frac{\partial L_f h}{\partial x_2} \right] f\{x\} \quad (9.10)$$

$$L_g L_f h\{x\} = \left[\frac{\partial L_f h}{\partial x_1} \quad \frac{\partial L_f h}{\partial x_2} \right] g\{x\} \quad (9.11)$$

The same simplifying assumption made above can be made again in defining the partial derivatives needed to calculate Equations (9.10) and (9.11), giving the partials represented by Equations (9.12) and (9.13).

$$\frac{\partial L_f h}{\partial x_1} = 0 \quad (9.12)$$

$$\frac{\partial L_f h}{\partial x_2} = \frac{\partial h}{\partial x_1} \quad (9.13)$$

Since Equation (9.13) is nonzero, the control input will appear explicitly in Equation (9.9) and the relative degree of the feedback linearized system is equal to two. This means that the nonlinear control valve system can be transformed into a system that is both linear and controllable by means of a local change of coordinates and a local static state feedback law as discussed in [68] as long as Equation (9.13) is nonzero throughout the domain of x . This can be ensured by enforcing that the sign function of a zero argument in Equation (9.7) is negative one

because $p_{A,g}$ is always greater than $p_{D,g}$ under normal operation. The local change of coordinates is not included here for brevity but does follow the so-called “standard form” in [68] where the first state of the transformed system is identical to y , or in this case Q_D . The local state feedback law is given by Equation (9.14) where v is an artificial control input that linearly maps to y .

$$u = \frac{1}{L_g L_f h\{x\}} (v - L_f^2 h\{x\}) \quad (9.14)$$

It should be noted here that Equation (9.14) does not require full state feedback, but only a measurement (or a good estimation) of the spool position. This means that a valve with an electronic position feedback would be needed in order to implement this controller experimentally. However, depending on the method used to generate v here, the spool velocity may be necessary. In this study, full state feedback is assumed to be available and a model following control law given by Equations (9.15) and (9.16) was written.

$$\varepsilon = Q_D - Q_{D,ref} \quad (9.15)$$

$$v = -0.01 \frac{d^2 Q_{D,ref}}{dt^2} - 160\pi \frac{d\varepsilon}{dt} - (80\pi)^2 \varepsilon \quad (9.16)$$

While Equation (9.16) could include an integral term to reduce steady-state errors, this form gives favorable results as illustrated by Figure 88.

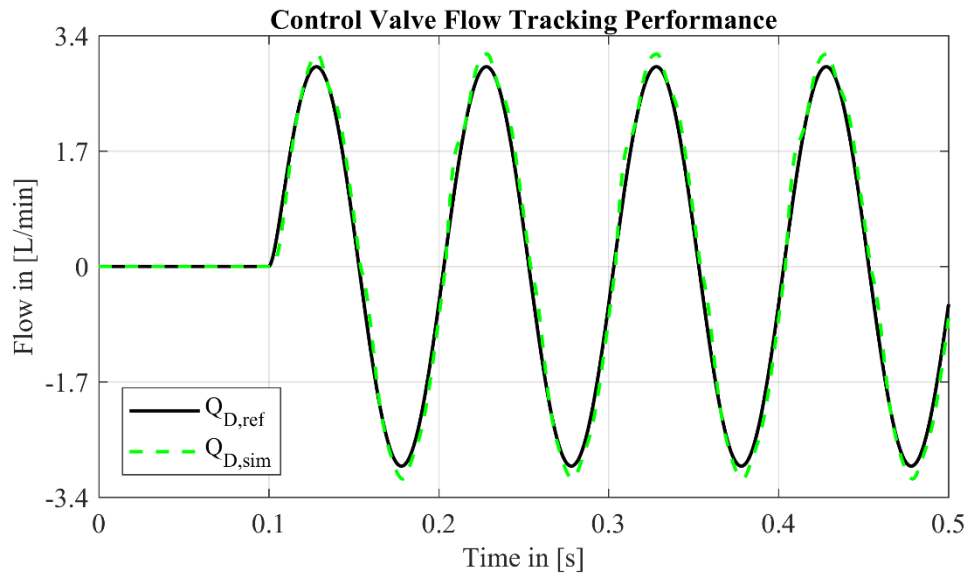


Figure 88: Control valve flow tracking using the nonlinear model following controller given by Equations (9.14) through (9.16) assuming constant pressures $p_{A,g}$ and $p_{D,g}$.

Figure 88 was generated by simulating the system with the assumption that the pressures $p_{A,g}$ and $p_{D,g}$ are constant. The tracking performance degrades when variable pressures are used and for higher frequency $Q_{D,ref}$ profiles. Nevertheless, Figure 88 indicates that the nonlinear model following control law defined by Equations (9.14) through (9.16) works well and will be used throughout the remainder of this chapter to regulate the flow of the control valve.

9.3 VDVP Displacement Control

As Figure 87 indicates, the structure of the VDVP displacement control law is identical to the control valve flow control law. The state space model used here, however, is based on Equations (8.13) and (8.14) and given by Equations (9.17) through (9.19). The internal moment of the pump M_1^* in Equation (9.18) is not included in the $f\{x\}$ but is instead considered to be an exogenous input despite its dependence on β . This assumption is valid because of the strong dependence M_1^* has on both $p_{A,g}$ and n which are taken as an external state and truly exogenous (from the perspective of the case study pump) input, respectively.

$$x = \begin{bmatrix} \beta \\ \frac{d\beta}{dt} \\ p_{D,g} \end{bmatrix} \quad (9.17)$$

$$\frac{dx}{dt} = \begin{bmatrix} x_2 \\ \frac{b_L k\{x_1\}}{I_S} (l_f - (b_L \sin(x_1) + l_0)) - \frac{C_S}{I_S} x_2 + \frac{\tau_{RC}}{I_S} x_3 \\ \frac{K_{mix}}{\left(\frac{\partial V_D}{\partial \beta} x_1 + V_{D,0}\right)} \left(-\frac{\partial V_D}{\partial \beta} x_2\right) \end{bmatrix} + \begin{bmatrix} 0 \\ 1 \\ 0 \end{bmatrix} \frac{1}{I_S} M_1^* \quad (9.18)$$

$$+ \begin{bmatrix} 0 \\ 0 \\ \frac{K_{mix}}{\left(\frac{\partial V_D}{\partial \beta} x_1 + V_{D,0}\right)} \end{bmatrix} u$$

$$y = x_1 \quad (9.19)$$

As the Lie derivative procedure is the same here as in the previous section, only the relevant nontrivial partial derivatives will be included in this section. Following the procedure reveals that the output must be derived three times before u shows up explicitly, so the relative

order is three and there exists a local state feedback control law that transforms the system described by Equations (9.17) through (9.19) into a system that is both linear and controllable with the standard local coordinate transform because Equation (9.24) is strictly nonzero. This control law is given by Equation (9.25).

$$\frac{\partial L_f^2 h}{\partial x_1} = \frac{-210b_L \operatorname{sech}^2(60x_1 - 4.08)}{I_S} \left(l_f - (b_L \sin(x_1) + l_0) \right) - \frac{(b_L)^2 k\{x_1\} \cos(x_1)}{I_S} \quad (9.20)$$

$$\frac{\partial L_f^2 h}{\partial x_2} = -\frac{C_S}{I_S} \quad (9.21)$$

$$\frac{\partial L_f^2 h}{\partial x_3} = \frac{\tau_{RC}}{I_S} \quad (9.22)$$

$$L_f^3 h\{x\} = \frac{\partial L_f^2 h}{\partial x_1} x_2 + \frac{\partial L_f^2 h}{\partial x_2} f_2\{x, M_1^*\} + \frac{\partial L_f^2 h}{\partial x_3} f_3\{x\} \quad (9.23)$$

$$L_g L_f^2 h(x) = \frac{\partial L_f^2 h}{\partial x_3} g_3\{x\} \quad (9.24)$$

$$u = \frac{1}{L_g L_f^2 h(x)} \left(v - \frac{\partial L_f^2 h}{\partial x_1} x_2 - \frac{\partial L_f^2 h}{\partial x_2} f_2\{x, M_1^*\} \right) \quad (9.25)$$

Note that Equation (9.25) does not include the third term of $L_f^3 h$ shown in Equation (9.23). This third term was shown in initial simulations to cancel out a stabilizing term in the third state equation. The more traditional local state feedback control law can still be used as long as v contains a replacement for this canceled term that then stabilizes the control chamber pressure dynamics. Here, however, Equation (9.25) will be used with the model following control law given by Equations (9.26) and (9.27) where γ is 320π . Note that this controller requires measurement or an accurate estimation of the pump eccentricity β to be implementable.

$$\varepsilon = \beta - \beta_{ref} \quad (9.26)$$

$$v = -0.001 \frac{d^3 \beta_{ref}}{dt^3} - 3\gamma \frac{d^2 \varepsilon}{dt^2} - 3\gamma^2 \frac{d\varepsilon}{dt} - \gamma^3 \varepsilon \quad (9.27)$$

Employing the controller defined by Equations (9.25) through (9.27) in simulation gives the results depicted in Figure 89. These simulations were conducted considering a constant pump speed. As Figure 89 illustrates, the control valve bandwidth has a profound impact on the tracking performance. For the three simulations, only the valve bandwidth was changed while the flow gain was held constant.

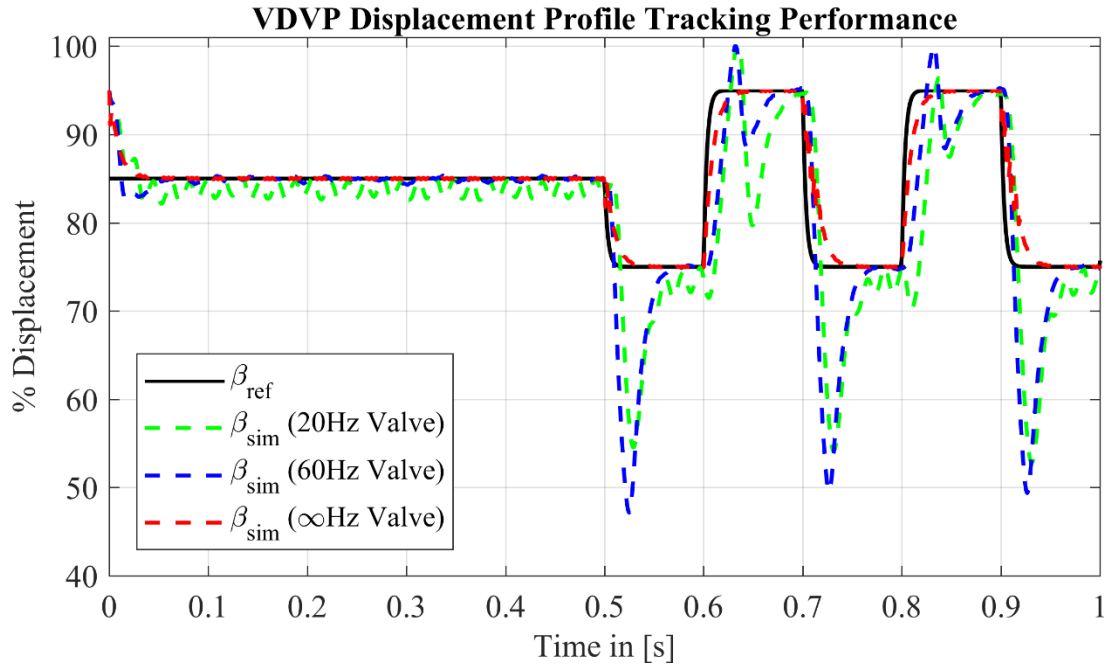


Figure 89: VDVP displacement tracking using the nonlinear model following control described by Equations (9.25) through (9.27) and assuming a constant pump speed for three valve bandwidth settings to highlight the impact of the valve dynamics.

These results reveal that the bandwidth recommendation made in Section 8.1 limits the controller's ability to cancel out oscillations in the pump displacement that arise from the oscillating component of M_1^* and which can be easily seen in the first half second of Figure 89. This choice of bandwidth also results in longer transients, but the displacement does eventually converge to within a few percent of the reference displacement level. Equation (9.27) could be augmented with an integral term or further tuned for this configuration to further reduce this steady-state error, but this is not completely necessary as the results in Section 9.5 will show. The impact of the increased 60Hz bandwidth will also be further explored in Section 9.5.

Nevertheless, the performance of the controller developed in this section is sufficient within the scope of this dissertation and provides a good starting point for future work. Future developments could include improving the robustness of the controller by adding a fast-

switching sliding mode control term to better handle parameter variations, adding leakage to the nonlinear model's control chamber pressure dynamics to provide an additional stabilizing term and reintroducing the third component of $L_f^3 h$ in Equation (9.25), or even incorporating the valve dynamics more explicitly in a backstepping control approach. Even without these improvements, the supervisory pressure control law presented in the next section can still make use of the current displacement controller to give good pressure tracking results by correcting for some of the errors seen in Figure 89.

9.4 Supervisory Level Pressure Control

This supervisory pressure control law consists of both a feedforward element and a feedback element as Figure 87 indicates. The feedforward term is derived from the load model given by Equation (8.23) and the theoretical flow rate of the pump to give Equation (9.28) which includes a simple first order transfer function to act as a rate limiter. The feedback term described by Equation (9.29) is a combination of a low-pass filter and a scaled version of the PI control law given by Equation (8.20).

$$\beta_{d,ff} = \frac{\sqrt{227.75p_{A,ref} + 675.34} - 25.99}{0.025n} \left(\frac{100\pi}{s + 100\pi} \right) \quad (9.28)$$

$$\beta_{d,fb} = \frac{62.83s + 125.7}{100(s^2 + 12.57s)} (p_{A,ref} - p_{A,g}) \quad (9.29)$$

$$\beta_d = \frac{5.6\pi}{180} (\beta_{d,ff} + \beta_{d,fb}) \quad (9.30)$$

Equations (9.28) and (9.29) each output a normalized displacement reference command for pressures in bar and speeds in RPM. Because of this, Equation (9.30) includes a coefficient to convert the final reference command, the sum of Equations (9.28) and (9.29) bounded to remain on an interval between 0.1 and 1, to the appropriate units required by the displacement controller developed in Section 9.3.

While this supervisory control is relatively simple, it does produce favorable results and is a good starting point for future work. Its performance as a supervisory pressure control law will be evaluated and compared to the performance of the simple PI controlled system in Chapter 8 and available vehicle data utilizing the baseline pump control system discussed in Chapter 7.

9.5 Results and Comparison

Just as in Section 8.2, the pump speed and reference pressure profile associated with available vehicle data from the case study were used as inputs to the proposed electrohydraulic system using the nonlinear controller described in this chapter. Figure 90 presents an overall comparison of the predicted performance.

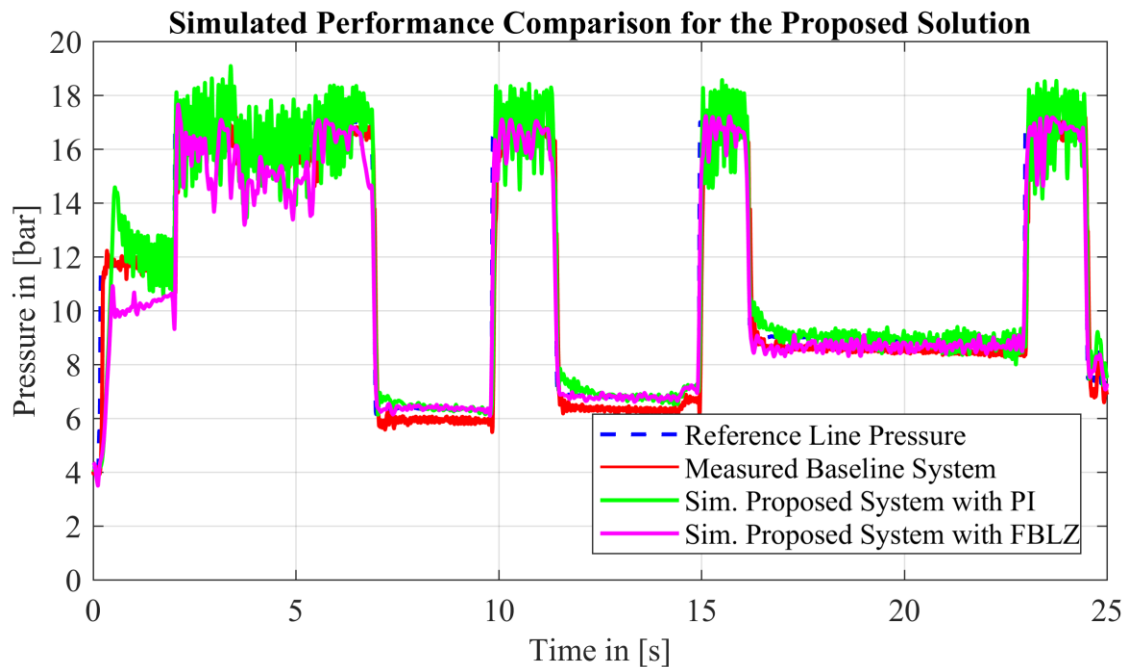


Figure 90: Simulated performance comparison of the proposed electrohydraulic solution with the advanced nonlinear controller featuring feedback linearization (FBLZ) with the results presented in Section 8.2.4.

The results depicted in Figure 90 consider a 20Hz (at $\pm 100\%$) control valve bandwidth for both versions of the proposed system. The discrepancies between the reference pressure profile and the simulated pressure profile from the nonlinearly controlled proposed system in the first 5 seconds of the plot are due to a combination of initialization error and higher variations in the pump speed. After this initial period of poor performance, the nonlinearly controlled system converges on the reference profile and appears to slightly outperform the PI controlled system.

This comparison in performance is more clearly seen in Figure 91. As this figure shows, the performance of the nonlinearly controlled system is comparable to the PI controlled one. While it does exhibit a greater steady-state tracking error at higher pressures than the PI controlled system, the nonlinearly controlled system also has a 20% faster response time at 80ms.

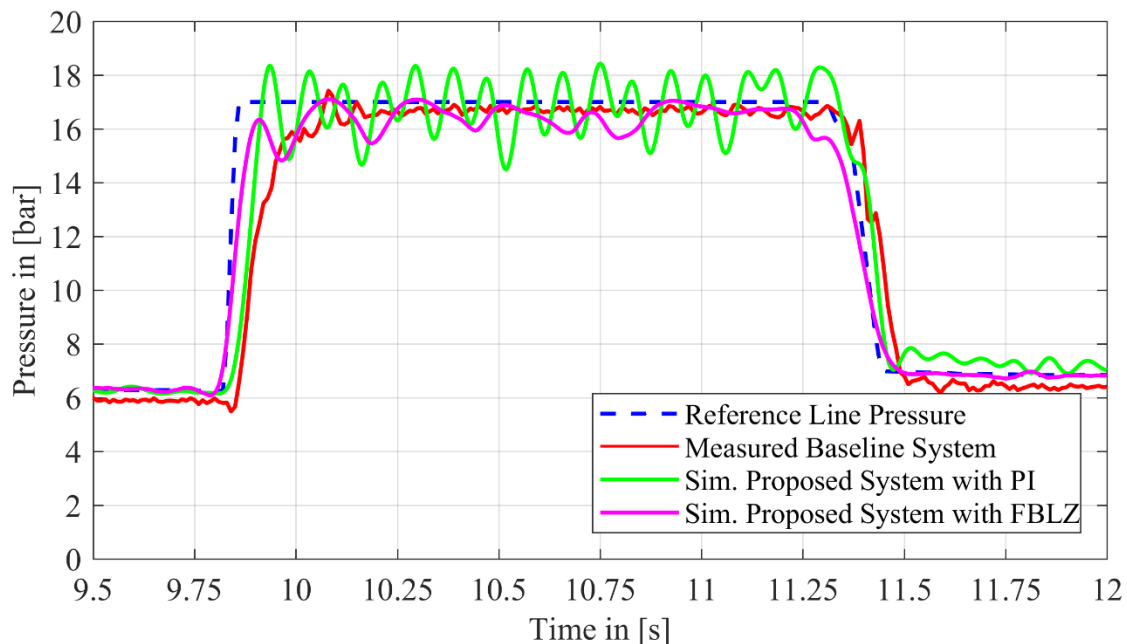


Figure 91: Zoomed in view of the results depicted in Figure 90.

If the control valve bandwidth is increased to 60Hz (at $\pm 100\%$) as was done in Section 9.3, the performance improves slightly as indicated by Figure 92. In fact, the response time here drops to roughly 50ms. Nevertheless, it still suffers from similar tracking performance problems.

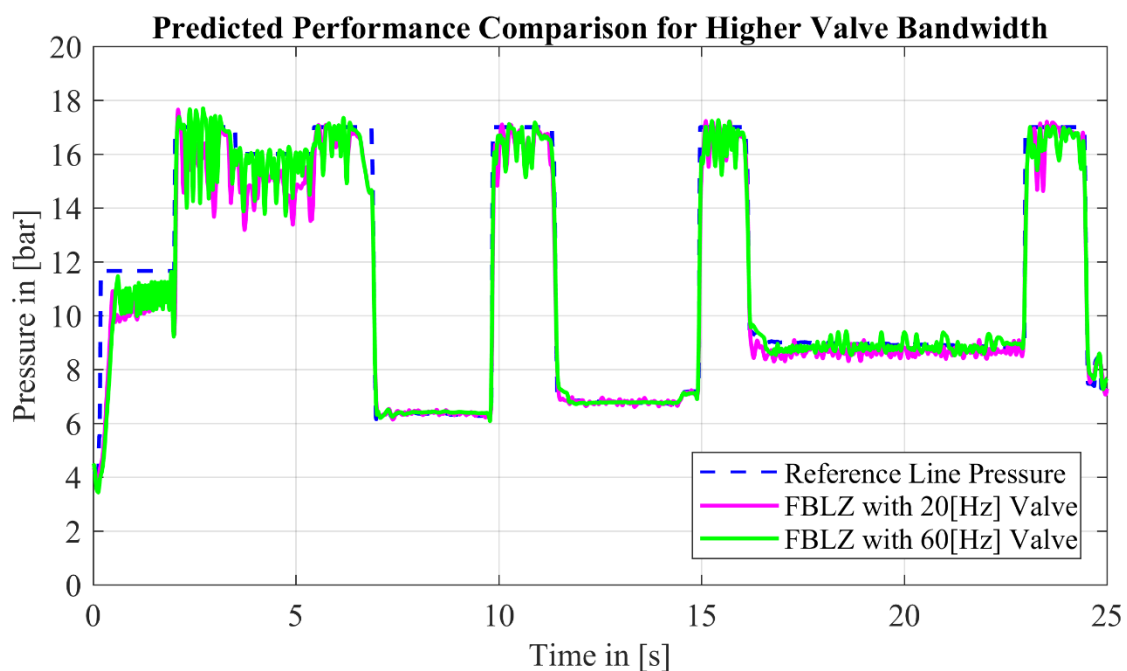


Figure 92: Performance comparison of the nonlinearly controlled proposed system with two different control valve bandwidths.

Seeing this, it is clear that the effect of solver and initialization error is low while the impact of varying parameters (pump speed, volumetric efficiency, fluid bulk modulus, bias spring rate, etc.) is more prominent. This can be addressed by improving the robustness of the controllers presented in this chapter, but is outside the scope of this chapter which aims to provide an initial example of the possibilities offered by advanced control techniques only.

Even with a more sophisticated control law and an improved valve bandwidth, the added complexity in the controller and need for more and better components appears to offer only marginal improvements in the overall pressure compensation performance of the VDVP. In this context, then, it will be more economically feasible to employ a PI controlled system especially since an improved control valve bandwidth will also benefit the PI controlled system.

This is further supported by looking at Figure 93 which shows the normalized spool position of the control valve for the high bandwidth case over the course of the cycle analyzed in Figure 90. While the PI controlled case has periods of time where the valve is oscillating between the two most extreme positions, it still spends at least half of the time during the cycle at positions within about a $\pm 20\%$ amplitude. The nonlinearly controlled case sees positions within $\pm 50\%$ amplitude for more like 80% of the time.

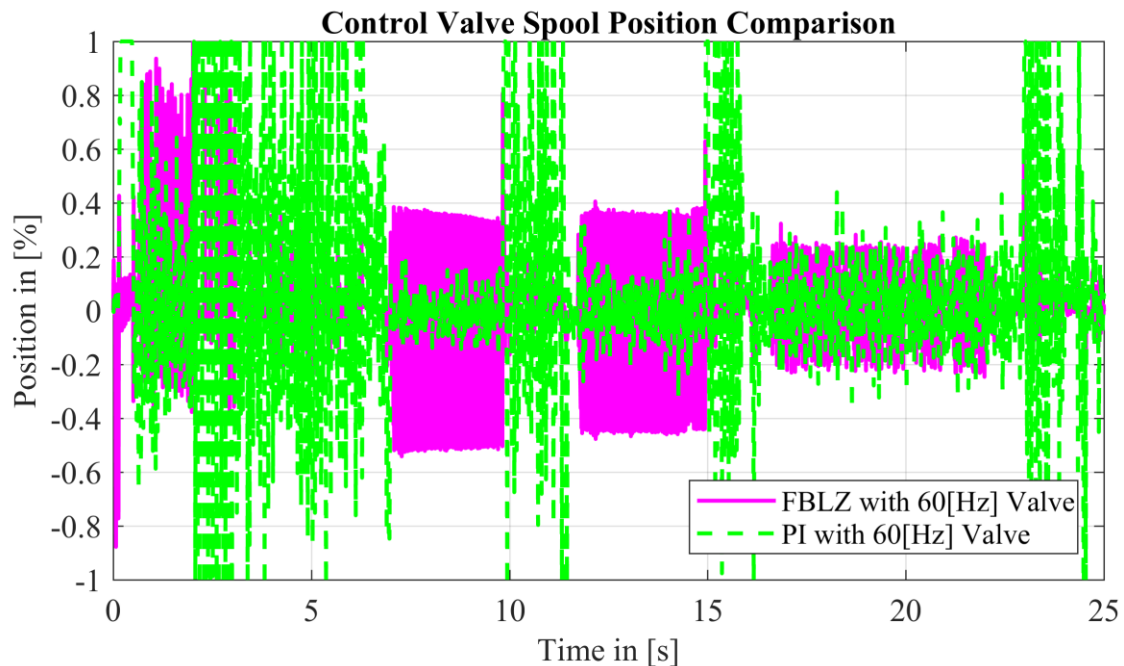


Figure 93: Comparison of the normalized control valve spool positions for the two controller cases when a high valve bandwidth is assumed.

This observation is significant because many valves have a higher bandwidth for lower amplitude changes than higher ones. Thus, finding a control valve capable of 60Hz at $\pm 50\%$ is not as difficult as finding one capable of the same 60Hz response at $\pm 100\%$. In fact, the Moog valve that was used in the experimental work of Chapter 8 is reported to exhibit this desired frequency response (see the specifications summary in APPENDIX C).

9.6 Summary

While the performance of the nonlinear controller developed in this chapter is nowhere near perfect, it does still accomplish the task of pressure compensation. However, part of the value of this controller lies in the fact that the feedback linearization process results in the local change of coordinates. This change of coordinates can be very useful for developing more robust controllers which act directly on the process variable (output) and its derivatives. This is the rationale behind the statement in the introduction to this chapter regarding feedback linearization being a first step toward other controllers.

Furthermore, feedback linearization could also be applied to this system as a whole (i.e. taking the control valve and pump together as a single super-component) instead of approaching the system in a cascaded control manner. Doing this would give a very different nonlinear controller and would likely reduce the number of additional sensors needed. The disadvantage would be a higher order system and much more difficult controller synthesis task. The cascaded approach adopted here is comparatively much simpler. However, simpler still is to find a PI controller as was done in Chapter 8.

Other control methods that would be valuable to explore in future work include loop shaping using lead-lag compensators, fuzzy PID, and gain scheduling. These methods represent options that will not require many, if any, additional sensors and still give good results at low development and implementation costs. Regardless of the method chosen, however, the proposed electrohydraulic system offers improved performance over the baseline case study system as the results in both this and the preceding chapter show.

10. CONCLUSIONS

At the conclusion of this dissertation, a return to the research objectives outlined in Section 1.4 and the intended contributions listed in Section 2.4 will highlight the main accomplishments of this work.

The first item from each of these lists deals with the development of a pivoting-cam type VDVP model. This model is presented in Chapters 3 and 6 and provides a realistically representative pump dynamics by modeling the displacement chamber pressure dynamics, the dynamic motion of the stator, and their fully coupled interaction while neglecting external leakage flows and friction forces associated with the various tribological interfaces of the pump. Measurements collected using the experimental setup and procedures presented in Chapters 4, 5 and 6 indicated that the effect of these leakages on the DC pressures, and subsequent internal forces acting on the stator, are negligible. Neglecting the friction merely translates into a reduced damping simplification that is beneficial for the dynamics analysis presented in this dissertation as it represents a “worst case” scenario. Ultimately, Chapter 3 provides mathematical models not available in the current literature and, along with Chapters 4 through 6, clearly shows this modeling approach to be powerful while remaining relatively simple with a high degree of utility for dynamic analyses.

Chapters 4 and 5 also address both the second research objective listed in Section 1.4 and the second intended contribution listed in Section 2.4 by discussing the design of a custom experimental setup and a novel approach to the measurement of the DC pressures. This novel “baton-passing” approach in Chapter 5 provides accurate measurements of both the pressure profiles of each individual DC as well as the angular size of each individual DC for small automotive vane pumps with a minimum number of required sensors. The resulting profiles were used to adequately validate the lumped parameter model.

Chapter 7 addresses the next two research objectives and provides a clear assessment of the system dynamics for the case study architecture that satisfies the third of the intended contributions. This analysis indicates that the limiting component of the case study system is the low-cost variable bleed solenoid valve V3. This solenoid valve limits the performance in two critical aspects. First, its inherent low bandwidth and time delay result in a controllable bandwidth of only 1.84Hz and a response time of 190ms. Second, its location within the control

system architecture leads to an unstable zero in the control system transfer function from the pump outlet pressure to the regulation valve flow. These limitations both contribute to a difficult situation for the development of simple automatic controllers (such as PID) and clearly answer the question of whether improved performance is more easily achieved through the evolution of the pump control system or the pump itself.

The final three research objectives listed in Section 1.4 and final intended contribution listed in Section 2.4 are treated in Chapters 8 and 9. The proposed electrohydraulic pressure compensation control system features a 3/2 proportional control valve that, based on the information available at the time of this work, should be sized for a 5(L/min)/bar flow rate with a frequency response of ideally 60Hz at $\pm 50\%$ amplitude and at least 20Hz at $\pm 100\%$ amplitude. Given these valve characteristics, good pressure compensation performance is possible with a simple PI control law or a more advanced controller methodology. In specific, simulations were used here to show that the PI controlled system cut the step response time in half (with respect to the baseline passive system) and up to a quarter of the time when the system was controlled using a cascaded nonlinear model following controller based on feedback linearization. Each of these proposed system configurations for an automotive transmission supply application represent novel contributions in the literature and clearly illuminate a path for future research in improving pressure compensated supply systems for automotive applications (see the end of Section 8.4 for an example).

Furthermore, the performance of the proposed system under PI control was also demonstrated experimentally and showed significant improvements in the pressure response time while using an available valve with appropriate frequency response characteristics while being undersized for the flow demand. This indicates that the proposed system architecture is valuable even if the optimal valve is unavailable as improved performance is still achievable and should receive serious consideration in the development of more efficient automotive oil supply systems featuring variable displacement vane pumps.

REFERENCES

- [1] M. Rundo and N. Nervegna, "Lubrication pumps for internal combustion engines: a review," *International Journal of Fluid Power*, vol. 16, no. 2, pp. 59-74, 2015.
- [2] J. Ivantysyn and M. Ivantysynova, *Hydrostatic Pumps and Motors*, New Delhi: Academic Books International, 2001.
- [3] H. Gholizadeh, R. Burton and G. Schoenau, "Fluid Bulk Modulus: Comparison of Low Pressure Models," *International Journal of Fluid Power*, vol. 13, no. 1, pp. 7-16, 2012.
- [4] H. Gholizadeh, D. Bitner, R. Burton and G. Schoenau, "Modeling and Experimental Validation of the Effective Bulk Modulus of a Mixture of Hydraulic Oil and Air," *Journal of Dynamic Systems, Measurement, and Control*, vol. 136, no. 5, pp. 051013-051013-14, 2014.
- [5] Z. Sun and K. Hebbale, "Challenges and Opportunities in Automotive Transmission Control," in *Proceedings of the 2005 American Control Conference*, Portland, Oregon, 2005.
- [6] S. P. Kemp and J. L. Linden, "Physical and Chemical Properties of a Typical Automatic Transmission Fluid," *SAE Technical Paper*, no. 902148, 1990.
- [7] A. M. Karmel, "Dynamic modeling and analysis of the hydraulic system of automotive automatic transmissions," in *American Control Conference*, Seattle, Washington, 1986.
- [8] R. Ahlawat, H. K. Fathy, B. Lee, J. L. Stein and D. Jung, "Modelling and simulation of a dual-clutch transmission vehicle to analyse the effect of pump selection on fuel economy," *Vehicle System Dynamics*, vol. 48, no. 7, pp. 851-868, July 2010.
- [9] S. Mancò, N. Nervegna, M. Rundo and G. Armenio, "Modelling and Simulation of Variable Displacement Vane Pumps for IC Engine Lubrication," *SAE Technical Paper*, no. 2004-01-1601, 2004.
- [10] M. Rundo and G. Altare, "Lumped Parameter and Three-Dimensional Computational Fluid Dynamics Simulation of a Variable Displacement Vane Pump for Engine Lubrication," *Journal of Fluids Engineering*, vol. 140, no. 6, pp. 061101-061101-9, 2018.

- [11] J. Harrison, R. Aihara, M. Eshraghi and I. Dmitrieva, "Modeling Engine Oil Variable Displacement Vane Pumps in 1D to Predict Performance, Pulsations, and Friction," *SAE Technical Paper*, no. 2014-01-1086, 2014.
- [12] G. Cantore, F. Paltrinieri, F. Tosetti and M. Milani, "Lumped parameters numerical simulation of a variable displacement vane pump for high speed ICE lubrication," *SAE Technical Paper*, no. 2008-01-2445, 2008.
- [13] Siemens Industry Software, *LMS Imagine.Lab AMESim® 15 User Manual*, 2016.
- [14] F. Furno, L. Vasile and D. Andersson, "The LMS Imagine.Lab AMESim® tool for the analysis and the optimization of hydraulic vane pumps," in *11th Scandinavian International Conference on Fluid Power*, Linköping, Sweden, 2009.
- [15] E. Mucchi and G. Dalpiaz, "Analysis of the evolution of the pressure forces in variable displacement vane pumps using different approaches," in *Proceedings of the ASME 2013 International Design Engineering Technical Conferences and Computers and Information in Engineering Conference*, Portland, Oregon, 2013.
- [16] A. M. Karmel, "A Study of the Internal Forces in a Variable-Displacement Vane-Pump-- Part I: A Theoretical Analysis," *Journals of Fluids Engineering*, vol. 108, no. 2, pp. 227-232, June 1986.
- [17] A. M. Karmel, "A Study of the Internal Forces in a Variable-Displacement Vane-Pump-- Part II: A Parametric Study," *Journal of Fluids Engineering*, vol. 108, no. 2, pp. 233-237, June 1986.
- [18] A. M. Karmel, "Modeling and Analysis of the Dynamics of a Variable-Displacement Vane-Pump With a Pivoting Cam," *Journal of Dynamic Systems, Measurement, and Control*, vol. 110, pp. 197-202, June 1988.
- [19] B. Geist and W. Resh, "Dynamic Modeling of a Variable Displacement Vane Pump Within an Engine Oil Circuit," in *Proceedings of the ASME 2011 Internal Combustion Engine Division Fall Technical Conference*, Morgantown, West Virginia, 2011.
- [20] D. Q. Truong, K. K. Ahn, N. T. Trung and J. S. Lee, "Theoretical investigation of a variable displacement vane-type oil pump," *Proceedings of the Institution of Mechanical*

Engineers, Part C: Journal of Mechanical Engineering Science, vol. 227, no. 3, pp. 592-608, 2013.

- [21] M. Köster and A. Fidlin, "Variable displacement vane pump, part I: a minimal nonlinear model," *Nonlinear Dynamics*, vol. 90, no. 2, pp. 1077-1089, 2017.
- [22] G. Bianchi, F. Fatigati, S. Murgia and R. Cipollone, "Design and analysis of a sliding vane pump for waste heat to power conversion systems using organic fluids," *Applied Thermal Engineering*, vol. 124, pp. 1038-1048, 2017.
- [23] E. Frosina, A. Senatore, D. Buono and M. Olivetti, "A Tridimensional CFD Analysis of the Oil Pump of an High Performance Engine," *SAE Technical Paper*, no. 2014-01-1712, 2014.
- [24] P. E. Sullivan and M. Sehmbly, "Internal Force Analysis of a Variable Displacement Vane Pump," *SAE Technical Paper*, no. 2012-01-0409, 2012.
- [25] D. M. Wang, H. Ding, Y. Jiang and X. Xiang, "Numerical Modeling of Vane Oil Pump with Variable Displacement," *SAE Technical Paper*, no. 2012-01-0637, 2012.
- [26] M. Rundo and N. Nervegna, "Geometry Assessment of Variable Displacement Vane Pumps," *Journal of Dynamic Systems, Measurement, and Control*, vol. 129, no. 4, pp. 446-455, July 2007.
- [27] D. Q. Truong, K. K. Ahn, N. T. Trung and J. S. Lee, "Performance analysis of a variable-displacement vane-type oil pump for engine lubrication using a complete mathematical model," *Proceedings of the Institution of Mechanical Engineers, Part D: Journal of Automobile Engineering*, vol. 227, no. 10, pp. 1414-1430, 2013.
- [28] A. Zouani, G. Dziubinski, V. Marri and S. Antonov, "Optimal Vanes Spacing for Improved NVH Performance of Variable Displacement Oil Pumps," *SAE Technical Paper*, no. 2017-01-1062, 2017.
- [29] U. Wieczorek and M. Ivantysynova, "CASPAR-A Computer Aided Design Tool for Axial Piston Machines," in *Bath Workshop on Power Transmission and Motion Control*, Bath, UK, 2000.

- [30] T. Kim, P. Kalbfleisch and M. Ivantysynova, "The effect of cross porting on derived displacement volume," *International Journal of Fluid Power*, vol. 15, no. 2, pp. 77-85, 2014.
- [31] E. Mucchi, G. Cremonini, S. Delvecchio and G. Dalpiaz, "On the Pressure Ripple Measurement in Variable Displacement Vane Pumps," *Journal of Fluids Engineering*, vol. 135, no. 9, pp. 091103-091103-11, September 2013.
- [32] A. Bianchini, G. Ferrara, L. Ferrari, F. Paltrinieri, F. Tosetti and M. Milani, "Design and Optimization of a Variable Displacement Vane Pump for High Performance IC Engine Lubrication: Part 1-Experimental Analysis of the Circumferential Pressure Distribution with Dynamic Pressure Sensors," *SAE Technical Paper*, no. 2009-01-1045, 2009.
- [33] S. Barbarelli, S. Bova and R. Piccione, "Zero-dimensional Model and Pressure Data Analysis of a Variable-Displacement Lubricating Vane Pump," *SAE Technical Paper*, no. 2009-01-1859, 2009.
- [34] S. Barbarelli, R. Piccione and S. Bova, "A Model Investigation on the Pressure Transducer Dynamics for Measurements in Lubricating Vane Pumps: Influence of Dissolved Air and of Transducer/Tubing Geometry," *SAE Technical Paper*, no. 2010-32-0059, 2010.
- [35] L. Ljung, "Perspectives on system identification," *Annual Reviews in Control*, vol. 34, no. 1, pp. 1-12, 2010.
- [36] L. Ljung, "System Identification," Linköping, Sweden, 2007.
- [37] R. Pintelon, P. Guillaume, Y. Rolain, J. Schoukens and H. Van hamme, "Parametric Identification of Transfer Functions in the Frequency Domain--A Survey," *IEEE Transactions on Automatic Control*, vol. 39, no. 11, pp. 2245-2260, November 1994.
- [38] A. Juditsky, H. Hjalmarsson, A. Benveniste, B. Delyon, L. Ljung, J. Sjöberg and Q. Zhang, "Nonlinear black-box models in system identification: Mathematical foundations," *Automatica*, vol. 31, no. 12, pp. 1725-1750, 1995.
- [39] J. Paduart, L. Lauwers, J. Swevers, K. Smolders, J. Schoukens and R. Pintelon, "Identification of nonlinear systems using Polynomial Nonlinear State Space models," *Automatica*, vol. 46, no. 4, pp. 647-656, 2010.

- [40] A. M. Karmel, "Stability and Regulation of a Variable-Displacement Vane-Pump," *Journal of Dynamic Systems, Measurements, and Control*, vol. 110, no. 2, pp. 203-209, June 1988.
- [41] B. Geist, W. Resh and K. Aluru, "Calibrating an Adaptive Pivoting Vane Pump to Deliver a Stepped Pressure Profile," *SAE Technical Paper*, no. 2013-01-1729, 2013.
- [42] M. Rundo, "Piloted Displacement Controls for ICE Lubricating Vane Pumps," *SAE International Journal of Fuels and Lubricants*, vol. 2, no. 2, pp. 179-184, 2009.
- [43] M. Axin, B. Eriksson and P. Krus, "Flow versus pressure control of pumps in mobile hydraulic systems," *Proceedings of the Institution of Mechanical Engineers, Part I: Journal of Systems and Control Engineering*, vol. 228, no. 4, pp. 245-256, 2014.
- [44] D. F. Thompson and G. G. Kremer, "Quantitative Feedback Design for a Variable-Displacement Hydraulic Vane Pump," in *Proceedings of the American Control Conference*, Albuquerque, New Mexico, 1997.
- [45] M. Köster and A. Fidlin, "Variable displacement vane pump, part II: nonlinear volume flow control," *Nonlinear Dynamics*, vol. 90, no. 2, pp. 1091-1103, 2017.
- [46] P. J. Paluszewski, M. C. Desai and R. C. Millar, "Variable Displacement Vane Pump for Turbine Engine Applications," in *Proceedings of the ASME Turbo Expo 2007: Power for Land, Sea, and Air*, Montreal, Canada, 2007.
- [47] P. J. Paluszewski and M. C. Desai, "Transient Response and Thermal Performance of a Variable Displacement Vane Pump-Based Actuation System for Turbo Jet and Turbofan Aircraft Engines," in *Proceedings of ASME Turbo Expo 2008: Power for Land, Sea and Air*, Berlin, Germany, 2008.
- [48] K. A. Edge, "The control of fluid power systems--responding to the challenges," *Proceedings of the Institution of Mechanical Engineers, Part I: Journal of Systems and Control Engineering*, vol. 211, no. 2, pp. 91-110, 1997.
- [49] S. J. Lin and A. Akers, "Optimal Control Theory Applied to Pressure-Controlled Axial Piston Pump Design," *Journal of Dynamic Systems, Measurements, and Control*, vol. 112, no. 3, pp. 475-481, 1990.

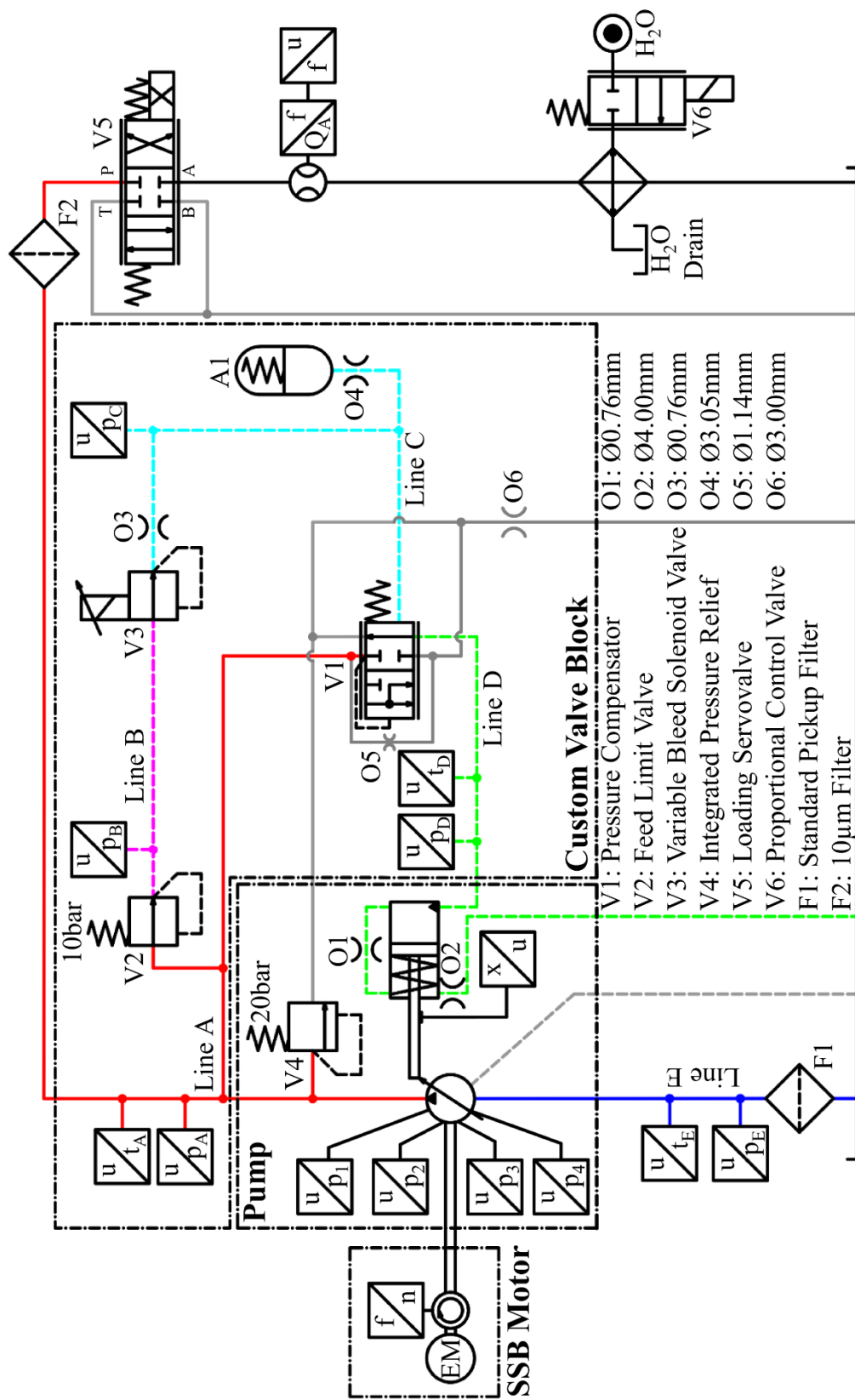
- [50] G. S. Beard and D. P. Stoten, "Energy Efficient Pressure Control of a Hydraulic Actuator Circuit Using MCS Adaptive Control," in *UKACC International Conference on Control. Control '96*, Exeter, UK, 1996.
- [51] M. Di Bernardo, U. Montanaro and S. Santini, "Novel hybrid MRAC-LQ control schemes: synthesis, analysis and applications," *International Journal of Control*, vol. 81, no. 6, pp. 940-961, 2008.
- [52] Z. You, R. T. Burton and P. R. Ukrainetz, "Feasibility study of sliding mode control in the operation of a variable displacement axial piston pump," *Proceedings of the JFPS International Symposium on Fluid Power*, vol. 1993, no. 2, pp. 267-272, 1993.
- [53] A. Klein and W. Backé, "An intelligent optimisation of a state loop controller with fuzzy-set-logic," in *Proceedings of the Fifth Bath International Fluid Power Workshop*, Bath, 1995.
- [54] D. A. Newton, "Design and implementation of a neural network controlled electrohydraulic drive," *Proceedings of the Institution of Mechanical Engineers, Part I: Journal of Systems and Control Engineering*, vol. 208, no. 11, pp. 31-42, 1 February 1994.
- [55] K. J. Åström and T. Hägglund, "PID Control," in *The Control Handbook: Control System Fundamentals*, 2nd ed., W. S. Levine, Ed., Boca Raton, Florida: CRC Press, 2010, pp. (9-70)-(9-90).
- [56] K. J. Åström and T. Hägglund, "The future of PID control," *IFAC Proceedings Volumes*, vol. 33, no. 4, pp. 19-30, April 2000.
- [57] B.-H. Cho, G.-H. Jung, J.-W. Hur and K.-I. Lee, "Modeling of Proportional Control Solenoid Valve for Automatic Transmission Using System Identification Theory," *SAE Technical Paper*, no. 1999-01-1061, 1999.
- [58] Y. Wang, M. Kraska and W. Ortmann, "Dynamic Modeling of a Variable Force Solenoid and a Clutch for Hydraulic Control in Vehicle Transmission System," in *Proceedings of the 2001 American Control Conference*, Arlington, Virginia, USA, 2001.
- [59] M. Zecchi, "Development of a mathematical model for the Exxon DTE 10 Excel 32 hydraulic fluid," Maha Fluid Power Research Center, Lafayette, IN, 2013.

- [60] T. Arata, N. Novi, K. Ariga, A. Yamashita and G. Armenio, "Development of a Two-Stage Variable Displacement Vane Oil Pump," *SAE Technical Paper*, no. 2012-01-0408, 2012.
- [61] P. Krus, K. Weddfelt and J.-O. Palmberg, "Fast Pipeline Models for Simulation of Hydraulic Systems," *Journal of Dynamic Systems, Measurement, and Control*, vol. 116, no. 1, pp. 132-136, March 1994.
- [62] N. Johnston, M. Pan and S. Kudzma, "An enhanced transmission line method for modelling laminar flow of liquid in pipelines," *Journal of Systems and Control Engineering*, vol. 228, no. 4, pp. 193-206, 2014.
- [63] R. P. Jenkins and M. Ivantysynova, "Investigation of Instability of a Pressure Compensated Vane Pump," in *9th FPNI Ph. D. Symposium on Fluid Power*, Florianópolis, SC, Brazil, 2016.
- [64] R. G. Budynas and J. K. Nisbett, *Shigley's Mechanical Engineering Design*, 9th ed., M. Lange, Ed., New York, New York: McGraw-Hill, 2011.
- [65] C. J. Freitas, "Perspective: Selected Benchmarks From Commercial CFD Codes," *Journal of Fluids Engineering*, vol. 117, no. 2, pp. 208-218, 1995.
- [66] O. Reinertz, "A comparative study on dither signals and their parameterization," in *Proceedings of the 11th IFK International Conference on Fluid Power*, Aachen, Germany, 2018.
- [67] A. Plummer, "Electrohydraulic servovalves - past, present, and future," in *Proceedings of the 10th IFK International Conference on Fluid Power*, Dresden, Germany, 2016.
- [68] W. S. Levine, *The Control Systems Handbook: Control System Advanced Methods*, 2nd ed., Boca Raton, Florida: CRC Press, 2010.

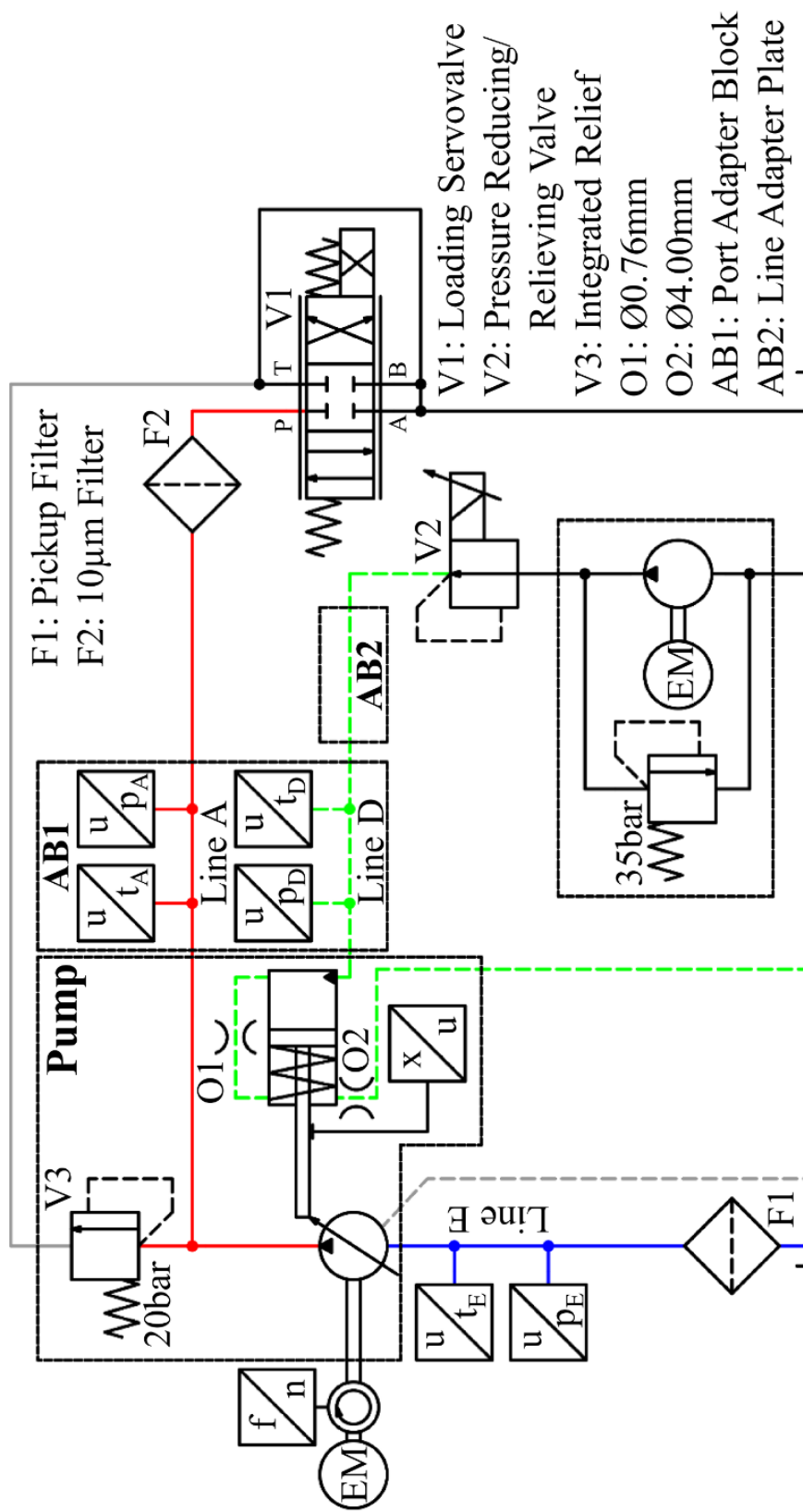
APPENDIX A

This appendix contains the hydraulic circuit diagrams used throughout this dissertation. These diagrams represent different configurations of the experimental test rig for different purposes and a list of them is found below with each diagram following on its own page.

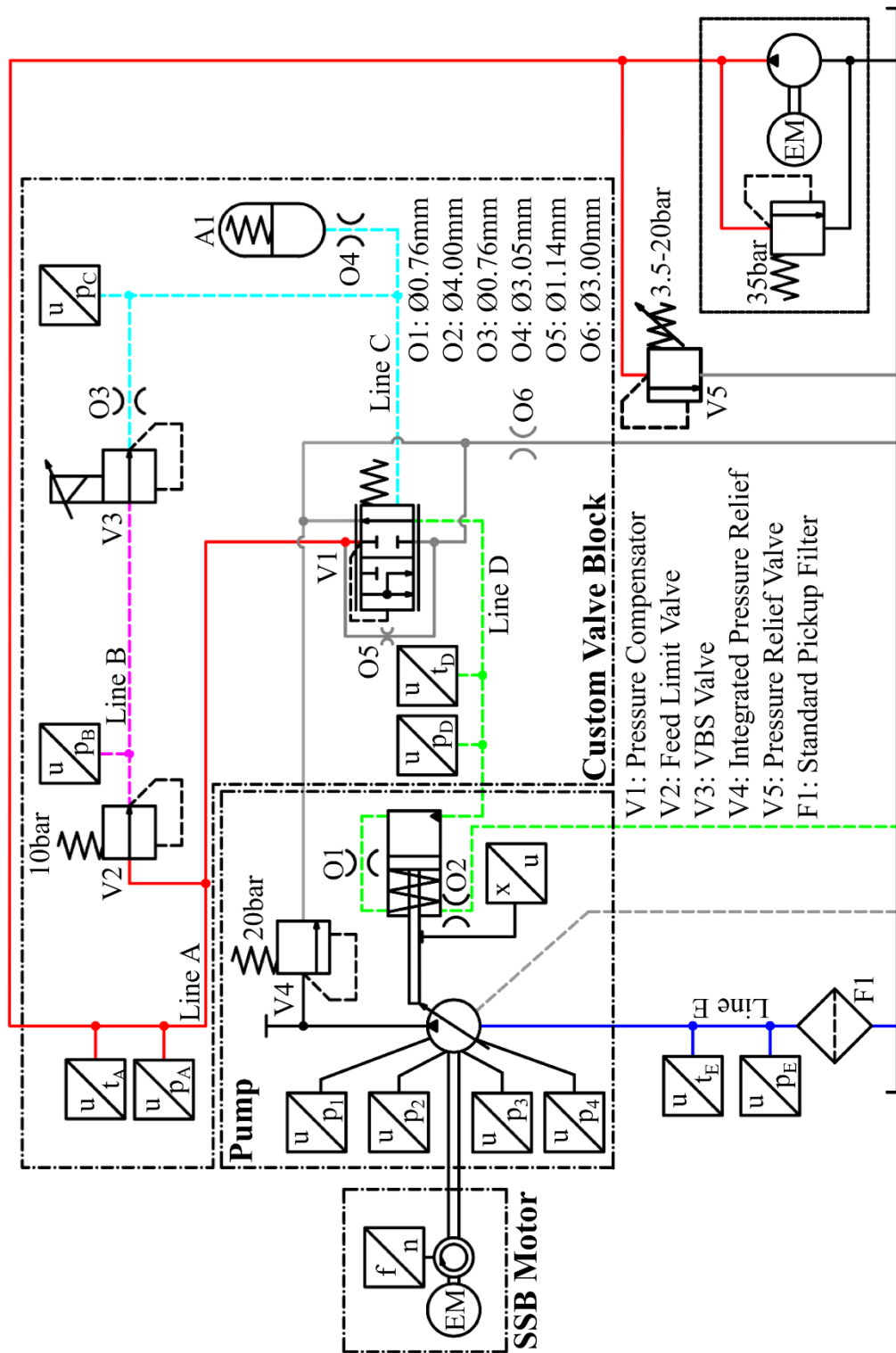
1. Circuit 1 is the standard hydraulic circuit diagram for the case study system. This configuration was used to perform the DC pressure validation measurements, some stator dynamics validation measurements, and the majority of the case study valve block characterization measurements. Circuit 1 is the subject of Chapter 4 in that the components described in that chapter were designed for this circuit.
2. Circuit 2 is a variation of Circuit 1 where the case study valve block was replaced with a custom adapter plate and a pressure control valve supplied by an independent pressure source. This configuration was the primary setup used to collect measurements for the stator dynamics validation.
3. Circuit 3 is also a variation of Circuit 1, but with the case study valve block still installed. This configuration is characterized by blocking the pump outlet with a custom plug to disable the pump and isolate the valve block from as much of the pump dynamics as possible. An external source was used to supply the valve block with pressure. This configuration was used for some of the valve block characterization measurements and is discussed in Chapter 7.
4. Circuit 4 is a variation of Circuit 2 with a different custom adapter plate required to install an available servovalve to serve the purpose of a 3/2 proportional control valve. This configuration was used to collect measurements for the experimental proof of concept for the proposed electrohydraulic pressure compensation control system.



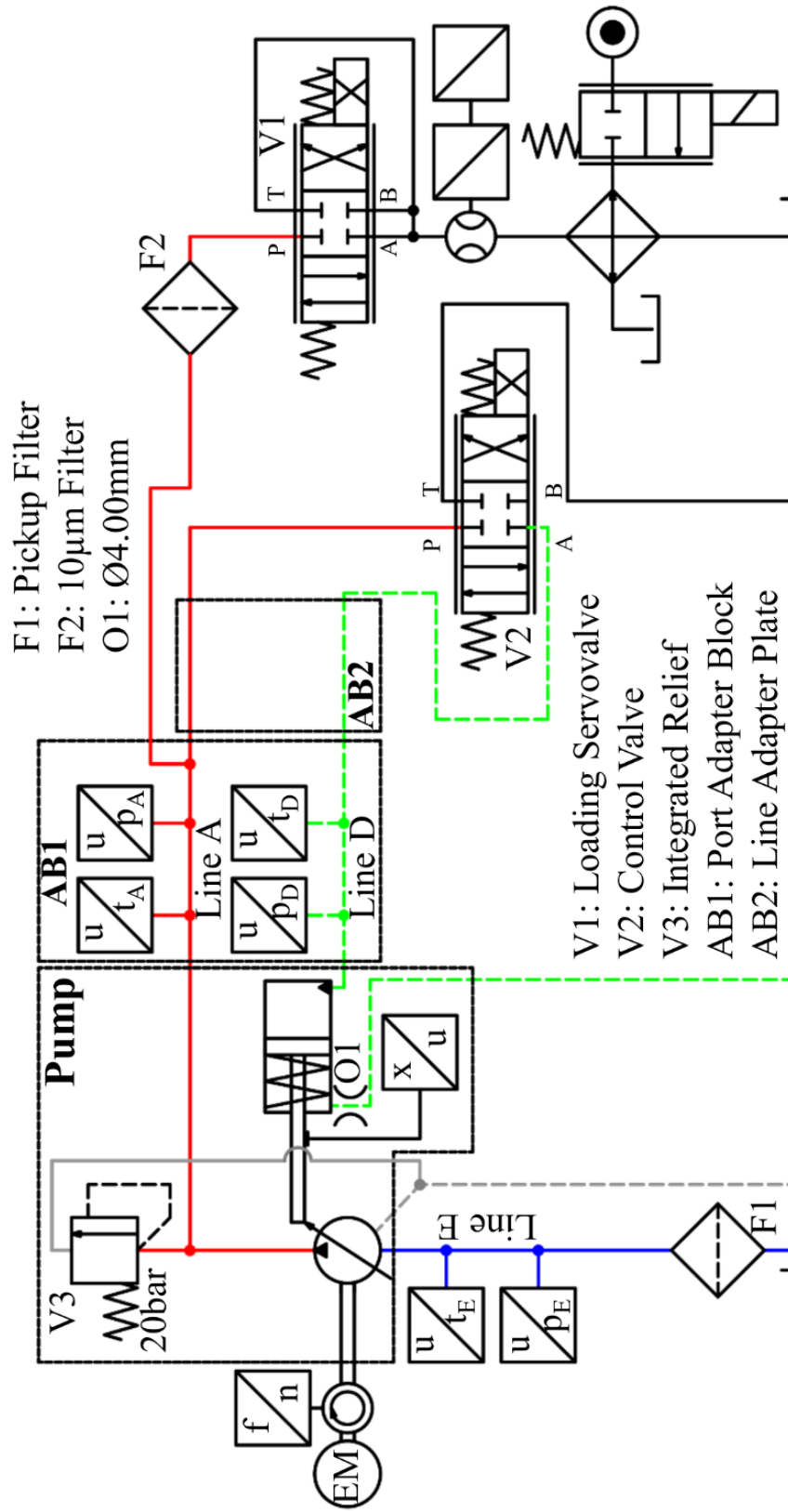
Circuit 1: Hydraulic circuit diagram corresponding to the custom test rig featuring the case study pressure compensation control system and modified pump.



Circuit 2: Hydraulic circuit diagram corresponding to the stator dynamics validation configuration of the experimental test rig.



Circuit 3: Hydraulic circuit diagram corresponding to the valve block characterization configuration with the pump outlet blocked and “off”.



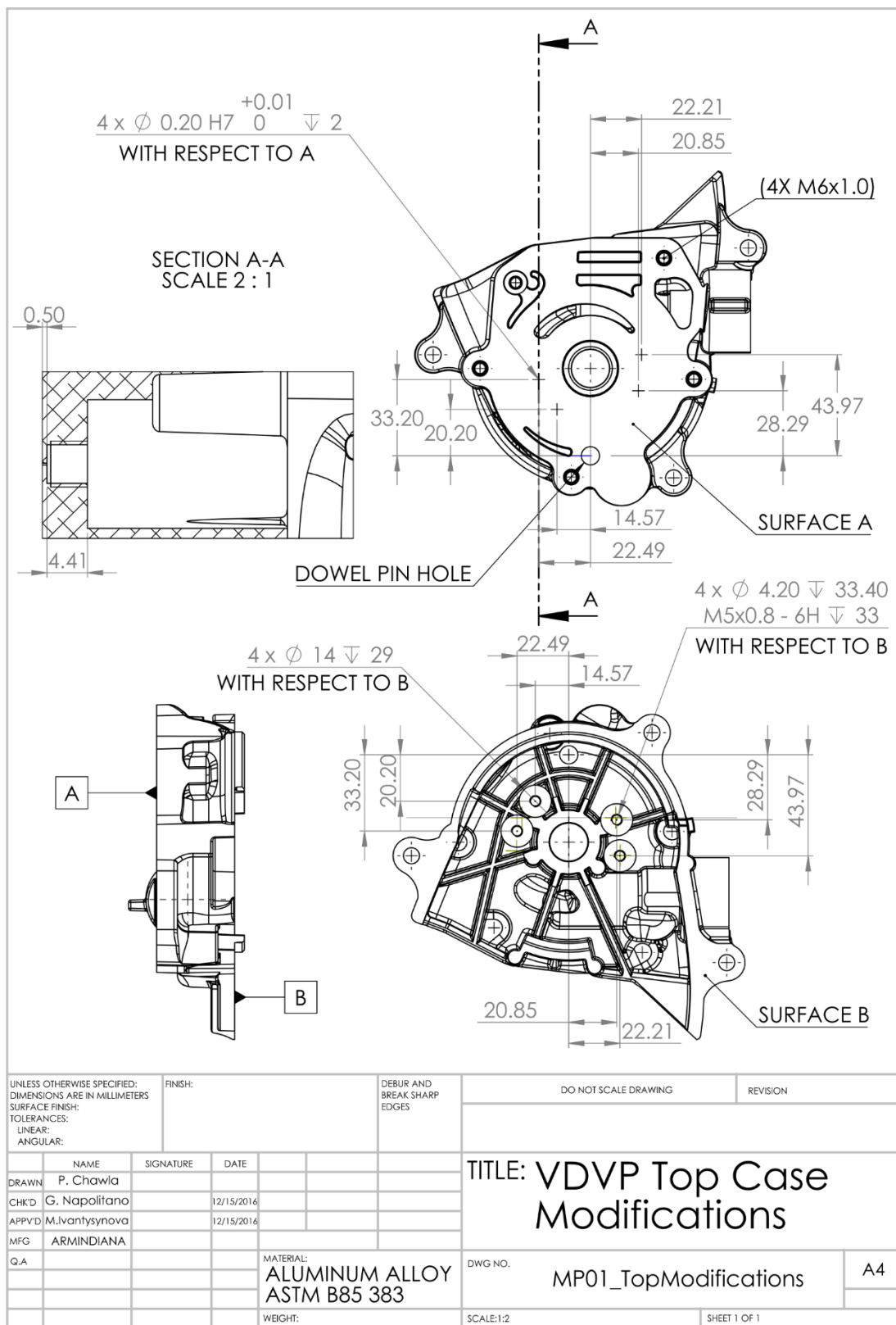
Circuit 4: Hydraulic circuit diagram corresponding to the proposed electrohydraulic control system configuration of the experimental test rig.

APPENDIX B

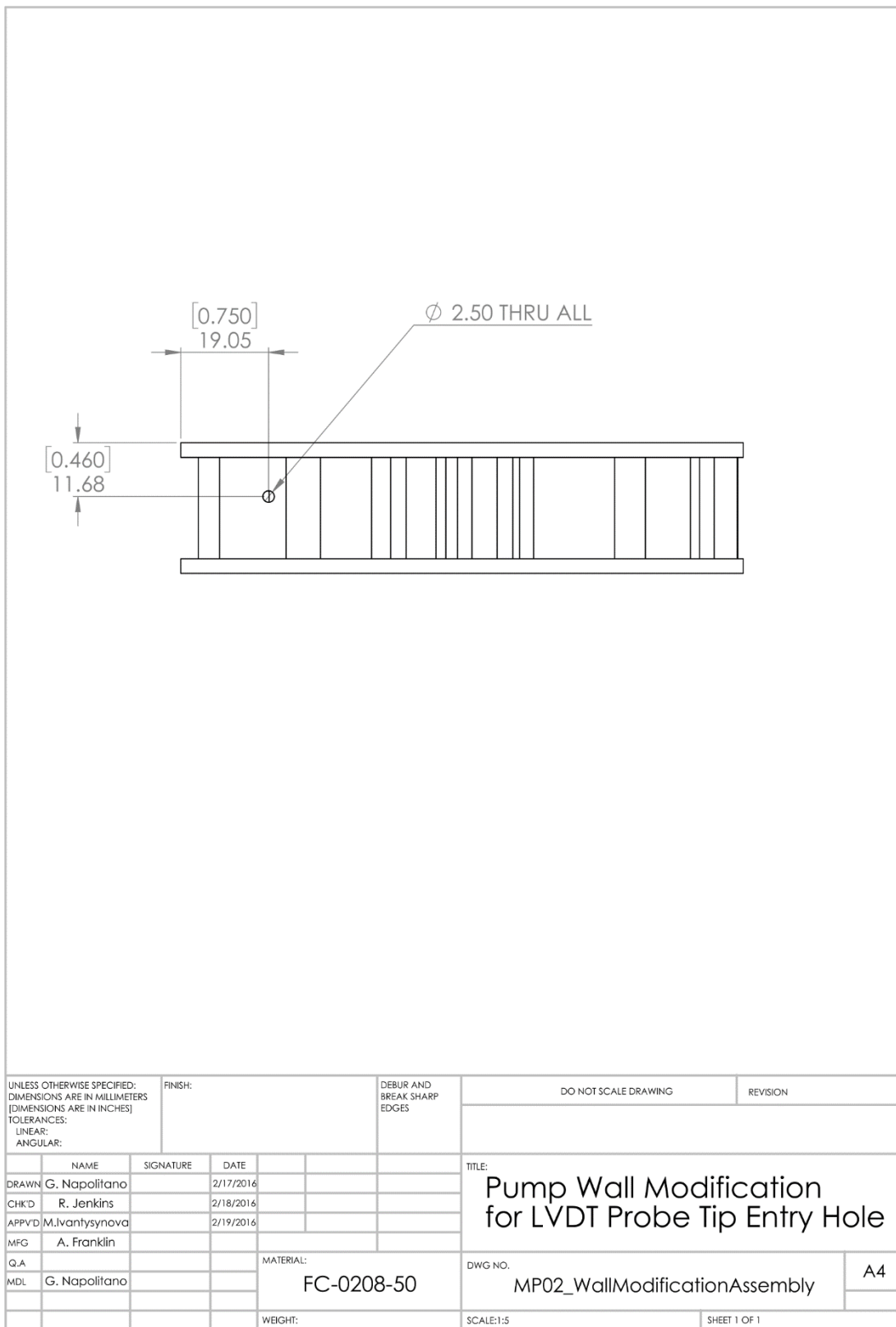
This appendix contains engineering drawings for manufacturing and assembly of the various test rig components designed over the course of this dissertation research. Each drawing is on its own page and the list below provides a “table of contents” for this section.

Drawing 1: Engineering drawing used for machining the four DC pressure transducer mounting holes and their corresponding pilot holes.	184
Drawing 2: Manufacturing assembly drawing for the pump wall modification. Proper orientation in the mill is effected with the plates described in the Drawings 3 and 4.....	185
Drawing 3: Drawing for the top plate used in the pump wall modification.	186
Drawing 4: Drawing for the bottom plate used in the pump wall modification.	187
Drawing 5: Engineering drawing for the custom LVDT probe tip.....	188
Drawing 6: Assembly drawing and shaft modification details.....	189
Drawing 7: Manufacturing drawing for the pump shaft extension.....	190
Drawing 8: Manufacturing drawing for the inlet adapter block used to locate the LVDT and provide pump inlet instrumentation.....	191
Drawing 9: Manufacturing drawing for the mounting bracket used to secure the inlet port adapter block to the pump case via existing pump bolts and bolt locations.....	192
Drawing 10: Pump mounting flange assembly drawing giving overall geometric constraints for the finished welded piece.....	193
Drawing 11: Sheet 1 of the engineering drawing for the main plate of the pump mounting flange giving overall dimensions.	194
Drawing 12: Sheet 2 of the engineering drawing for the main plate of the pump mounting flange defining the pump mounting features.	195
Drawing 13: Sheet 3 of the engineering drawing for the main plate of the pump mounting flange giving details for the tank component mounting holes.....	196
Drawing 14: Sheet 4 of the engineering drawing for the main plate of the pump mounting flange defining the loading servovalve mounting features.	197
Drawing 15: Manufacturing drawing for the bottom plate of the pump mounting flange.	198

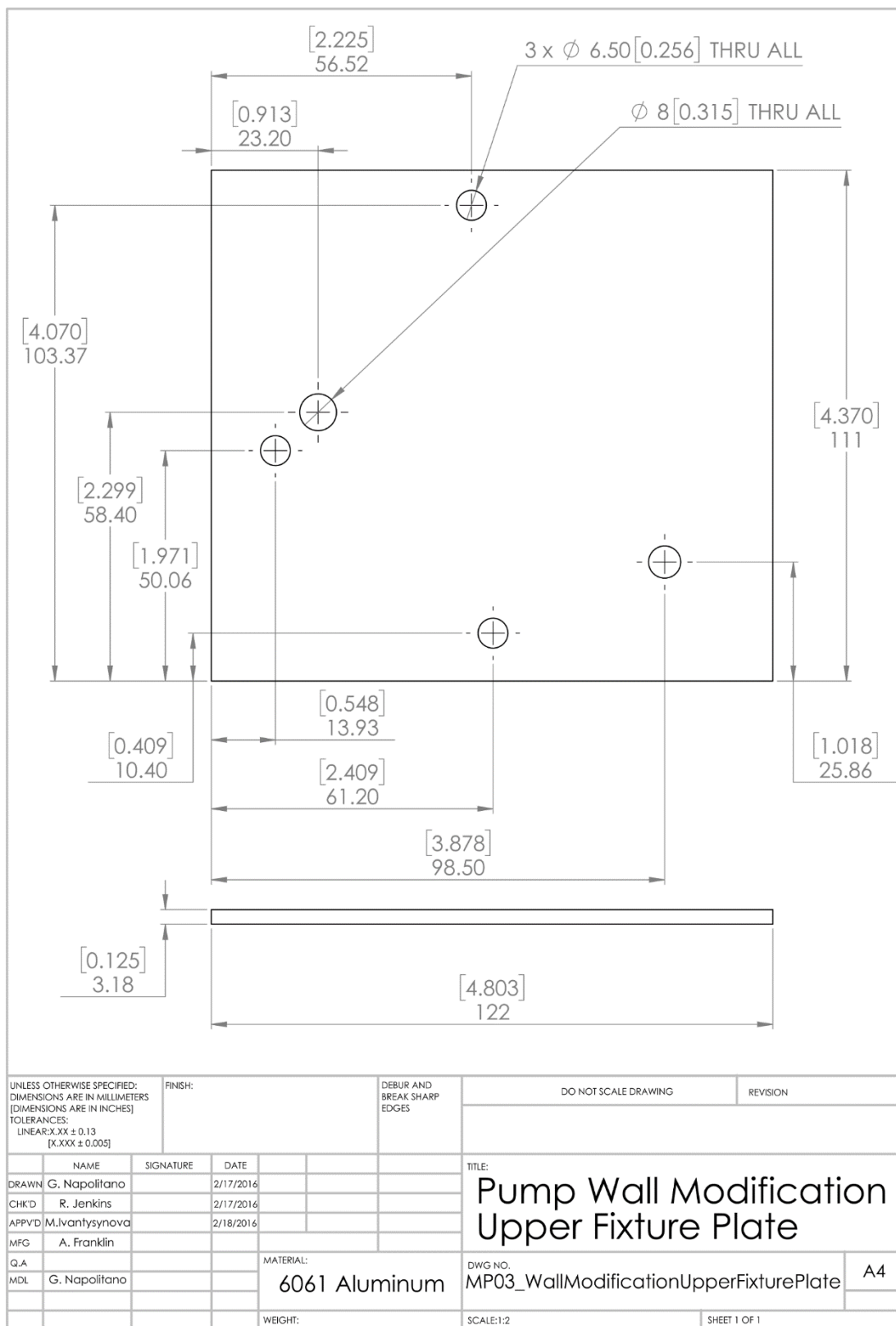
Drawing 16: Manufacturing drawing for the tank bottom plate.	199
Drawing 17: Engineering drawing for the polycarbonate tank wall piece.	200
Drawing 18: Engineering drawing for the polycarbonate top cover to the tank.....	201
Drawing 19: Engineering drawing for the polycarbonate dividing wall inside the tank.	202
Drawing 20: Manufacturing drawing for the bearing plate.	203
Drawing 21: Manufacturing drawing for the return line port adapter block.	204
Drawing 22: Assembly drawing for the bearing and shaft seal assembly.	205
Drawing 23: Manufacturing drawing for the Line A port adapter block interfacing with the loading servovalve pattern.	206
Drawing 24: Manufacturing drawing for the return line port adapter block.	207
Drawing 25: Manufacturing drawing for the adapter plate used in the stator dynamics study providing standard port features for a pressure control valve.....	208
Drawing 26: Pump outlet plug for use in the pump port adapter block in Circuit 3.	209
Drawing 27: Manufacturing drawing for the adapter plate used in the proposed solution study providing mounting features for a control valve.....	210



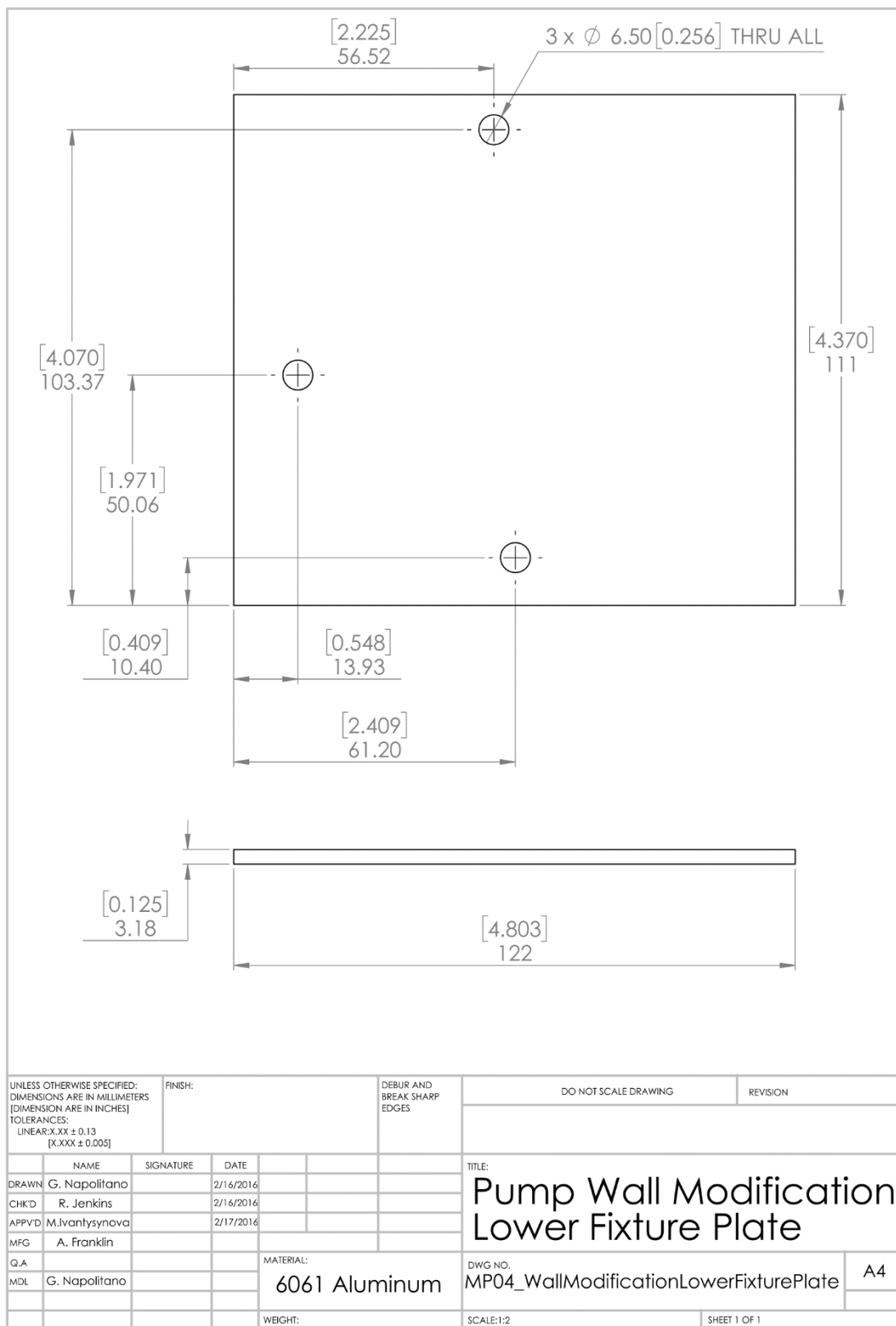
Drawing 1: Engineering drawing used for machining the four DC pressure transducer mounting holes and their corresponding pilot holes.



Drawing 2: Manufacturing assembly drawing for the pump wall modification. Proper orientation in the mill is effected with the plates described in the Drawings 3 and 4.

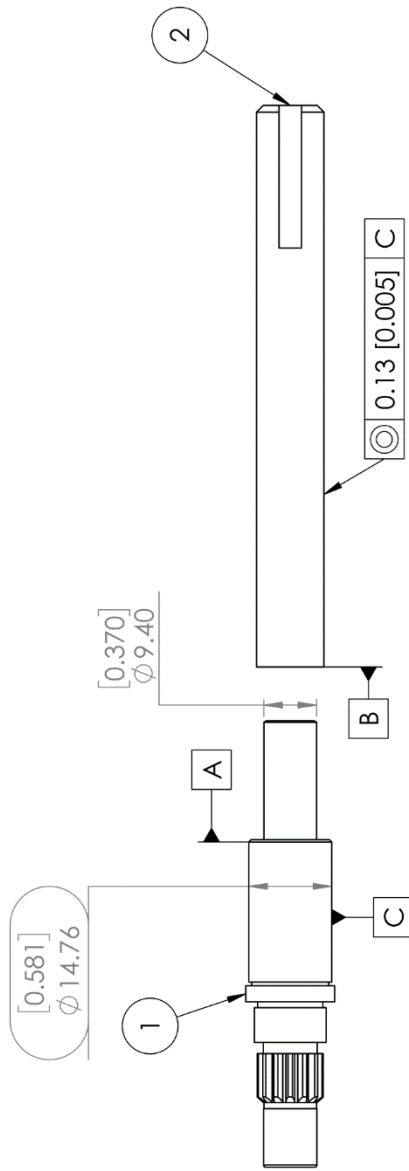


Drawing 3: Drawing for the top plate used in the pump wall modification.



Drawing 4: Drawing for the bottom plate used in the pump wall modification.

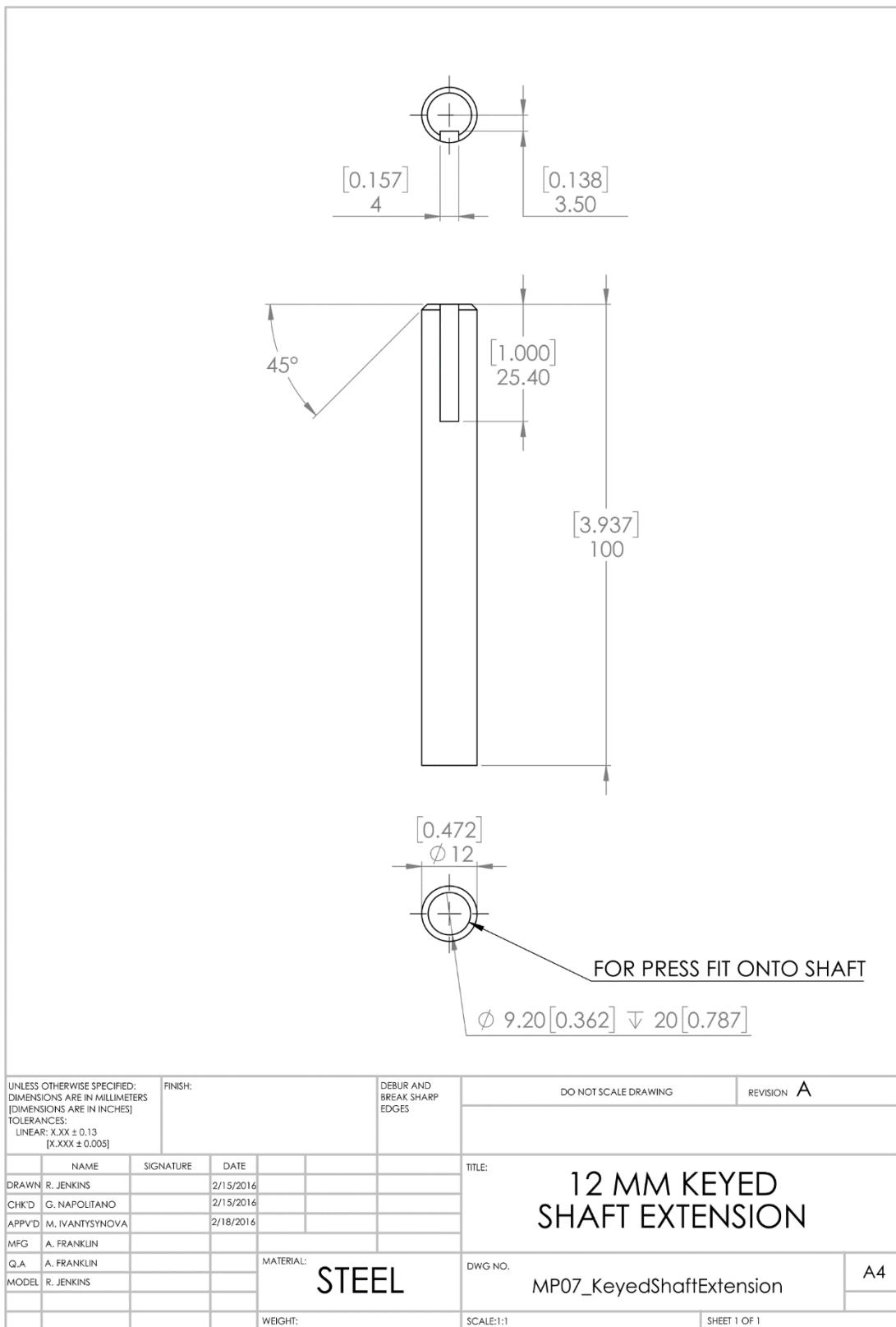
ITEM NO.	PART NUMBER	DESCRIPTION	QTY.
1	VDVP SHAFT	Standard shaft modified by turning the splines off down to dimension shown.	1
2	SHAFT EXTENSION	Ø12 mm Standard shaft stock machined to print per the drawing "12 MM KEYED SHAFT EXTENSION".	1



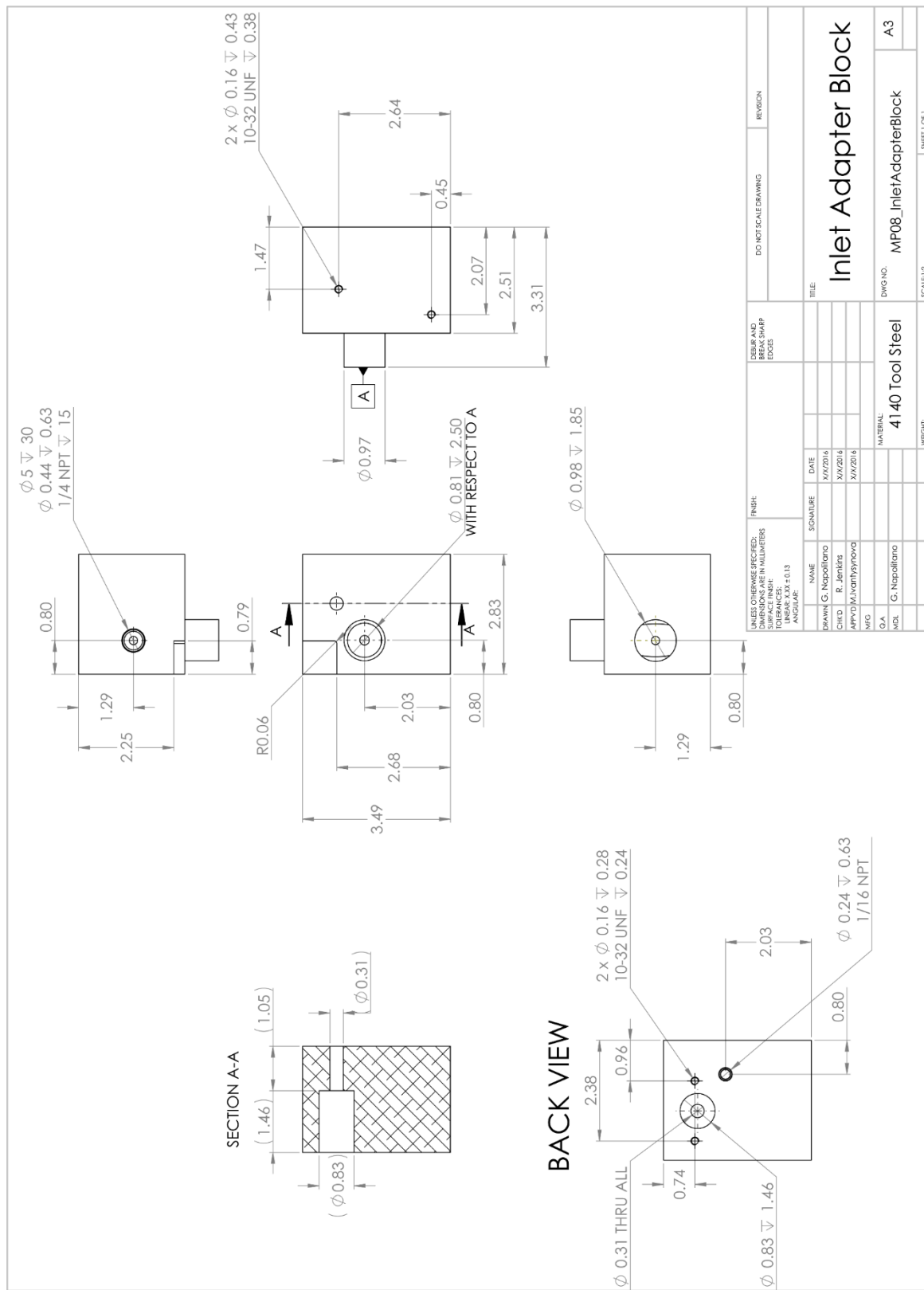
- ASSEMBLY ORDER:**
1. PRESS SHAFT EXTENSION ONTO VDVP SHAFT.
 2. WELD PARTS TOGETHER BETWEEN EDGES A AND B.
 3. TURN DOWN WELD AREA TO REFERENCE DIMENSION OF FACE C.

UNLESS OTHERWISE SPECIFIED: DIMENSIONS ARE IN MILLIMETERS DIMENSIONS ARE IN INCHES		FINISH:		DEBUR AND BREAK SHARP EDGES		DO NOT SCALE DRAWING		REVISION	
TOLERANCES:		LINEAR: X.XX ± 0.13 [K.XXX ± 0.005]						A	
NAME	SIGNATURE	DATE	TITLE:						
DRAWN R. JENKINS		2/16/2016	Modified Pump Shaft Assembly						
CHKD. G. NAPOLIANO		2/16/2016	DWG NO.						
APPVD. M. WANTSYNOVA		4/16/2016	MP06_ModifiedShaftAssembly						
MFG. A. FRANKLIN			SCALE:1:1						
Q.A. A. FRANKLIN			WEIGHT:						
MODEL R. JENKINS			SHEET 1 OF 1						

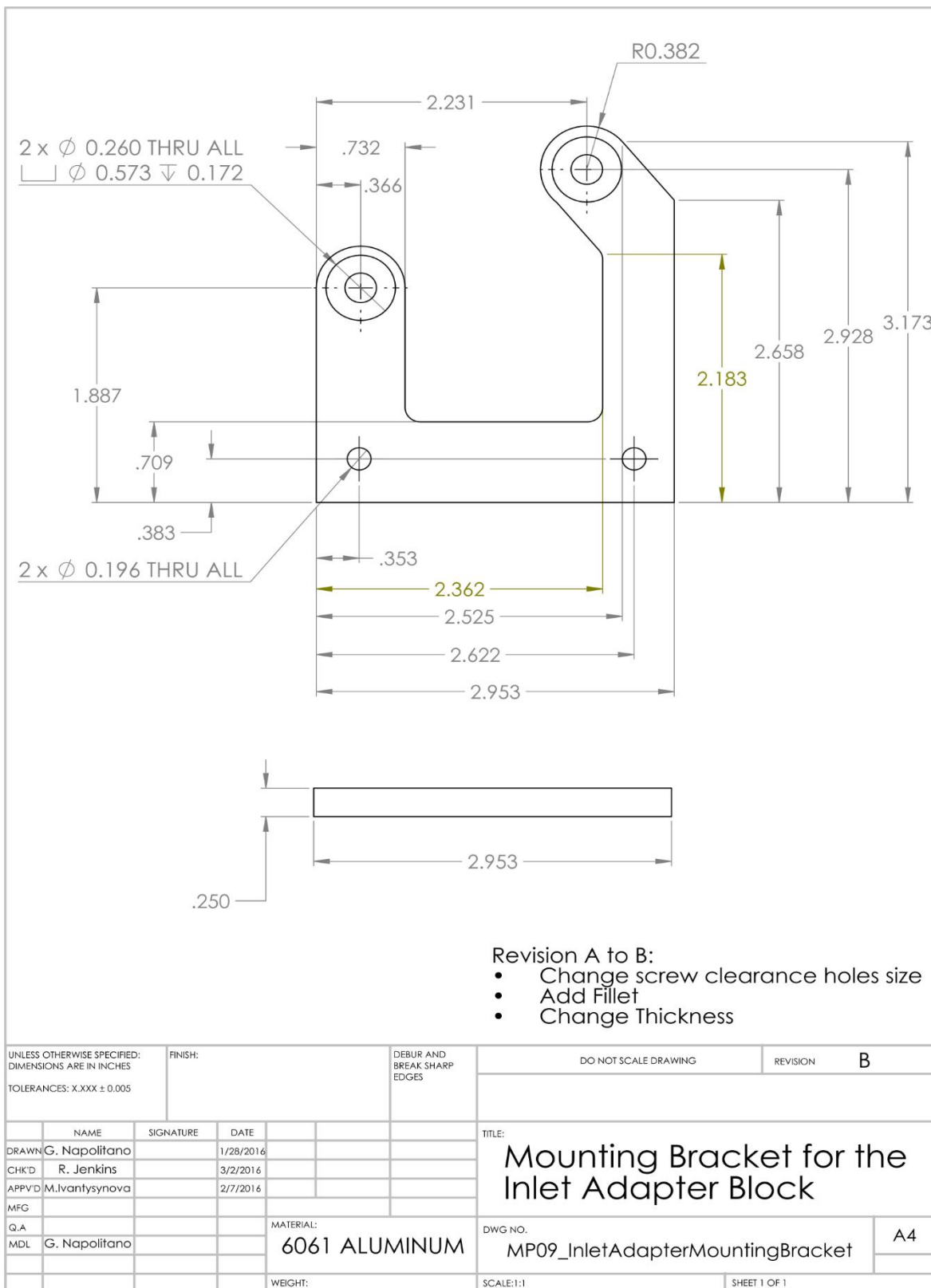
Drawing 6: Assembly drawing and shaft modification details.



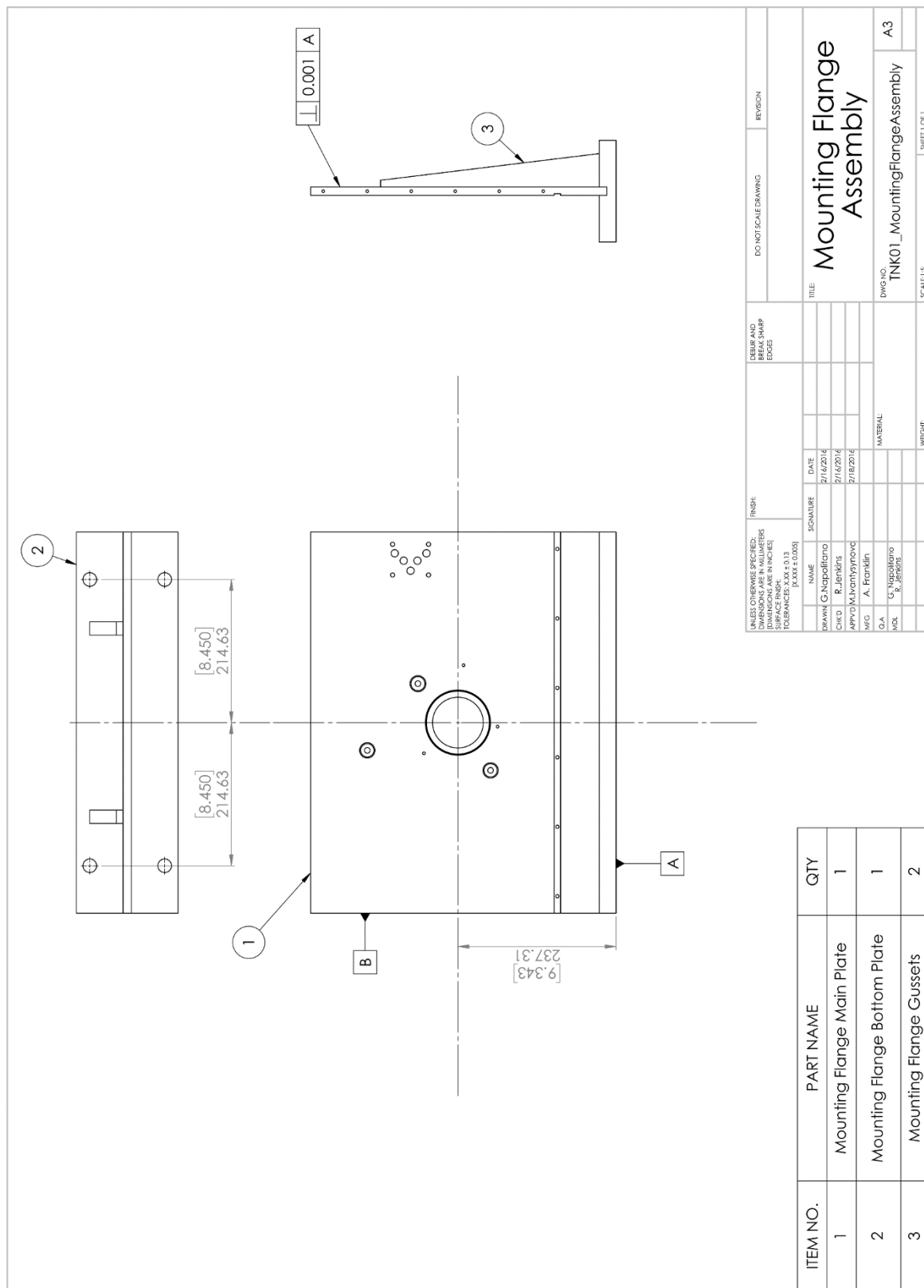
Drawing 7: Manufacturing drawing for the pump shaft extension.



Drawing 8: Manufacturing drawing for the inlet adapter block used to locate the LVDT and provide pump inlet instrumentation.



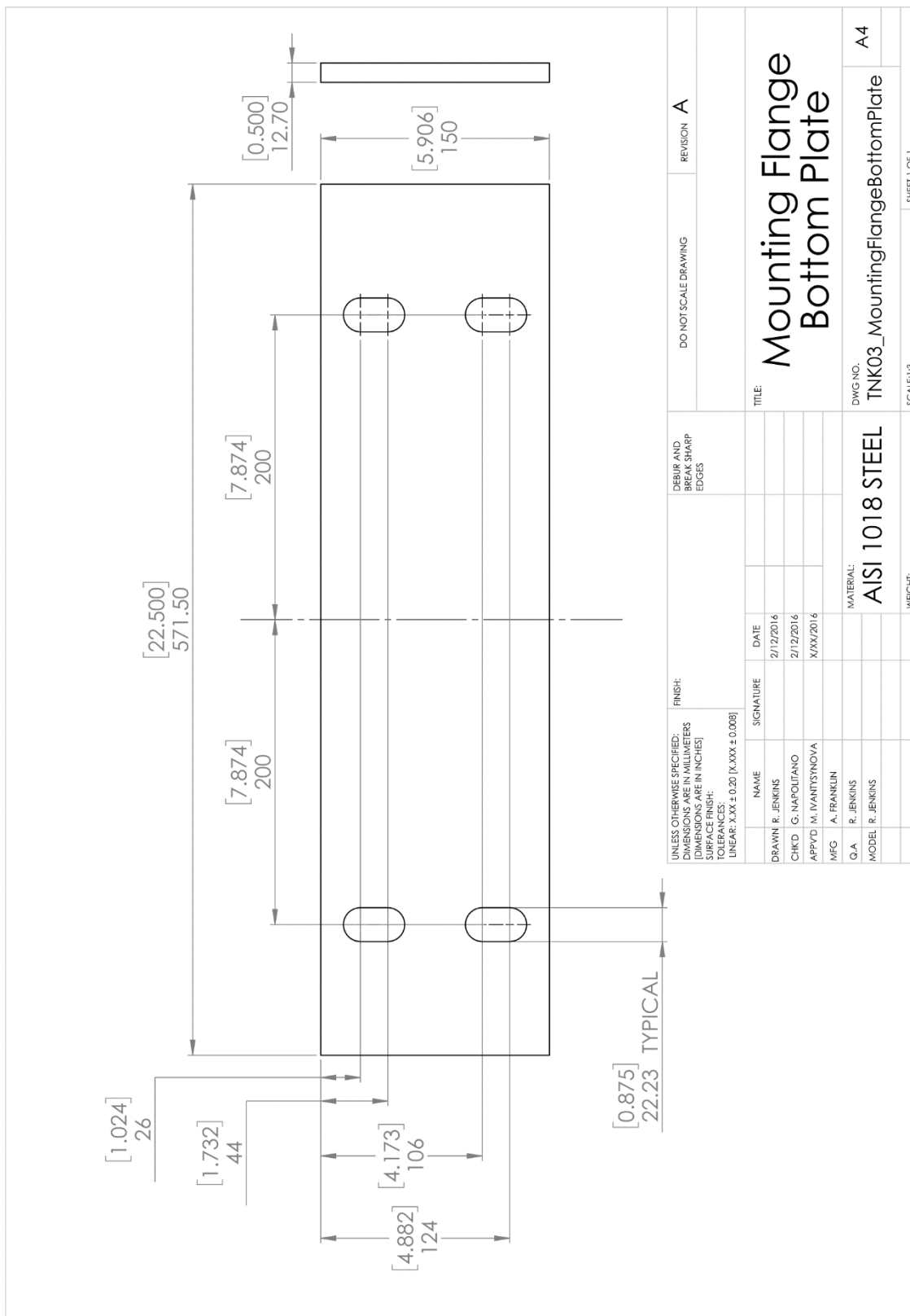
Drawing 9: Manufacturing drawing for the mounting bracket used to secure the inlet port adapter block to the pump case via existing pump bolts and bolt locations.



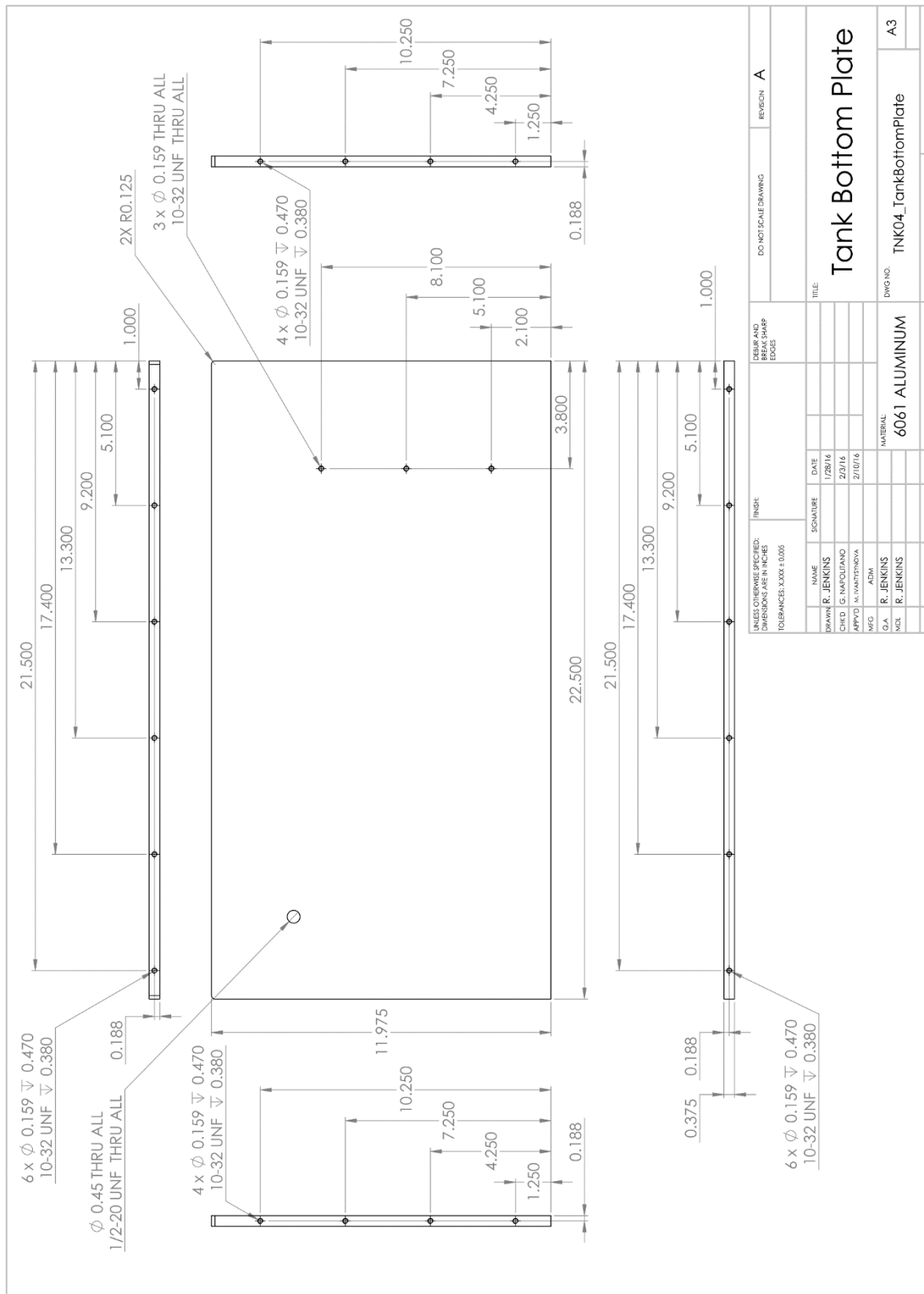
ITEM NO.	PART NAME	QTY
1	Mounting Flange Main Plate	1
2	Mounting Flange Bottom Plate	1
3	Mounting Flange Gussets	2

UNLESS OTHERWISE SPECIFIED: DIMENSIONS ARE IN MILLIMETERS (DIMENSIONS IN PARENTHESES ARE IN INCHES) SURFACE FINISH: TOLERANCES: XXXX ± 0.13 (XXX ± 0.005)		FINISH:	DEBURK AND BREAK SHARP EDGES	DO NOT SCALE DRAWING	REGION
DRAWN: G. Napolitano	DATE: 2/16/2016	SIGNATURE:			
CHECKED: R. Jenkins	DATE: 2/16/2016				
APP'D: M. Vanhyning	DATE: 2/18/2016				
MFG: A. Franklin					
G.A.					
MOL: C. Napolitano R. Jenkins					
TITLE: Mounting Flange Assembly			DWG. NO. TNK01_MountingFlangeAssembly		
			SCALE: 1:1		
			SHEET 1 OF 1		

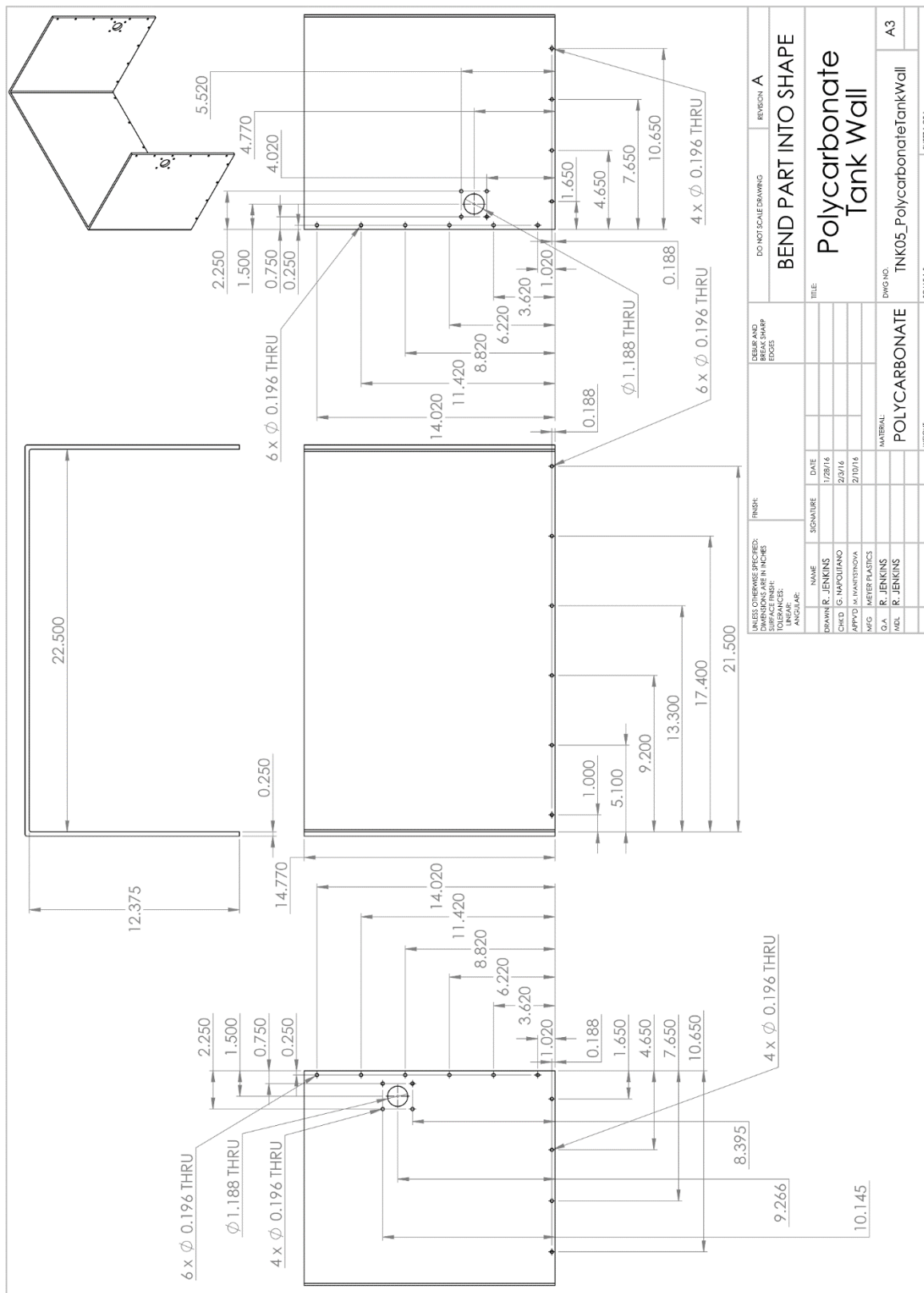
Drawing 10: Pump mounting flange assembly drawing giving overall geometric constraints for the finished welded piece.



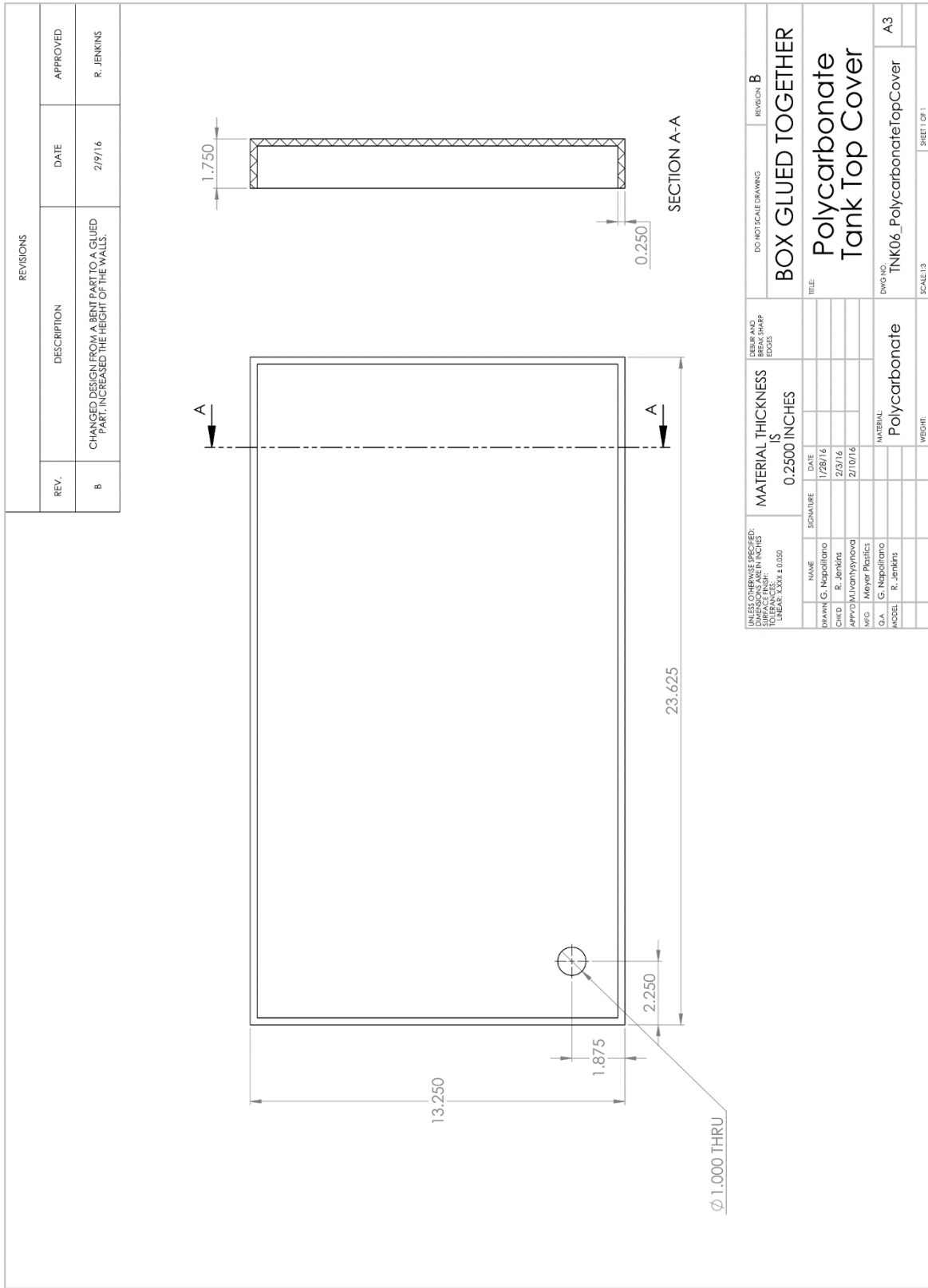
Drawing 15: Manufacturing drawing for the bottom plate of the pump mounting flange.



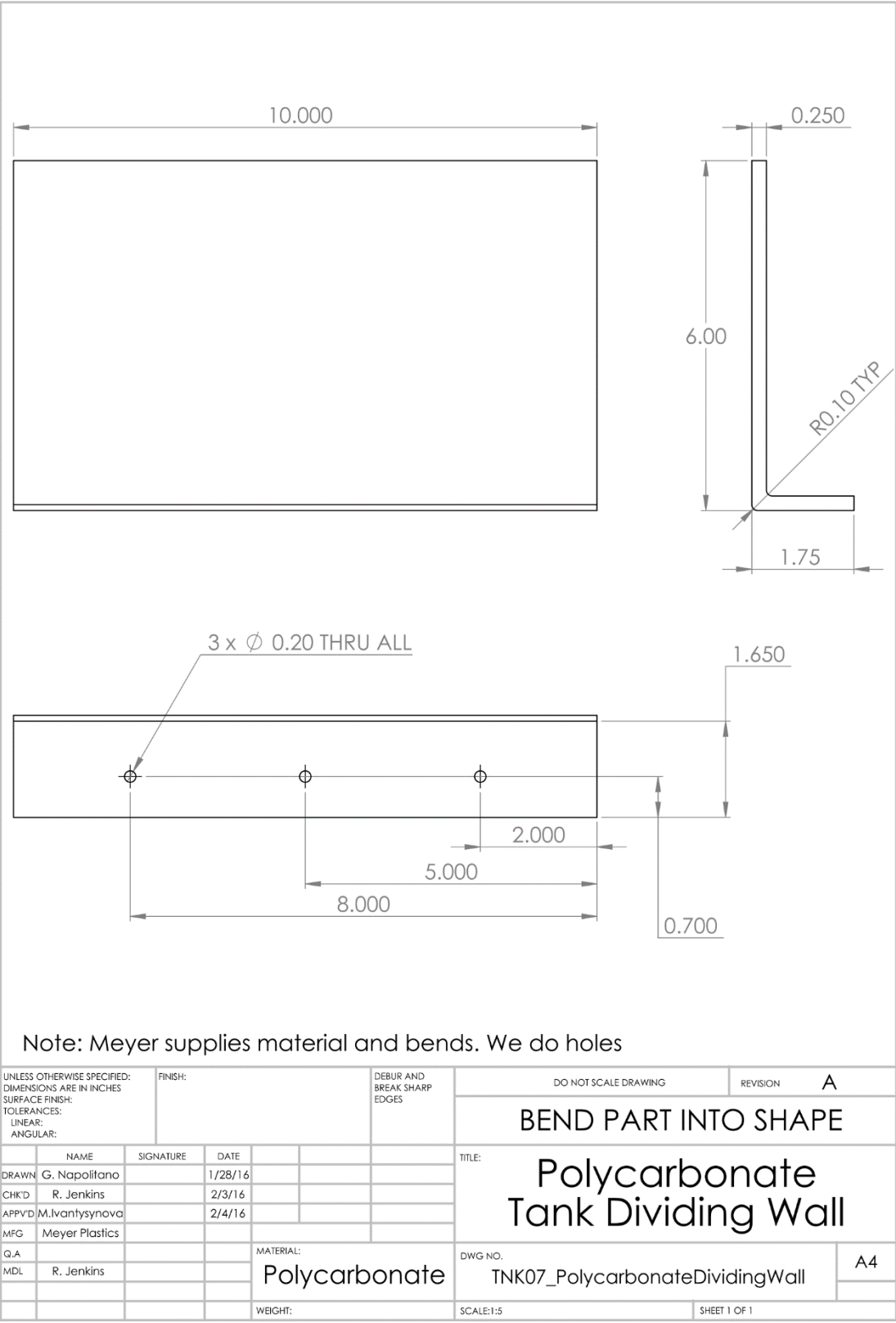
Drawing 16: Manufacturing drawing for the tank bottom plate.



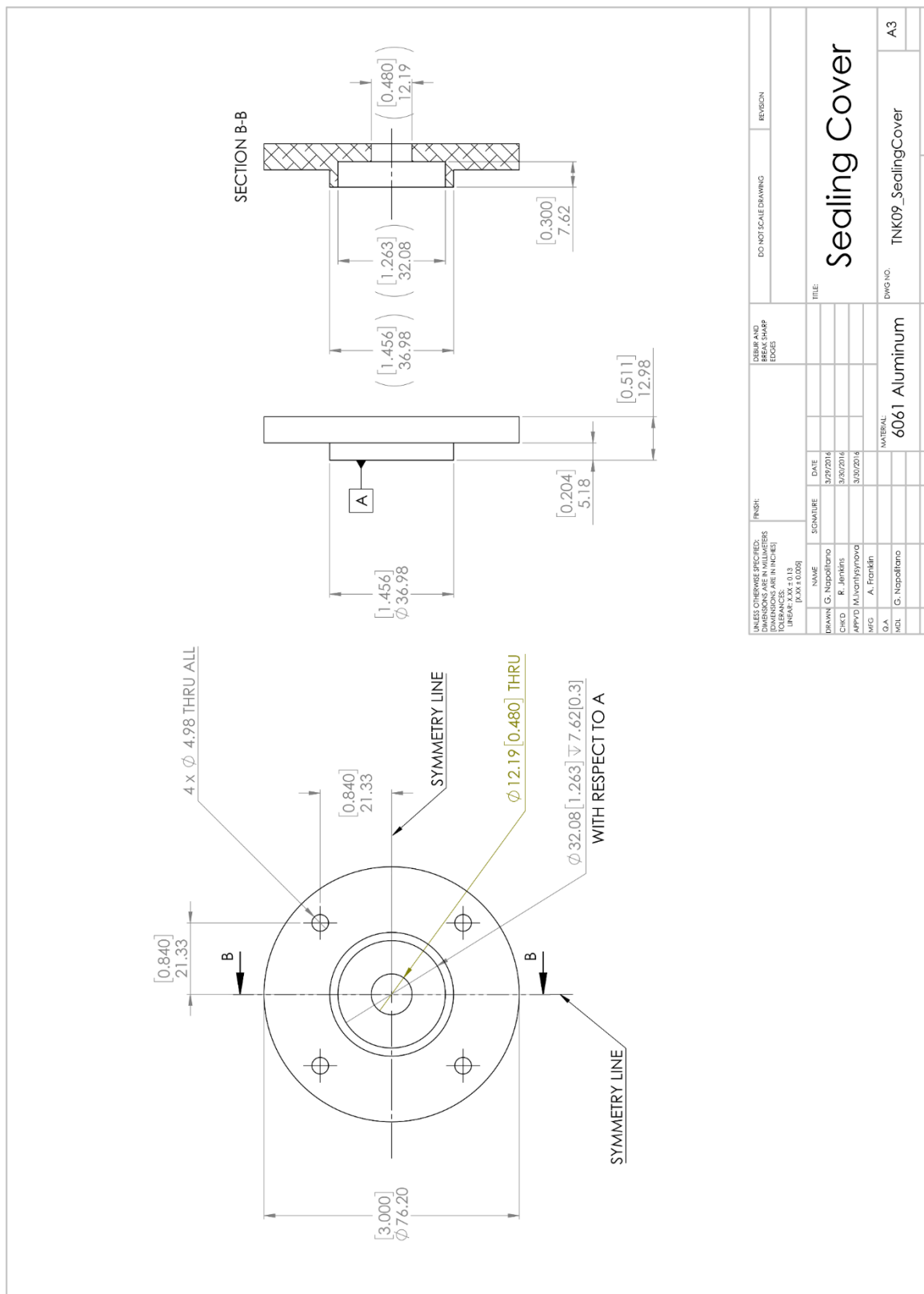
Drawing 17: Engineering drawing for the polycarbonate tank wall piece.



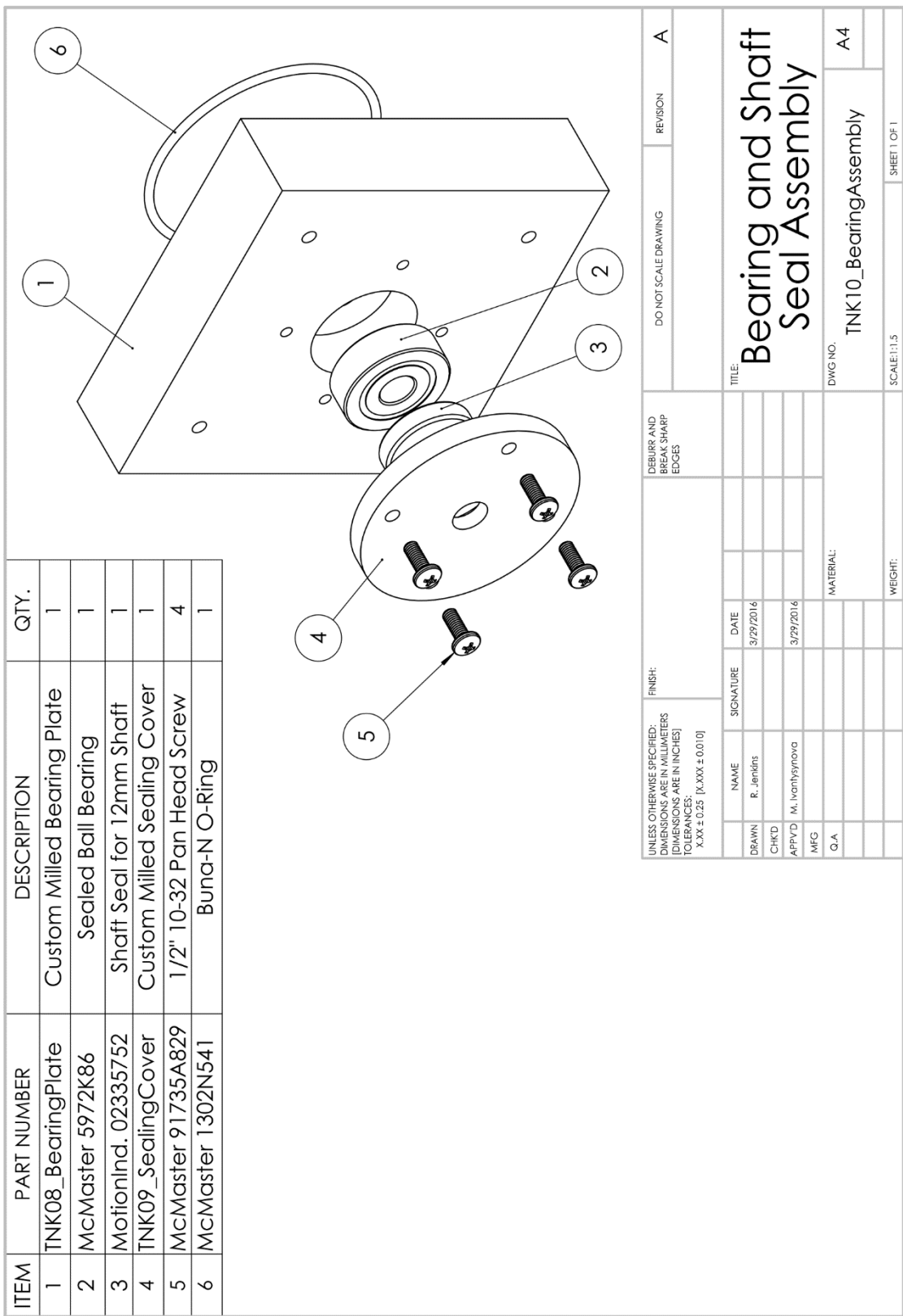
Drawing 18: Engineering drawing for the polycarbonate top cover to the tank.



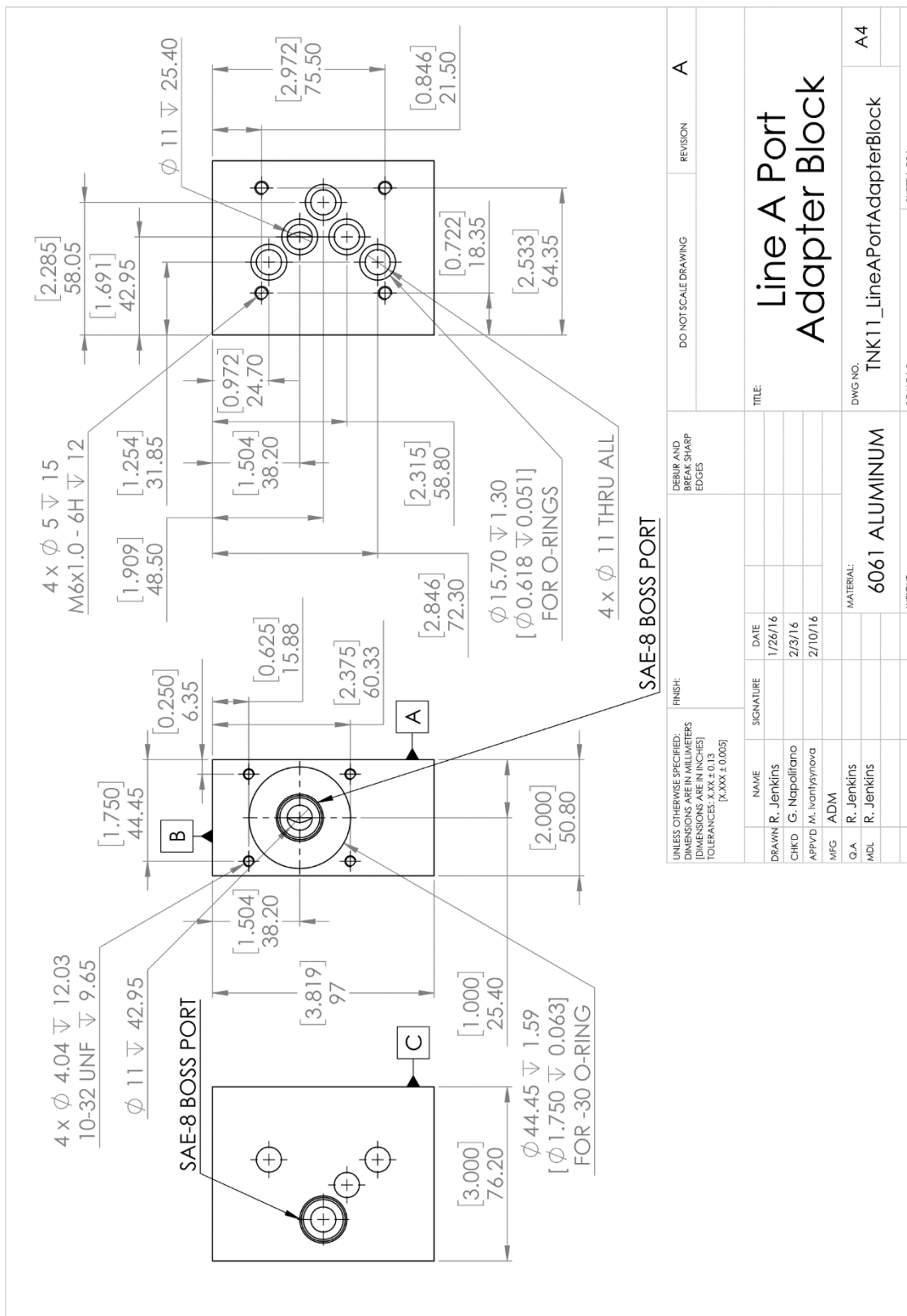
Drawing 19: Engineering drawing for the polycarbonate dividing wall inside the tank.



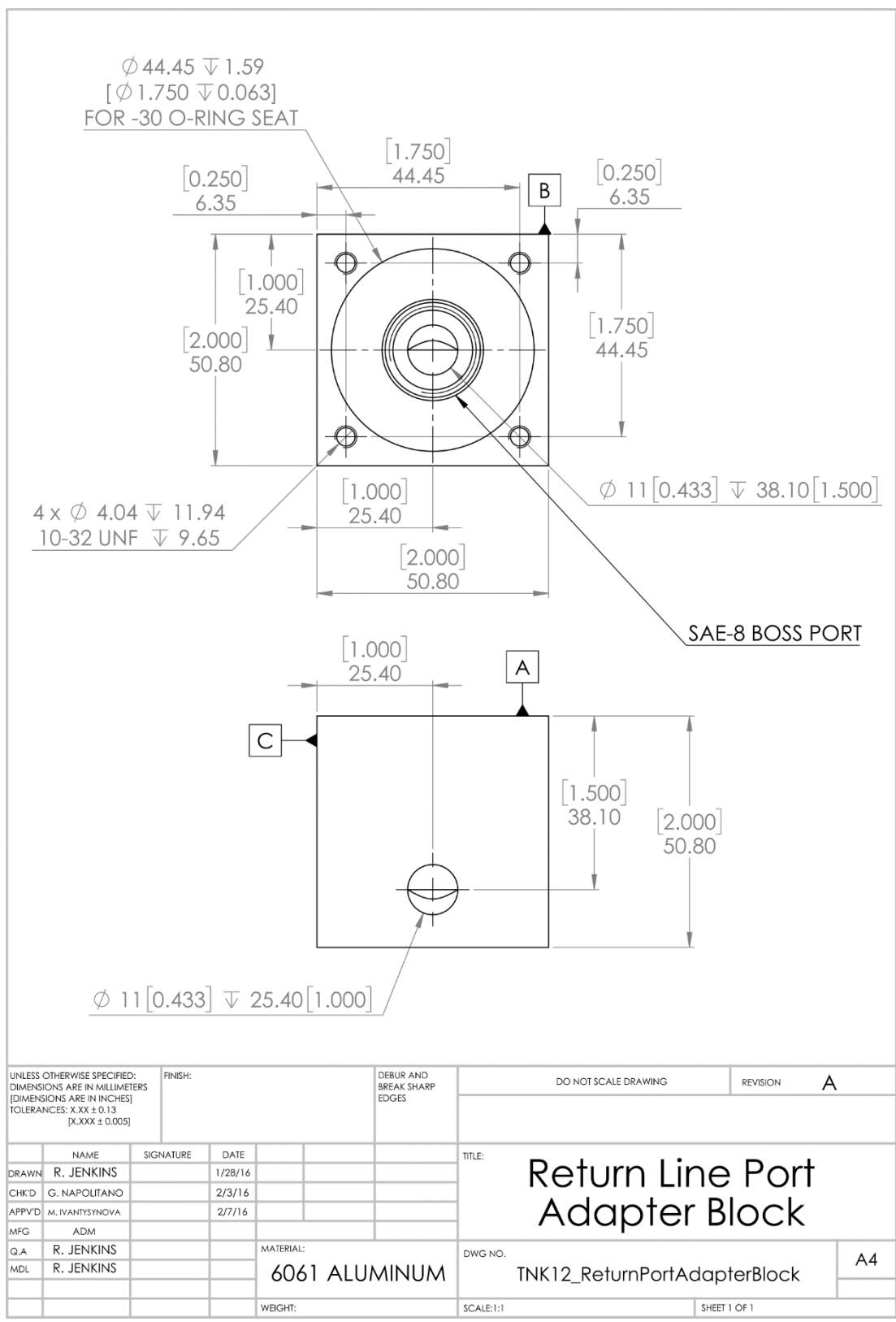
Drawing 21: Manufacturing drawing for the return line port adapter block.



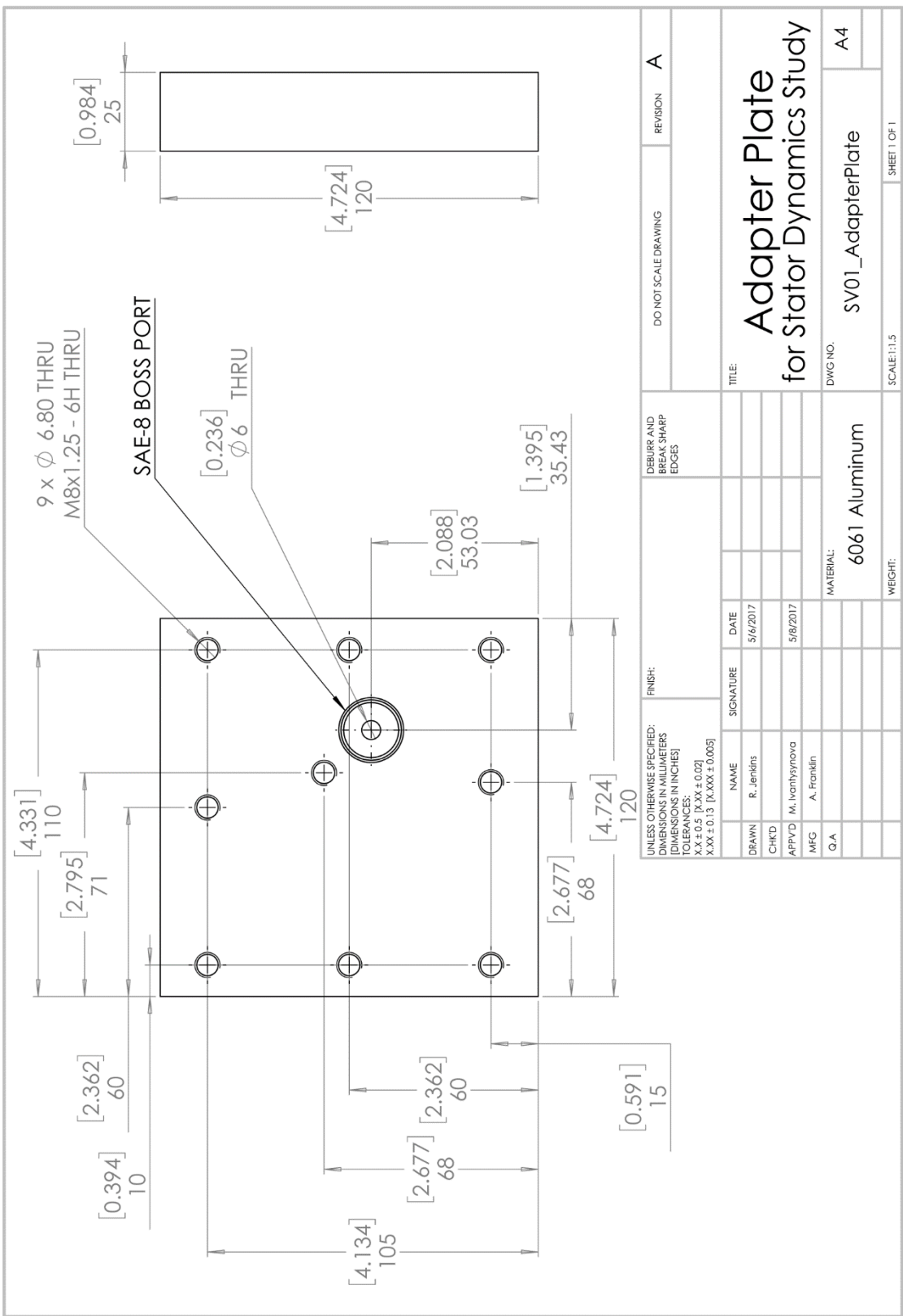
Drawing 22: Assembly drawing for the bearing and shaft seal assembly.



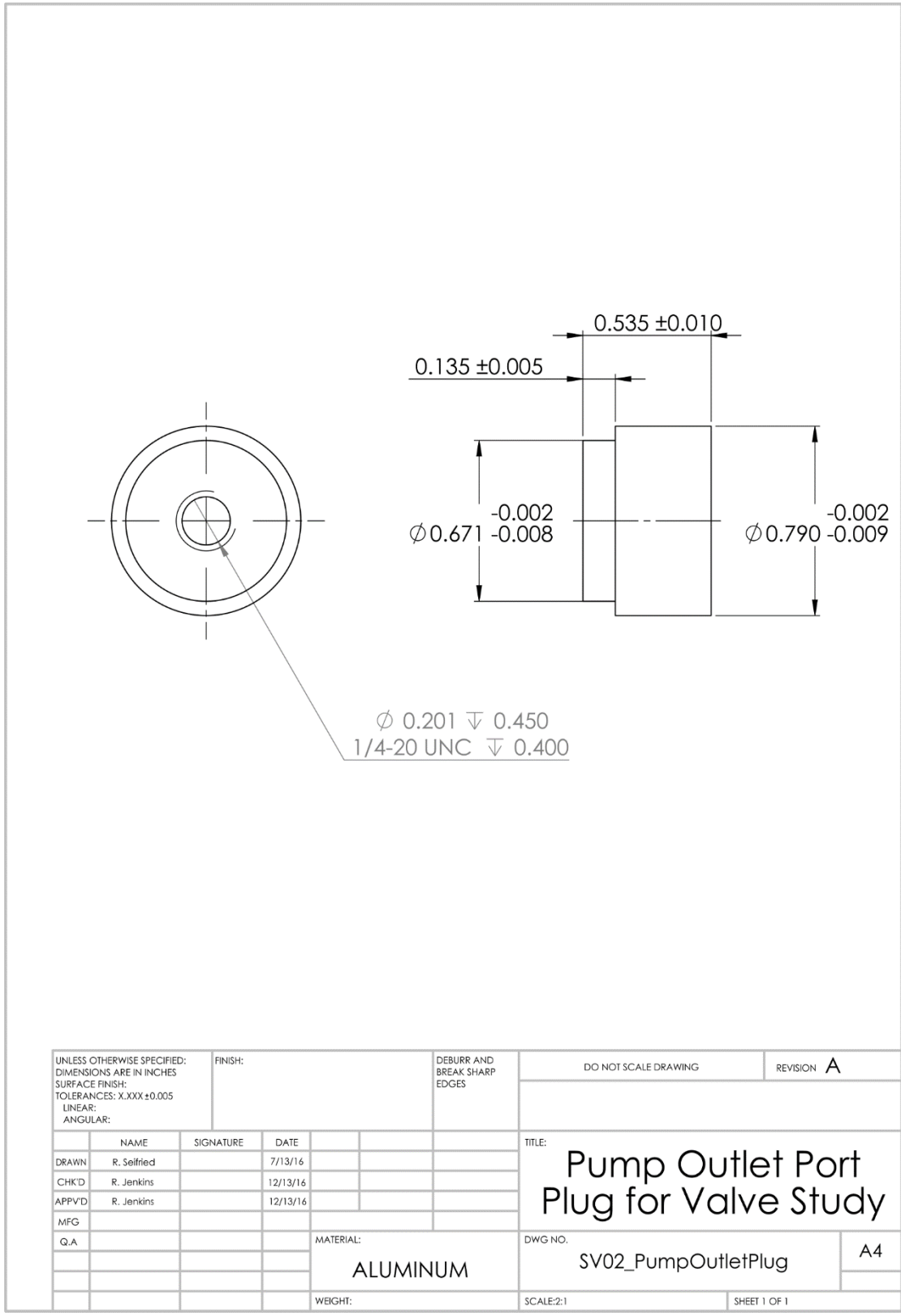
Drawing 23: Manufacturing drawing for the Line A port adapter block interfacing with the loading servovalve pattern.



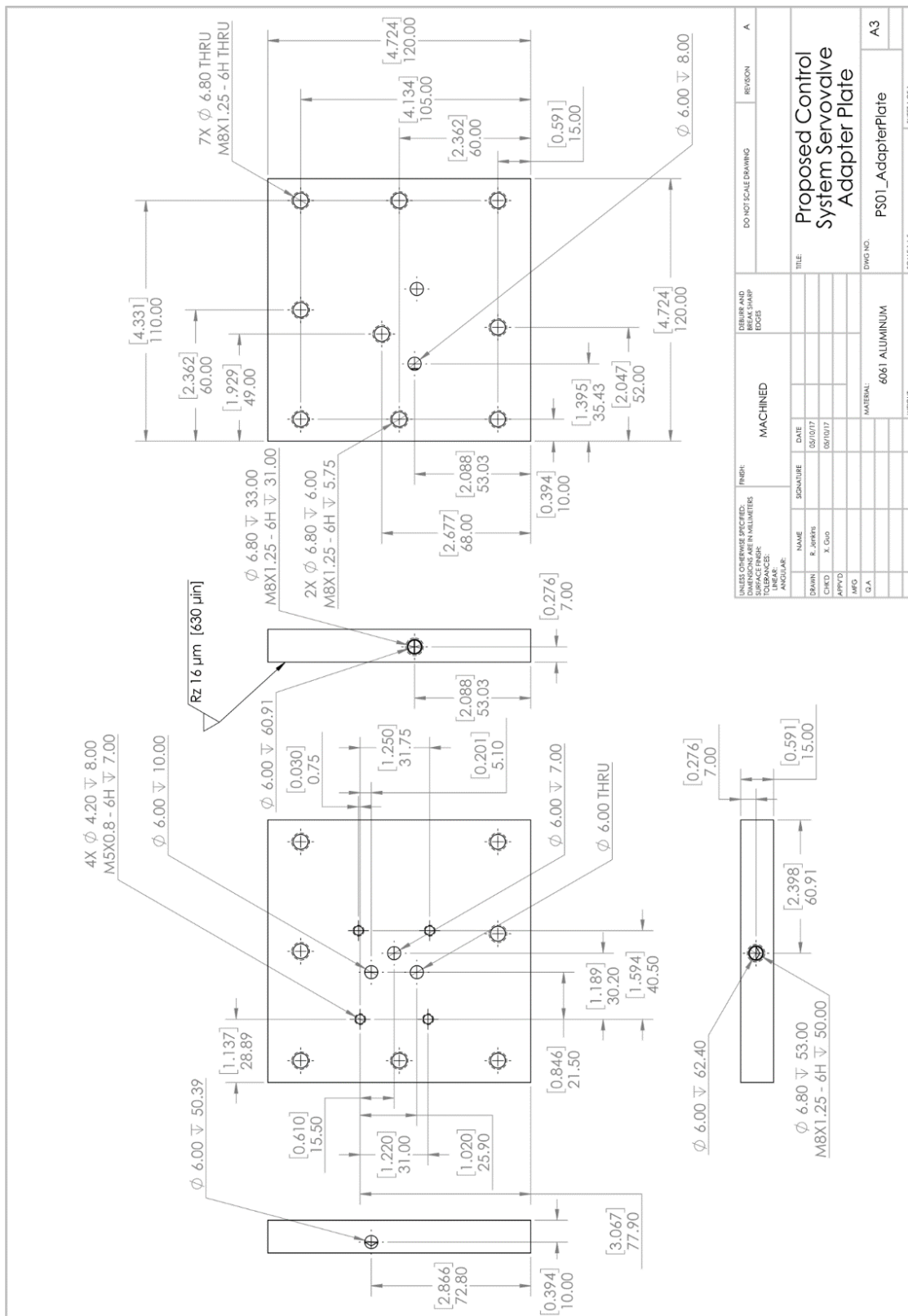
Drawing 24: Manufacturing drawing for the return line port adapter block.



Drawing 25: Manufacturing drawing for the adapter plate used in the stator dynamics study providing standard port features for a pressure control valve.



Drawing 26: Pump outlet plug for use in the pump port adapter block in Circuit 3.

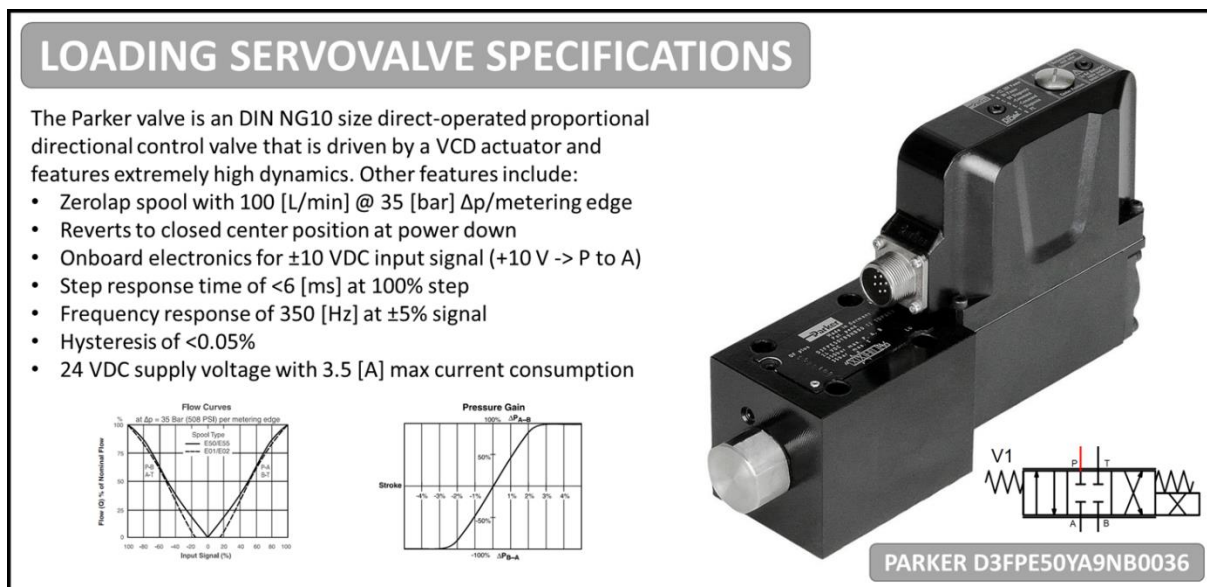


Drawing 27: Manufacturing drawing for the adapter plate used in the proposed solution study providing mounting features for a control valve.

APPENDIX C

This appendix consists of specification summaries for the valves and some of the electronic components used in the experimental work of this dissertation.

This page includes a summary of the loading servovalve specifications. The next page provides summaries of other components used in the model validation studies. The page following that provides the specifications summaries for the control valve used in the experimental proof of concept work for the proposed electrohydraulic solution.



VALVE DRIVER SPECIFICATIONS

The Lynch LE PDC proportional valve driver accepts a proportional voltage signal input and outputs a proportional current signal at a voltage level of the user's choice. Features include:

- Maximum current output adjustable from 0.20-3.00 [A]
- Operating voltage range of 9-36 [VDC]
- Adjustable ramp time from 0-99.5 [s]
- Adjustable dither/PWM frequency from 40-450 [Hz]
- Linearity error of 1%
- Current sensing to maintain output regardless of changes in supply voltage and coil resistance

Settings for V3 Control
 PWM frequency of 450 [Hz]
 Maximum current of 1 [A]



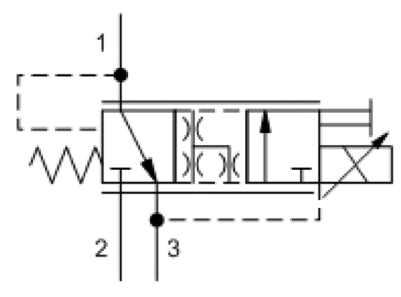
LYNCH LE PDX

PRESSURE CONTROL VALVE SPECIFICATIONS

This Sun Hydraulics valve is an electro-proportional, direct-acting, pressure reducing/relieving valve with an open transition. The cartridge valve is installed in a standard ECA model manifold.

Features for the selected configuration include:

- Operating range of 0.7-7 [bar]
- Flow capacity of 20 [L/min]
- Maximum valve leakage of 330 [cc/min]
- Linearity error less than 2% with a dither frequency of 140 [Hz]
- Hysteresis (with dither) of 6%
- Maximum supply pressure of 350 [bar]



M-Control

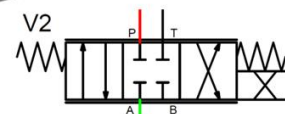
Valve V2 used in the cam dynamics validation setup given in Circuit 2.

SUN PRDLMSN224-ECA

CONTROL SERVOVALVE SPECIFICATIONS

The Moog valve is a Mini-DDV (Direct Drive Valve) with a permanent magnet linear force motor which can actively stroke the spool from its spring centered position in both directions. This valve has the following characteristics:

- 3% Overlap spool configuration sized for a flowrate of 10 [L/min] @ 35 [bar] Δp /metering edge
- No onboard electronics resulting in an input signal of ± 1000 [mA] for full stroke
- 24 VDC operating voltage
- Reverts to center position at power down
- Step response of < 5 [ms] for 100% step
- Hysteresis of $< 10\%$
- Frequency response of 60 [Hz] @ up to 50% stroke

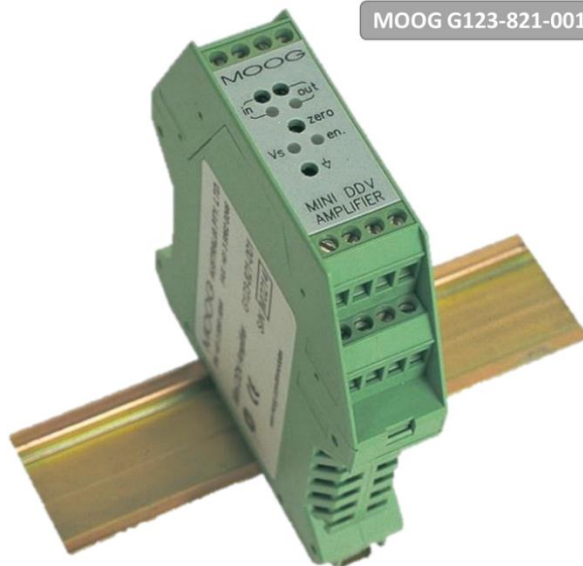


MOOG D633-7104 A04KA4M0VBJ

CONTROL SERVOVALVE AMPLIFIER SPECIFICATIONS

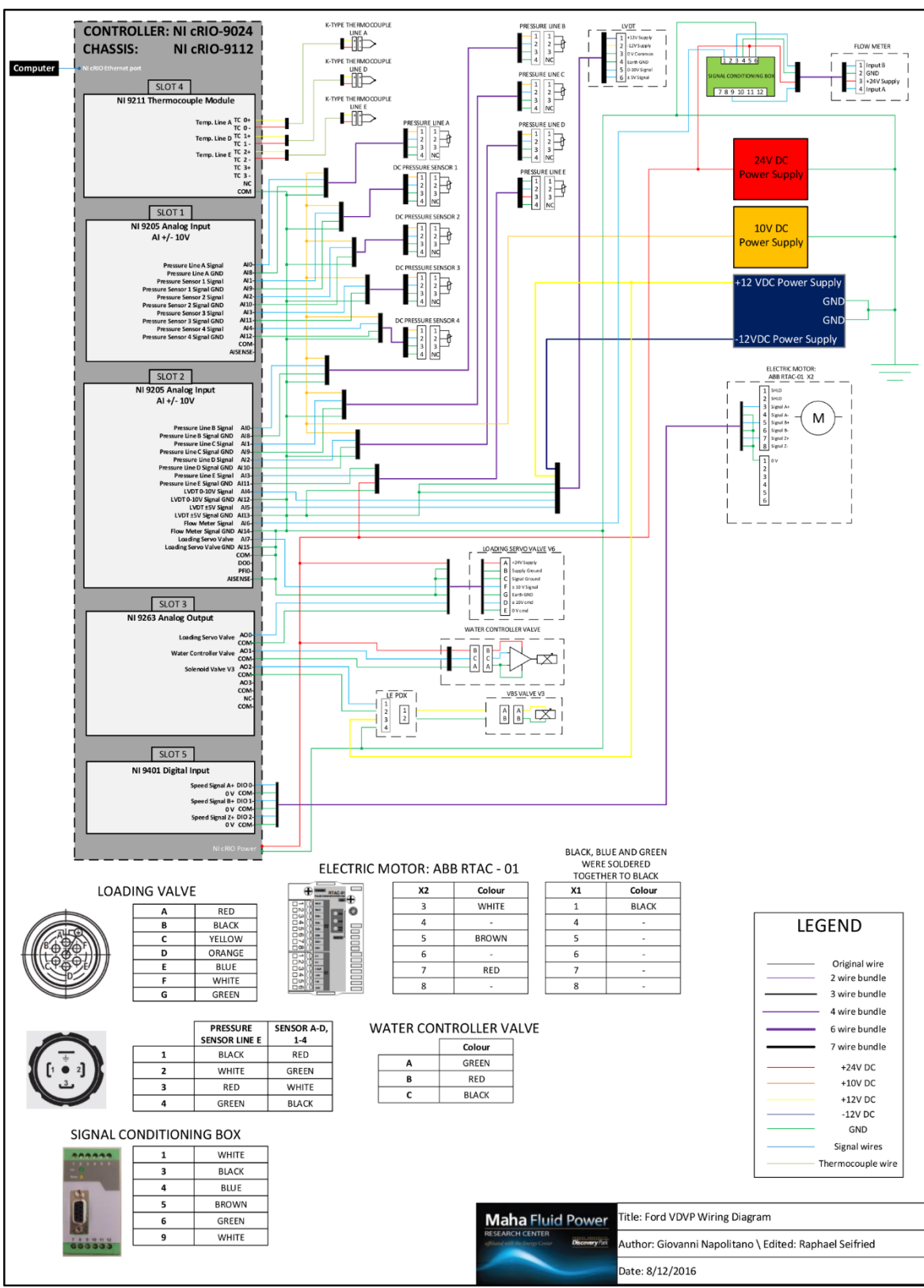
The Moog G123-821-001 Mini-DDV Amplifier has a ± 1 [A] output suitable for bidirectional control of the Moog D633-7 valve. This amplifier has the following characteristics:

- ± 10 VDC input signal for proportional ± 1 [A] output
- 24 VDC operating voltage
- 0 to ± 0.2 [A] Zero adjustment
- Flat frequency response of 100 [Hz] @ ± 1 [A]
- Flat frequency response of 600 [Hz] @ ± 0.4 [A]
- Flat frequency response of 2.0 [kHz] @ ± 0.1 [A]



MOOG G123-821-001

APPENDIX D



VITA

Ryan P. Jenkins

Degrees and Certificates

- B.S. in Mechanical Engineering from Brigham Young University located in Provo, Utah, awarded April 2014 with a cumulative GPA of 3.81. Capstone Project: A 2-DOF robot for the rehabilitation of the range of motion in the wrist joints of stroke patients sponsored by the Edwards Lifesciences Fund.
- Graduate Certificate in Hybrid Vehicle Systems from Purdue University located in West Lafayette, Indiana, awarded May 2017. Poster Title: “A Hardware-in-the-Loop Test Bed for Hydraulic Hybrid Transmission Research.”
- Ph.D. in Mechanical Engineering with an emphasis in Systems, Measurement, and Controls under the supervision of Monika Ivantysynova (Aug. 2014 to Aug. 2018) and Andrea Vacca (Aug. 2018 to Feb. 2019) from Purdue University located in West Lafayette, Indiana, awarded May 2019 with a cumulative GPA of 3.91. Ph.D. Thesis: “An Analysis of a Pressure Compensated Control System of an Automotive Vane Pump.”

Research Experience

- Undergraduate Research Assistant in the Vocal Fold Lab at Brigham Young University in Provo, Utah, from September 2012 to July 2014.
- Graduate Research Assistant at the Maha Fluid Power Research Center at Purdue University in Lafayette, Indiana, from August 2014 to May 2019.

Notable Upper-Level Coursework

- Brigham Young University courses: Applications of Fluid Dynamics (ME412, B+), Kinematics (ME437, A-), CAE Applications (ME471, A-), and Integrated Product and Process Design (ME 475/476, B+/A).
- Purdue University courses: Multidisciplinary Design Optimization (AAE550, A), Vehicle Dynamics (ME565, A+), Design of Control Systems (ME575, A), Design of Fluid Power Systems (ME597, A), Fuzzy Approaches in Engineering (NUCL570, A), Multivariable Control System Design (ME675, A), Adaptive Control (ME689, A-), and Hydraulic Power Trains & Hybrid Systems (ME697, A+)

PUBLICATIONS

Peer Reviewed Conference Publications

- Jenkins, R. and Ivantysynova, M. 2016. Investigation of Instability of a Pressure Compensated Vane Pump. *Proceedings of the 9th FPNI Ph.D. Symposium on Fluid Power*. October 26-28, 2016, Florianópolis, SC, Brazil. FPNI2016-1535. **Recognized Paper Award**
- Jenkins, R. and Ivantysynova, M. 2018. A Semi-Empirical Lumped Parameter Model of a Pressure Compensated Vane Pump. *Proceedings of the 11th IFK International Conference on Fluid Power*, Vol. 1, pp. 168-181. March 19-21, 2018, Aachen, Germany. IFK2018-6009.
- Jenkins, R. and Ivantysynova, M. 2018. An Empirically Derived Pressure Compensation Control System for a Variable Displacement Vane Pump. *Proceedings of the 2018 Bath/ASME Symposium on Fluid Power and Motion Control*. September 12-14, 2018, Bath, United Kingdom. FPMC2018-8857.

Journal Publications

- Jenkins, R.P. and Ivantysynova, M. 2018. A Lumped Parameter Vane Pump Model for System Stability Analysis. *International Journal of Hydromechatronics*, Vol. 1, No. 4, pp. 361-383. DOI 10.1504/IJHM.2018.10018394
- Jenkins, R.P. and Ivantysynova, M. 2019. An Electrohydraulic Pressure Compensation Control System for an Automotive Vane Pump Application. *International Journal of Fluid Power*. **Submitted**